Ab initio Studies on Properties of Nanostructures

By

C. Kamal

(PHYS03200904008)

Raja Ramanna Centre for Advanced Technology, Indore

A thesis submitted to the

Board of Studies in Physical Sciences

In partial fulfillment of requirements

For the Degree of

DOCTOR OF PHILOSOPHY

of

HOMI BHABHA NATIONAL INSTITUTE

January, 2014

Homi Bhabha National Institute

Recommendations of the Viva Voce Board

As members of the Viva Voce Board, we certify that we have read the dissertation prepared by Shri. C. Kamal entitled "*Ab initio* Studies on Properties of Nanostructures" and recommend that it may be accepted as fulfilling the dissertation requirement for the Degree of Doctor of Philosophy.

Date: 18.7.2015

Chairman - Dr. S. B. Roy

Aparna Chakrabarti **Date:** 18.7.2014

Guide / Convener - Dr. Aparna Chakrabarti

Arup Banerjee **Date:** 18.07.2014

Member - Dr. Arup Banerjee

Tapan Kumar Ghanty **Date:** 18/07/2014

Member - Dr. Tapan Kumar Ghanty

Priya Mahadevan **Date:** 18.7.14

External Examiner - Prof. Priya Mahadevan

Final approval and acceptance of this dissertation is contingent upon the candidate's submission of the final copies of the dissertation to HBNI.

I hereby certify that I have read this dissertation prepared under my direction and recommend that it may be accepted as fulfilling the dissertation requirement.

Aparna Chakrabarti

Date: 18.7.14

Place: RRCAT

STATEMENT BY AUTHOR

This dissertation has been submitted in partial fulfillment of requirements for an advanced degree at Homi Bhabha National Institute (HBNI) and is deposited in the Library to be made available to borrowers under rules of the HBNI.

Brief quotations from this dissertation are allowable without special permission, provided that accurate acknowledgment of source is made. Requests for permission for extended quotation from or reproduction of this manuscript in whole or in part may be granted by the Competent Authority of HBNI when in his or her judgment the proposed use of the material is in the interests of scholarship. In all other instances, however, permission must be obtained from the author.

C Kamal

C. Kamal

DECLARATION

I, hereby declare that the investigation presented in the thesis has been carried out by me. The work is original and has not been submitted earlier as a whole or in part for a degree / diploma at this or any other Institution / University.

C Kamal

C. Kamal

List of Publications Arising From The Thesis

In Journals

1. *Ab initio* Study Of Stoichiometric Gallium Phosphide Clusters
   C. Kamal, Tapan K. Ghanty, Arup Banerjee, and Aparna Chakrabarti
   *Journal of Chemical Physics, **130**, 024308 (2009)*

2. The van der Waals Coefficients Between Carbon Nanostructures And Small Molecules: A Time-Dependent Density Functional Theory Study
   C. Kamal, Tapan K. Ghanty, Arup Banerjee, and Aparna Chakrabarti
   *Journal of Chemical Physics, **131**, 164708 (2009)*

3. Interesting Periodic Variations In Physical And Chemical Properties Of Homonuclear Diatomic Molecules
   C. Kamal, Arup Banerjee, Tapan K. Ghanty, and Aparna Chakrabarti
   *International Journal of Quantum Chemistry, **112**, 1097 (2012)*

4. Silicene Beyond Mono-layers - Different Stacking Configurations And Their Properties
   C. Kamal, Aparna Chakrabarti, Arup Banerjee, S. K. Deb
   *Journal of Physics: Condensed Matter, **25**, 085508 (2013)*

5. *Ab initio* Studies Of Effect Of Intercalation On The Properties Of Single Walled Carbon And Gallium Phosphide Nanotubes
   C. Kamal, Aparna Chakrabarti, Arup Banerjee, S. K. Deb
   *Physica E: Low-dimensional Systems and Nanostructures, **54**, 273 (2013)*

6. *Ab initio* Investigation On Hybrid Graphite-like Structure Made Up Of Silicene And Boron Nitride
   C. Kamal, Aparna Chakrabarti, Arup Banerjee
   *Physics Letters A, **378**, 1162 (2014)*

In Edited Volumes

1. Properties Of Two-Dimensional Silicon Versus Carbon Systems
   C. Kamal, Arup Banerjee, and Aparna Chakrabarti
   Graphene Science Handbook: Size-Dependent Properties, CRC Press, Taylor & Francis Group (Invited, submitted)

In Conferences

1. Properties of Multi-layered and Hybrid Structures of Silicene : A Detailed DFT Study
   C. Kamal *(Invited)*
   International Conference Superstripes 2014, Ettore Majorana Foundation and Centre for Scientific Culture, Sicily, ITALY (25-31 July 2014).

2. Computational Studies On Two Dimensional Graphene-like Structures
   C. Kamal *(Invited)*
   Workshop on Advances in Computational Physics (ACP2013), Central University of Tamil Nadu, Thiruvarur, INDIA (14-16 February 2013).

3. *Ab initio* Studies On Properties Of Graphene-like Honeycomb Structures
   C. Kamal, Aparna Chakrabarti, Arup Banerjee and S. K. Deb
   An Advanced School On Modeling Transition Metal Oxides (ATHENA-2012), S. N. Bose National Centre for Basic Sciences, Kolkata, INDIA (09 - 12 Apr, 2012)

4. The van der Waals Interaction Between Diatomic Molecules
   C. Kamal, Arup Banerjee, Tapan K. Ghanty and Aparna Chakrabarti
   Topical Conference on Interaction of EM Radiation with Atoms, Molecules and Clusters (TC -2010), Raja Ramanna Centre for Advanced Technology, Indore, INDIA (03 - 06 Mar, 2010)

5. Electronic Structures Of Transition Metal Doped Group IV And III-V Nanotubes
   Aparna Chakrabarti and **C. Kamal**
   Psi-K conference 2010, Henry Ford Building, Fritz–Haber–Institut der Max–Planck–Gesellschaft, Berlin, GERMANY (12 - 16 Sep, 2010)

6. The van der Waals Interaction Between Carbon Nanotubes, Fullerenes And Small Molecules
   C. Kamal, Tapan K. Ghanty, Arup Banerjee, and Aparna Chakrabarti
   International Conference on Materials for Advanced Technologies (ICMAT 2009), Symposium H: Carbon nanotubes: Synthesis, Characterization and Applications, Suntec Singapore International Convention & Exhibition Centre, SINGAPORE (28 Jun - 03 Jul, 2009)

ACKNOWLEDGMENT

I express my sincere gratitude and deep sense of indebtedness to my thesis supervisor Dr. Aparna Chakrabarti for her valuable guidance, enthusiastic encouragement, motivation, patience, and constant support from the onset of my research career. The duration of the present Ph.D work is a part of it. I am highly obliged to her for the constructive criticism, valuable suggestions and critical reading of all my scientific communications including the present thesis.

I am extremely grateful to all the members of my Ph.D doctoral committee for monitoring the progress of my research work over these years. I thank Dr. S. B. Roy, chairman of the doctoral committee for his valuable suggestions and comments. I am highly thankful to Dr. Arup Banerjee for many fruitful discussions, valuable suggestions, critical comments and support. I have learned a lot about scientific writing from both my supervisor and him. I also thank Dr. Tapan K. Ghanty for his valuable suggestions, comments and kind help in performing *ab initio* wave function based electronic structure calculations.

I extend my sincere thanks to Dr. S. M. Oak, Dr. S. K. Deb, Dr. G. S. Lodha and Dr. P. D. Gupta for their constant support and encouragement.

I thank Dr. S. R. Barman and Dr. J. Jayabalan for critical reading of some of the manuscripts included in the present thesis. I would like to thank Mr. P. Thander and the scientific computing group, Computer Centre, RRCAT for providing computational facility and help.

I am also thankful to all the staff members of Semiconductor Laser Section and Indus Synchrotrons Utilization Division for providing enjoyable and stimulating working atmosphere. My special thanks are also to Mr. Himanshu Srivastava, Mr. Anuj Upadhyay, Mr. Siddesh Pai, Mr. R. Sundar, Mr. Krishnakanta Mondal, Mr. Tufan Roy and Mr. Kiran Baraik for their help and company during this period.

I take this opportunity to express my sincere thanks to my teachers, Prof. S. V. M. Satyanarayana and Prof. A. Santhanam, for their inspiring role which had a profound influence on my personal life and scientific career. It is my pleasure to thank all my friends, specially Dr. S. Ganesamoorthy for his help, support and advice at several stages.

I am thankful to my wife Devikala for her care, understanding and unconditional support. I thank my son Yaazh for providing a cheerful atmosphere at home. Finally, I would like to convey my deepest regards to my parents and all my family members for their never-ending love, and affection to me.

C. Kamal

Contents

Synopsis

Study on properties of nanostructures, such as nanosheets, nanotubes, nanowires and nanoclusters, has been an active area of research during the last few decades since they possess many exciting and novel properties. They are also potential candidates for possible applications in nanotechnology. Nanostructures have a large surface-to-volume ratio which plays an important role in determining many of their physical and chemical properties. The properties of nanostructures strongly depend on their size, shape and chemical compositions. Functionalization, intercalation and doping by addition of electron acceptors or donors are the ways of modifying the properties of these nanostructures. The properties of nanostructures can also be tuned by applying mechanical stress and external electric and magnetic fields.

With the advancement of sophisticated experimental methods and characterization techniques, many novel nanostructures have been synthesized and their properties have also been investigated. Among these nanostructures, carbon based nanostructures such as graphene, nanotubes and fullerenes have received considerable attention from both experimentalists and theoreticians[1–7]. Graphene is a two-dimensional honeycomb-like structure of carbon and is one of the most well studied materials during the last decade. The reason for the tremendous interest in this material is due to the fact that it possesses many exciting and novel properties. For example, the charge carriers in this system behave like massless Dirac-Fermions which give rise to a linear dispersion around the Fermi energy at a highly symmetric k-point (K) in the reciprocal lattice [1, 2]. Similar to graphene, carbon nanotubes are also considered as potential candidates for applications in nanotechnology because of their unique properties such as outstanding electrical and thermal conductivity, excellent field emission, tunable optical properties and very good mechanical properties [5, 6]. Carbon nanotube and fullerene can be considered as wrapped graphene sheet in cylindrical and spherical shapes, respectively. The interesting properties associated with carbon based nanostructures have prompted us to search for similar nanostructures made up of other group IV and also group III-V materials. The graphene-like structure made up of silicon is called *silicene* where Si atoms are arranged in a two-dimensional honeycomb lattice similar to the arrangement of carbon atoms in graphene [8]. Major advantage with the nanostructures of silicon, germanium and other group III-V materials is that they can be compatible with the existing semiconductor technology.

Over the last few decades, *ab initio* density functional theory (DFT) [9] based electronic structure calculations have been widely used to study the properties of several materials including the nanostructures. DFT based calculations have been highly successful in predicting many ground state properties of several materials [10, 11]. In this thesis, we investigate various physical properties of nanostructures namely graphene-like structure - silicene, single walled carbon (SWCNT) and gallium phosphide nanotubes (SWGaPNT), group III-V clusters and homonuclear diatomic molecules using *ab initio* density functional theory based methods. A systematic study on the evolution of many properties of nanostructures as a function of their sizes has been carried out. We also study the effect of external influences such as doping of different elements as well as external electric field on the properties of nanostructures.

The thesis is organized in the following manner.

In **Chapter 1** of the thesis, we provide an overview of properties of nanostructures such as graphene, carbon nanotubes and nanoclusters.

A brief introduction to the computational methods employed in the electronic structure calculations based on DFT and time-dependent DFT (TDDFT) is given in **Chapter 2.**

Discussions on the results for the geometric, electronic and optical properties of graphene-like structure - silicene have been presented in **Chapter 3**. The electronic structure calculations of silicene show that it is a semi-metal and the charge carriers in this two-dimensional system behave like massless Dirac-Fermions since it possesses linear dispersion around Dirac point. Thus, the electronic properties of silicene are similar to those of graphene. Though graphene possesses many novel properties, its application in nanoelectronic devices is limited due to its zero band gap and hence it is difficult to control the electrical conductivity of graphene. It is desirable to have a band gap in materials in addition to their novel properties. We demonstrate through the results of our calculations that a band gap in silicene can be opened up at the Fermi level due to an external static electric field which leads to the breaking of inversion symmetry. Our results show that the induced band gap varies linearly with the strength of external electric field. Furthermore, the value of band gap can be tuned over a wide range of energies. Hence, there is a possibility of using silicene monolayer in nanodevice applications. We also discuss the optical response properties of silicene in **Chapter 3**. We identify and characterize the important electronic transitions which are prominent in the optical absorption spectra of silicene. At the end of **Chapter 3**, we also discuss the results of our investigation on the effect of doping of various elements on the properties of silicene.

It is known from the literature that the electronic properties of bi- and multi-layer of graphene are distinctly different from those of mono-layer. For example, bi-layer of graphene possesses parabolic dispersion around the highly symmetric k-point (K) in the reciprocal lattice as opposed to the linear dispersion in the case of mono-layer. In order to understand how the geometric and electronic properties of multi-layers of silicene are different from those of mono-layer of silicene, in **Chapter 4** we present our results of a detailed investigation on the geometric and electronic properties of bi- and multi-layers of silicene with different possible stacking configurations using *ab initio* DFT based calculations. We also study the evolution of geometric as well as electronic structures of multi-layers of silicene with increasing number of layers (n ranging from 1 to 10). Although a mono-layer of silicene possesses properties similar to those of graphene, our results show that the geometric and electronic properties of multi-layers of silicene are strikingly different from those of multi-layers of graphene. We observe that strong inter-layer covalent bonding exists between the layers in multi-layers of silicene as opposed to the weak van der Waals interaction which exists between the graphene layers. Our calculations show that the inter-layer bonding strongly influences the geometric and electronic structures of these multi-layers. Like bi-layers of graphene, silicene with two different stacking configurations AA and AB exhibits linear and parabolic dispersions around the Fermi level, respectively. However, unlike graphene, for bi-layers of silicene, these dispersion curves are shifted in the band diagram because of the strong inter-layer bonding present in the structure. For the multi-layers with $n \geq 3$, we study the geometric and electronic properties of multi-layers with four different stacking configurations, namely AAAA, AABB, ABAB and ABC. The results of cohesive energy calculation predict that rhombohedral (ABC) stacking sequence is the minimum energy configuration. Furthermore, our calculations predict that the Bernal (ABAB) stacking, which is energetically most stable stacking sequence in multilayer of graphene, is however the least stable stacking sequence in multilayers of silicene because of the different nature of hybridizations favored in the bulk Si and C. At the end of **Chapter 4**, we also discuss the results for the ground state properties of the hybrid structures made up of silicene and other graphene-like structures.

In **Chapter 5**, we present results for the geometric and electronic structures of quasi-one-dimensional (infinite-length) single walled nanotubes made up of carbon (SWCNT) and gallium phosphide (SWGaPNT) using *all-electron* based density functional theory calculations. Here, we study and compare the geometric and electronic properties of carbon and gallium phosphide nanotubes since the former has a rich π-electron density which is not expected in the case of the III-V nanotubes. Furthermore, we probe the effect of intercalation of alkali and transition metal atom clusters on the properties of these nanotubes. It has been observed in the literature that intercalation of atoms or clusters inside carbon nanotube systems can give rise to many interesting changes in their properties [12–15] such as presence of half-metalicity in transition metal atoms doped SWCNT(3,3) [12], Kondo effect [13], semiconductor-metal as well as metal-semiconductor transition in alkali metal doped SWCNT [14], metal induced adsorption of biomolecules on nanotubes [15].

Our calculations on undoped nanotubes show that unlike in SWCNT, there is a strong buckling effect in the optimized geometric structure of SWGaPNT. The amount of buckling can be characterized by the buckling length and it is found to be about 0.48 Å in SWGaPNT. The presence of buckling is due to the mixture of sp^2 and sp^3 hybridizations in SWGaPNT. The results of our calculations show that both SWCNT(10,0) and SWGaPNT(10,0) are semiconductors with direct band gaps of 0.83 and 1.48 eV, respectively. It is important to note that this is in contrast to the respective bulk materials, which are semiconductors with indirect band gaps. In case of nanotubes intercalated with alkali metal atom clusters, we observe that there is a semiconductor to metal transition due to significant amount of charge transfer from valence band of alkali metal atom to the unoccupied bands of nanotubes. On the other hand, our spin-polarized calculations of these nanotubes intercalated with chains of single transition metal atom indicate that SWCNT(10,0) undergoes a transition from semiconducting to a half-metallic state and a signature of similar transition is observed for SWGaPNT(10,0) as well. On the contrary, the electronic structures of these nanotubes show metallicity when they are intercalated with more number of transition metal atoms.

Having discussed the results on the ground state properties of infinite-length nanotubes in the previous chapter, we shall discuss the various properties of finite-length carbon nanotubes as well as fullerenes in **Chapter 6**. Understanding the response properties of nanostructures as function of their shape and size is an important aspect associated with the research in nanoscience. Keeping this in mind, in **Chapter 6**, we carry out detailed calculations to investigate the electronic polarizability and strength of van der Waals interaction (through the coefficient (C_6)) between the carbon nanostructures with two different shapes namely (a) tubular : finite-length carbon nanotubes with different chirality index and (b) spherical : fullerenes. We also study the evolution of these properties with the increasing size of the nanostructures. The dispersion coefficients (C_6) are obtained via Casimir-Polder relation. It is observed from our calculations that the values of polarizability and C_6 coefficients between the carbon nanotubes scale non-linearly with the length of nanotubes. Furthermore, our calculations show that nanotubes are more polarizable than the fullerenes having similar number of atoms. This can be attributed to the geometry of nanotubes, which can be easily polarized along the tube direction. Therefore, these quasi-one-dimensional structures have large anisotropy in polarizability and this large anisotropy can play an important role in electric field aligned growth of nanotubes. The oriented growth of nanotubes is important for nanoelectronics and Ural et al. has already grown aligned SWCNTs onto the surfaces of SiO2 / Si substrates in presence of strong electric fields [16]. Additionally, it is found that the values of C_6 are about 40 - 50 % lower for the carbon cages when compared to those of nanotubes with equal number of atoms.

The presence of large surface-to-volume ratio of the nanostructures plays a vital role in their potential application in storing significant quantities of several gas molecules and in gas sensors. For example, the storage of hydrogen by carbon based nanostructures, especially carbon nanotubes has shown great promise and the studies on adsorption of hydrogen atom or molecule as well as other small molecules have received overwhelming attention of the researchers [17–26]. Hence, to explore the potential of the adsorption of different gases, specically the environmentally important ones, by the carbon based nanostructures, detailed studies and microscopic understanding of various physical properties of these materials are essential. It is well known that the van der Waals interaction plays an important role in the physisorption of the gas molecules with the nanostructures. Therefore the knowledge and accurate estimate of the van der Waals interaction coefficients (C_6) between the carbon based nanostructures and different molecules of environmentally important gases are highly important. Hence, in this study, we also calculate the van der Waals interaction coefficients (C_6) between different gas molecules and carbon nanotubes as well as fullerene using the TDDFT method. It is observed from our calculations of the van der Waals coefficients between the small molecules and the carbon nanostructures that the environmentally important gas molecules such as green house and ozone depleting ones, possess reasonably higher values of C_6 coefficient. Hence, our estimation of the coefficients based on the *ab initio* calculations between the carbon nanostructures and the environmentally important gas molecules can be useful in providing the microscopic understanding in the studies of adsorption, specically physisorption, of these gases on carbon-based nanostructures.

In **Chapter 7**, we discuss the results of the various ground state and response properties of quasi-zero-dimensional semiconductor clusters namely stoichiometric gallium phosphide (Ga_nP_n) clusters with n = 2 - 5. The ground state properties such as the geometric, electronic and vibrational properties have been studied by employing DFT based calculations. The stability of these clusters is checked by the binding energy and vibrational frequency analysis. The static dipole polarizabilities of these clusters have been obtained by employing various *ab initio* wave function based methods as well as DFT / TDDFT with different exchange-correlation (XC) functionals, ranging from simple local density approximation (LDA) to an asymptotically correct model potential namely statistical average of orbital potential (SAOP). A systematic investigation is carried out to analyze the performance of different XC functionals used in DFT / TDDFT method in determining static dipole polarizability of these clusters. The results for most stable isomers show that the DFT / TDDFT method with different XC functionals underestimate the values of polarizability in comparison to the results of second order Møller-Plesset perturbation theory (MP2) method. We infer from our calculations that among the several XC functionals, the values of polarizability obtained within generalized gradient approximation (GGA) by using Perdew-Burke-Ernzerhof exchange with Lee-Yang-Parr correlation functional and Perdew-Burke-Ernzerhof exchange-correlation functionals are the closest to the corresponding results from Møller-Plesset perturbation theory for Ga_nP_n clusters. The values of polarizability obtained by the DFT/TDDFT calculations with model potential-SAOP are found to be lower than those obtained with the LDA and GGA XC functionals. Moreover, the LDA and GGA results for polarizability are closer to the corresponding MP2 values than those obtained by SAOP. This may be due to the accidental cancellation of errors arising from calculations of low lying and high lying excited states by LDA and GGA functionals, which contribute to the polarizability. However, no such cancellation of errors occurs when excited states are obtained with SAOP. Our study on the evolution of static polarizability per atom with size shows that it reaches the bulk limit from the above as the size of the clusters increases.

The results of our systematic investigation on the various ground state and response properties of homonuclear diatomic molecules (from hydrogen to rubidium, including transition metals) as a function of atomic number of the constituent atoms have been summarized in **Chapter 8**. We study the variation of different ground state and response properties of homonuclear diatomic molecules along the rows and columns of the periodic table by using state of the art DFT / TDDFT calculations. Our study includes the variation of properties such as the binding energy, highest occupied and lowest unoccupied molecular orbital (HOMO and LUMO, respectively), HOMO-LUMO gap, harmonic vibrational frequency, vertical ionization potential, vertical electron affinity as well as response properties such as static dipole polarizability and van der Waals interaction coefcient. We observe from our calculations that several properties of homonuclear diatomic molecules show periodic variations along rows and columns of the periodic table. The periodic variations in the ground state properties of diatomic molecules have been explained by the nature and type of the bond that exists between the constituent atoms. Similarly, the periodic variations in the response properties such as static dipole polarizability and strength of the van der Waals interaction between diatomic molecules have been correlated with the variations in metallic/nonmetallic character of the elements along the periodic table.

Finally, the thesis has been concluded in **Chapter 9** and then followed by a brief discussion on the possible future work.

References

[1] A. K. Geim and K. S. Novoselov, Nature Mater., **6**, 183 (2007)

[2] K. S. Novoselov, A. K. Geim, S. V. Morozov, D. Jiang, M. I. Katsnelson, I. V. Grigorieva, S. V. Dubonos, and A. A. Firsov, Nature, **438**, 197 (2005)

[3] K. S. Novoselov, E. McCann, S. V. Morozov, V. I. Fal'ko, M. I. Katsnelson, U. Zeitler, D. Jiang, F. Schedin and A. K. Geim, Nature Phys. **2**, 177 (2006)

[4] S. Iijima, Nature (London), **354**, 56 (1991)

[5] M. S. Dresselhaus, G. Dresselhaus, and P. Avouris, *Carbon Nanotubes: Synthesis, Structure, Properties and Applications*, Springer-Verlag, Berlin (2001)

[6] S. Reich, C. Thomsen, and J. Maultzsch, *Carbon Nanotubes: Basic Concepts and Physical Properties*, Wiley-VCH, Weinheim (2004)

[7] H. W. Kroto, J. R. Heath, S. C. O'Brien, R. F. Curl and R. E. Smalley, Nature, **318**, 162 (1985)

[8] S. Cahangirov, M. Topsakal, E. Akturk, H. Sahin, and S. Ciraci, Phys. Rev. Lett., **102**, 236804 (2009)

[9] P. Hohenberg and W. Kohn, Phys. Rev., **136**, B864 (1964); W. Kohn and L. J. Sham, ibid. **140**, A1133 (1965)

[10] R. M. Martin, *Electronic Structure Basic Theory and Practical Methods*, Cambridge University Press (2004)

[11] W. Koch, M. C. Holthausen, *A Chemists Guide to Density Functional Theory*, Wiley-VCH Verlag GmbH (2001)

[12] M. M. Rahman, M. Kisaku, T. Kishi, T. A. Roman, W. A. Dino, H. Nakanishi, H. Kasai, J. Phys. Soc. Japan, **74**, 742 (2005)

[13] P. P. Baruselli, A. Smogunov, M. Fabrizio, and E. Tosatti, Phys. Rev. Lett., **108**, 206807-1-4 (2012)

[14] X. Yang, J. Ni, Phys. Rev. B, **71**, 165438-1-5 (2005)

[15] C. M. Chang, A. F. Jalbout, Thin Solid Films, **518**, 2070 (2010)

[16] A. Ural, Y. Li, and H. Dai, Appl. Phys. Lett., **81**, 3464 (2002)

[17] A. C. Dillon, K. M. Jones, T. A. Bekkedahl, C. H. Kiang, D. S. Bethune and M. J. Heben, Nature, **386**, 377 (1997).

[18] L. Schlapbach and A. Zuttel, Nature, **414**, 353 (2001)

[19] P. Chen, X. Wu, J. Lin and K. L. Tan, Science, **285**, 91 (1999)

[20] C. Liu, Y. Y. Fan, M. Liu, H. T. Cong, H. M. Cheng and M. S. Dresselhaus, Science, **286**, 1127 (1999)

[21] Y. Ye, C. C. Ahn, C. Witham, B. Fultz, J. Liu, A. G. Rinzler, D. Colbert, K. A. Smith and R. E. Smalley, Appl. Phys. Lett., **74**, 2307 (1999)

[22] F. Picaud, C. Girardet and A. M. Rao, J. Appl. Phys., **105**, 014315 (2009)

[23] S. Kim, H. R. Lee, Y. J. Yun, S. Ji, K. Yoo, W. S. Yun, J. Y. Koo and D. H. Ha, Appl. Phys. Lett., **91**, 093126 (2007)

[24] H. Y. Jung, S. M. Jung, J. Kim and J. S. Suh, Appl. Phys. Lett., **90**, 153114 (2007)

[25] S. Kim, Sensors, **6**, 503 (2006)

[26] A. Ricca and C. W. Bauschlicher Jr., Chem. Phys., **323**, 511 (2006)

List of Publications

In Journals (Included in the thesis)

1. *Ab initio* Study Of Stoichiometric Gallium Phosphide Clusters
   C. Kamal, Tapan K. Ghanty, Arup Banerjee, and Aparna Chakrabarti
   *Journal of Chemical Physics, **130**, 024308 (2009)*

2. The van der Waals Coefficients Between Carbon Nanostructures And Small Molecules: A Time-Dependent Density Functional Theory Study
   C. Kamal, Tapan K. Ghanty, Arup Banerjee, and Aparna Chakrabarti
   *Journal of Chemical Physics, **131**, 164708 (2009)*

3. Interesting Periodic Variations In Physical And Chemical Properties Of Homonuclear Diatomic Molecules
   C. Kamal, Arup Banerjee, Tapan K. Ghanty, and Aparna Chakrabarti
   *International Journal of Quantum Chemistry, **112**, 1097 (2012)*

4. Silicene Beyond Mono-layers - Different Stacking Configurations And Their Properties
   C. Kamal, Aparna Chakrabarti, Arup Banerjee, S. K. Deb
   *Journal of Physics: Condensed Matter, **25**, 085508 (2013)*

5. *Ab initio* Studies Of Effect Of Intercalation On The Properties Of Single Walled Carbon And Gallium Phosphide Nanotubes
   C. Kamal, Aparna Chakrabarti, Arup Banerjee, S. K. Deb
   *Physica E: Low-dimensional Systems and Nanostructures, **54**, 273 (2013)*

6. *Ab initio* Investigation On Hybrid Graphite-like Structure Made Up Of Silicene And Boron Nitride
   C. Kamal, Aparna Chakrabarti, Arup Banerjee
   *Physics Letters A, **378**, 1162 (2014)*

In Edited Volumes

7. Properties Of Two-Dimensional Silicon Versus Carbon Systems
   C. Kamal, Arup Banerjee, and Aparna Chakrabarti
   Graphene Science Handbook: Size-Dependent Properties, CRC Press, Taylor & Francis Group (Invited, submitted)

In Conferences

8. Properties of Multi-layered and Hybrid Structures of Silicene : A Detailed DFT Study
   C. Kamal *(Invited)*
   International Conference Superstripes 2014, Ettore Majorana Foundation and Centre for Scientific Culture, Sicily, ITALY (25-31 July 2014).

9. Computational Studies On Two Dimensional Graphene-like Structures
   C. Kamal *(Invited)*
   Workshop on Advances in Computational Physics (ACP2013), Central University of Tamil Nadu, Thiruvarur, INDIA (14-16 February 2013).

10. *Ab initio* Studies On Properties Of Graphene-like Honeycomb Structures
    C. Kamal, Aparna Chakrabarti, Arup Banerjee and S. K. Deb
    An Advanced School On Modeling Transition Metal Oxides (ATHENA-2012), S. N. Bose National Centre for Basic Sciences, Kolkata, INDIA (09 - 12 Apr, 2012)

11. The van der Waals Interaction Between Diatomic Molecules
    C. Kamal, Arup Banerjee, Tapan K. Ghanty and Aparna Chakrabarti
    Topical Conference on Interaction of EM Radiation with Atoms, Molecules and Clusters (TC -2010), Raja Ramanna Centre for Advanced Technology, Indore, INDIA (03 - 06 Mar, 2010)

12. Electronic Structures Of Transition Metal Doped Group IV And III-V Nanotubes
    Aparna Chakrabarti and **C. Kamal**
    Psi-K conference 2010, Henry Ford Building, Fritz–Haber–Institut der Max–Planck–Gesellschaft, Berlin, GERMANY (12 - 16 Sep, 2010)

13. The van der Waals Interaction Between Carbon Nanotubes, Fullerenes And Small Molecules
    C. Kamal, Tapan K. Ghanty, Arup Banerjee, and Aparna Chakrabarti
    International Conference on Materials for Advanced Technologies (ICMAT 2009), Symposium H: Carbon nanotubes: Synthesis, Characterization and Applications, Suntec Singapore International Convention & Exhibition Centre, SINGAPORE (28 Jun - 03 Jul, 2009)

Not included in the thesis (from 2009 to 2014)

In Journals

1. Density Functional Study of α-Amino Acids : Structural, Energetic And Vibrational Properties
   L. M. Ramaniah, A. Chakrabarti, R. J. Kshirsagar, **C. Kamal**, A. Banerjee
   *Molecular Physics, **109**, 875 (2011)*

2. Nonlinear Optical Properties Of Au19M (M = Li, Na, K, Rb, Cs, Cu, Ag) Clusters
   A. Banerjee, T. K. Ghanty, A. Chakrabarti, and **C. Kamal**
   *Journal of Physical Chemistry C, **116**, 193 (2012)*

3. How Universal Are Hydrogen Bond Correlations ?: A Density Functional Study Of Intramolecular Hydrogen Bonding In Low-Energy Conformers Of α - Amino Acids
   L. M. Ramaniah , **C. Kamal** , R. J. Kshirsagar , A. Chakrabarti, A. Banerjee
   *Molecular Physics, **111**, 3067 (2013)*

4. Density Functional Investigation On The Structures And Properties Of Li Atom Doped Au20 Cluster
   K. Mondal , T. K. Ghanty , A. Banerjee , A. Chakrabarti and **C. Kamal**
   *Molecular Physics, **111**, 725 (2013)*

5. First Principles DFT Study Of Weak $C - HO$ Bonds In Crystalline Amino Acids Under Pressure : Alanine
   L. M. Ramaniah, **C. Kamal**, S. K. Sikka
   *AIP Conf. Proc., **1512**, 110 (2013)*

6. Experimental And First Principle Studies On Electronic Structure Of BaTiO3
   A. Sagdeo, H. Ghosh, A. Chakrabarti, **C. Kamal**, T. Ganguli, D. M. Phase, S. K. Deb
   *AIP Conf. Proc., **1591**, 1142 (2014)*

7. Local Structure Investigation Of Co And Mn Doped ZnO Nanocrystals And Its Correlation With Magnetic Properties
   S. Basu, D. Inamdar, S. Mahamuni, A. Chakrabarti, **C. Kamal**, G. Kumar, S. N. Jha, D. Bhattacharyya
   *Journal of Physical Chemistry C, **118**, 9154 (2014)*

In Edited Volumes

8. Properties Of Nanomaterials From First Principles Study
   A. Banerjee, A. Chakrabarti, **C. Kamal** and T. K. Ghanty
   Chapter 20, Pages 527-548, Theoretical and Computational Developments in Modern Density Functional Theory, Edited by Amlan K. Roy, Nova Science Publishers, Inc.

In Conferences

9. Tuning The Properties Of Tetrahedral Au20 Cluster By Li Doping
   K. Mondal, **C. Kamal**, A. Chakrabarti, A. Banerjee, T. K. Ghanty
   DAE-BRNS- 4th Interdisciplinary Symposium On Materials Chemistry (ISMC 2012), Bhabha Atomic Research Center, Mumbai, INDIA (11 - 15 Dec, 2012)

10. Properties Of Au20 Clusters
    A. Banerjee, T. K. Ghanty, A. Chakrabarti, K. Mondal, and **C. Kamal**
    DAE-BRNS Symposium on Atomic, Molecular and Optical Physics (2012), Indian Institute of Science Education and Research, Kolkata, INDIA (14 - 17 Dec, 2012)

11. First Principles Study Of Linear And Nonlinear Optical Response Properties Of Some Amino Acids
    A. Chakrabarti, **C. Kamal**, A. Banerjee and L. M. Ramaniah
    DAE-BRNS National Laser Symposium (NLS-19), Raja Ramanna Centre for Advanced Technology, Indore, INDIA (01 - 04 Dec, 2010)

List of Figures

List of Tables

Chapter 1

Introduction

The word "nano" in Greek means "dwarf". It is used as a prefix in science and engineering to denote a billionth (10^{-9}) of a unit, like nanometer (nm) for length and nanosecond (ns) for time. Nanoscience is a branch of science that involves the studies of properties of materials at the scale of nanometers. It is one of the most active areas of scientific research in twenty first century. In 1959, the Nobel Laureate Richard P. Feynman gave a famous talk[1] entitled "There's Plenty of Room at the Bottom". In this talk, he had discussed many aspects regarding manipulation of atoms and molecules at nanoscale and also outlined the promise of nanotechnology. Since then there has been a rapid progress in the fields of nanoscience and nanotechnology[2–16] due to the availability of sophisticated experimental techniques for the growth and characterization of materials at nanoscale. Another important factor which has played a significant role in the development of this field is the miniaturization of devices in semiconductor industry. Over the years, the field of nanoscience has evolved enormously and it is now influencing several branches of science including physics, chemistry, biology, materials science and medicine.

The main reason for the tremendous interest in this field is the fact that the nanostructures i.e the nm sized materials, possess many exciting and novel properties which are drastically different from those of atoms as well as their bulk counterparts. For example, bulk gold is an inert material, however, nanoparticles made up of gold are highly reactive[17, 18]. The modifications in the properties of materials at nanoscale are mainly due to the (i) large surface-to-volume ratio and (ii) strong effect of quantum confinement.

In bulk materials, the number of atoms on the surface is a negligible proportion of the total number of atoms. Thus, the surface atoms play an insignificant role in the properties of bulk materials. However, when the size of the materials is reduced to nanoscale, the ratio of number of atoms on the surface and the total number of atoms in the material becomes very large and hence the physical and chemical properties of the nanomaterials strongly depend on the surface properties. This may result in modification or enhancement of several existing properties of the bulk materials or even emergence of new properties. As mentioned above, the high reactivity of gold nanoparticles is a good example. Moreover, the color of gold nanoparticles can be orange, purple, red or greenish depending upon the size of the nanoparticle. This is due to the presence of surface plasmon resonance[19] where the electron cloud surrounding the metal nuclei oscillates coherently with the electric field of the incoming light. Similar effect is also observed in silver nanopartiles[20]. Colloidal gold nanoparticles were already well known in the middle ages and they were used as dyes in stained glass windows of cathedrals and palaces. Because of their enhanced surface plasmons, the noble metal nanoparticles have also been used in biological sensing application[21].

Similar to metal nanomaterials, carbon based nanostructures have also been extensively studied by both experimentalists and theoreticians since they possess many extraordinary properties and due to their potential applications in nanodevices[22–33]. For example, two-dimensional graphene possesses many novel properties, namely, the charge carriers in this system behave like massless Dirac-Fermions, an anomalous half-integer quantum Hall effect, Klein tunneling, non-zero minimum conductivity, etc[24–26]. Similarly, quasi-one-dimensional carbon nanotubes possess exceptional electrical, mechanical and optical properties[27–33]. For instance, metallic carbon nanotubes can carry an electric current density which is more than thousand times greater than that of normal metals like copper[34]. Because of the large surface-to-volume ratio, the nanostructures have also become promising materials for several applications, including catalytic activity, storage and sensor devices. There exist several studies on the adsorption of various gases on the surface of nanostructures. For example, storage and adsorption of hydrogen and many other gas molecules by carbon based nanostructures have received a lot of interest in the scientific community[35–49]. It has been reported in the literature that significant quantity of hydrogen can be stored in carbon nanostructures. Thus, they can be used as a good hydrogen-storage material for fuel-cell electric vehicles[35]. Possibility of using carbon based nanostructures for gas sensor application has also been proposed in the literature[50–58]. It is expected that sensors made from nanomaterials have enhanced sensitivity and selectivity as compared to those made up of their bulk counterparts.

Another important consequence of reducing the size of materials to nanoscale is the appearance of quantum confinement effects. We know from the elementary quantum mechanics that if any one of the physical dimensions of the material is comparable to the de Broglie wavelength of the charged particles, the energy levels of the system become discrete due to the confinement of the wave function of particles. The dependence of values of these energy levels and thus the energy gap on the size of the system can be easily explained by the simple potential well problems in quantum mechanics. The energy gap, difference between valence and conduction band edges, is of fundamental importance since most of the properties of materials, such as intrinsic conductivity, electronic transitions and optical properties, strongly depend on it. Thus, finding possible ways of controlling the value of band gap of the materials is important from the application point of view. For instance, the size dependence of the HOMO$-$LUMO gap of CdSe-CdS core-shell nanoparticles has been experimentally demonstrated in ref[59]. It has been shown in ref[59] that the fluorescence can be tuned between blue and red by varying the size of these nanoparticles.

If only one of the three physical dimensions of a material is in nanometer range, then it is called a quantum well. In this case, the charge carriers are confined in one direction while they can move in the other two directions similar to that in the corresponding bulk material. One of the classic examples is a semiconductor quantum well structure in which a narrow band gap material, like GaAs, is sandwiched between the wide band gap materials, like $\mathrm{Al}_x\mathrm{Ga}_{(1-x)}\mathrm{As}$ [60]. The depth of the well can be adjusted by the composition of the AlGaAs layer. On the other hand, if two of the three physical dimensions are in nanometer range, then it is called a quantum wire. Similarly, if all the three physical dimensions are in nanometer range then it called a quantum dot. Fullerenes and carbon nanotubes are the examples for the quantum dot and wire respectively. Most important applications of the artificial quantum structures made up of semiconducting materials are the quantum well lasers and detectors which have revolutionized the field of semiconductor electronic and optoelectronic devices[60–63].

It is also possible to modify the properties of nanostructures by applying mechanical stress as well as by external electric and magnetic fields. Functionalization, intercalation and doping by different atoms, molecules and functional groups are the additional methods of modifying the properties of nanostructures. Our ability to control over the size, shape and chemical composition of the nanostructures and then modify their properties in a desired manner will create a profound effect on the development of novel nanodevices.

In the following section, we give a brief introduction to the properties of carbon based nanostructures namely graphene and nanotube as well as semiconductor cluster which are relevant to the content of the present thesis. The objectives of the present thesis are discussed at the end of the chapter.

1.1 Introduction to Graphene and Carbon Nanotubes

Carbon is one of the important elements present in nature which forms a basis of living organism in earth. Carbon can exist in various allotropes and some of them are shown in Figure 1.1. Among these allotropes, the two well known bulk forms of carbon are graphite and diamond in which carbon atom exists in sp^2 and sp^3 hybridizations respectively. Physical properties of these two forms are very different. For example, graphite is a soft layered material and it conducts electricity (semi-metal) whereas diamond is the hardest material with very high thermal and negligible electrical conductivity (wide band gap material). Carbon also exists in other bulk forms such as hexagonal Lonsdaleit and amorphous forms. The discoveries of low dimensional forms of carbon namely fullerene (C_{60}) in 1985 [22] and nanotube in 1991[23] and the successful isolation of graphene in 2004[24–26], have led to a flurry of activities in the field of carbon based nanoscience and nanotechnology during the last three decades. Consequently, many fascinating properties of these nanostructures have been unveiled through several studies. Carbon nanotube and fullerene can be considered as wrapped graphene sheet in cylindrical and spherical shapes, respectively. Furthermore, the bulk graphite is also considered as infinitely stacked graphene sheets.

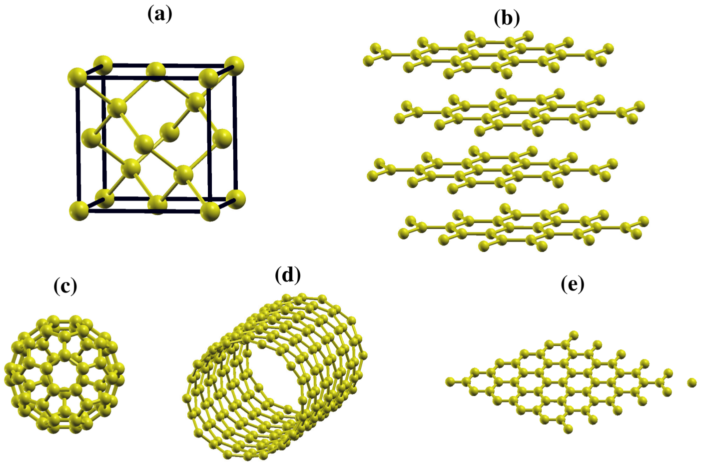

Figure 1.1: Various allotropes of carbon: (a) diamond, (b) graphite, (c) C_{60}, (d) carbon nanotube and (e) graphene.

1.1.1 Graphene

In 2004, A. Geim and K. Novoselov have successfully isolated single-layer graphene by exfoliating pieces of graphite using scotch tape and demonstrated the existence of many exciting and novel properties of graphene[24–26]. For their outstanding work, they have received the Nobel Prize in physics for the year 2010.

Graphene is a two-dimensional honeycomb-like structure in which carbon atoms are arranged in a hexagonal lattice. It has space group of P6/mmm. The primitive unit cell of graphene is shown in Figure 1.2 (a) and it contains two carbon atoms say A and B. The unit cell can be translated via primitive lattice vectors $\hat{a}_1$ and $\hat{a}_2$. The value of bond length (d_{C-C}) between carbon atoms in graphene is found to be 1.42 Å. Brillouin

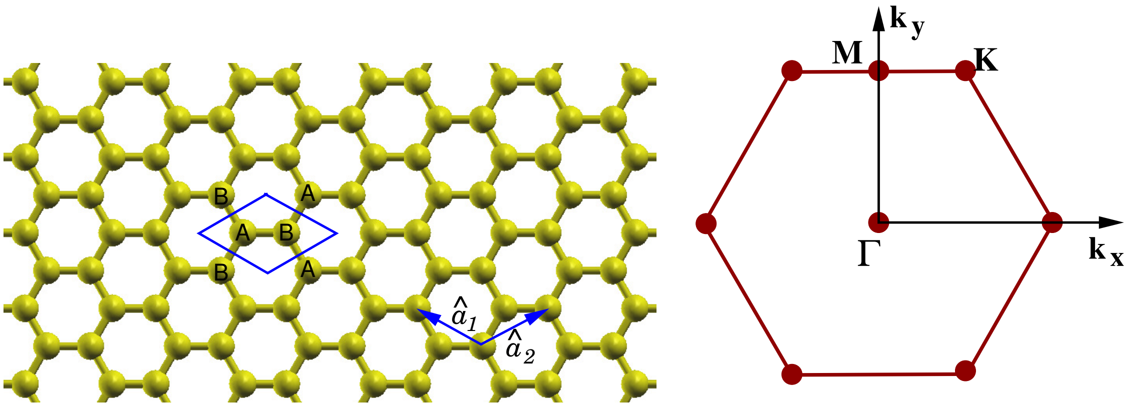

Figure 1.2: (a) Direct and (b) reciprocal lattices of graphene. Unit cell containing two carbon (A and B) atoms is shown in blue color. $\hat{a}_1$ and $\hat{a}_2$ represent the primitive lattice vectors of graphene.

zone of graphene with the highly symmetric k-points is shown in Figure 1.2 (b). In graphene, carbon atom exists in sp^2 hybridization due to the superposition of the 2s, 2p$_x$ and 2p$_y$ orbitals of atomic carbon which gives rise to three σ bonds with their nearest neighbors. The unhybridized 2p$_z$ orbital forms π bonds similar to those of benzene and other aromatic molecules. In this sense, graphene can be considered as the extreme size limit of planar aromatic molecules. The strong σ bonds are responsible for the excellent mechanical properties of graphene whereas the delocalized electrons in the π bonds lead to several exciting and novel electronic properties of graphene. For example, the charge carriers in this system behave like massless Dirac-Fermions due to the presence of linear dispersion around the Fermi energy at a highly symmetric k-point (K) in the reciprocal lattice (see Figure 1.2 (b)).

The presence of the linear dispersion in the electronic band structure of graphene can be explained by simple tight binding (TB) approximation[64]. As mentioned above, the electronic properties of graphene arise mainly due to the 2p$_z$ electrons. The unit cell of graphene contains two electrons, one each from A and B atoms. Within this TB approximation, the wavefunction of the system can be constructed by linear combinations of 2p$_z$ orbitals of two carbon atoms (at the sites A and B) and it is given by

$$\Psi(\mathbf{r}) = c_A\, \phi_A(\mathbf{r}) + c_B\, \phi_B(\mathbf{r}) \tag{1.1}$$

where ϕ_A and ϕ_B are the p$_z$ orbitals corresponding to the two carbon atoms at the sites A and B respectively. By considering only nearest neighbor interaction, the TB Hamiltonian for the system can be written as

$$\hat{H} = \begin{pmatrix} H_{AA} & H_{AB} \\ H_{BA} & H_{BB} \end{pmatrix} = \begin{pmatrix} \epsilon_{2p_z} & -t_0 f(\vec{k}) \\ -t_0 f(\vec{k})^* & \epsilon_{2p_z} \end{pmatrix} \tag{1.2}$$
$$\text{with} \quad f(\vec{k}) = exp(i\vec{k}\cdot\vec{R}_1) + exp(i\vec{k}\cdot\vec{R}_2) + exp(i\vec{k}\cdot\vec{R}_3)$$

where ϵ_{2p_z} is the energy of the 2p$_z$ orbital. The parameters ϵ_{2p_z} and t$_0$ are found by fitting experimental or first-principles data. In practice, the value of ϵ_{2p_z} is set to zero. The empirical value of the interaction integral (t$_0$) between the nearest neighbor atoms

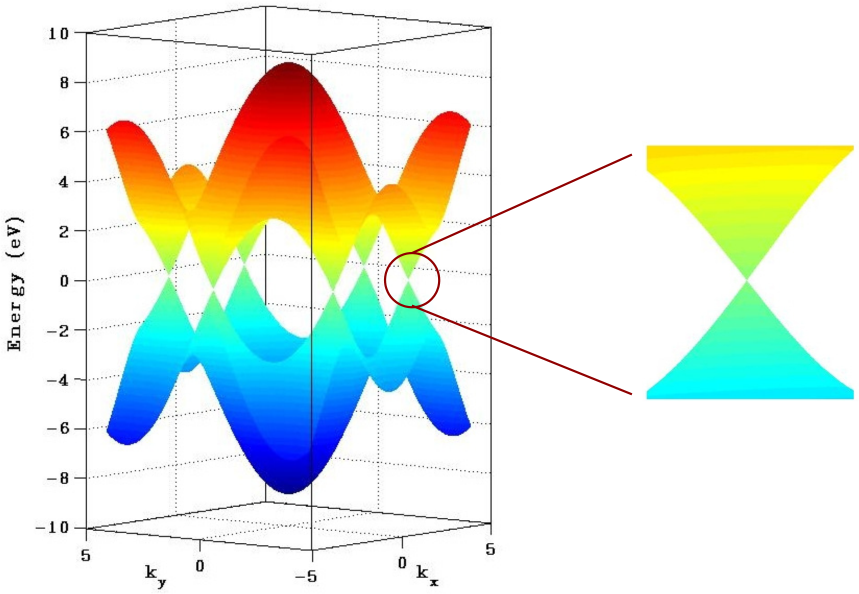

Figure 1.3: Three-dimenisonal plot of the electronic band structure of graphene. The energies of bands are given with respect to the Fermi level.

is chosen to be 2.9 eV since this value gives the best fit. The function $f(\vec{k})$ contains the sum of the phase factors and the vectors $\vec{R}_1$, $\vec{R}_2$ and $\vec{R}_3$ represent the positions of the three nearest B atoms relative to A atom or vice versa. The dispersion relation for the electronic band structure of graphene is obtained by diagonalizing the above Hamiltonian and it is found to be

$$E(k_x, k_y) \quad = \quad \epsilon_{2p_z} \pm t_0 \sqrt{1 + 4\, cos\left(\frac{\sqrt{3}k_x a}{2}\right) cos\left(\frac{k_y a}{2}\right) + 4\, cos^2\left(\frac{k_y a}{2}\right)} \qquad (1.3)$$

Figure 1.3 shows the three-dimensional plot of the electronic band structure of graphene obtained by the above relation. The energies of the bands are given with respect to the Fermi level. The conduction (above) and valence (below the Fermi level) bands are due to the anti-bonding π^* and bonding π states respectively. The valence and conduction bands touch each other only at the highly symmetric k-points K of the Brillouin zone but there is no overlap between these two bands. The points in energy versus k-points (E-k) diagram where the conduction and valence bands touch each other at E_F are called the Dirac points. In the three-dimensional plot of energy versus k_x and k_y, the dispersion around K and K' points forms the so called Dirac cones.

The behavior of charge carriers in graphene at the Fermi energy is of great interest in condensed matter physics due to the linear dispersion in the band structure which gives rise to the massless Dirac-Fermions in graphene. Around the Dirac point, the dynamics of the charge carriers in graphene can be described by the relativistic Dirac-like Hamiltonian[64],

$$\hat{H} = \begin{pmatrix} \Delta & \hbar v_F(k_x - ik_y) \\ \hbar v_F(k_x + ik_y) & -\Delta \end{pmatrix} \tag{1.4}$$

where k, v_F and Δ are momentum, Fermi velocity of the charge carriers and the onsite energy difference between the carbon atoms at sites A and B, respectively. Diagonalization of the above Hamiltonian yields the following dispersion relation,

$$E = \pm\sqrt{\Delta^2 + (\hbar v_F k)^2} \tag{1.5}$$

For pristine graphene, the onsite energy difference Δ is zero due to the presence of inversion symmetry. This leads to the linear dispersion around the Dirac point

$$E = \pm\hbar v_F k \tag{1.6}$$

The presence of linear dispersion and thus, the Dirac-Fermions in graphene leads to many exciting phenomena such as an anomalous half-integer quantum Hall effect, Klein tunneling, non-zero minimum conductivity, etc[24–26]. Another interesting consequence of the linear dispersion is the ambipolar electric field effect i.e. the possibility of continuously tuning the amount as well as type of charge (from electrons to holes) through the application of a gate voltage by shifting the Fermi-level up and down[24].

1.1.2 Carbon Nanotubes

Carbon nanotube (CNT) is another fascinating nanostructure with extraordinary mechanical, electrical and thermal properties[27–33]. CNT exists in two forms: (a) single walled carbon nanotube (SWCNT) and (b) multi-walled carbon nanotube (MWCNT). As mentioned earlier, the geometric structure of SWCNT can be considered as rolled graphene. In absence of any effect of curvature due to the folding of graphene sheet, the

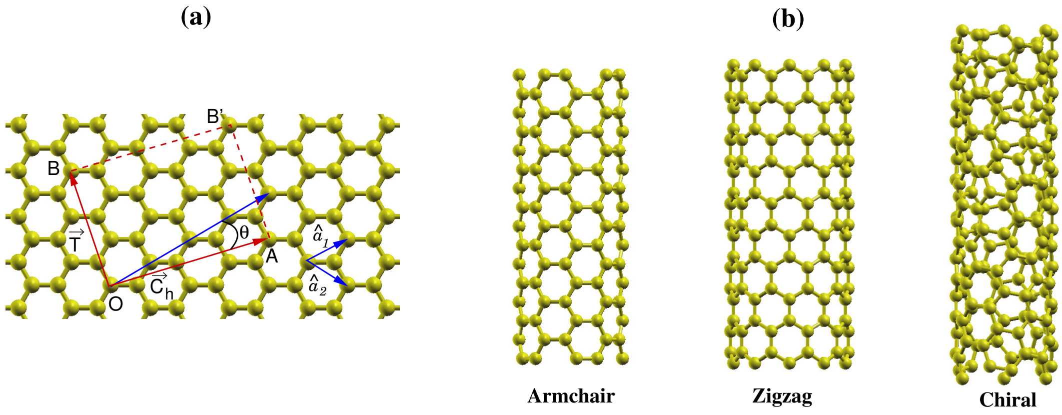

Figure 1.4: (a) Chiral ($\vec{C_h}$) and translation ($\vec{T}$) vectors of SWCNT. (b) Three different types of SWCNTs

bonding arrangement in SWCNT is similar to that in graphene and thus, the electronic properties of SWCNT can be obtained from those of graphene by mapping the Brillouin zone of graphene into that of SWCNT. The approximation used in this case is called the zone folding approximation. The properties of SWNCT strongly depend upon the way in which a graphene sheet is rolled up into SWCNT. The vector which defines the direction along which the graphene plane is rolled up is called the chiral vector ($\vec{C_h}$) [27, 29]. The chiral vector can be expanded in terms of primitive lattice vectors of graphene (see Figure 1.4 (a)) and it is given by

$$\vec{C_h} = n\,\hat{a}_1 + m\,\hat{a}_2 \tag{1.7}$$

Thus, the pair of wrapping indices (n,m) decides the chirality of the SWNCT. The magnitude of the chiral vector ($|\vec{C_h}|$) gives the value of circumference of SWCNT. Furthermore, in accordance with its shape of edge, a SWCNT is classified into three types and they are : (a) zigzag (n,0), (b) armchair (n,n) and (c) chiral (n,m). In Figure 1.4 (b), we give the geometric structures of these three types of SWCNTs.

One can also derive the expressions for the diameter (d) and chiral angle (θ), which are defined by the angle between the chiral vectors and the lattice vector $\hat{a}_1$, of the SWCNT in terms of the wrapping indices (n,m) and they are

$$d = \frac{\sqrt{\vec{C_h}\cdot\vec{C_h}}}{\pi} = a\frac{\sqrt{n^2+m^2+nm}}{\pi} \tag{1.8}$$

$$\cos\,\theta = \frac{2n+m}{2\sqrt{n^2+m^2+nm}} \tag{1.9}$$

where a is the lattice constant of graphene which is equal to $\sqrt{3}d_{C-C}$. From the above relation, we can obtain the values of 30° and 0° for the chiral angles of armchair and zigzag SWCNTs respectively. The chiral angle for the chiral nanotubes lies in between these two values.

A periodicity of the quasi-one-dimensional SWCNT along the axis of tube is defined by a lattice translation vector $(\vec{T})$([27, 29])

$$\vec{T} = \frac{2m+n}{d_{gcd}}\hat{a}_1 + \frac{2n+m}{d_{gcd}}\hat{a}_2 \tag{1.10}$$

where d_{gcd} is the greatest common divisor of $(2m+n)$ and $(2n+m)$. It is important to note that the translation vector $(\vec{T})$ is perpendicular to the chiral vector $(\vec{C}_h)$.

Similar to the chiral and translation vectors, the reciprocal lattice vectors of the SWCNT can also be derived from those of graphene. There are two reciprocal lattice vectors for SWCNTs namely (i) $\vec{K}_c$ along the circumference of nanotube and (ii) $\vec{K}_a$ along the axis of nanotube. The chiral, translation and reciprocal lattice vectors of the SWCNT need to obey the following boundary conditions[27, 29],

$$\vec{T}\cdot\vec{K}_c = 0 \quad ; \quad \vec{T}\cdot\vec{K}_a = 2\pi \tag{1.11}$$

$$\vec{C}_h\cdot\vec{K}_c = 2\pi \quad ; \quad \vec{C}_h\cdot\vec{K}_a = 0 \tag{1.12}$$

Thus, the magnitudes of these two reciprocal vectors ($\vec{K}_c$ and $\vec{K}_a$) are inversely proportional to those of the chiral and the translation vectors respectively. Applying the periodic boundary conditions on the wave vector (k_z) of Bloch wave function along the tube axis, we get the following relation for the allowed values of wave vector within the first Brillouin zone $(-\frac{\pi}{T} \leq k_z \leq \frac{\pi}{T})$.

$$k_z = \frac{2\pi}{N_t|\vec{T}|}l \qquad \text{with} \qquad l = 0, 1, 2, \cdots N_t - 1 \tag{1.13}$$

where N_t is the number of unit cells present in the SWCNT. For an infinitely long SWCNT,

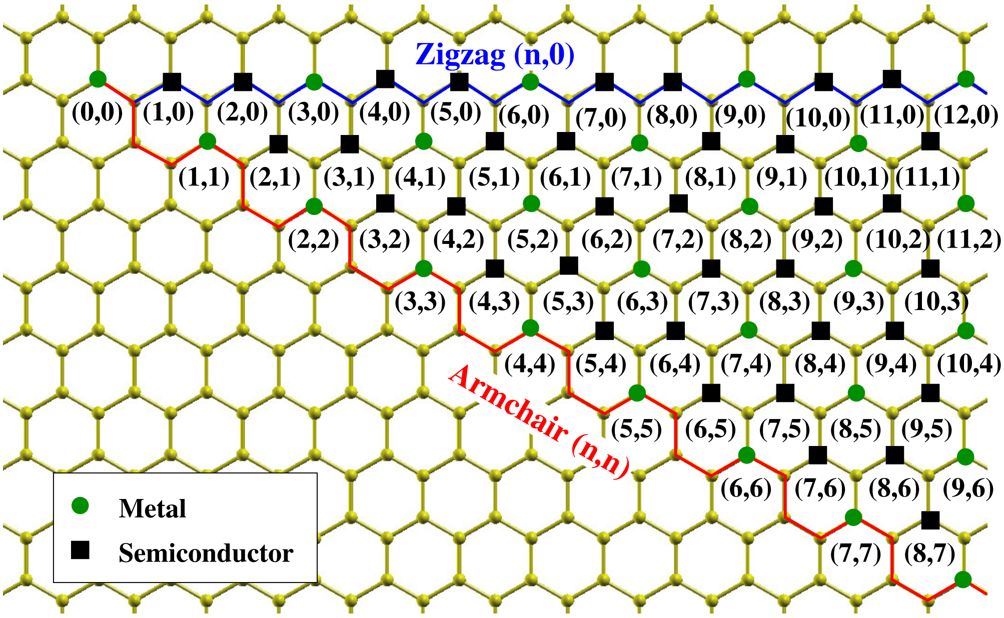

Figure 1.5: Condition for metallicity of SWCNT obtained from zone folding approximation. Numbers in the brackets represent the wrapping indices (n,m).

the allowed values of the wave vector are continuous.

Similarly, applying the boundary conditions on the wave vector ($k_\perp$) along the circumference (direction perpendicular to the tube axis), we get

$$k_\perp = \frac{2\pi}{|\vec{C}_h|} q = \frac{2}{d} q \tag{1.14}$$

where q is an integer. In contrast to the case of wave vector along the tube direction, there is a constraint on the allowed values of $k_\perp$ due to the finite value of the diameter. Thus, the allowed values of wave vectors (k_z and $k_\perp$) of the SWCNT form equi-distant k-lines in the Brillouin zone of graphene. It is important to note that whenever these k-lines of SWCNT pass through the highly symmetric k-point K of graphene, the SWCNT becomes metallic since, only at this k-point, the conduction and valence bands touch each other in graphene. It is now straight forward to derive the condition for metallicity of the SWCNT in the following manner. In order for a SWCNT to be metallic, its chiral vector should satisfy the following conditions[27, 29],

$$\begin{aligned} \vec{C}_h \cdot \vec{K} &= 2\pi q \quad (q \text{ is an integer}) && (1.15) \\ (n\hat{a}_1 + m\hat{a}_2) \cdot (2\hat{b}_1 + \hat{b}_2)/3 &= \frac{2n+m}{3} = q && (1.16) \end{aligned}$$

where $\hat{b}_1$ and $\hat{b}_2$ are the primitive reciprocal lattice vectors. This leads to the condition for metallicity of SWCNT that $(2n + m)$ or equivalently $(n - m)$ needs to be an integral multiple of 3. Figure 1.5 shows the metallic and semiconducting SWCNTs obtained by the above condition. It is to be noted that the armchair SWCNT (n,m) is always metallic whereas the zigzag SWCNT (n,0) is metallic when n is an integral multiple of 3, otherwise the SWCNT is a semiconductor. The above condition for metallicity is not valid for the SWCNTs with very small diameter due to the large influence of the effect of curvature.

1.2 Introduction to Semiconductor Clusters

Nanoclusters are aggregates of atoms containing a few up to a few thousands of atoms. Similar to two- and one-dimensional nanostructures, the properties of quasi-zero-dimensional nanoclusters are also different from those of the corresponding materials in the bulk form. There exists a variety of clusters made up of different atoms and molecules. According to the nature of chemical bonding which exists between the constituent atoms and molecules, the nanoclusters are classified into the following types , namely, (i) van der Waals clusters, (ii) metal clusters, (iii) network clusters and (iv) clusters of ionic materials[65]. The covalent bond that exists between the constituent atoms in semiconductor clusters leads to the formation of atomic networks and hence they are called the network clusters[65]. The binding energies of the clusters depend on the type of bonds present in the clusters.

There are two important discoveries which have made tremendous influences in the field of cluster science. The first one is the discovery of the magic numbers in the abundance of the alkali metal clusters by Knight et al.[66] in 1984. The occurrence of the magic numbers is correlated with the electronic shell structure of the clusters. It has been observed that the clusters with filled electronic shells are more stable than the clusters with open shells. This is similar to the atoms where the noble gas atoms with completely filled valence shell are chemically inert. Thus, the nanocluster is also called as superatom. The second one is the discovery of fullerene (C_{60}) by Kroto et al.[22] in 1985. C_{60} is one of the stable forms of carbon and it has a closed electronic shell with the HOMO-LUMO gap of 1.57 eV[67]. The fullerene and its solid-like structures possess many interesting physical properties. For example, the solid-like structures of C_{60} doped with alkali-metal atoms exhibit superconductivity[68].

After these two discoveries, there has been an increased interest in the field of semiconductor nanoclusters due to their interesting properties and their potential applications in the semiconducting industry. It is a hope of the researchers working in this field that the future miniaturization of semiconductor microelectronic devices can be achieved using semiconductor cluster based nanomaterials. As discussed earlier, many interesting properties of nanoclusters arise due to the large surface-to-volume ratio as well as due to the quantum confinement effect. The physical and chemical properties of nanoclusters strongly depend on their sizes, shapes and chemical compositions. For example, strong size dependance of the optical properties and reactivity of the clusters have been observed in the literature[59, 69–74]. It is well known that the surfaces of semiconductor bulk systems undergo structural relaxations in order to reduce the number of dangling bonds and consequently the surface energy. The clusters have larger ratio between number of surface and bulk atoms than the corresponding value in the bulk materials and hence the effect of dangling bonds is much more dominant on the properties of clusters. For example, small silicon clusters (Si_n; $n \leq 10$) exhibit higher coordination than the tetrahedral bonding arrangement in bulk silicon. Moreover, it has also been observed that silicon clusters of intermediate size show dramatic changes in their chemical reactivity, depending on the number of atoms in the cluster[73]. The abnormal optical properties (bright photo-luminescence) in porous silicon have been attributed to the quantum confinement of electrons and/or surface effects. Thus, several studies on the electronic and optical properties of silicon clusters with different sizes have been carried out to understand the effect of quantum confinement[75–79].

There exist a lot of theoretical and experimental studies on homogeneous and heterogeneous clusters made up of several semiconductor materials comprising of elements from group IV and III-V[80–121]. The heterogeneous semiconductor clusters such as GaAs, GaN and GaP, are considered to be more attractive than the homogeneous clusters (C, Si and Ge) since the properties of former can be controlled by changing their chemical compositions, in addition to their sizes. One of the earliest experimental studies on binary semiconductor clusters was by Smalley and coworkers[114]. They have observed that the relative abundance of larger GaAs clusters followed a binomial distribution whereas the smaller clusters deviated strongly from this distribution. More recent experimental studies on semiconductor clusters have been made by Neumark and coworkers[115–120] and by Weltner et al.[121]. Most of the existing studies mentioned above on nanoclusters are directed towards an understanding of the changes in structural and electronic properties with increasing size of clusters. However, it is worthwhile to mention here that there is no systematic experimental method to extract the equilibrium geometry of clusters. Thus, theoretical studies play a crucial role in identifying the ground state structure and hence these are helpful in understanding several physical and chemical properties of nanoclusters.

1.3 Objectives of the Present Thesis

With enormous increase in the power of modern computers and recent progress in computational techniques, there has been a large increase in the number of computational studies performed on the properties of materials including nanostructures. In computational material science, *ab initio* density functional theory (DFT) [122, 123] has become an important and widely used computational tool to study the properties of various systems since it provides accurate results for the ground state properties and also due to its favourable scaling of computational time with the size of the system[124, 125]. In DFT, the ground state electron density of a system is used as a basic variable instead of a complex many-body wave function. All the properties of a system have became a functional of density. With modern computational facilities, it is now possible to perform *ab initio* DFT based calculations for relatively large systems and similar calculations are not possible with the wave function based *ab initio* methods. Without any empirical parameters, DFT is capable of not only explaining the properties of existing materials, but also reliably predicting unknown properties of novel electronic systems. The DFT calculations would provide detailed information about the system which will help us to understand the interesting properties of materials under investigations.

The interesting properties[24–26] associated with graphene have motivated many researchers to search for new graphene-like two-dimensional materials made up of other elements. Up to now, several graphene-like structures composed of elements from group IV, III-V, II-VI and Metal dichalcogenides have been proposed in the literature[126–130]. Among these graphene-like structures, silicene - graphene analogue of silicon has received a lot of attention [128–145] during last few years. The existing studies on the properties of mono-layer silicene show that it possesses many exciting novel properties similar to those of mono-layer of graphene. Initially, it has been predicted that the electronic structure of silicene possesses linear dispersion around the Dirac point and thus the charge carriers in this two-dimensional system behave like massless relativistic Dirac-Fermions[128–131]. Recently, the existence of linear dispersion in the electronic structure of silicene mono-layer has been experimentally confirmed by the angle-resolved photo emission spectroscopy (ARPES) measurement[146]. We wish to mention here that silicon based nanostructures like silicene have an important added advantage over carbon based nanostructures like graphene due to their compatibility with the existing semiconductor technology. Thus, it is important to explore various possibilities of modifying the properties of silicene.

There exist several theoretical and experimental studies on various properties of bi- and multi-layers of graphene in the literature [147–162]. These studies show that many properties of graphene strongly depend on the number of layers, the inter-layer interactions and the stacking sequences. However, it is important to note that there are no detailed investigations on the properties of bi- and multi-layers of silicene. Thus, it will be interesting to probe the properties of the same.

In chapter 3 of this thesis, we present the results of our study on the geometric, electronic and optical properties of mono-layer of silicene and then compare with those of graphene. We also investigate the effect of two external influences namely, (a) hydrogenation and (b) transverse external static electric field on the properties of mono-layer of silicene.

In chapter 4 of this thesis, we present the results of a detailed computational study on the geometric and electronic properties of multi-layers of silicene as well as the evolution of these properties as a function of number of layers. For this purpose, we consider different stacking configurations for the multi-layers of silicene with number of layers (n) ranging from 1 to 10. We also probe several ground state properties of hybrid structure made up of honeycomb silicene and boron nitride layers.

As mentioned earlier, carbon nanotube (CNT) is a fascinating carbon based nanostructure, having excellent electrical, mechanical and optical properties[27–33]. Recently, nanotubes and nanowires made up of other group IV and III-V elements received considerable attention due to their interesting properties and also due to the possible technological importance of these materials in semiconductor industries. Among the group III-V materials, there exist some investigations on the physical properties of phosphide-based nanotubes and nanowires[163–174]. Recently, synthesis of GaPNT have been reported by Wu *et. al.*[163] and the optical studies on this nanotube show an emission peak corresponding to the direct band gap transition of GaPNT. Thus, it can be a potential candidate for applications in the light emitting devices. We know that the CNTs have a rich π-electron density which is, however, not expected in the nanotubes made up of group III-V materials. Thus, it will be interesting to study in microscopic detail the similarity and difference between the geometric and electronic properties of carbon and group III-V NTs, specifically, when these NTs are intercalated with various AM or TM atoms.

Keeping these points in mind, in chapter 5 of this thesis, we investigate the geometric and electronic properties of SWCNT(10,0) and SWGaPNT(10,0). Main emphasis is to study the effect of intercalation of alkali (AM) and transition metal (TM) atom clusters on the properties of these two NTs. For this purpose, we choose alkali metal atom (Na_n; n = 1 - 4) and transition metal atom (TM_n; n = 1 - 2; TM = Mn, Fe, Co) clusters. Here, n is the number of dopant atoms in the unit cell.

It is well known that the long range weak van der Waals (vdW) interaction plays an important role in many physical, chemical and biological phenomena. For example, it is the main driving force behind the formation of solid-like superstructures, thin films, ropes and bundles made up of carbon nanotube or fullerene units as well as in physisorption of various gas molecules on surface of nanomaterials. Thus, a detailed microscopic study of the vdW interaction and a quantitative estimation of strength of this interaction between different carbon nanostructures are extremely helpful to understand the above mentioned processes. However, we would like to mention here that there does not exist a reliable estimation of strength of the vdW interaction (through C_6 coefficient) between the carbon nanostructures using the first-principle methods.

In chapter 6 of the present thesis, we discuss the results of the calculation of vdW interaction coefficient between different cages and nanotubes, containing maximum about 100 carbon atoms, by using *all-electron* calculations based on DFT and time dependent density functional theory (TDDFT). We also investigate the variation of the static dipole polarizability and C_6 coefficient as a function of different physical parameters such as size and shape of the nanostructures. In addition, we also estimate the vdW coefficients between the carbon nanostructures and different gas molecules, specifically the environmentally hazardous ones, in order to explore the possibility of adsorption of these gases by the carbon based nanostructures.

Similar to one-dimensional systems, the properties of zero-dimenisonal semiconductor clusters, both homogeneous (Si_n, Ge_n, ...) and heterogeneous (Ga_mAs_n, Ga_mP_n, Ga_mN_n and Al_mP_n, ...) have also been extensively investigated in the literature [80–100]. However, in case of GaP clusters, all the existing studies are devoted to understanding the ground state properties[101–113]. To the best of our knowledge, there exists only one study [100] in which the calculation of polarizability of hydrogen terminated GaP clusters with tetrahedral geometries have been performed by employing time dependent Hartree-Fock (TDHF) method.

Thus, in chapter 7 of the present thesis, we investigate the static dipole polarizability of stoichiometric gallium phosphide clusters (Ga_nP_n with $n = 2-5$) by employing various *ab initio* wave function based methods as well as DFT / TDDFT. In order to study the performance of different XC functionals used in DFT / TDDFT method in determining static dipole polarizability of these clusters, we carry out the calculations of polarizability, within DFT / TDDFT, by employing various XC functionals, ranging from simple local density approximation (LDA) to asymptotically correct model potential - statistical average of orbital potential (SAOP). Furthermore, we also study the evolution of polarizability with the size of the clusters.

As we know that many physical and chemical properties, such as atomic and ionic radii, ionization energy, electron affinity, electronegativity, metallic and non-metallic character, and chemical reactivity, of elements in periodic table exhibit a periodic trend. The existence of the periodic trend is essentially a manifestation of the shell structure in the electronic configuration of elements. However, it is not well established in the literature whether the molecules also exhibit similar periodic variation of properties or not. Even in case of one of the simplest molecules present in nature i.e. homonuclear diatomic molecules, there is no systematic study on how several physical and chemical properties vary along the rows and columns of the periodic table, though there exist several experimental and theoretical studies on the properties of diatomic molecules. This has motivated us to carry out a systematic investigation on variation of different ground state and optical response properties of homonuclear diatomic molecules as a function of atomic number of constituent atoms. The results of this investigation are discussed in chapter 8.

In the next chapter, we briefly discuss the computational methods employed in the present thesis.

Chapter 2

Computational Methodology

In the present thesis, we employ the density functional theory (DFT)[122, 123] and the time-dependent density functional theory (TDDFT)[175] based calculations to study the ground state and optical response properties of the nanostructures, respectively. In this chapter, we give a brief introduction to the basics of DFT and TDDFT based calculations.

It is well known that the physical and chemical properties of materials are determined by the behavior of electrons which glue the atoms together to form a variety of molecules and solids. These electrons interact among themselves and also with the nuclei of the constituent atoms present in the system. The electronic structure calculations based on quantum mechanical theory play an important role in understanding many physical and chemical properties of materials. In quantum mechanics, the ground state properties of many-particle systems, like molecules and solids containing electrons and nuclei, are described by the time-independent Schrödinger Equation

$$\mathscr{H}|\Psi\rangle = E|\Psi\rangle \tag{2.1}$$

with the Hamiltonian ($\hat{H}$)

$$\begin{aligned}\mathscr{H} = -\frac{\hbar^2}{2m_e}\sum_{i=1}^{N}\nabla_i^2 - \frac{\hbar^2}{2}\sum_{I=1}^{N_I}\frac{\nabla_I^2}{M_I} + \frac{1}{4\pi\epsilon_0}\sum_{i<j}^{N}\frac{e^2}{|\mathbf{r_i}-\mathbf{r_j}|} + \frac{1}{4\pi\epsilon_0}\sum_{I<J}^{N_I}\frac{Z_I Z_J e^2}{|\mathbf{R_I}-\mathbf{R_J}|} \\ -\frac{1}{4\pi\epsilon_0}\sum_{i,I}^{N,N_I}\frac{Z_I e^2}{|\mathbf{r_i}-\mathbf{R_I}|}\end{aligned} \tag{2.2}$$

where

$\hbar$ & ϵ_0 - Planck's constant and permittivity of vacuum.

$\mathbf{r_i}$ & $\mathbf{R_I}$ - positions of electrons and nuclei.

m_e & M_I - masses of electrons and nuclei.

e & $Z_I e$ - charges of electrons and nuclei.

N & N_I - numbers of electrons and nuclei in the system.

Now onwards, we use atomic units in which the following fundamental constants - $\hbar$, e, m_e, and $\frac{1}{4\pi\epsilon_0}$ are taken as unity. In the above equation, the first two terms represent the kinetic energy operators for electrons and nuclei. The next two terms correspond to the repulsive potentials due to electron-electron and nucleus-nucleus interactions. The attractive interaction between the electrons and nuclei is described by the last term. Solving the many-body Schrödinger equation (2.1) associated with the full Hamiltonian (2.2) for any realistic system is a formidable task. It requires dealing with $3(N+N_I)$ degrees of freedom to obtain a desired solution. The complexity arises due to the electrostatic interaction terms which couple the degrees of freedom of the particles among themselves and also with those of others. As a result, one needs to look for reasonable approximations to simplify the complex situation. Fortunately, in many physical problems, we can decouple the nuclear and electronic degrees of freedom with the *Born-Oppenhemier* approximation[176] and solely focus attention on the Schrödinger equation for the electrons.

2.1 Born-Oppenhemier Approximation

According to this approximation[176], the electrons move much faster than the nuclei since the mass of an electron is much smaller than that of a nucleus. Thus the motion of electrons can be treated as instantaneous with respect to the motion of the nuclei. Moreover, it is assumed that the electrons remain always in the same adiabatic state during the motion of nuclei. Hence, the degrees of freedom of these two particles can be considered to be decoupled. By using this approximation, one can neglect the kinetic energy of nuclei from the Hamiltonian. Furthermore, the positions of the nuclei can be treated as parameters and thus the nucleus-nucleus interaction term becomes constant for a fixed set of nuclei. Then, the Hamiltonian which governs the electronic structure of the matter can be represented as

$$\hat{H} = -\frac{1}{2}\sum_{i=1}^{N}\nabla_i^2 + \sum_{i<j}^{N}\frac{1}{|\mathbf{r_i}-\mathbf{r_j}|} - \sum_{i,I}^{N,N_I}\frac{Z_I}{|\mathbf{r_i}-\mathbf{R_I}|} \tag{2.3}$$

Even after invoking the *Born-Oppenhemier* approximation, finding the solution of many-electron Schrödinger equation with this Hamiltonian (2.3) is still a difficult task. Again, the reason for the difficulty is due to the second term which couples the coordinates of electrons. This term prevents the reduction of a many-electron problem to an effective single-electron problem.

2.2 Solving Many-Electron Problems

2.2.1 Wave Function Based Methods

In order to solve the Schrödinger equation for a many-electron system, an independent particle approach was introduced by D. R. Hartree[177] (called Hartree method) and then it was modified by V. Fock (called Hartree-Fock (HF) method)[178].

Within the Hartree method, the electrons are considered as independent and they interact with each other only via a mean-field Coulomb potential. Thus, the many-body wave function $\Psi(\mathbf{r}_1, \mathbf{r}_2, \ldots, \mathbf{r}_N)$ can be written as a product of single-particle orbitals $\phi_i(\mathbf{r})$

$$\Psi(\mathbf{r}_1, \mathbf{r}_2, \ldots, \mathbf{r}_N) = \phi_1(\mathbf{r}_1)\phi_2(\mathbf{r}_2)\ldots\phi_N(\mathbf{r}_N) \tag{2.4}$$

Minimization of the energy expectation value

$$\langle E \rangle = \frac{\langle \Psi | \hat{H} | \Psi \rangle}{\langle \Psi | \Psi \rangle} \tag{2.5}$$

with the wave function in Eq.(2.4) and subject to the orthonormalization condition

$$\int \phi_i^\star(\mathbf{r})\phi_j(\mathbf{r})d\mathbf{r} = \delta_{ij} \tag{2.6}$$

leads to a single-electron-like Schrödinger equation,

$$\left(-\frac{\nabla^2}{2} + V_{mean}(\mathbf{r})\right)\phi_i(\mathbf{r}) = \epsilon_{ij}\phi_i(\mathbf{r}) \tag{2.7}$$

By an unitary transformation $\phi_i = \sum_j^N U_{ij}\phi_j^{'}$ (U_{ij} is unitary matrix i.e. $U^{\dagger}U = I$), we get

$$\left(-\frac{\nabla^2}{2} + V_{mean}(\mathbf{r})\right)\phi_i^{'}(\mathbf{r}) = \epsilon_i\phi_i^{'}(\mathbf{r}) \tag{2.8}$$

where $V_{mean}(\mathbf{r})$ is the mean field potential in which the electron moves. This potential includes the following two terms. (a) The external potential due to the electron-nuclear interaction and (b) the Hartree potential due to classical electrostatic repulsion between the electrons

$$V_H(\mathbf{r}) = \frac{1}{2}\int d\mathbf{r}'\frac{n(\mathbf{r}')}{|\mathbf{r}-\mathbf{r}'|} \tag{2.9}$$

It is to be noted that this term includes the spurious effect due to the self-interaction. The electron density of a system can be written as a sum of squares of the single-particle orbitals

$$n(\mathbf{r}) = \sum_i^N |\phi_i^{'}(\mathbf{r})|^2 \tag{2.10}$$

To solve Eq.(2.8), one should know the $V_{mean}(\mathbf{r})$ which depends on $n(\mathbf{r})$. However, the calculation of density requires the knowledge of single-particle orbitals $\phi_i(\mathbf{r})$ - which are the solutions of the equation we intend to solve. Hence, the equation is solved self-consistently.

The major problem with the Hartree method is that the Hartree wave function does not satisfy one of the fundamental properties of many-body wave function for the Fermions i.e the anti-symmetry property. In the HF method, the anti-symmetry property is incorporated by forming a Slater determinant[179] of the single-particle orbitals

$$\Psi(\mathbf{x}_1,\mathbf{x}_2,\ldots,\mathbf{x}_N) = \frac{1}{\sqrt{N!}}\begin{vmatrix} \phi_1(\mathbf{x}_1) & \phi_1(\mathbf{x}_2) & \ldots & \phi_1(\mathbf{x}_N) \\ \phi_2(\mathbf{x}_1) & \phi_2(\mathbf{x}_2) & \ldots & \phi_2(\mathbf{x}_N) \\ \vdots & \vdots & & \vdots \\ \phi_N(\mathbf{x}_1) & \phi_N(\mathbf{x}_2) & \ldots & \phi_N(\mathbf{x}_N) \end{vmatrix} \tag{2.11}$$

where $\mathbf{x_i} \equiv (\mathbf{r_i}, \sigma_i)$ includes spatial and spin-coordinates (σ_i). The above wave function is normalized. Similar to the previous case, the minimization of the energy expectation value with the above wave function leads to the single-particle HF equation

$$\begin{aligned}\left(-\frac{\nabla^2}{2}+V_{ext}(\mathbf{r})\right)\phi_i(\mathbf{r})+\sum_j\int d\mathbf{r}'\frac{|\phi_j(\mathbf{r}')|^2}{|\mathbf{r}-\mathbf{r}'|}\phi_i(\mathbf{r})\\-\sum_j\delta_{\sigma_i,\sigma_j}\int d\mathbf{r}'\frac{\phi_j^\star(\mathbf{r}')\phi_i^\star(\mathbf{r}')}{|\mathbf{r}-\mathbf{r}'|}\phi_j(\mathbf{r})=\epsilon_i\phi_i(\mathbf{r})\end{aligned} \tag{2.12}$$

In the above equation, the first two terms correspond to the kinetic energy and the external potential respectively. The third term is the Hartree potential due to classical Coulomb electrostatic repulsion between the electrons. The last term on the left-hand side is called the exchange term which arises due to the inclusion of the Pauli's exclusion principle through the anti-symmetric wave function. This term adds considerable complexity in the Hartree-Fock equation due to its non-local character. Physically, because of the exclusion principle the electrons with same spin avoid each other and thus, a depleted region of the charge density in the immediate vicinity of a given electron is created which is called the exchange hole. The exchange energy is considered due to the interaction between the exchange hole and the electrons. Within the HF method, a definite meaning can be assigned to the eigen values of single-particle orbitals with the help of Koopman's theorem. The theorem states that each eigen value gives the energy required to remove an electron from the corresponding single-electron state.

There are two major improvements in the HF method as compared to the Hartree method. First, it includes the anti-symmetry property of the many-body wave function and thus exactly takes into account of the contribution due to the exchange effect. Secondly, there is no self-interaction in HF method since the self-interaction contribution present in the Hartree potential is exactly equal and opposite to that in the exchange potential and thus they cancel each other. However, it is important to note that the complex many-body wave function can never be a single Slater determinant of single-particle orbitals or a simple combination of few determinants. Thus, the energy obtained from the HF method is always higher than the true value. The error in the calculations of the HF energy with respect to the true one is called the *correlation energy* which arises due to the many-body correlation between the electrons[180]. Later on, several Post-

Hartree-Fock methods were developed to include the effect of correlations[181]. Some of these methods are (i) Configuration interaction (CI), (ii) Coupled cluster (CC) and (iii) Møller-Plesset perturbation theory (MP2, MP3, MP4, etc.). The performance of these methods are impressive and they are able to produce accurate results. However, the practical applicability of these methods is strongly restricted to a system of few atoms or molecules since these methods are computationally expensive due to an unfavorable scaling with the size of the system[182]. For example, the scaling of computational time in CI method goes as M^6 for single and double excitations, and as M^8 and M^{10} for triply and quadruple excitations, respectively, where M is the size of the basis set used in the calculations. Similarly, the computational time in nth order Møller-Plesset perturbation theory scales as M^{n+3}. Thus, in order to carry out the electronic structure calculations for a wider range of materials, one requires an alternative theory which can handle much larger systems containing many electrons more efficiently.

2.2.2 Density Based Method - Density Functional Theory

Density functional theory is an alternative way to study the electronic structure of matter in which the ground state electron density of a system is used as a basic variable instead of a many-body wave function. Conceptually, it is easy to work with density rather than a many-body wave function since the former is a function of three variables in contrast to the 3N variables of the latter. This theory has become a widely popular tool for the electronic structure calculations of condensed matter. DFT has also become popular in quantum chemistry due to recent developments in the modern approximate functionals[125]. The calculations based on DFT with these approximate functionals provide an useful balance between accuracy and computational cost. Thus, it allows us to perform calculations on much larger systems, which are not possible with wave function based *ab initio* methods, while retaining much of their accuracy.

For the first time, a theory based on the ground state electronic density $n(\mathbf{r})$ was proposed by Thomas[183] and Fermi[184, 185] in 1927. In this theory, the kinetic energy functional is derived from non-interacting electrons in homogenous electron gas. However, this theory does not include the quantum effects such as exchange and correlation. The theory is unable to predict the stability of the molecular systems since the total energy of a molecule is higher than its constituent atoms. Over the years, several attempts have been made to improve the Thomas-Fermi like density based approach by including better kinetic energy functional as well as the effect of exchange and correlation[186–188]. However, the theory lacks formal justifications for using the ground state electronic density $n(\mathbf{r})$ as a basic variable.

Foundations of DFT

The theoretical foundation for the density functional theory was laid by P. Hohenberg and W. Kohn in 1964[122]. The theory is based upon the following two theorems.

Theorem 1: For any system of interacting particles in an external potential $V_{ext}(\mathbf{r})$, the potential $V_{ext}(\mathbf{r})$ is determined uniquely, except for a trivial additive constant, by the ground state particle density $n(\mathbf{r})$.

Since the Hamiltonian is thus completely determined with a constant shift in the energy, it follows that the many-body wave functions for all the states of the system are determined. Hence, all the properties of the system are functionals of density and they can be completely determined if the ground state particle density $n(\mathbf{r})$ is known.

Theorem 2: (Variational Principle) There exists an universal functional $F[n]$ for any valid external potential $V_{ext}(\mathbf{r})$. For any particular $V_{ext}(\mathbf{r})$, the exact ground state energy of the system is the global minimum value of the total energy functional $E[n]$, and the density $n(\mathbf{r})$ that minimizes the functional is the exact ground state density.

The proofs of these theorems for the non-degenerate ground state are very simple. Let us assume that there are two different external potentials $V_{ext}(\mathbf{r})$ and $V'_{ext}(\mathbf{r})$ which differ by more than an additive constant and both give the same ground state density $n(\mathbf{r})$. For the external potential $V_{ext}(\mathbf{r})$, the Hamiltonian $\hat{H}$ has the ground state energy E_0 and ground state wave function Ψ. Similarly, E'_0 and Ψ' are the ground state energy and ground state wave function corresponding to $\hat{H}'$ with the external potential $V'_{ext}(\mathbf{r})$. The Hamiltonians for the above mentioned two systems are given by

$$\hat{H} = \hat{T} + \hat{W} + V_{ext}(\mathbf{r}) \quad ; \quad \hat{H}' = \hat{T} + \hat{W} + V'_{ext}(\mathbf{r}) \tag{2.13}$$

where $\hat{T}$ and $\hat{W}$ represent the kinetic energy and the electron-electron repulsive potential respectively. Since Ψ' is not the ground state wave function of $\hat{H}$, it follows that

$$E_0 = \langle\Psi|\hat{H}|\Psi\rangle < \langle\Psi'|\hat{H}|\Psi'\rangle \tag{2.14}$$

The inequality in the above equation is strictly valid due to the assumption that the system has non-degenerate ground state. One can re-write the last term in above equation as

$$\begin{aligned}\langle\Psi'|\hat{H}|\Psi'\rangle &= \langle\Psi'|\hat{H}'|\Psi'\rangle + \langle\Psi'|\hat{H} - \hat{H}'|\Psi'\rangle && (2.15)\\ &= E_0' + \int d^3r\,[V_{ext}(\mathbf{r}) - V_{ext}'(\mathbf{r})]\,n(\mathbf{r}) && (2.16)\end{aligned}$$

Substituting Eq.(2.16) in Eq.(2.14), we get

$$E_0 < E_0' + \int d^3r\,[V_{ext}(\mathbf{r}) - V_{ext}'(\mathbf{r})]\,n(\mathbf{r}) \tag{2.17}$$

One can estimate the expectation value of $\hat{H}'$ with the wave function Ψ and we arrive at a similar result as above

$$E_0' < E_0 + \int d^3r\,[V_{ext}'(\mathbf{r}) - V_{ext}(\mathbf{r})]\,n(\mathbf{r}) \tag{2.18}$$

Now, adding Eq.(2.17) and Eq.(2.18) we get the following contradictory inequality

$$E_0 + E_0' < E_0' + E_0 \tag{2.19}$$

This proves the fact that there cannot be two different external potentials, differing by more than an additive constant, which yield the same ground state density. Thus, there should be a one-to-one correspondence between the external potential and the ground state density.

Universal Functional

The total energy functional of the system can be written as

$$\begin{aligned} E[n] &= \langle\Psi|\hat{H}|\Psi\rangle = \langle\Psi[n]|\hat{T}+\hat{W}|\Psi[n]\rangle + \int d^3r V_{ext}(\mathbf{r})n(\mathbf{r}) && (2.20) \\ &= F[n] + \int d^3r V_{ext}(\mathbf{r})n(\mathbf{r}) && (2.21) \end{aligned}$$

where $T[n] = \langle\Psi[n]|\hat{T}|\Psi[n]\rangle$ and $W[n] = \langle\Psi[n]|\hat{W}|\Psi[n]\rangle$ are the kinetic and electron-electron interaction energy functionals respectively. The functional $F[n] = T[n] + W[n]$ is called universal functional since it is independent of the external potential and consequently of the system. The ground state energy of a system can be obtained by minimizing the above energy functional. The ground state density is the one which minimizes the $E[n]$ and hence satisfy the Euler-Lagrange equation

$$\frac{\delta F[n]}{\delta n(\mathbf{r})} + V_{ext}(\mathbf{r}) = \mu \tag{2.22}$$

where μ is the Lagrange multiplier associated with the constraint

$$\int n(\mathbf{r})d\mathbf{r} = N \tag{2.23}$$

If we know the exact form of $F[n]$, Eq.(2.22) can be solved exactly to obtain the ground state density and thus, the ground state energy. Unfortunately, the exact form of the universal functional is not known.

2.2.3 The Kohn-Sham Approach

In 1965, soon after the discovery of the DFT, a practical approach of utilizing DFT for performing the electronic structure calculations was proposed by Kohn and Sham (KS)[123]. This approach has made DFT the most widely used tool in computational material science. In this approach, KS has ingeniously mapped the problem of a complicated interacting system onto a problem of much easier-to-solve non-interacting system. They have considered a fictitious auxiliary non-interacting system, with an effective potential V_{ks}, having the same density $n(\mathbf{r})$ as that of the original interacting system. The main idea behind the KS approach is that the universal functional is written in terms of the kinetic energy $T_s[n]$ of the fictitious auxiliary non-interacting system.

$$\begin{aligned} F[n] &= T[n] + W[n] \\ &= T_s[n] + (T[n] - T_s[n]) + E_H[n] + (W[n] - E_H[n]) \\ &= T_s[n] + E_H[n] + E_{xc} \end{aligned} \tag{2.24}$$

where E_{xc} is the exchange-correlation functional

$$E_{xc}[n(\mathbf{r})] = T[n] - T_s[n] + W[n] - E_H[n] \tag{2.25}$$

and $E_H[n]$ represents the Hartree energy due to the classical Coulomb interaction between the electrons. Though $T_s[n]$ is not the true kinetic energy of the system, it can be exactly determined by

$$T_s[n] = -\sum_i^N \int \phi_i(\mathbf{r})^* \left[\frac{\nabla^2}{2}\right] \phi_i(\mathbf{r}) d\mathbf{r} \tag{2.26}$$

Then, the small error or difference between the kinetic energies of the original interacting and fictitious auxiliary non-interacting systems is clubbed into the $E_{xc}[n]$. However, we do not know the form of this functional and thus one needs to use an approximation for it.

The single-electron eigen states $\phi_i(\mathbf{r})$ corresponding to the auxiliary non-interacting system are obtained by solving the Kohn-Sham equation

$$\left(-\frac{\nabla^2}{2} + V_{ks}[n(\mathbf{r})]\right) \phi_i(\mathbf{r}) = \epsilon_i \phi_i(\mathbf{r}) \tag{2.27}$$

and then the density of the system (interacting and non-interacting) can be written as sum of squares of the occupied orbitals

$$n(\mathbf{r}) = \sum_i^N |\phi_i(\mathbf{r})|^2 \tag{2.28}$$

By incorporating the first Hohenberg-Kohn theorem, the Kohn-Sham potential V_{ks} of the fictitious system can be related to the external potential V_{ext} of the real system in the following manner since both these two potentials correspond to the same density.

$$V_{ks}[n(\mathbf{r})] = V_{ext}[n(\mathbf{r})] + V_H[n(\mathbf{r})] + V_{xc}[n(\mathbf{r})] \tag{2.29}$$

$$\text{where} \qquad V_H[n(\mathbf{r})] = \frac{1}{2}\int \frac{n(\mathbf{r}')}{|\mathbf{r}-\mathbf{r}'|}d\mathbf{r}' \qquad \text{and} \qquad V_{xc}[n(\mathbf{r})] = \frac{\delta E_{xc}[n(\mathbf{r})]}{\delta n(\mathbf{r})} \tag{2.30}$$

are the Hartree and the exchange-correlation potentials respectively.

The total energy of the system can be obtained from the solutions of the KS equation and it is given by

$$\begin{aligned} E[\phi_i(\mathbf{r})] &= \sum_i^N \int \phi_i(\mathbf{r})^* \left[-\frac{\nabla^2}{2}\right] \phi_i(\mathbf{r}) d\mathbf{r} + \int V_{ext}(\mathbf{r}) n(\mathbf{r}) d\mathbf{r} + \frac{1}{2}\int\int \frac{n(\mathbf{r})n(\mathbf{r}')}{|\mathbf{r}-\mathbf{r}'|} d\mathbf{r} d\mathbf{r}' \\ &\quad + E_{xc}[n(\mathbf{r})] + E_{NN} \\ &= \sum_i^N \epsilon_i - \frac{1}{2}\int\int \frac{n(\mathbf{r})n(\mathbf{r}')}{|\mathbf{r}-\mathbf{r}'|} d\mathbf{r} d\mathbf{r}' - \int V_{xc} n(\mathbf{r}) d\mathbf{r} + E_{xc}[n(\mathbf{r})] + E_{NN} \end{aligned} \tag{2.31}$$

where E_{NN} is the energy due to the interaction between the nuclei.

2.2.4 Exchange-Correlation Functional

Within the Kohn-Sham scheme, all the quantum mechanical effects are included in the the exchange-correlation functional. However, the exact form for E_{xc} as a functional of density is not known. Though the DFT is exact in principle, it is required to use an approximation to the unknown E_{xc} functional for the practical applications. Till date, several approximations to the exchange-correlation functional have been proposed in the literature[123, 189–196].

Local Density Approximation

A simplest approximation to the exchange-correlation functional is the local density approximation (LDA) which is suggested by KS in their seminal paper. Within the LDA, the exchange-correlation functional is written as

$$E_{xc}[n(\mathbf{r})] = \int n(\mathbf{r})\ \epsilon_{xc}^{homo}(n,\mathbf{r})\ d\mathbf{r} \tag{2.32}$$

where the exchange-correlation energy density ($\epsilon_{xc}[n(\mathbf{r})]$) of a system at each point is replaced by the exchange-correlation energy density ($\epsilon_{xc}^{homo}(n,\mathbf{r})$) of a homogeneous electron gas with density at that point. In this sense, the functional is purely local. Within the DFT formalism, the exchange-correlation density (ϵ_{xc}) can be divided into two contributions namely the exchange (ϵ_x) and the correlation (ϵ_c). The exact form of the exchange part for homogeneous gas is given by Dirac and it is called the Dirac exchange[186]. In case of correlation, the analytical form is available only for low and high density limits. However, highly accurate numerical quantum Monte-Carlo simulations of the homogeneous electron gas are available from the work of Ceperly and Alder[197]. Based on the results of this work, the analytical expressions for the correlation energy density have been obtained by using sophisticated interpolation schemes. The most widely used representation is VWN, developed by Vosko, Wilk, and Nusair[189] while the recent one has been given by Perdew and Wang[190].

The LDA can be extended to the spin polarized case which is called as the local spin density approximation (LSDA) in which the up and down spins are treated separately.

$$E_{xc}[n^{\uparrow}(\mathbf{r}),n^{\downarrow}(\mathbf{r})] = \int n(\mathbf{r})\ \epsilon_{xc}^{homo}(n^{\uparrow}(\mathbf{r}),n^{\downarrow}(\mathbf{r}))\ d\mathbf{r} \tag{2.33}$$

The performance of LDA/LSDA is quite satisfactory. It is expected that it would provide good results for the homogeneous system like nearly-free-electron metal. However, it is found to give reasonably good results for the inhomogeneous systems like atoms and molecules as well. One of the reasons for the success is that it obeys the sum rules for the exchange and correlation holes. It typically underestimates the contribution of exchange energy and overestimates the contribution of correlation energy which result in cancellation of errors. This leads to unexpectedly good results for the E_{xc} values. However, there are some failures of LDA, namely it tends to overestimate the binding energy but underestimate atomic ground-state energies, ionization energies and bang gaps.

Generalized Gradient Approximation

After the LDA, a further improvement to the approximation of exchange-correlation energy leads to the generalized gradient approximation (GGA) in which the exchange-correlation energy density depends not only on the density of the electrons, but also on the gradient of the density ($|\nabla n^{\downarrow}(\mathbf{r})|$, $|\nabla n^{\downarrow}(\mathbf{r})|$). Thus, the GGA is expected to give better results for the inhomogeneous systems.

$$\begin{aligned} E_{xc}^{GGA}[n(\mathbf{r})] &= \int n(\mathbf{r})\ \epsilon_{xc}(n^{\uparrow}(\mathbf{r}), n^{\downarrow}(\mathbf{r}), |\nabla n^{\uparrow}(\mathbf{r})|, |\nabla n^{\downarrow}(\mathbf{r})|)\ d\mathbf{r} \\ &= \int n(\mathbf{r})\ \epsilon_{xc}^{homo} F_{xc}(n^{\uparrow}(\mathbf{r}), n^{\downarrow}(\mathbf{r}), |\nabla n^{\uparrow}(\mathbf{r})|, |\nabla n^{\downarrow}(\mathbf{r})|)\ d\mathbf{r} \qquad (2.34) \end{aligned}$$

where F_{xc} is a dimensionless quantity and it satisfies the sum rules. Numerous forms of the F_{xc} have been proposed in the literature[191, 195]. In many systems, the GGA gives improved results for the binding energies and the bond lengths as compared to the LDA. For most of our calculations for the ground state properties, we use one of the most popular GGA forms given by Perdew-Burke-Ernzerhof (PBE)[195].

2.2.5 Solving the Kohn-Sham Equation

In practice, the Kohn-Sham equation is solved numerically by an iterative procedure which is called as the self-consistent field (SCF) method. The steps involved in the SCF calculations are given below. The flow chart of these steps is also given in Figure 2.1.

1. Choose the approximate geometric structure of a system
2. Make an initial guess for the electron density $n(\mathbf{r})$
3. Construct the Kohn-Sham potential based on this density
4. Solve the Kohn-Sham equation to obtain the Kohn-Sham orbitals and energies
5. Construct a new density using these orbitals
6. Check the self-consistency. If the difference between the total energy of the system in two consecutive cycles is smaller than the threshold value, the self-consistency is achieved. Otherwise, go to step 7
7. Obtain new density by mixing the densities of the present and previous cycles. Then go back to step 3

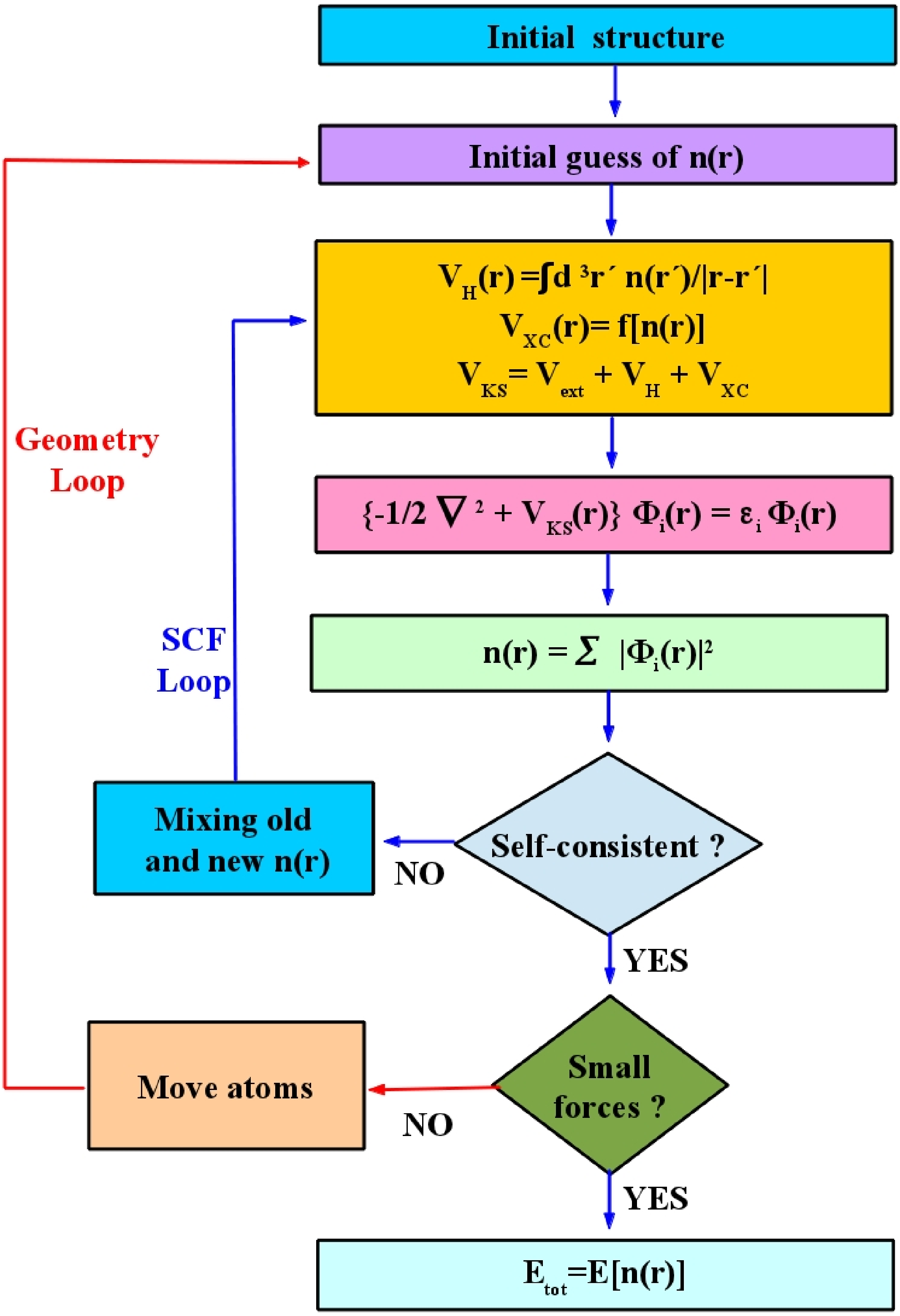

Figure 2.1: The flow chart of the steps involved in DFT calculations including geometry optimization

The procedure will be continued until self-consistency is reached. These calculations have been performed for the initial geometry (with a set of fixed nuclei) and it may not correspond to the correct geometric structure of the system. In order to obtain the correct geometric structure, we calculate the Hellmann-Feynman force on each of the atoms at the end of the SCF cycle. If the forces are more than the threshold value, new geometric structure is created by appropriately moving the corresponding atoms. Now, the above mentioned steps in the SCF calculations are followed for the new geometric structure. The outer geometry loop is continued until we obtain the optimized geometric structure of the given system. At the end of these calculations, we can obtain all the ground state properties of the system from the KS orbitals and energies.

To solve the Kohn-Sham equation, we use a few numerical codes. Here, we summarize some of the salient features of these codes which we have used in our calculations. Though all the below mentioned codes solve same KS equation, the practical implementations are different. The main differences arise due to (a) the type of basis sets used to expand the KS orbitals (plane waves vs atom-centered basis functions) and (b) the way in which the interaction between the nucleus and electrons is treated (full-potential vs pseudopotential/projector augmented wave). For most of our electronic structure calculations based on the DFT, we use the PBE[195] XC potential.

WIEN2k

We have used WIEN2k package[198] to perform the *all-electron* DFT based electronic structure calculations for the periodic solids. It employs the full-potential linearized augmented plane-wave (FP-LAPW) and local-orbitals as basis set to solve the Kohn-Sham equation. In this method, the unit cell is divided into two regions, namely (i) non-overlapping atomic spheres and (ii) an interstitial region. Atomic orbitals and plane waves are used as basis sets in the regions (i) and (ii) respectively. This method is considered to be one of the most accurate schemes for band structure calculations. We also include the relativistic effects in our calculations. The SCF calculations are performed with the convergence criterion for the total energy to be less than 0.1 mRy. The structures are optimized by minimizing the Hellmann-Feynmann forces till the forces on individual atoms are small (below 5 mRy/a.u).

Vienna Ab initio Simulation Package (VASP)

Using VASP[199], we have performed the electronic structure calculations for periodic solids within the framework of the projector augmented wave (PAW) method. PAW method considerably reduces the number of plane wave required for the calculations. In this code, the convergence criteria for energy in SCF cycles is chosen to be 10^{-6} eV. All the structures are optimized by minimizing the forces on individual atoms with the criterion that the total force on each atom is below 10^{-2} eV/ Å.

Spanish Initiative for Electronic Simulations with Thousands of Atoms (SIESTA)

We have also used SIESTA package[200–202] for performing a fully self-consistent DFT calculation by solving the standard Kohn-Sham equations. The KS orbitals are expanded using a linear combination of pseudoatomic orbitals proposed by Sankey and Niklewski[203]. All our calculations have been carried out by using triple-zeta basis set with polarization function. The standard norm conserving Troullier-Martins pseudopotentials[204] have been utilized.

Amsterdam Density Functional (ADF)

We use the ADF package [205] to perform the ground state and response properties calculations for the finite non-periodic systems, within the framework of DFT / TDDFT. For ground state properties, we use the triple-ξ Slater-type orbital (STO) basis set with two added polarization functions (TZ2P basis set of ADF basis set library [205]). We use the Mayer formalism[206] as implemented in the ADF package[205] for the calculations of bond order. For these calculations, the convergence criteria for the norm of energy gradient and energy were fixed at 10^{-4} atomic units (a.u.) and 10^{-6} a.u., respectively.

Super-cell Approach

Many of the above mentioned codes use periodic boundary conditions to simulate three-dimensional periodicity of the bulk solids. But, the low dimensional nanostructures either lack or possess periodicity along only one or two directions. In order to simulate these low-dimensional nanostructures using the periodic code, we use super cell approach in which

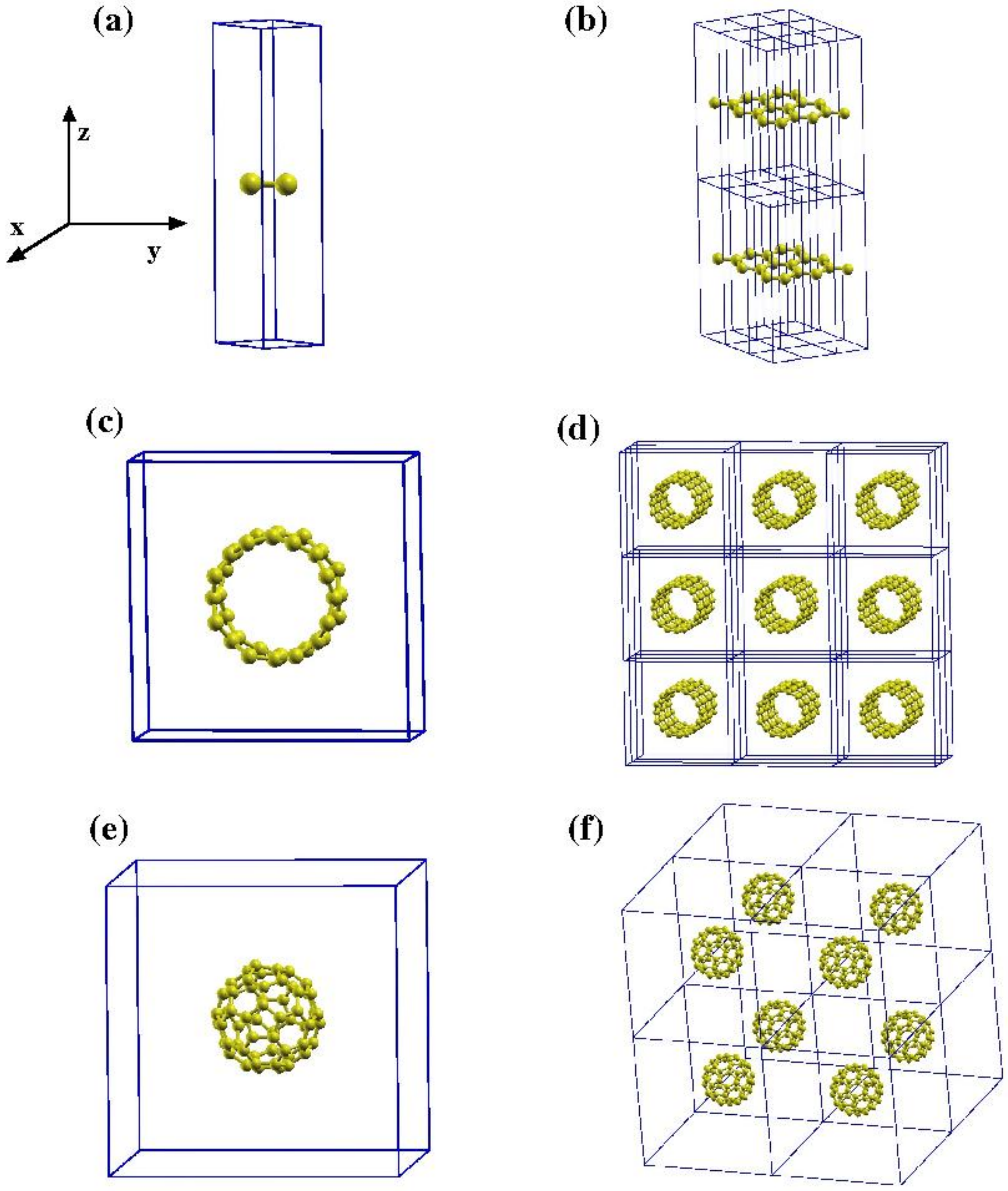

Figure 2.2: Unit and super cells of low dimensional nanostructures: graphene (a, b) - two-dimensional system with vacuum in one direction, carbon nanotube (c, d) - one-dimensional system with vacuum in two directions, and fullerene (e, f) - zero-dimensional system with vacuum in all the three directions.

an artificial unit cell is constructed with a large vacuum along the non-periodic directions. The vacuum is provided along the non-periodic directions to avoid the interaction between the nanostructures in the adjacent unit cells. In case of two-dimensional planar structures (along x- & y- axes), a vacuum space is given along the direction (z-axis) perpendicular to the plane. Similarly, for one (along x-axis) and zero-dimensional structures, the vacuum space is given in two (along y- and z-axes) and all the three (along x-, y- and z-axes) non-periodic directions respectively. In Figure 2.2, we give examples for unit cells (first column) and super cells (second column) of low-dimensional systems such as graphene (a, b), carbon nanotube (c, d) and fullerene (e, f).

2.3 Time Dependent Density Functional Theory

In this section, we briefly describe the basics of the time-dependent density functional theory (TDDFT) which has been employed to calculate the frequency dependent polarizability.

Foundations

Formal foundation of TDDFT is based on the Runge-Gross (RG) theorem (1984)[175] and it is the time-dependent analogue of the Hohenberg-Kohn (HK) theorem (1964)[122]. The RG theorem shows that, for a given initial wavefunction, there is an unique mapping between the time-dependent external potential of a system and its time-dependent density. This implies that one can work with time-dependent density (3 variables) instead of the many-body wavefunction (3N variables). Hence, all the properties of a system can be determined from the knowledge of the density alone. Unlike in DFT, there is no general minimization principle in the time-dependent case. Consequently, the proof of the RG theorem is more involved than that of the HK theorem. It has been shown by many people, namely Ghosh, Deb, Bartolotti, Runge, Gross, Kohn and others[207–214] that several important concepts in the ground state DFT can be extended to time-dependent case in a rigorous manner. Thus, the TDDFT can be used to calculate the dynamic response properties such as polarizability, hyper-polarizability, excited state energies, optical absorption spectra and strength of the van der Waals interaction.

The evolution of many-body wavefunction with time is given by the time-dependent Schrödinger equation

$$\hat{H}(t)|\Psi(t)\rangle = i\frac{\partial}{\partial t}|\Psi(t)\rangle, \quad \text{with } |\Psi(t=0)\rangle = |\Psi(0)\rangle. \tag{2.35}$$

and the Hamiltonian $\hat{H}(t)$ of a system is given by

$$\hat{H}(t) = \hat{T} + \hat{W} + \hat{V}_{\text{ext}}(t), \tag{2.36}$$

where $\hat{T}$, $\hat{W}$ and $\hat{V}_{ext}(t)$ are the kinetic energy, the electron-electron repulsive and time-dependent external potentials respectively. The time-dependent density can be obtained from the many-body wave function as

$$n(\mathbf{r}, t) = N \int d\mathbf{r_2} \ldots \int d\mathbf{r_N} |\Psi(\mathbf{r}, \mathbf{r_2}....\mathbf{r_N}, t)|^2 \tag{2.37}$$

and it has the interpretation that $n(\mathbf{r}, t)d\mathbf{r}$ is the probability of finding an electron in a region $d\mathbf{r}$ around $\mathbf{r}$ at a time t. Then, the density is normalized to the total number of electrons

$$\int n(\mathbf{r}, t)d\mathbf{r} = N \tag{2.38}$$

2.3.1 Runge-Gross Theorem

The RG theorem states that two densities $n(\mathbf{r}, t)$ and $n'(\mathbf{r}, t)$ evolving from a common initial state $|\Psi(0)\rangle$ under the influence of two Taylor expandable external potentials $V_{ext}(\mathbf{r}, t)$ and $V'_{ext}(\mathbf{r}, t)$, respectively, will be different if the potentials differ by more than a purely time-dependent (r-independent) function

$$V_{ext}(\mathbf{r}, t) - V'_{ext}(\mathbf{r}, t) \neq c(t) \Rightarrow n(\mathbf{r}, t) \neq n'(\mathbf{r}, t) \tag{2.39}$$

Now, in this situation, there is a one-to-one correspondence between the time-dependent density and potential. In order to prove this theorem, let us first show that current densities corresponding to these potentials must differ. The current density can be written as

$$j(\mathbf{r}, t) = N \int dr_2 \ldots \int dr_N \quad \Im\left(\Psi(\mathbf{r}, \mathbf{r_2}....\mathbf{r_N}, t)\nabla\Psi^{\dagger}(\mathbf{r}, \mathbf{r_2}....\mathbf{r_N}, t)\right) \tag{2.40}$$

where $\Im$ denotes the imaginary part and the corresponding continuity equation for the current density is given by

$$\frac{\partial}{\partial t}n(\mathbf{r},t)+\nabla\cdot j(\mathbf{r},t)=0 \tag{2.41}$$

Since the Hamiltonians of the two systems considered here differ only in their one-body external potentials, the equation of motion for the difference in their current densities can be written in the following manner
At $t=0$

$$\begin{aligned}\frac{\partial}{\partial t}\{j(\mathbf{r},t)-j'(\mathbf{r},t)\}_{t=0} &= -i\langle\Psi(0)|\left[j(\mathbf{r},0),\{\hat{H}(0)-\hat{H}'(0)\}\right]|\Psi(0)\rangle\\ &= -i\langle\Psi(0)|\left[j(\mathbf{r},0),\{V_{ext}(\mathbf{r},0)-V'_{ext}(\mathbf{r},0)\}\right]|\Psi(0)\rangle\\ &= -n(\mathbf{r},0)\nabla\{V_{ext}(\mathbf{r},0)-V'_{ext}(\mathbf{r},0)\}\end{aligned} \tag{2.42}$$

where $n(\mathbf{r},0)$ is the initial density. It is seen from the above equation that if the two potentials differ (by more than just a constant) at the initial time, then the first derivative of the currents must be different. Similarly, we can also show that the higher order derivative of current densities will differ by

$$\frac{\partial^{k+1}}{\partial t^{k+1}}\{j(\mathbf{r},t)-j'(\mathbf{r},t)\}_{t=0} = -n(\mathbf{r},0)\nabla\frac{\partial^{k}}{\partial t^{k}}\{V_{ext}(\mathbf{r},t)-V'_{ext}(\mathbf{r},t)\}_{t=0} \tag{2.43}$$

If the equation (2.39) is satisfied and the two external potentials are Taylor expandable about $t=0$, then there must be some finite k for which the right hand side (RHS) of equation (2.42) does not vanish, so that

$$j(r,t)\neq j'(r,t) \tag{2.44}$$

Thus, the two Taylor-expandable potentials, different by more than just a trivial constant, give two different current densities. In other words, there must be a one-to-one correspondence between the current densities and external potentials.

Substituting the equation of continuity in (2.43), we get

$$\frac{\partial^{k+2}}{\partial t^{k+2}}\{n(\mathbf{r},t)-n'(\mathbf{r},t)\}_{t=0} = -\nabla\cdot\left[n(\mathbf{r},0)\nabla\frac{\partial^{k}}{\partial t^{k}}\{V_{ext}(\mathbf{r},t)-V'_{ext}(\mathbf{r},t)\}_{t=0}\right] \tag{2.45}$$

If the RHS of the above equation is non-zero for some value of k, then the two densities will be different. In order to show that the RHS is non-vanishing, let us assume that

$$\nabla\cdot\left[n(\mathbf{r},0)\nabla f(\mathbf{r},t)\right]=0 \tag{2.46}$$

where the function $f(\mathbf{r})$ is defined as

$$f(\mathbf{r})=\frac{\partial^k}{\partial t^k}\{V_{ext}(\mathbf{r},t)-V'_{ext}(\mathbf{r},t)\}_{t=0}\} \tag{2.47}$$

Now, consider the following integral

$$\int f(\mathbf{r},t)\nabla\cdot\{n(\mathbf{r},0)\nabla f(\mathbf{r},t)\}d\mathbf{r}=\int n(\mathbf{r},0)f(\mathbf{r})\nabla f(\mathbf{r},t)\cdot d\mathbf{S}-\int n(\mathbf{r},0)\left[\nabla f(\mathbf{r},t)\right]^2 d\mathbf{r} \tag{2.48}$$

We use the Green's theorem to obtain the RHS of the above equation. The left-hand side of the above equation should be zero due to our initial assumption in Eq.(2.46). The first term on RHS with surface integral vanishes since both the density and potential decay to zero as $r\to\infty$. Equality in the above equation requires that the second term should also go to zero. But, the second term on RHS will vanish only when density or ∇f is zero. The first choice is obviously ruled out. The second possibility contradicts our assumption that the two potentials differ by more than a time-dependent constant. Hence, there exists a one-to-one correspondence between the time-dependent density and the time-dependent potential. In other words, any two potentials which differ by more than a time-dependent constant will always give two different densities and vice versa. This completes the proof of the RG theorem.

2.3.2 Time Dependent Kohn-Sham Equation

Consider a fictitious non-interacting Kohn-Sham system with a potential $V_{ks}(\mathbf{r},t)$ having a time-dependent density $n(\mathbf{r},t)$. Then the time-dependent Kohn-Sham (TDKS) equation is given by

$$i\frac{\partial}{\partial t}\phi(\mathbf{r},t) = \left[-\frac{\nabla^2}{2}+V_{ks}[n](\mathbf{r},t)\right]\phi(\mathbf{r},t) \tag{2.49}$$

where the time-dependent density is defined as

$$n(\mathbf{r}, t) = \sum_{i=1}^{N} |\phi_i(\mathbf{r}, t)|^2 \tag{2.50}$$

The $V_{ks}(\mathbf{r}, t)$ and the initial condition are chosen such that the time-dependent density of non-interacting system is equal to that of a real interacting system with a time-dependent potential V_{ext}. Now, by virtue of the one-to-one correspondence proven in the previous subsection, the potential $V_{ks}(\mathbf{r}, t)$ can be written as

$$V_{ks}(\mathbf{r}, t) = V_{ext}(\mathbf{r}, t) + V_H(\mathbf{r}, t) + V_{xc}(\mathbf{r}, t) \tag{2.51}$$

where V_H and $V_{xc}(\mathbf{r}, t)$ are the time-dependent Hartree and exchange-correlation potentials respectively. To solve the above TDKS equation, one requires a knowledge of the $V_{xc}(\mathbf{r}, t)$. Unfortunately, the exact form of the function is not known and hence in practice we need to use an approximation for it.

2.3.3 Linear Response Theory and Adiabatic Local Density Approximation

When the strength of perturbing potential is weak, we can employ the linear response theory using perturbation theory to study the dynamic response properties of a system. We assume here that the initial state of the system is non-degenerate ground state and then we can expand the density $n(\mathbf{r}, t)$ close to the initial state as

$$n(\mathbf{r}, t) = n^{GS}(\mathbf{r}, t) + \delta n(\mathbf{r}, t) \tag{2.52}$$

where $\delta n(\mathbf{r}, t)$ is the first order change in the ground state density due to a small change in the external potential,

$$\delta n(\mathbf{r}, t) = \int dt' \int dr' \chi[n^{GS}](\mathbf{r}, \mathbf{r}', t - t') \delta V_{ext}(\mathbf{r}', t') \tag{2.53}$$

In the above equation, the χ represents the susceptibility of the system which tells us how the density of the system changes at a point $\mathbf{r}$ and time t due to the change in the external potential at an arbitrary point $\mathbf{r}'$ and at time t'. Here, $t > t'$. Similarly, the response of density due to a small change in the KS potential is determined by χ_{KS}. It is to be noted that the susceptibility of a real interacting system χ is different from that of a fictitious non-interacting system. However, both these susceptibilities should yield same response to the density.

$$\begin{aligned}\delta n(\mathbf{r},t) &= \int dt' \int dr' \chi_{KS}[n^{GS}](\mathbf{r},\mathbf{r}',t-t')\delta V_{KS}(\mathbf{r}',t') \\ &= \int dt' \int dr' \chi_{KS}[n^{GS}](\mathbf{r},\mathbf{r}',t-t')\{\delta V_{ext}(\mathbf{r}',t') + \delta V_H(\mathbf{r}',t') + \delta V_{xc}(\mathbf{r}',t')\} \quad (2.54)\end{aligned}$$

Taking Fourier transform of Eq.(2.53) and (2.54), and then comparing these two equations, we get

$$\begin{aligned}\chi(\mathbf{r},\mathbf{r}',\omega) = \chi_{KS}(\mathbf{r},\mathbf{r}',\omega) + \\ \int dr_1 \int dr_2 \chi_{KS}(\mathbf{r},\mathbf{r_1},\omega)\{\frac{1}{|\mathbf{r_1}-\mathbf{r_2}|} + f_{xc}(\mathbf{r_1},\mathbf{r_2},\omega)\}\chi(\mathbf{r_2},\mathbf{r}',\omega) \quad (2.55)\end{aligned}$$

where f_{xc} is called the exchange-correlation kernel and it is given by

$$f_{xc}[n](\mathbf{r},\mathbf{r}',t-t') = \frac{\partial V_{xc}[n]}{\partial n(\mathbf{r},t)} \quad (2.56)$$

The expression (2.55) is central equation in the linear response theory within the TDDFT. This is a Dyson-like equation. The $\chi(\mathbf{r},\mathbf{r}',\omega)$ has poles at the excitation energies of the system and the strengths of the poles are related to the intensity of optical absorption. The susceptibility of the KS system can be written in terms of the ground state KS eigen functions and eigen values

$$\begin{aligned}\chi_{KS}(\mathbf{r},\mathbf{r}',\omega) = 2\lim_{\eta\to 0^+}\sum_i\sum_a\{\frac{\phi_i(\mathbf{r},t)\phi_a(\mathbf{r},t)\phi_i^*(\mathbf{r}',t')\phi_a^*(\mathbf{r}',t')}{\omega-\omega_{ia}+i\eta} + \\ \frac{\phi_i(\mathbf{r},t)\phi_a(\mathbf{r},t)\phi_i^*(\mathbf{r}',t')\phi_a^*(\mathbf{r}',t')}{\omega+\omega_{ia}-i\eta}\} \quad (2.57)\end{aligned}$$

where $\phi_i(\mathbf{r}, t)$ and ω_i are the eigen functions and the corresponding eigen values of the KS states. The suffixes i and a represent the occupied and unoccupied KS states respectively.

It is clear from the equations (2.55) and (2.57) that the TDDFT based response property calculations require approximation for the XC functional at two levels. The first one is the static XC potential required to calculate the ground-state Kohn-Sham (KS) orbitals and orbital energies. The second approximation is needed to represent the XC kernel $f_{xc}(\mathbf{r}, \mathbf{r}', \omega)$.

The exact exchange-correlation potential depends on the entire history of the density, as well as the initial wave functions of both the interacting and the Kohn-Sham systems. However, the dependence of initial wave functions can be lifted if we start from a non-degenerate ground state (in both interacting and non-interacting systems) where the initial wave functions themselves are functionals of the initial density. Still, $V_{xc}(\mathbf{r}, t)$ has a functional dependence not just on $n(\mathbf{r}, t)$ but on $n(\mathbf{r}', t')$ at an arbitrary point $\mathbf{r}'$ in space and $t > 0$. Thus this potential is non-local in both space and time. In other words, this potential remembers all the densities in past, and hence it has memory. Therefore, the V_{xc} in TDDFT is much more complex than that in DFT.

Adiabatic Local Density Approximation

A widely used approximation for the XC kernel f_{xc} is the adiabatic local density approximation (ALDA). In this approximation, the functional derivative of the V_{xc} is taken as static i.e XC kernel f_{xc} is frequency independent. Thus, the adiabatic approximation ignores the dependence of density in the past and the V_{xc} depends only on the instantaneous density.

$$V_{xc}^{ALDA}[n](\mathbf{r}, \mathbf{t}) = V_{xc}[n(\mathbf{r})] \tag{2.58}$$

Thus, the above functional is local in time. For the exchange-correlation kernel, the $V_{xc}[n](\mathbf{r})$ of the homogeneous electron gas is used

$$f_{xc}^{ALDA}(\mathbf{r}t, \mathbf{r}'t') = \frac{\partial V_{xc}^{LDA}[n(\mathbf{r}), \mathbf{r}]}{\partial n(\mathbf{r}')} \delta(t - t') \tag{2.59}$$

This approximation is expected to perform better for slowly changing potentials. Now, it is being regularly used to study several optical response properties of the finite systems and the results obtained from these calculations are quite satisfactory[215, 216].

2.3.4 Response Property Calculations

In this thesis, we study the optical response properties such as static electric dipole polarizability and strength (through C_6 coefficient) of the van der Waals interaction of nanostructures (non-periodic systems) by employing TDDFT based calculations. The average dipole polarizability ($\bar{\alpha}$) and its anisotropy ($\Delta\alpha$) can be expressed in terms of second-rank polarizability tensor (α).

$$\bar{\alpha}(\omega) = \frac{\alpha_{xx}(\omega) + \alpha_{yy}(\omega) + \alpha_{zz}(\omega)}{3} \tag{2.60}$$

$$|\Delta\alpha| = \left[\frac{3\ \mathrm{Tr}\ \alpha^2\ -\ (\mathrm{Tr}\ \alpha)^2}{2}\right]^{\frac{1}{2}} \tag{2.61}$$

The strength (C_6) of attractive van der Waals interaction between two neutral systems (A and B) is obtained via Casimir-Polder expression[217] which relates C_6 with the dynamic polarizability of the interacting systems evaluated at imaginary frequency.

$$C_6 = \frac{3}{\pi}\int_0^{\infty}\ \bar{\alpha}^A(i\omega)\ \bar{\alpha}^B(i\omega)\ d\omega \tag{2.62}$$

where $\bar{\alpha}^A(\omega)$ and $\bar{\alpha}^B(\omega)$ are the isotropic average dynamic polarizability of the systems A and B respectively. For the calculations of polarizability of nanostructures, we use the RESPONSE module[218] available in the ADF package. This module employs the linear response theory of many-body systems and uses exact analytical expressions for polarizability in terms of the moment of the first-order induced density. For the calculations of the Kohn-Sham orbitals and energies, we use several approximate exchange-correlation functionals, ranging from simple local density approximation to asymptotically correct model potential - statistical average of orbital potential (SAOP)[219, 220]. For the XC kernel f_{xc}, we use the above mentioned adiabatic local density approximation (ALDA).

For these response property calculations, we use one of the largest basis sets, namely, the all electron even tempered basis set ET-QZ3P-2DIFFUSE (ET) with two sets of diffuse functions as available in the ADF basis set library [205].

In this chapter, we have briefly discussed the basics of the DFT and TDDFT which we have employed in the electronic structure calculations to study several ground state and optical response properties of the nanostructures. The results of these investigations will be discussed in the following chapters. In Chapter 3, we start our discussion on the properties of two-dimensional graphene-like honeycomb structure made up of silicon atoms.

Chapter 3

Physical Properties of Mono-layer of Silicene

The fascinating physical properties[24–26] associated with graphene have motivated many researchers to search for new graphene-like two-dimensional (2D) materials made up of other elements. Various possibilities of producing different graphene-like structures with exciting novel as well as unexpected new properties have widened the area of research in 2D materials since they are considered as promising candidates for many technological applications in future nanoelectronic devices. Until now, several graphene-like structures composed of elements from group IV (Si, Ge, SiC, GeC, SnGe, SiGe, SnSi, SnC)[128–130], group III-V (BN, AlN, GaN, InN, InP, InAs, InSb, GaAs, BP, BAs, GaP, AlSb, BSb)[127, 129, 130], group II-VI (ZnO, BeO, ZnS)[127] and Metal dichalcogenides (MCh2 with M = Mo, W, Nb, Ta and Ch = S, Se, Te)[126] have been proposed and their physical and chemical properties are being investigated.

The graphene analogue of silicon is called silicene in which silicon atoms are arranged in a two-dimensional honeycomb lattice similar to carbon atoms in graphene. For the first time, the term silicene was used by Guzman-Verri et. al[131] in 2007. Among the above mentioned graphene-like two-dimensional materials, silicene has received much attention[128–145] during last few years. The reason for the tremendous interest in this material is due to the fact that it possesses many exciting novel properties similar to those of graphene. For example, theoretical studies have predicted that the electronic structure of silicene possesses linear dispersion around the Dirac point and thus the charge carriers in this two-dimensional system behave like massless Dirac-Fermions[128–131]. The quantum spin Hall effect in silicene has also been theoretically studied[137, 138]. Presence of a relatively large induced energy gap of about 1.55 meV in silicene due to the spin-orbit coupling is also reported in the literature[139]. Silicon based nanostructures (like silicene, silicon clusters, silicon nanotubes etc.) have an important added advantage over the carbon based nanostructures (like graphene, fullerene, carbon nanotubes, etc.) as they are expected to be compatible with the existing semiconductor technology. Thus, silicene is considered as one of the promising materials for the applications in nanotechnology.

Though carbon and silicon atoms possess same number of electrons (four) in the valence shell, the physical and chemical properties of systems based on these two elements are typically very different. For example, the former forms a basis of living organism. On the other hand, silicon is one of the most important ingredients for the semiconductor industry. Origin of differences in the properties between carbon and silicon based systems is due to the kind of hybridizations which exists in these two systems. Carbon atoms can exhibit all the three sp, sp^2 and sp^3 hybridizations whereas silicon favors sp^3 hybridization. This is due to the fact that the energy difference between the sub-levels (3s and 3p) in silicon is much smaller as compared to that between 2s and 2p sub-levels in carbon. Thus, the sub-level 3s of silicon can easily mix with all 3p sub-levels (3p$_x$, 3p$_y$ and 3p$_z$) which favors the sp^3 hybridization. Due to the above mentioned reason, naturally silicon does not exist in graphite-like layered form. Thus, silicene can not be produced by exfoliation method which is the simplest method used for the production of graphene. Hence, the growth or synthesis of silicene requires sophisticated experimental methods. Recently, silicene sheet and nanoribbon have been successfully grown on various substrates such as silver, diboride thin films and iridium[146, 221–236] and many of the theoretical predictions on the properties of silicene are now being verified. One of the important achievements in this direction is that the existence of linear dispersion in the electronic structure of silicene has been experimentally confirmed by the angle-resolved photo emission spectroscopy (ARPES) measurement[146] and thus, the Dirac-Fermions in silicene is now well established. In another experiment, a possible superconducting gap of about 35 meV is also observed in silicene on Ag(111) substrate by scanning tunneling spectroscopy[237]. At present, the scientific community working in this area is actively exploring various possibilities of modifying and tuning many physical and chemical properties of silicene[238–244] and these efforts will be crucial in making silicene a potential material for wide variety of applications.

In this chapter, we discuss the results of our detailed studies on the geometric, electronic and optical properties of mono-layer of silicene and then compare them with those of graphene. Though silicene possesses the novel properties as mentioned above, the practical applications of this material in nanoelectronics and nanodevices necessitate efficient schemes to control and modify its properties. As mentioned in the introductory chapter, the properties of nanostructures can be altered by chemical doping and also by application of external electric and magnetic fields. Thus, in this chapter, we also choose to study the effect of two external influences namely, (a) transverse external static electric field and (b) hydrogenation on the properties of silicene. We observe from our calculations that silicene undergoes semi-metal to semiconductor transition due to hydrogenation. In case of transverse external electric field, our calculations predict that a band gap can be opened up and tuned in a controlled manner in mono-layer of silicene by applying an external transverse electric field. On the contrary, it is well known that, inducing a band gap in a mono-layer of graphene by applying an electric field is not possible.

3.1 Geometric Structures

We start this sub-section with discussions on the geometrical properties of silicene. Figure 3.1 shows portions (6×6×1 super cell) of infinitely extending two-dimensional honeycomb lattice of both (a) silicene and (b) graphene. The unit cell of silicene (graphene) contains two Si (C) atoms which are denoted by 'A' and 'B'. The results of electronic structure calculations based on DFT show that the minimum energy structure of silicene is slightly different from the planar structure of mono-layer of graphene[129, 130]. In case of silicene the atoms present in the unit cell are buckled (see the side views of Figure 3.1). In other words, A and B atoms in the unit cell of silicene do not lie on the same plane. Consequently, the ground state structure of silicene lacks 6-fold rotational and two mirror plane symmetries which are present in the planar structure of graphene. Hence, the space group of silicene reduces to P$\bar{3}$m1 instead of P6/mmm of graphene. We use SIESTA package[200–202] for all the electronic structure calculations presented in this chapter. For exchange-correlation potential generalized gradient approximation given by Perdew-

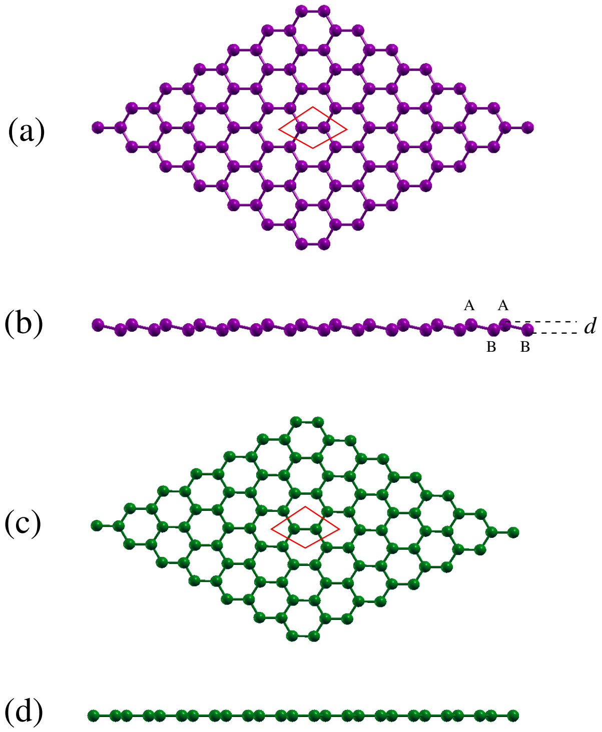

Figure 3.1: The geometric structures of (6×6×1) super cell of silicene ((a) top and (b) side view) and graphene ((c) top and (d) side view). The lines in (a) and (c) represent the unit cells. The vertical distance between two Si atoms at sites A and B is represented by '*d*', which arises due to buckling.

Burke-Ernzerhof[195] has been used. An energy cutoff of 400 Ry is used and the mesh of k-points for Brillouin zone integrations is chosen to be 45×45×1. Our results on the geometric properties of silicene and graphene are summarized in Table 3.1 . It can be clearly observed from the table that hybridization in graphene is of sp^2 type due to the well defined angle of 120° between the nearest neighbor carbon atoms. On the other hand, in silicene, the bond length and bond angles between the silicon atoms are 2.309 Å and 115.4° respectively. It is important to note here that the value of bond angle in silicene lies in between corresponding angles in sp^2 (120°) and sp^3 (109.47°) hybridized structures. Thus, the hybridization in silicene is not purely of sp^2 or sp^3 character but a mixture of sp^2 and sp^3. Moreover, the Si-Si distance in silicene is much larger than the C-C distance in graphene. This is due to fact that there exists a much weaker π bond in the former as compared to that in the latter. This results in buckling in silicene which in turn causes a greater overlap between orbitals leading to higher binding energy. The amount of buckling can be characterized by a buckling length denoted by d, which is defined as the vertical distance between silicon atoms at sites A and B in the unit cell.

Table 3.1: The results of optimized geometries of mono-layers of silicene and graphene obtained by DFT with PBE exchange-correlation functional. Experimental values are given in parentheses[146, 245]

System	Space Group	Lattice Constant (Å)	Bond Length (Å)	Bond Angle (°)	Buckling Length (Å)
Graphene	P6/mmm	2.468 (2.462)	1.425 (1.421)	120	0.0
Silicene	P$\bar{3}$m1	3.903	2.309 (2.2^a)	115.4	0.501

a - value of Si-Si bond length in silicene on Ag(111) substrate[146].

We find that the value of d in silicene is 0.501 Å while that in graphene is zero. We would like to mention here that the finite value of d in silicene plays an important role in determining the electronic structure of silicene under the influence of external electric field and we will discuss these details later. Before proceeding further we wish to point out that our results on the geometric structure of silicene match well with the already existing data[129, 130].

3.2 Electronic Structures

Now, we present our results for the electronic structure of mono-layers of silicene and then compare these results with those of graphene. In Figure 3.2 (a) and (b), we plot the band structure (BS) along the high symmetry points in Brillouin zone and density of states (DOS) for silicene and graphene respectively. The magnified view of BS close to the Fermi level (E_F) is displayed in the insets of Figure 3.2 since the characteristic of electronic structures around the E_F plays an important role in deciding the transport properties of a material. Figure 3.2(a) clearly elucidates the semi-metallic nature of silicene since the value of DOS at E_F is zero. It is also observed that the conduction and valence bands touch each other only at the highly symmetric point K. Our detailed investigation of BS and DOS indicates that the contributions to the DOS just below and above the E_F are due to the π and π^* orbitals respectively. The most important feature in the BS is the existence of a linear dispersion around the point K (see inset in Figure 3.2(a)). The point in energy vs. momentum (E-k) diagram where the conduction and valence bands touch each other at E_F is called the Dirac point. Comparison of the BS of silicene (as presented in Figure 3.2(a)) with that of graphene (in Figure 3.2(b)) clearly shows that around the

E_F, the electronic structures of silicene and graphene are very similar. The presence of linear dispersion in the BS of silicene implies that the charge carriers around the E_F behave like massless Dirac-Fermions. Analogous to graphene, the electronic structure of silicene around the Dirac point can be described by relativistic Dirac-like Hamiltonian[64]

$$\hat{H} = \begin{pmatrix} \Delta & \hbar v_F(k_x - ik_y) \\ \hbar v_F(k_x + ik_y) & -\Delta \end{pmatrix} \tag{3.1}$$

where k, v_F and Δ are the momentum, the Fermi velocity of charge carriers and the onsite energy difference between the Si atoms at sites A and B, respectively. Then, the dispersion around the Dirac point is given by

$$E = \pm\sqrt{\Delta^2 + (\hbar v_F k)^2} \tag{3.2}$$

For pristine silicene, the onsite energy difference Δ is zero and hence Eq.(3.2) becomes

$$E = \pm\hbar v_F k \tag{3.3}$$

which explains the presence of linear dispersion around the Dirac point in silicene.

3.3 Optical Properties

The study of interaction of electromagnetic radiations with materials is an important area of research in material science and spectroscopy. These studies would provide information about the electronic structures of materials. Keeping this in mind, we have carried out calculations of dielectric function and absorption spectra of silicene which characterize its linear optical properties. The frequency dependent dielectric function is calculated by employing first order time-dependent perturbation theory as implemented in SIESTA package[200–202]. These calculations within the framework of DFT require the Kohn-Sham (KS) eigen functions and eigen values. However, it is important to note that one needs to solve the KS equation with finer mesh of k-points for accurate calculation of optical response properties. Thus, in the present case, we use large mesh size of

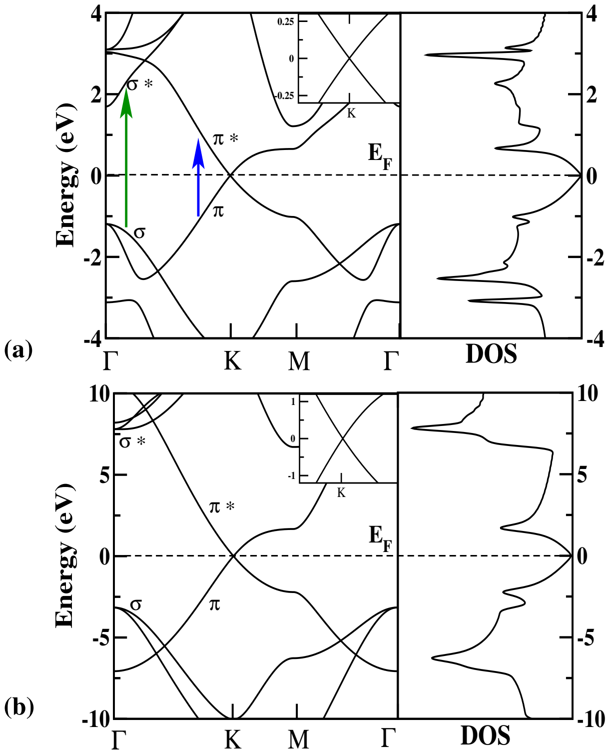

Figure 3.2: Band structure and density of states for the optimized structures of (a) silicene and (b) graphene. The energies of bands are with respect to the Fermi level.

250×250×1 for the calculations. Using eigen functions and eigen values of the KS states, we calculate the imaginary part of dielectric functions for the light polarized parallel and perpendicular to the plane of silicene sheet. The real part of dielectric functions is then obtained via Kramers-Kronig relation. The results for real and imaginary parts of dielectric function obtained for the mono-layer of silicene are plotted in Figure 3.3 along with the corresponding results for graphene. We observe that the contributions of dielectric function along the directions parallel (ε_{xx} and ε_{yy} represented by $\varepsilon_{\parallel}$) and perpendicular (ε_{zz} represented by $\varepsilon_{\perp}$) to the plane of silicene sheet are different. This anisotropy in dielectric function is a consequence of the two-dimensional nature of the silicene sheet. The results for dielectric function clearly show that $\varepsilon_{\parallel}$ and $\varepsilon_{\perp}$ dominate in different energy regimes. The comparison of dielectric function of silicene with that of graphene (Figure 3.3(b)) shows that they are similar to each other but the variations are in different energy ranges[246].

We also calculate the optical absorption spectra of both graphene and silicene from the corresponding imaginary parts of the dielectric function and they are plotted in Figure 3.4. From the absorption spectra, we observe that there is no cut-off energy in absorption

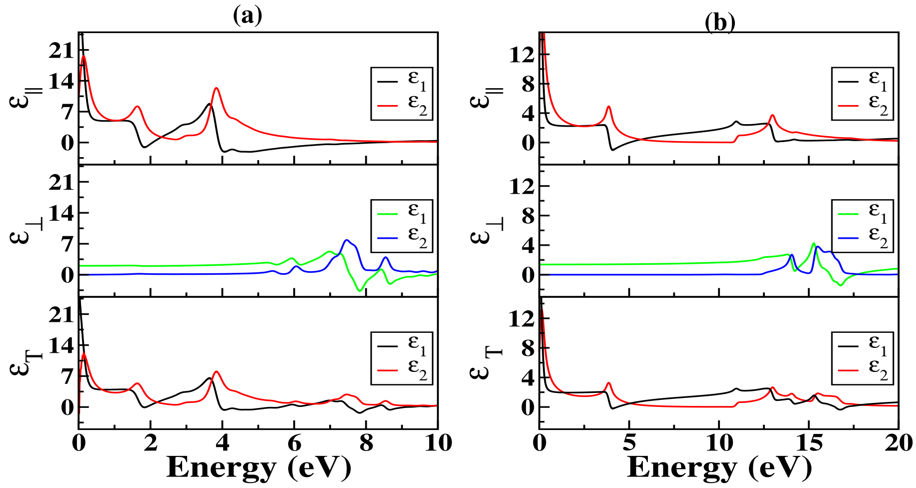

Figure 3.3: The calculated real (ε_1) and imaginary (ε_2) part of dielectric function of (a) silicene and (b) graphene. The upper, middle and lower panels depict the parallel, perpendicular and total contributions of the dielectric functions respectively.

coefficient of graphene and silicene. This corroborates to the fact that there is no band gap in both silicene and graphene, as discussed in the previous sub-section. Our detailed analysis of optical absorption spectra shows that silicene possesses two major peaks in energy range from 0 to 6 eV. These two peaks correspond to the two important transitions (see the arrows in Figure 3.2 (a)) which occur between the electronic states of silicene. The first peak (around 1.74 eV) in the absorption spectra corresponds to the transitions from states π to π^* which are close to the Fermi level. The value of the absorption peak matches well with 1.69 eV of peak to peak (above and below E_F) energy difference in DOS (see in Figure 3.2(a)). On the other hand, the broader second peak (maximum around 3.94 eV and extends beyond 6 eV) corresponds to the transitions from occupied σ to unoccupied σ^* states. The broad energy range of this peak is due to the large band width of both σ and σ^* states. Akin to the results of dielectric functions, the absorption spectra of both silicene and graphene (Figure 3.4) look similar but the energy scales are in variance due to the involvement of different valence shells in Si (M shell) and C (L shell).

3.4 Effect of External Influences

As mentioned in the introduction, external fields and chemical doping can be exploited to modify the properties of materials in a controlled manner. In this sub-section, we discuss

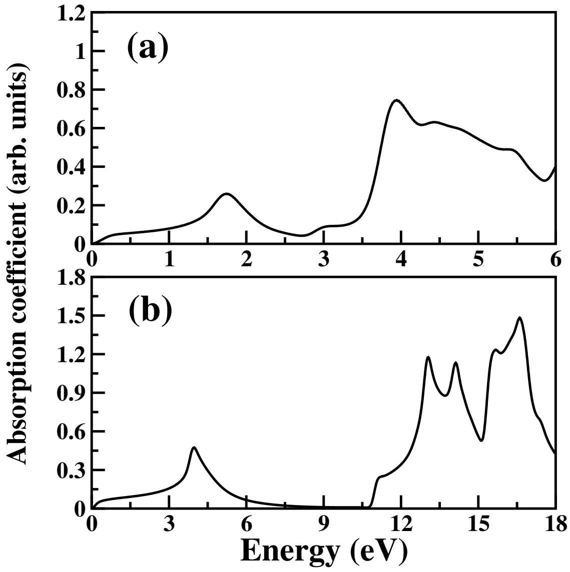

Figure 3.4: The optical absorption spectra of (a) silicene and (b) graphene.

the effect of (a) transverse static electric field and (b) hydrogen doping on the properties of silicene. We start our discussion with the results for silicene when it is subjected to transverse external electric field and then compare these with the corresponding results for graphene.

3.4.1 Transverse Static External Electric Field

To understand the response of silicene and graphene to the transverse static electric field, we perform the electronic structure calculations of both the mono-layers under influence of electric field with varying strength. It is to be noted that in practice, the strength of electric field can be easily controlled and varied by the applied gate voltage. We find that the change in the value of lattice constant of silicene due to the application of an external electric field is less than 1%. The results of band structures obtained for silicene and graphene around the Dirac point for various strengths of electric field are shown in Figure 3.5. First observation from Figure 3.5 is that a band gap is opened up at the Fermi level in silicene due to the electric field. In contrast to this, for graphene, it is not possible to induce a band gap by applying an electric field. Note that both systems - silicene and graphene, exhibit similar electronic structure around the Fermi level in absence of external electric field, but they show distinctly different characteristics in the presence of an external electric field. This obviously raises the question: why do they behave so

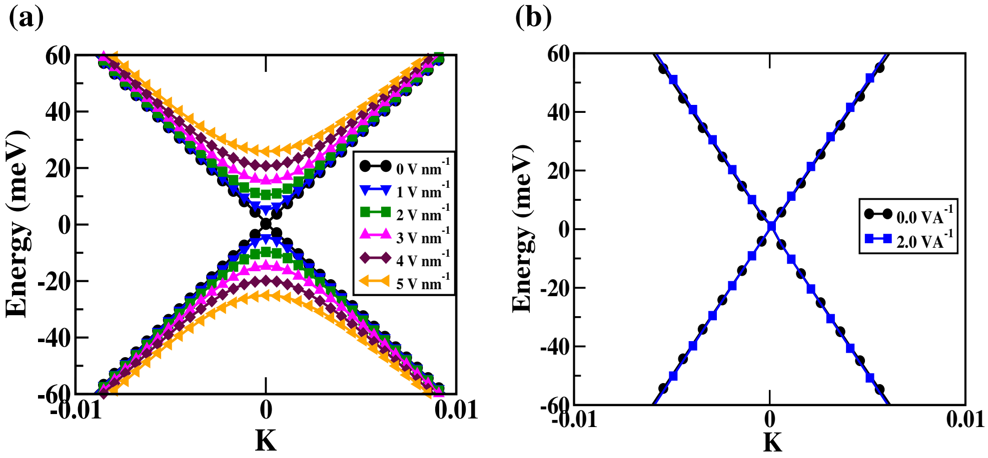

Figure 3.5: The band structures of (a) silicene and (b) graphene around the Dirac point for different strengths of transverse static electric field.

differently in the presence of an external electric field.

As we mentioned in the previous sub-section, the charge carriers in both silicene and graphene behave as massless Dirac-Fermion in the absence of any external influences. However, there is a breaking of inversion symmetry in case of silicene when we apply an external electric field unlike in case of graphene. This is due to the fact that the potentials, V_A and V_B, seen by the silicon atoms at the sites A and B, respectively, are different, since these two atoms are located at different positions along the electric field direction. In other words, the presence of buckling in geometric structure of silicene leads to a finite value of onsite energy difference. In this case, the dispersion around the Dirac point becomes

$$E = \pm\sqrt{\Delta^2 + (\hbar v_F k)^2} \tag{3.4}$$

Very close to the high symmetry point K, $\quad \hbar v_F k \ll \Delta$, then

$$E = \pm\Delta\sqrt{1 + \left(\frac{\hbar v_F k}{\Delta}\right)^2} \approx \pm\Delta\left[1 + \frac{1}{2}\left(\frac{\hbar v_F k}{\Delta}\right)^2\right] \tag{3.5}$$

Hence, the induced band gap, which is the energy difference between the conduction and valence bands, becomes twice that of the onsite energy difference. It is also interesting to note that the above equation also explains the appearance of parabolic-like dispersions near the highly symmetric point K in silicene (see Figure 3.5(a)). On the other hand,

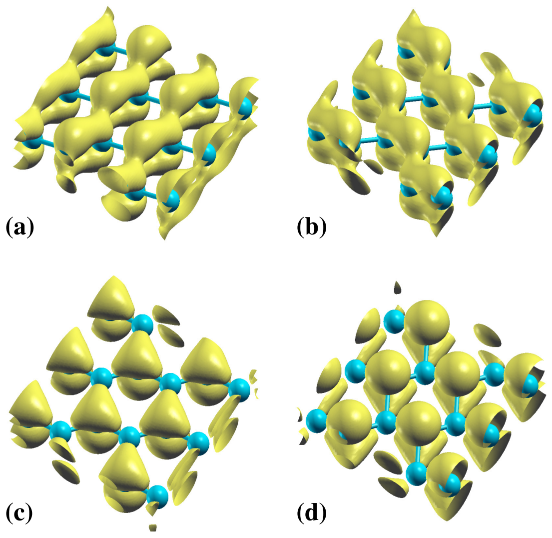

Figure 3.6: Spatial distribution of highest occupied (without electric field (a) and with 5 V/nm (c)) and lowest unoccupied states (without electric field (b) and with 5 V/nm (d))

the onsite energy difference in graphene is zero ($\Delta = 0$) because the potentials seen by the carbon atoms at the sites A and B are same. Consequently, there is no opening up of energy gap in graphene (see Figure 3.5(b)). We would like to mention here that the spin-orbit coupling (SOC) does induce a very small gap of the order of μeV in graphene and about 1.55 meV in silicene[139, 247]. However, these values are much smaller compared to the thermal energy k$_B$T at room temperature ($\sim$ 25 meV) and hence they will not be useful in operating or controlling nanoelectronic devices made up of graphene/silicene at ambient conditions.

In order to comprehend the effect of transverse electric field on the electronic properties of silicene, we plot the spatial distribution of the highest occupied (π) and the lowest unoccupied states (π^*) of silicene with and without electric field in Figure 3.6. From the band structure in Figure 3.2, it can be clearly seen that these two above mentioned states touch each other exactly at the highly symmetric point K. In the absence of electric field, the spatial distributions of these two states (see Figure 3.6(a) and 3.6(b)) clearly show the presence of inversion symmetry. However, when we apply the electric field, the inversion symmetry present in these two states is destroyed. Due to this, the spatial distribution of charges above and below the silicene sheet are completely different (see Figure 3.6(c) and 3.6(d)). This breaking of inversion symmetry in silicene leads to the opening up of band gap.

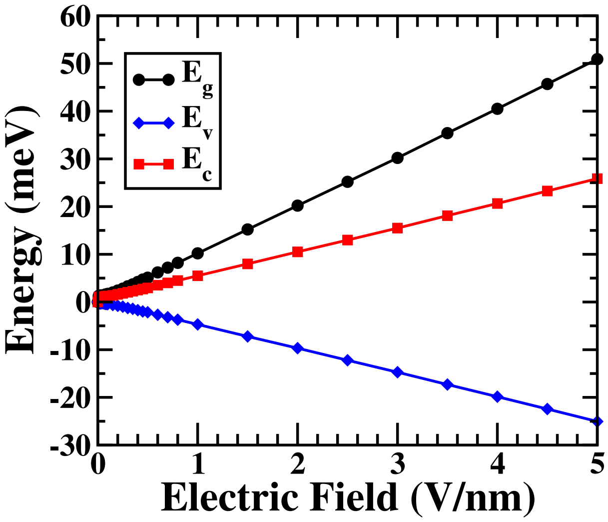

Figure 3.7: The variation of band gap (E_g), valence (E_v) and conduction (E_c) band edges of silicene with the strength of external external field applied perpendicular to the plane of silicene sheet.

Furthermore, to study the relationship between the magnitude of induced band gap and the strength of electric field, in Figure 3.7 we plot the variation in the values of band gap as a function of the strength of electric field. We observe from Figure 3.7 that the band gap varies linearly with the strength of external electric field. Therefore, the band gap can be tuned over a wide range of energies by varying the strength of the field. Moreover, we also observe that both valence and conduction band edges move symmetrically away from the Fermi level as the strength of field is increased. The linear relationship between the band gap and the strength of electric field can be explained as follows. As mentioned earlier, the value of induced band gap can be written as $E_g = 2\Delta$, where Δ is proportional to the difference in potentials $(V_A - V_B)$ seen by the silicon atoms at the sites A and B which in turn is equal to the product of strength of the field (F) and the buckling length (d). This demonstrates that E_g is proportional to the strength of the applied field. From Figure 3.7, the value of the proportionality constant is found to be 10.14 meV per V/nm. The finite value of d in silicene mono-layer plays an important role in breaking the symmetry in the presence of an electric field and thereby opening a band gap which is consistent with the available results in the literature[133–135]. The possibility of opening and tuning a band gap in silicene makes it more useful from device application point of view as compared to graphene[136].

Optical absorption spectra of silicene when it is subjected to different strengths of

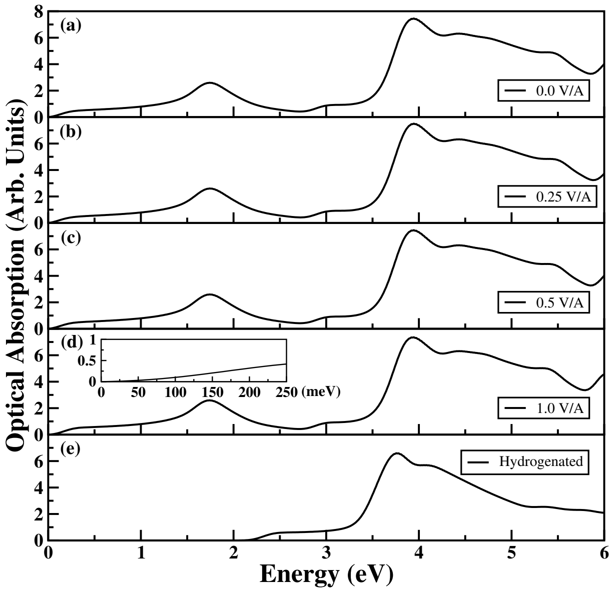

Figure 3.8: The optical absorption spectra of silicene: (a) without electric field, with fields (b) 0.25 V Å^{-1}, (c) 0.5 V Å^{-1},(d) 1.0 V Å^{-1} and (e) hydrogenated.

transverse static electric field are given in Figure 3.8(b)-(d). The figures (See inset in (d)) clearly indicate that there is no absorption of light having energy below a certain cut-off value which increases with the strength of electric field. These results are also consistent with our discussions of the effect of transverse electric field on the electronic structure of silicene. Interestingly, the features of spectra with electric field, such as the width and position of peaks, corresponding to different transitions remain similar to those of silicene without electric field. Hence, we conclude from our results that the transverse electric field affects the electronic states which are only very close to the Fermi level.

3.4.2 Hydrogenation

The method of chemical doping of different elements has been used in material science, over many decades, in order to modify or tune the properties of a material. The degree of modification of a property depends strongly on both the nature and concentration level of the dopant atoms. In present case, we consider the simplest element - hydrogen as a dopant, for the modifications of properties of silicene. The fully hydrogenated silicene is called silicane (Si_2H_2) in analogy to graphane. We observe the following modifications in the geometric structure. The value of lattice constant of silicane is 3.92 Å. We find that the values of bond length between Si-Si and Si-H are 2.37 Å and 1.52 Å respectively.

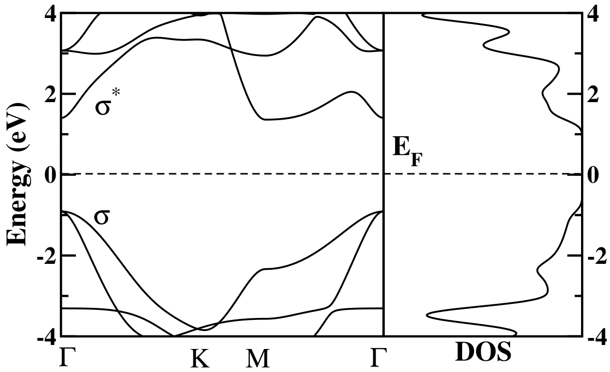

Figure 3.9: The band structure and DOS of hydrogenated silicene.

Further, the bond angles obtained are 111.1° and 107.8° respectively for Si-Si-Si and H-Si-Si. The buckling length in silicane is 0.74 Å which is about 48 % more as compared to that of pure silicene. Our results on the geometric properties of silicane match well with the results available in the literature[144, 248–250]. It is interesting to note that the values of bond length and angle between Si atoms in silicane are higher and lower respectively compared to the corresponding values in silicene. Furthermore, both these values are quite closer to those of bulk silicon(2.35 Å and 109.5°). These results suggest the presence of sp^3-like hybridization in silicane[144, 248–250].

The BS and DOS of silicane are shown in Figure 3.9. We observe from this figure that the character of silicene changes from semi-metal to semiconductor due to hydrogenation with an indirect band gap of 2.27 eV along Γ-M direction. However, the BS of silicane also possesses a direct band gap of 2.31 eV at Γ point which is about 1.8% higher than the indirect one. Our results on BS match well with the corresponding data available in the literature[144, 248–250]. However, it is important to note that the values of band gap estimated from DFT calculations are underestimated by approximately about 30-50% and hence the true gap may be larger. We also calculate the optical absorption spectra of silicane and the results are displayed in Figure 3.8(e). The main influence of hydrogenation on optical absorption spectra is the disappearance of the first peak at around 1.74 eV since there are no π bands present in system. However, the second peak which corresponds to σ to σ^* transition is not much influenced by hydrogenation as these states are not modified by this effect. These results again suggest that the behavior of silicene under influence of hydrogenation is akin to that of graphene[251].

3.5 Summary

In this chapter, we have presented our results for the geometric, electronic and optical properties of graphene-like structure - silicene obtained from the DFT based calculations. We observe from these results that the electronic structures of both silicene and graphene mono-layers around the Fermi level are similar. Both these two materials are semi-metal and possess linear dispersion around the Dirac point. Thus, the charge carriers in silicene and graphene behave like massless Dirac-Fermions. However, interestingly, the electronic structures of mono-layer of silicene and graphene under transverse electric field are different. Our calculations predict that a band gap in mono-layer of silicene can be opened up and also tuned over a wide range of energies by ab external electric field. Furthermore, the value of induced band gap can be more than the thermal energy for the applied electric field strength of few V/nm and hence, there is a possibility of using mono-layer of silicene in nanodevice even at room temperature. The results on optical response property calculations show that the dielectric function strongly depend on the direction of polarization of incident light. The anisotropic response in dielectric function is a consequence of two-dimensional characteristic of silicene. The optical absorption spectra of silicene possess two major peaks due to the π to π^* and σ to σ^* transitions. In case of hydrogenation, we observed from the geometry analysis that the hybridization in silicene goes from mixture of sp^2 and sp^3 to sp^3 . Consequently, the electronic structure of silicene gets modified drastically and it undergoes a transition from semi-metal to semiconductor due to hydrogenation. Therefore, we infer from our results that both these external influences strongly modify the electronic states (π and π^*) of silicene which are close to the Fermi level.

Publication based on this chapter

Properties Of Two-Dimensional Silicon Versus Carbon Systems

C. Kamal, Arup Banerjee, and Aparna Chakrabarti

Graphene Science Handbook: Size-Dependent Properties, CRC Press, Taylor & Francis Group (submitted)

Chapter 4

Physical Properties of Multi-layers of Silicene

Having discussed the physical properties of mono-layer of silicene and the effect of two external influences on them in the previous chapter, we now focus our attention on our results for the geometric and electronic structures of bi- and multi-layers of silicene as well as a hybrid structure made up of honeycomb silicene and boron nitride (BN) in the present chapter.

We would like to mention here that, unlike the case of bi- and multi-layers of graphene, there are no detailed investigations on the properties of bi- and multi-layers of silicene. Given the importance of silicon based nanostructures because of their compatibility with the existing semiconductor technology, it is interesting to study the properties of bi- and multi-layers of silicene and investigate how the properties evolve as a function of number of layers. For this purpose, we carry out a computational study on the geometric and electronic properties of bi- and multi-layers of silicene with different stacking configurations using DFT based calculations. We also investigate the evolution of these properties with increasing number of layers (n) ranging from 1 to 10.

Before starting our discussion on the properties of multi-layers of silicene, we shall see how the properties of graphene change as the number of layers increases. There exist several theoretical and experimental studies on various properties of bi- and multi-layers of graphene in the literature [147–162]. These studies show that many properties of graphene strongly depend on the number of layers, the inter-layer interactions and the stacking sequences. For example, the electronic properties of graphene bi-layer in Bernal stacking are distinctly different from the corresponding properties of mono-layer of graphene. The linear dispersion present in the band structure of graphene mono-layer changes to parabolic dispersion in case of graphene bi-layer. Thus, the behavior of the charge carriers transforms drastically from massless Dirac-Fermions to nearly-free-particles as we go from mono-layer to bi-layer. From the application point of view, the bi-layer structure is considered to be more important as compared to the mono-layer though the latter possesses many interesting properties. This is due to the fact that there is no band gap in the pristine mono- and bi-layer of graphene, however, it has been shown both theoretically and experimentally that a band gap can be opened up in bi-layer of graphene by applying a gate voltage. Furthermore, the value of band gap can be tuned over a wide range which may have potential applications in nanoelectronics and nanodevices [147, 148].

4.1 Geometric Structures

First, we begin with the discussions on the geometric properties of multi-layers of silicene. As we have seen in the previous chapter, the unit cell of mono-layer of silicene contains two Si atoms (Si1 and Si2) with space group of P$\bar{3}$m1. For the construction of multi-layers with different stacking configurations, we consider three possible unit cells in which these two Si atoms are placed at symmetric positions. The geometric structures of these three

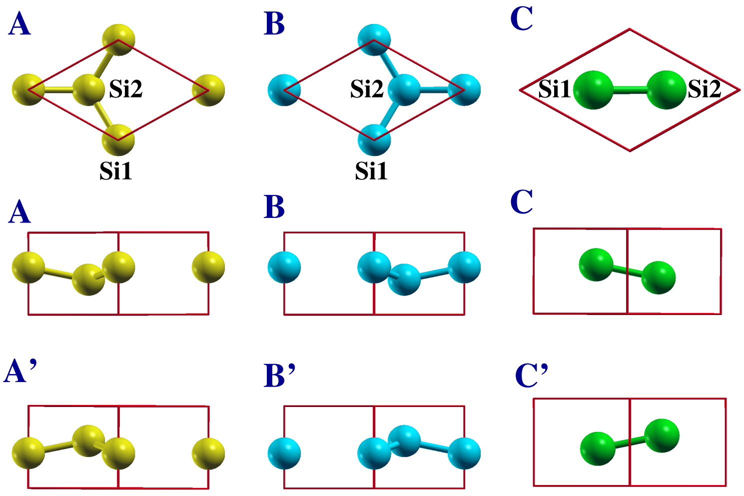

Figure 4.1: Three types of unit cells for mono-layer of silicene in which two Si atoms are at highly symmetric positions. Top view (top panel) and side view (middle and bottom panels)

types of unit cells are shown in Figure 4.1. These arrangements are (i) A: Si1 (0, 0, 0), Si2 (2/3, 1/3, z), (ii) B: Si1 (0, 0, 0), Si2 (1/3, 2/3, z), and (iii) C: Si1 (2/3, 1/3, 0), Si2 (1/3, 2/3, z). The variable 'z' in the fractional coordinates along the z-axis indicates that the two silicon atoms in the unit cell are not in the same plane and this is due to the effect of buckling. The relative position of Si2 can be below (A, B and C) or above (A', B' and C') the Si1 atom. In this study, we consider following four different stacking configurations : (1) AAAA - simple hexagonal, (2) AABB - double hexagonal, (3) ABC - rhombohedral, and (4) ABAB - Bernal stacking. The first three stacking configurations lead to a tetrahedral arrangement of Si atoms which is a favourable configuration for silicon based systems. We would like to mention here that the ABC stacking configuration leads to a multi-layered structure with stacking of diamond structure of bulk silicon along (111) direction. In case of multi-layers of graphene, the Bernal stacking corresponds to the minimum energy configuration and hence we include this stacking as well to study the multi-layers of silicene. We carry out the geometry optimization of multi-layers of these four stackings with number of layers up to ten. For these calculations, we use the VASP code[199] within the framework of the PAW method. The cutoff for the plane wave expansion is taken to be 400 eV and the mesh of k-points for Brillouin zone integrations is chosen to be 21×21×1. The optimized geometries of ten layers with all the four stacking configurations are shown in Figure 4.2 (i).

Cohesive Energy: In order to study the stability of the multi-layers of silicene with different stackings, the cohesive energy E_c of all the multi-layers has been calculated by using the expression

$$E_c = 2nE_{Si} - E_n, \tag{4.1}$$

where E_n and E_{Si} are the energies of multi-layers (n- layers) and Si atom respectively. The variation in values of cohesive energy per atom with increasing number of layers for different stackings is plotted in Figure 4.2 (ii). The dashed line indicates the value of cohesive energy per atom (4.553 eV/atom) of bulk silicon (diamond structure). We observe that all the multi-layered structures considered in the present study are energetically stable. Our calculations suggest that the rhombohedral stacking (ABC) is the minimum energy configuration. However, the values of cohesive energy of ABC stacking are much

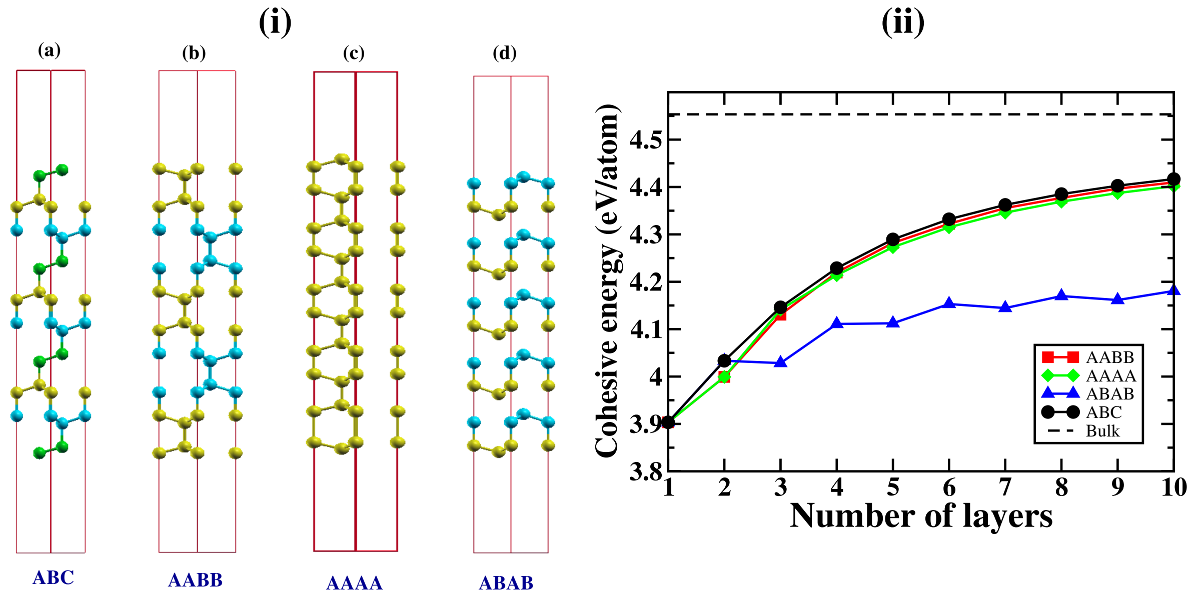

Figure 4.2: (i) The optimized geometric structures of multi-layers ($n = 10$) with four stacking configurations : (a) ABC, (b) AABB, (c) AAAA and (d) ABAB. (ii) Variation of the cohesive energy per atom with the increasing number of layers for these stacking configurations. The dashed line indicates the value of cohesive energy per atom of bulk silicon (diamond structure).

closer to those of AAAA, and AABB stackings. The cohesive energy per atom of 10 layers in AABB and AAAA stackings are 7 and 15 meV/atom lower than that of ABC stacking, respectively. The cohesive energies per atom of three stacking configurations, AAAA, AABB and ABC increase smoothly with the number of layers. Interestingly, cohesive energy of Bernal stacking (ABAB) is much lower than those of all the other stackings. In case of 10 layers, the cohesive energy per atom of ABAB stacking configuration is 236 meV/atom lower than that of ABC stacking. This result is in contrast to that of multi-layers of graphene where ABAB stacking is the lowest energy configuration. We also observe an oscillation in the values of cohesive energy of Bernal stacking. In order to understand these results for cohesive energies of multi-layers of silicene, we carry out a detailed investigation on the geometric structures of all the multi-layers of silicene.

4.1.1 Bi-layers

For bi-layers, there are only two possible stackings namely, AA and AB. We perform geometry optimization of the bi-layers of silicene with a starting inter-layer separation equivalent to that of bi-layers of graphene. The optimized geometric structures of the

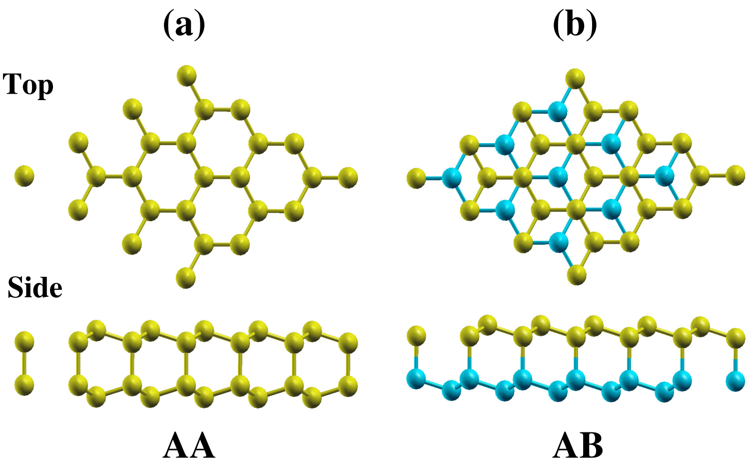

Figure 4.3: The optimized geometric structures of (a) AA and (b) AB stacked bi-layers of silicene. Top and side views of (3×3) super cell.

bi-layers are displayed in Figure 4.3. Our results for the geometric structure of bi-layers are summarized in Table 4.1. For comparison, we also include the bond length and bond angle between Si atoms in mono-layer of silicene in the table. These results show that there exists a strong covalent bond between the atoms in the layers of silicene as opposed to a weak van der Waals (vdW) interaction which exists in the multi-layers of graphene and graphite. Consequently, the E_c per atom for bi-layers of silicene increases significantly from that of mono-layer. It is also observed that AB stacking is lower in energy as compared to the AA stacking and difference in the E_c per atom between these two structures is 34 meV/atom. In order to further examine the nature of bonding between the two layers of silicene, we study the valence charge density distributions of bi-layers. In Figure 4.4, we show the valence charge density distributions of AA and AB stacked bi-layers of graphene ((a) and (b)) as well as silicene ((c) and (d)). The analysis of valence charge density distribution in both AA and AB stackings of silicene corroborates

Table 4.1: The results of optimized geometries of mono- and bi-layers of silicene obtained by DFT with PBE exchange-correlation functional. First and second values of bond lengths and angles in the bi-layers correspond to the intra-layer and inter-layer data.

System	Lattice Constant (Å)	Bond Lengths (Å)	Bond Angles (°)	Buckling Length (Å)
Mono-layer	3.867	2.279	116.08	0.457
Bi-layer AB	3.851	2.321, 2.528	112.10, 106.69	0.667
Bi-layer AA	3.858	2.324, 2.464	112.21, 106.57	0.663

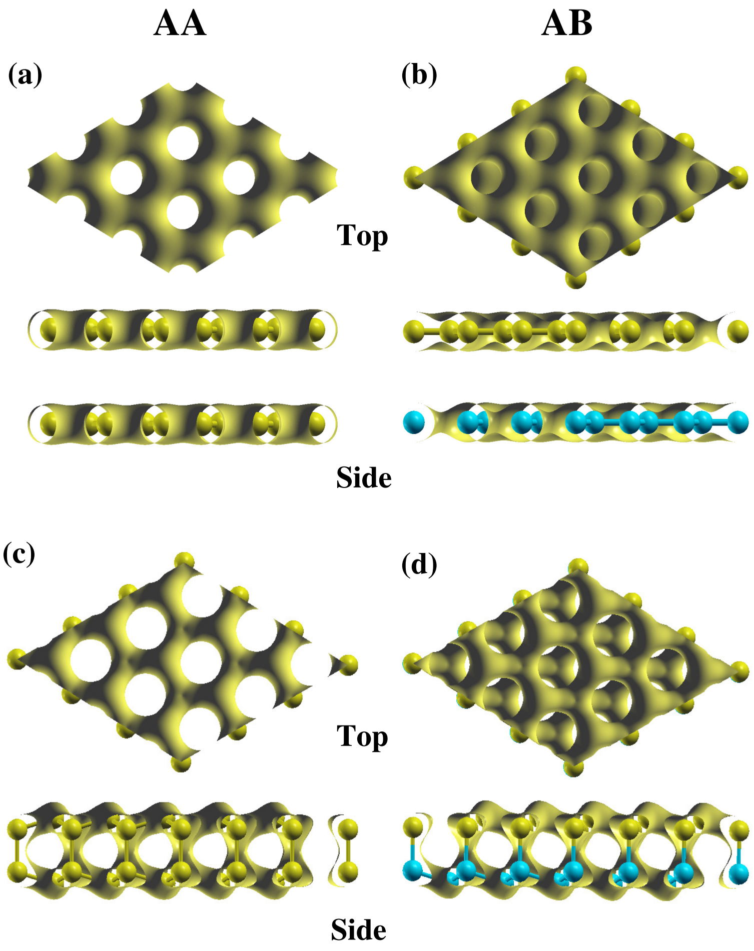

Figure 4.4: The valence charge density distributions of AA and AB stacked bi-layers of graphene ((a) and (b)) and silicene ((c) and (d)). Top and side views of (3×3) super cell.

to the results of optimized geometries discussed above. The significant charge density distribution around the inter-layer bonds establishes the covalent nature of these bonds. This is different from a weak vdW coupling which exists between two graphene layers (see Figure 4.4(a) and (b)). We also observe that the buckling and the bond lengths in both AA and AB stacked bi-layers have increased compared to corresponding results for the mono-layer of silicene. Furthermore, the results presented in Table 4.1 show that there is a reduction in the values of bond angles between atoms in same layer (intra- layer) and there is an increase in the values of bond angles between atoms in two layers (inter-layer). These results suggest that the contribution of sp^3 hybridization has increased as compared to that of mono-layer of silicene.

4.1.2 Multi-layers

Now, we discuss the results for optimized geometry and cohesive energy of multi-layers of silicene with four different stacking configurations. In Figure 4.2, we show the optimized structures of multi-layers ($n = 10$). This figure clearly elucidates the existence of a inter-layer covalent bonding in the multi-layers of silicene similar to the case of bi-layers. As discussed above, the cohesive energies of multi-layers with the three stacking configurations AAAA, AABB and ABC are significantly higher than that of the structure with ABAB stacking. This can be attributed to the fact that all the inner layers are covalently bonded with the adjacent layers in these three stackings. Due to this inter-layer bonding, all the silicon atoms in these three stackings, except those on surfaces, have four nearest neighbors (three intra-layer and one inter-layer) in nearly tetrahedral configurations. Hence, all the valence electrons in the silicon atoms (except ones on surface) make four sigma bonds with their nearest neighbors, due to sp^3-like hybridization in these stackings. In ABAB stacking, Si1 atom in layer A makes a fourth inter-layer sigma bond with Si1 atom in layer B along z-direction (see Figure 4.2, both the atoms are at same point in the xy-plane)) and hence these atoms assume nearly tetrahedral configuration. However, Si2 atoms in layers A and B do not have strong sigma bonds with each other (they are at different point in xy-plane)) and Si2-Si2 distance is more than 3 Å. Each set of AB layers are well connected by Si1-Si1 bonds but the two Si2 atoms lack the fourth nearest neighbors to form the sigma bond. Therefore, the number of sigma bonds in this stacking is less and hence they have the lowest cohesive energy as compared to those of AAAA, AABB and ABC stacking configurations. The reason for closeness of cohesive energies of AAAA, AABB and ABC stacking configurations is the similar bonding environment of each Si atom in these three stackings.

Valence Charge Density: In Figure 4.5, we plot the valence charge density distribution for six layers with ABC and ABAB stacking configurations. This figure clearly brings out the differences in bonding properties in these two configurations, which are consistent with our results obtained from the optimized geometries of these multi-layers. Furthermore, we note here that the cohesive energy of ABAB stacking configuration shows an oscillations with increasing number of layers. This can be explained by examining the

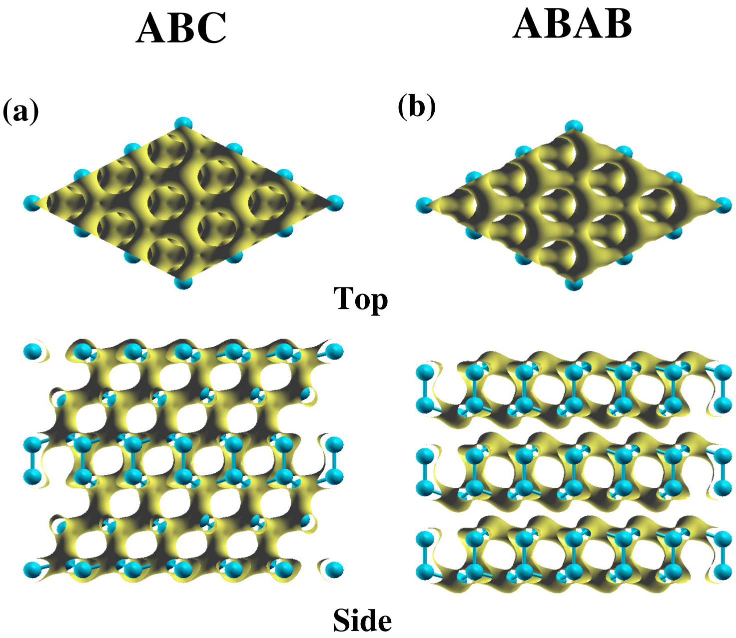

Figure 4.5: The valence charge density distributions of multi-layers of silicene ($n = 6$) with (a) ABC and (b) ABAB stacking configurations.

charge density distribution of this stacking configuration as shown in Figure 4.5 (b). It is observed that each bi-layer (AB) in ABAB stacking is strongly connected by inter-layer Si1-Si1 covalent bonds. However, the bonding between two adjacent AB bi-layers is weak and they are connected by the inter-layer Si2 atoms. The valence charge density presented in Figure 4.5 (b) confirms the presence of strong Si1-Si1 and weak Si2-Si2 bonds. Hence, the structures with even number of layers have large cohesive energy as compared to the structures with odd number of layers. This leads to an oscillation in cohesive energy per atom in ABAB stacking (see Figure 4.2(ii)).

4.2 Electronic Structures

4.2.1 Bi-layers

The band structure for AB and AA stackings along the highly symmetric k-points in Brillouin zone are shown in Figure 4.6 (b) and (c) respectively. We also include the band structure of mono-layer of silicene in Figure 4.6 (a) and (d) for comparison. It is clearly seen from the figures that dispersions around the E$_F$ for these two stackings are different and hence the electronic properties strongly depend upon the nature of stackings. For

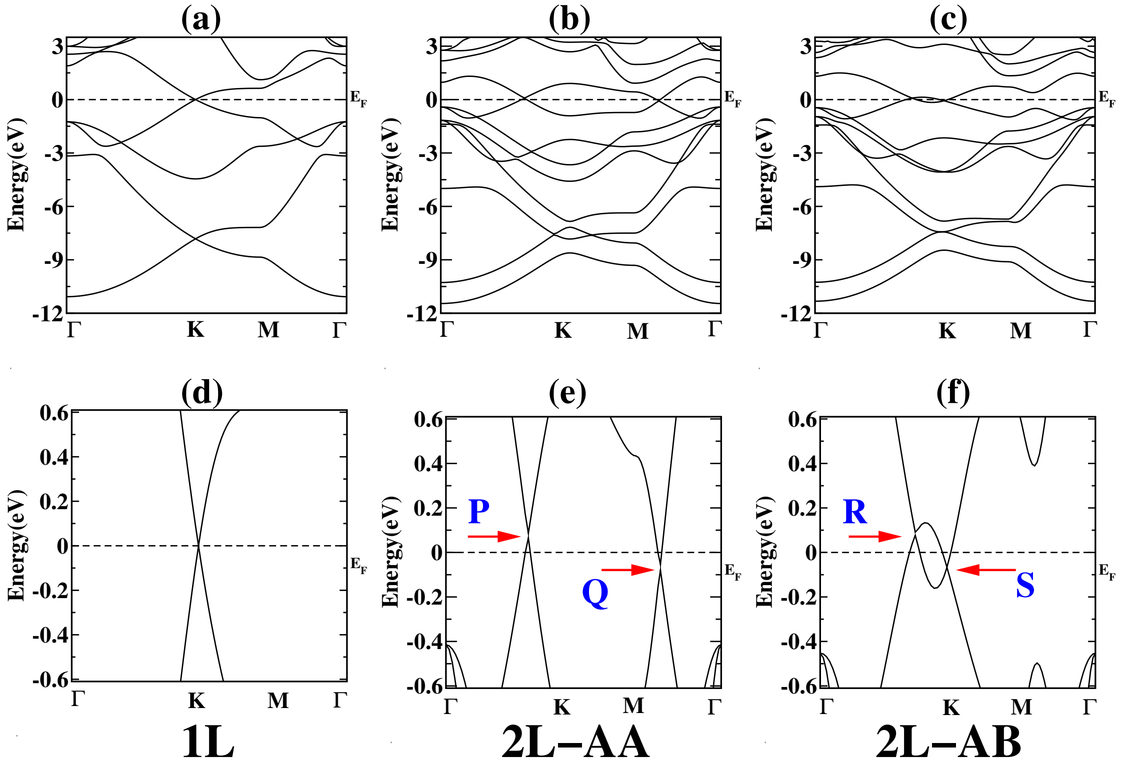

Figure 4.6: Band structures of mono-layer ((a) and (d)) and bi-layers ((b), (c), (e) and (f)) of silicene in two different energy ranges.

AA configuration, it is observed that there exists linear dispersion along two directions namely, Γ-K and Γ-M (see Figure 4.6 (e)). Each of these dispersion curves crosses at two points, denoted by P and Q in the band diagram (E-k). On the other hand for AB stacked bi-layer, we obtain a dispersion which is parabolic in nature (see Figure 4.6 (f)). These two dispersion curves also cross each other at two points namely R and S in the E-k diagram. It is interesting to note that all these four points do not coincide with the Fermi level. The presence of linear and parabolic dispersions in AA and AB stacked bi-layers respectively is similar to those present in bi-layers of graphene[153]. However, in case of bi-layers of graphene, all these crossing points (P, Q, R and S) lie at the E_F. The differences in the band structures of bi-layers of silicene from that of graphene may be due to the presence of strong inter-layer covalent bonding in bi-layers of silicene as compared to the weak vdW bonding between the layers of graphene. In order to verify this, we plot the band structure and charge density distributions for both AA and AB stacked bi-layers of silicene with different inter-layer separations in Figure 4.7.

Variation of Band Structure with Inter-layer Separation: It can be clearly observed from Figure 4.7 that these four crossing points (P, Q, R and S) slowly move

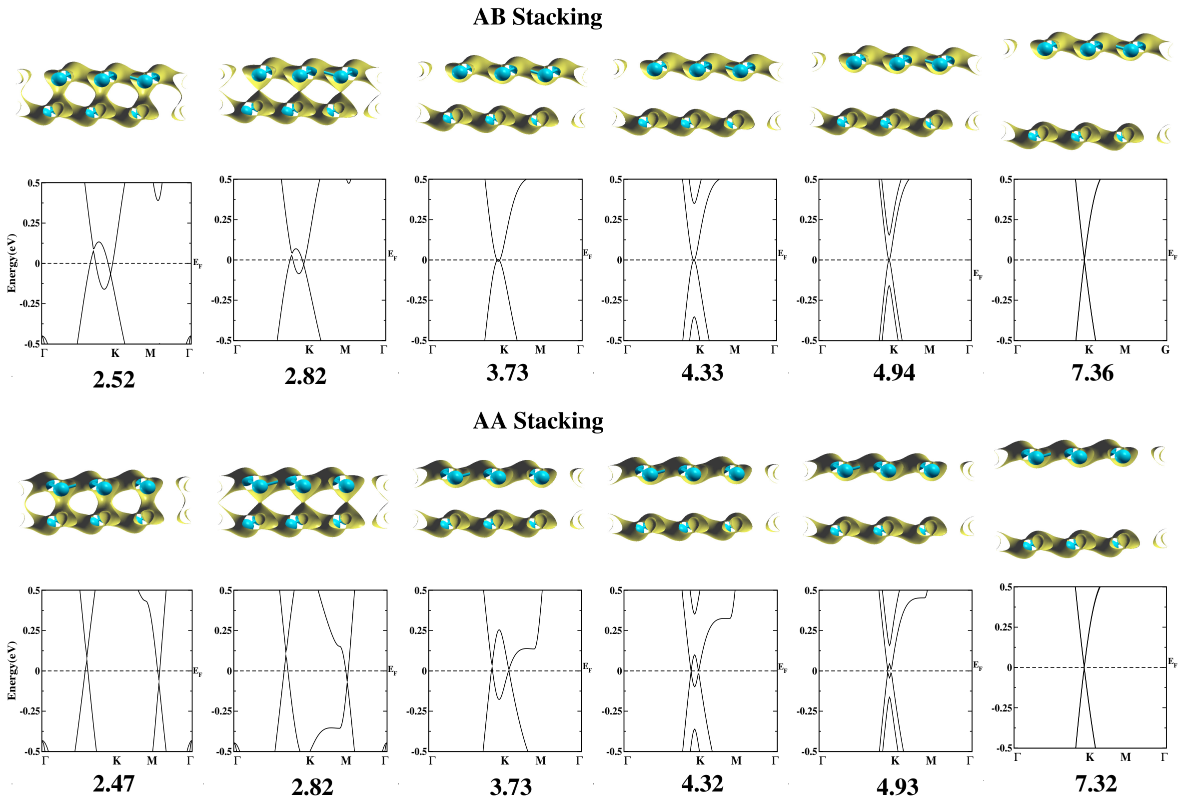

Figure 4.7: Variation of band structures and charge density distributions of AA and AB stacked bi-layers of silicene with different inter-layer separations. The value below the BS represents the inter-layer distance in Å

toward each other in E-k diagram and finally merge with each other at the E$_F$ for a distance larger than 7 Å between the two layers. Furthermore, the band structures of both AA and AB stacked bi-layers are reduced to that of mono-layer since there is a negligible interaction between the layers at a distance larger than 7 Å. We also observe that the band structures become similar to those of bi-layers of graphene for the intermediate inter-layer distances of about 3-4 Å. In this situation, we also observe that there is no overlap of charge densities between the layers. Therefore, we note that the origin of the differences in the band structures of bi-layers of silicene and graphene is indeed due to the presence of strong inter-layer coupling in the former.

4.2.2 Multi-layers

The interesting trends found in the bi-layer prompt us to probe the band structures of multi-layers of silicene with more than two layers in four different stacking configurations namely, AAAA, AABB, ABC and ABAB. We observe from our calculations that for given

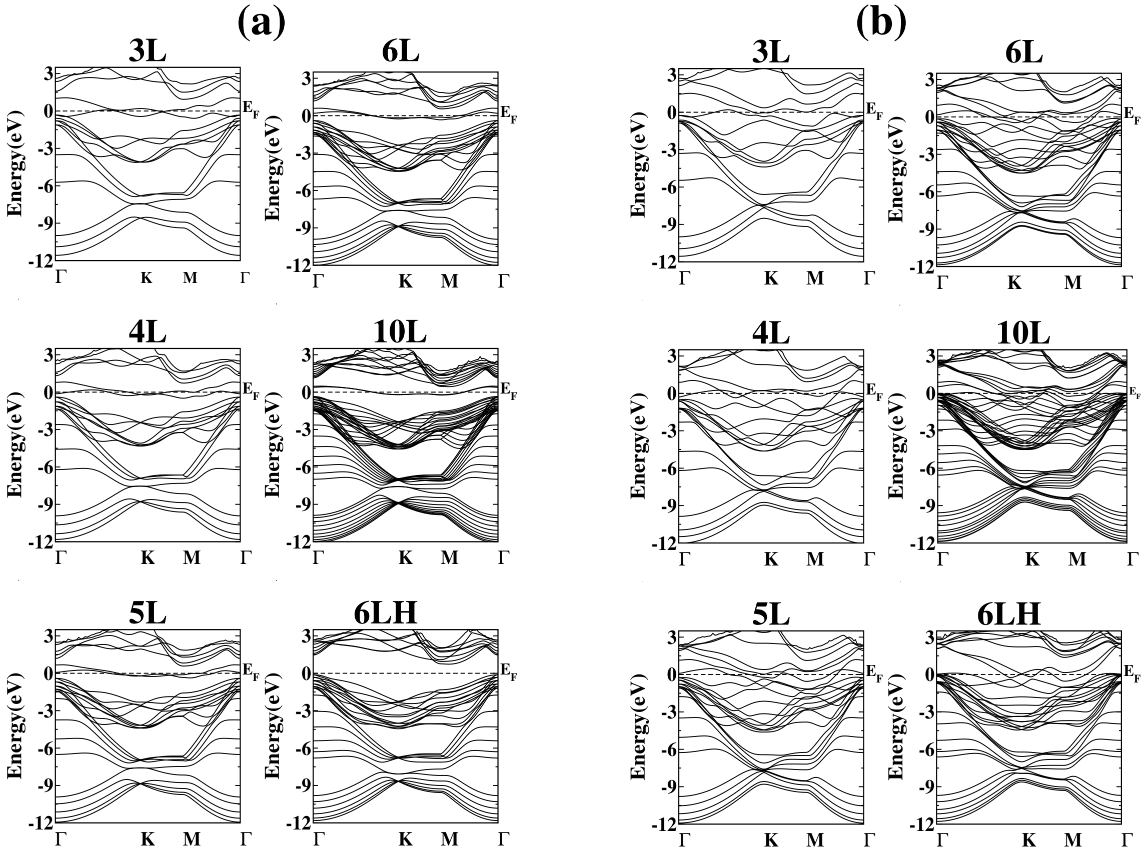

Figure 4.8: Evolution of band structures of (a) ABC and (b) ABAB stacked multi-layers of silicene with increasing number of layers.

number of layers (n), the band structures of multi-layers with AAAA, AABB and ABC stacking configurations are quite similar and on the other hand, they are different from those of multi-layer of silicene with Bernal stacking (ABAB). Hence, we present, in Figure 4.8, the results only for the band structures of (a) ABC and (b) ABAB stacked multi-layers with increasing value of n. The reason for similarity of band structures in AAAA, AABB and ABC is due to the similar local environment of silicon atoms in tetrahedral configurations in these stackings. However, they are different from the band structure of multi-layer with ABAB stacking due to different arrangement of silicon atoms in this stacking. Furthermore, for a given number of layers, we observe that there exists more number of bands with characteristic dispersion of σ bonds between Si atoms in ABC stacking as compared to those in ABAB structures (see Figure 4.8). Moreover, it can be observed that there exist two bands in multi-layers with ABC stacking which always cross the Fermi level. The width of these bands decreases with number of layers and hence they tend to be dispersionless as n goes beyond 6. To verify the nature of these two bands, we hydrogenate the multi-layers of silicene and study the effect of hydrogenation on their band structures. The band structures of hydrogenated multi-layers of silicene with 6 layers are also plotted in Figure 4.8 (denoted as 6LH) for comparison with bare multi-layers. These plots clearly show the absence of bands corresponding to the states at the Fermi level and thus a transition from semi-metallic to semiconductor state takes place. On the other hand, for Bernal stacking, we observe that there exist less number of bands corresponding to σ bonds while more number of bands corresponds to the weakly bound π bonds as compared to those of ABC stacking. These π bands arise from Si atoms present on every layer of multi-layers of silicene. Therefore, the saturation of Si atoms on the surface with hydrogen atoms does not cause the system to undergo a transition from semi-metallic to semiconductor state.

4.3 Hybrid Structure of Silicene and Boron Nitride

The results presented in the previous sections clearly indicate that the properties of multi-layers of silicene are drastically different from those of multi-layers of graphene. This is due to the fact that the multi-layers of silicene possess strong inter-layer covalent bonds in contrast to the weak vdW interaction between the layers of graphene multi-layers and bulk graphite. Due to this strong inter-layer covalent bonding, the multi-layers of silicene can no longer behave like two-dimensional layered materials similar to the multi-layers of graphene and graphite. However, it is desirable to obtain graphene-like silicon based layered systems possessing similar exciting and novel properties of multi-layer of graphene. We note here that the former has an important advantage over carbon based systems because of their compatibility with the existing semiconductor industry.

Keeping the above mentioned points in mind, we propose that there is a possibility of creating a graphite-like layered structure of silicon by inserting a buffer layer in between the multi-layers of silicene. The buffer layer prevents the strong inter-layer covalent bonds between the layers of silicene. Moreover, the buffer layer is expected not to alter the electronic properties of the multi-layers of silicene around the E_F. For this purpose, we consider a hybrid graphite-like layered system made up of alternate layers of honeycomb silicene and honeycomb boron nitride (BN). In this case, we choose BN as a buffer layer since the existing theoretical studies show that interaction between mono-layer of silicene and BN substrate is due to weak vdW[252–255]. We study the geometric and electronic structures of the hybrid graphite-like layered system by employing DFT based calculations. We want to probe whether it would be possible to have an energetically stable hybrid system with physical properties similar to those of bi-layers of graphene as well as bulk graphite.

4.3.1 Geometric Structures

We choose (2×2×1) and (3×3×1) super cells of free standing honeycomb silicene and BN respectively for the construction of an unit cell for the graphite-like hybrid structure. This configuration leads to matching of the lattice constants of these two different materials with a deviation of only about 1.7 %. Each layer of honeycomb silicene (BN) contains 8 silicon (9 boron and 9 nitrogen) atoms. The calculated optimized geometric structure of the hybrid graphite-like bulk system ($Si_{16}B_{18}N_{18}$) is shown in Figure 4.9 (a). Our results on geometric structure obtained by DFT based calculations with PBE XC functional show that the hybrid bulk system has a value of lattice constant 7.554 Å along a axis. The calculated values of Si-Si and B-N bond lengths in the basal plane are 2.246 and 1.454 Å respectively. We observe that the amount of buckling present in silicene layer in this hybrid system is slightly increased to 0.543 Å from its free standing value. The reason for increase in the buckling length is due to the interaction of silicene layer with the other layers present in the bulk system. Moreover, the increase in the value of buckling leads to a higher contribution of sp^3-like hybridization in Si atoms in silicene of the hybrid system as compared to that of Si atoms in free standing silicene. Our calculations give 14.695 Å for the value of lattice constant along c axis. Thus, the inter-layer distance between the silicene and BN layers becomes 3.674 Å. We also perform similar calculations for bi-layer of silicene with a single BN layer kept in between ($Si_{16}B_9N_9$). The optimized geometry of bi-layer is given in Figure 4.9 (b). In this case, the lattice constant along a axis and inter-layer distance of the hybrid bi-layer are estimated to be 7.607 and 4.011 Å respectively. It is to be noted that our calculations of cohesive energy for the hybrid systems show that they are energetically stable. We find that the cohesive energy per atom for the hybrid

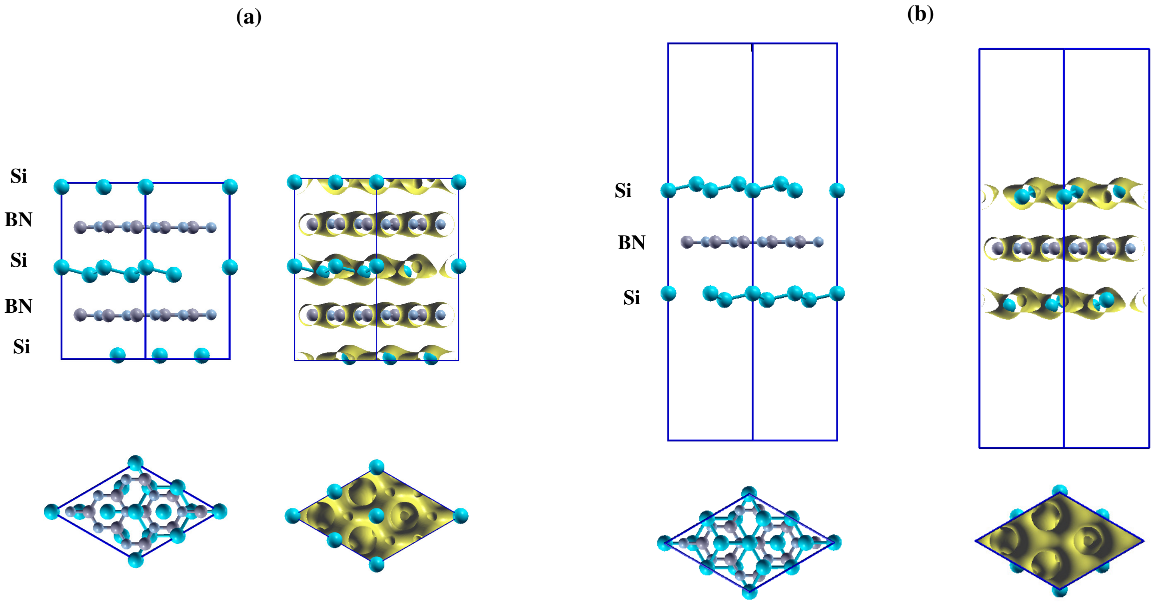

Figure 4.9: The optimized geometric structures and spatial charge density distributions of hybrid graphite-like structures made up of silicene and BN layers. (a) Bulk system ($Si_{16}B_{18}N_{18}$) and (b) bi-layer of silicene with a single BN layer ($Si_{16}B_9N_9$)

bulk and bi-layer systems are 6.07 and 5.57 eV/atom respectively.

In order to get deeper insight into the interaction between the layers of the hybrid systems, we also plot the spatial distribution of charge densities for the hybrid graphite-like bulk system ($Si_{16}B_{18}N_{18}$) and hybrid bi-layer of silicene ($Si_{16}B_9N_9$) in Figure 4.9. The figure clearly shows that the charge distribution of hybrid systems exhibits characteristic features of layered systems such as (i) presence of large charge densities in basal planes containing covalent bonds between atoms in each layer and (ii) negligible amount of charge densities present between the adjacent layers. Thus, our results clearly indicate that the hybrid systems are similar to those of graphite and multi-layers of graphene. From our calculations, the value of bulk modulus for the hybrid bulk system ($Si_{16}B_{18}N_{18}$) is estimated to be 48.5 GPa. For this purpose, we use Birch-Murnaghan formula for equation of state. This value of bulk modulus of hybrid bulk system is slightly higher than the corresponding values of layered structures such as bulk graphite (33.8 GPa)[256] and bulk hexagonal BN (25.6 GPa)[257]. However, they are much lower than that of bulk silicon (98 GPa)[258]. This result again corroborates with above mentioned charge density results which indicates the layered nature of the bulk hybrid system made up of silicene and BN. Thus, the hybrid system may also be used as a soft material similar to

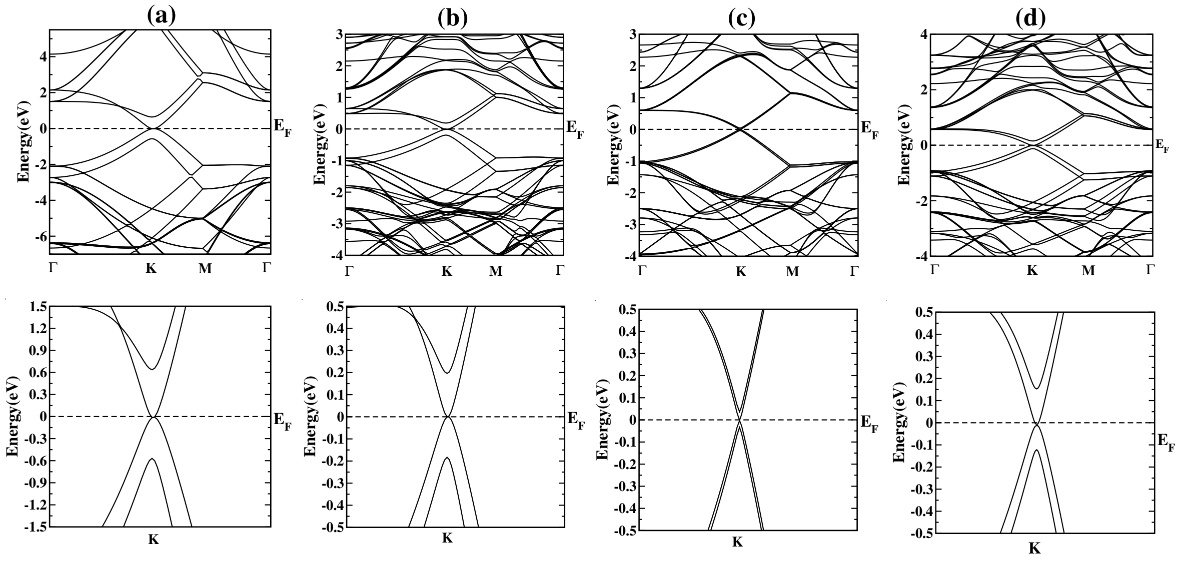

Figure 4.10: Band structures of layered systems in two energy ranges. (a) Bulk graphite with super cell (2×2×1), (b) hybrid bulk system ($Si_{16}B_{18}N_{18}$), as well as hybrid bi-layer ($Si_{16}B_9N_9$) with (c) optimized inter-layer distance and (d) inter-layer distance about 3.41 Å. The energies of bands are with respect to the respective Fermi level.

graphite and bulk BN.

4.3.2 Electronic Properties

Having analyzed the geometrical properties of hybrid graphite-like structures in the previous section, we now discuss our results on the electronic properties of these hybrid systems. In Figure 4.10, we plot the electronic band structures, in two different energy ranges, for both the hybrid bulk and bi-layered systems along the high symmetry points in Brillouin zone, which give dispersions corresponding to the motion of the charge particles along the planar directions. For the sake of comparison, we also include the electronic band structure of bulk graphite, with super cell (2×2×1) containing 16 carbon atoms, in Figure 4.10 (a) so that we can directly compare these results with the hybrid system. Our results on band structure for the hybrid bulk system show that the conduction and valence bands touch each other only at the highly symmetric point K in Brillouin zone. On comparison of the results for the hybrid bulk system, $Si_{16}B_{18}N_{18}$, (Figure 4.10 (b)) with those of bulk graphite (Figure 4.10 (a)), we find that the electronic band structures of these two systems are similar. However, we observe that the hybrid system contains additional number of bands which lie above ≈ 2.0 eV and below ≈ -2.0 eV. The contri-

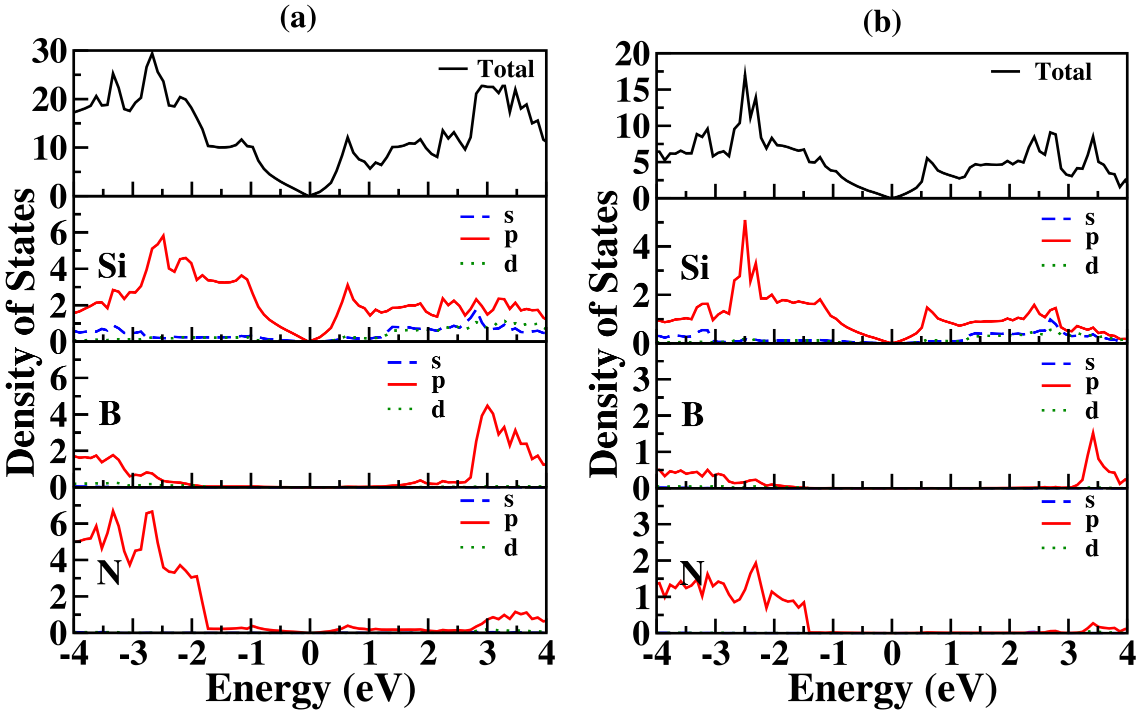

Figure 4.11: Total and partial density of states for hybrid graphite-like structure made up of silicene and BN layer: (a) bulk system ($Si_{16}B_{18}N_{18}$) and (b) bi-layer ($Si_{16}B_9N_9$). The values of energy are with respect to the Fermi level.

butions for these bands are mainly due to the BN layers. Furthermore, around the Fermi level, we observe a parabola-like dispersion for the hybrid bulk system (see Figure 4.10 (b)). Thus, the charge carriers in this system behave *nearly-free-particle-like.* It is clearly seen from Figure 4.10 (b) that the band structures of the hybrid bulk system and bulk graphite are rather similar close to the Fermi level. The combined results of geometric and electronic structure calculations lead to an important conclusion that the hybrid bulk system made up of alternate silicene and BN layers can be a possible material for silicon based layered structure similar to that of carbon based bulk graphite.

Interestingly, in case of the hybrid bi-layered system, we observe a linear dispersion around the Fermi level (see Figure 4.10 (c)) in contrast to the parabola-like dispersion present in bi-layer of graphene. Furthermore, this dispersion is also distinctly different from the corresponding dispersion for the pure bi-layer of silicene (without BN layer) given in Figure 4.6 (c) where the parabolic dispersions are shifted in both E and k direction in the band structure due to strong inter-layer covalent bonding. A closer look at the bands reveals that two linear dispersions are present in the band structure and they correspond to the two silicene layers of hybrid bi-layer. We also observe from our calculations that the characteristic of the dispersion has a strong dependence on the inter-layer distance. When the inter-layer distance is reduced to that of bi-layer of graphene, the linear dispersion present in hybrid bi-layer system transforms to the parabolic dispersion (see Figure 4.6 (d)) which is quite similar to that of bi- layer of graphene.

In order to investigate the contributions of different atoms to the electronic states, we also calculate the total density of states (DOS) and partial DOS for these two hybrid systems, namely bulk system ($Si_{16}B_{18}N_{18}$) and bi-layer ($Si_{16}B_9N_9$) (see Figure 4.11). First important observation is that the hybrid systems, both bulk as well as bi-layer, are semi-metallic since the values of DOS at E_F are zero. Investigation from the atom projected partial DOS clearly indicates that the contributions of DOS just below and above Fermi levels are mainly due to π and π^* orbitals of silicene layers. Moreover, we observe that there is no contribution from either boron or nitrogen around the Fermi level. These atoms contribute to DOS at about -1.8 eV (and below) and 2.5 eV (and above) compared to the Fermi level respectively for valence and conduction bands. Thus, the buffer BN layer does not contribute to the electronic states close to the Fermi level.

4.4 Summary

In this chapter, we have presented our results for the geometric and electronic properties of multi-layers of silicene with four different stacking configurations (AAAA, AABB, ABAB and ABC) which are obtained by employing DFT based calculations with PBE XC functional. In this study, we have investigated the evolution of these properties with increasing number of layers (n) ranging from 1 to 10. Our results on cohesive energy show that all the multi-layers considered in the present study are energetically stable. Though, mono-layer of silicene possesses properties similar to those of graphene, our results show that the geometric and electronic properties of multi-layers of silicene are strikingly different from those of multi-layers of graphene. We observe that there exist strong inter-layer covalent bondings between the layers in multi-layers of silicene as opposed to weak vdW bonding which exists between the graphene layers. The inter-layer bonding strongly influences the geometric and electronic structures of these multi-layers. Like bi-layers of graphene, silicene with two different stacking configurations AA and AB exhibits linear and parabolic dispersions around the Fermi level, respectively. However, unlike graphene, for bi-layers of silicene, these dispersion curves are shifted in band diagram; this is due to the strong inter-layer bonding present in the latter. For $n \geq 3$, we find that the ABC stacked multi-layers of silicene is the lowest energy configuration which is in contrast to the case of multi-layers of graphene where Bernal (ABAB) stacking configuration is reported to be the minimum energy configuration.

In addition, we have also proposed an energetically stable hybrid graphite-like system made up of silicene and BN layers. The results of our calculations predict that the hybrid bulk system possesses physical properties similar to those of bulk graphite. The coupling between the layers of silicene and BN of this hybrid system is due to weak vdW interaction which is same as that in graphite and multi-layers of graphene. We also observe from the results of the electronic band structure and the DOS that the hybrid bulk system is a semi-metal and it possesses the dispersion curve, around E_F, very similar to that of bulk graphite. Main contributions to the electronic states around E_F arise only due to silicene layers. Our calculations on bi-layer of silicene with a BN layer show that it possesses the characteristic linear dispersion around E_F. However, the nature of dispersion curve becomes parabola-like when the inter-layer distance reduces to that of bi-layer of graphene. These calculations indicate that the hybrid bulk system based on silicon and BN can be a possible candidate for two-dimensional layered soft material akin to graphite.

Publications based on this chapter

1. Silicene Beyond Mono-layers - Different Stacking Configurations And Their Properties
C. Kamal, Aparna Chakrabarti, Arup Banerjee, S. K. Deb
*Journal of Physics: Condensed Matter, **25**, 085508 (2013)*

2. *Ab initio* Investigation On Hybrid Graphite-like Structure Made Up Of Silicene And Boron Nitride
C. Kamal, Aparna Chakrabarti, Arup Banerjee
*Physics Letters A, **378**, 1162 (2014)*

Chapter 5

Effect of Intercalation on Properties of Carbon and Gallium Phosphide Nanotubes

In the last two chapters, we have discussed the physical properties of mono- and multilayers of two-dimensional graphene-like structure - silicene. Now, we begin our discussion on the physical properties of another fascinating nanostructure, quasi-one-dimensional nanotube (NT). In this chapter, we present our results for the geometric and electronic properties of single walled carbon (SWCNT) and gallium phosphide nanotubes (SWGaPNT). We also study the effect of intercalation of alkali (AM) and transition metal (TM) atom clusters on the properties of these two NTs.

Similar to graphene, there exist several studies on various physical properties of carbon nanotubes. These studies show that the carbon nanotubes possess extraordinary electrical, mechanical and thermal properties and thus they are considered as potential candidates for the building blocks of nanoscale devices[27–33]. Recently, there is a flurry of activities in understanding the nanostructures made up of other group IV and group III-V elements because of their interesting properties and also due to the technological importance of these materials in semiconductor industries. Among the group III-V materials, though the nitride-based III-V systems are well studied[259–272], there exist only a few investigations on the physical properties of phosphide-based one-dimensional systems such as nanotubes and nanowires[163–174]. We wish to note here that, recently, synthesis of GaPNT have been reported by Wu *et. al.*[163] and the optical studies on this nanotube show an emission peak corresponding to the direct band gap transition of GaPNT. Therefore, it can be a potential candidate for applications in the light emitting devices.

As mentioned in the introductory chapter, the properties of the nanostructures can be altered by chemical doping or intercalations of various atoms, molecules and their clusters. It has been observed in the literature that intercalation of atoms or clusters inside carbon nanotubes can give rise to many interesting changes in their properties[273–293]. We would like to mention a few interesting results from these studies. Half-metalicity has been observed in TM doped SWCNT(3,3) which is important for the spintronic applications[273]. Presence of Kondo effect[274], modifications of affinity and reactivity of TM clusters with nanotube[275], and the dopant TM acting as a glue between nanotube and graphene sheet[276], have been reported in the literature. Unusual freezing and melting behaviors have been studied for gallium intercalation inside carbon nanotubes[277]. From first principles calculations, Li et. al. have shown that the electronic structure of the silver filled SWCNTs can be altered systematically by varying the content of silver inside the nanotube[278]. In another study, Miyamoto et. al. have shown that filling up of thin carbon nanotubes by potassium (K) atom leads to charge transfer of one electron per K atom to the conduction bands of nanotube[279]. The doping of AM atoms or clusters inside the nanotubes can lead to other interesting properties such as semiconductor-metal as well as metal-semiconductor transitions in SWCNT[280], metal induced adsorption of biomolecules on nanotubes[281], influences of dopant atoms on work function of nanotubes[282–284], occurrence of phase transition between two different types of phases of alkali (Rb and Cs) intercalated SWCNTs[285] and drastic change in optical absorption spectra of semiconducting as well as metallic SWCNT [286].

We know that the hybridization in SWCNT, with larger diameter, is sp^2 type which is similar to that of graphene. Thus, SWCNTs have a rich π-electron density which is, however, not expected in the nanotubes made up of group III-V materials. Therefore, it will be interesting to study in microscopic detail the similarity and difference between the geometric and electronic properties of carbon and group III-V NTs, specifically, when these NTs are intercalated with various AM or TM atoms. The reason for choosing these two types of elements is the following: the AM elements are known to be nearly-free-electron systems. Hence we want to probe, if these atoms, when intercalated in an otherwise semiconducting nanotube, always result in metallicity as was found in

Ref.[279]. On the contrary, the purpose of probing the TM is to find out, if these atoms, upon intercalation in an otherwise non-magnetic nanotube, yield any magnetic properties or even half-metallicity as has been observed recently in Ref[273]. Keeping these aims in mind, we investigate the geometric and electronic properties of SWCNT(10,0) and SWGaPNT(10,0), with and without sodium atom (Na$_n$; n = 1 - 4) and transition metal atom (TM$_n$; n = 1 - 2) clusters. Here, n is the number of dopant atoms in the unit cell. The TM atom clusters considered in the present study comprise of manganese (Mn), iron (Fe) and cobalt (Co) atoms.

5.1 Geometric Structures

In this section, we discuss the results for the geometric properties of SWCNT as well as SWGaPNT with the chirality index (10,0). In Figure 5.1, we display the optimized geometries of undoped and some of the doped SWCNTs and SWGaPNTs. The results for the diameters, bond lengths and bond angles of undoped SWCNT and SWGaPNT are also summarized in Table 5.1. For *all-electron* based electronic structure calculations of NTs,

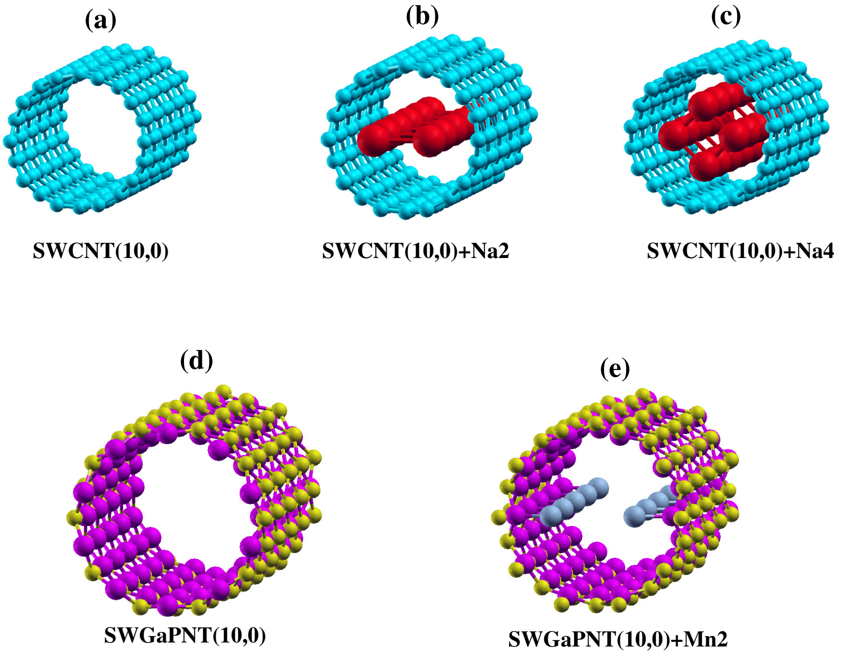

Figure 5.1: The optimized geometries of SWCNT(10,0) ((a) undoped, doped (b) with two Na atoms and (c) with four Na atoms) and SWGaPNT(10,0) ((d) undoped and (e) doped with two Mn atoms)

Table 5.1: The results of optimized geometries of SWCNT(10,0) and SWGaPNT(10,0) obtained by DFT calculations with PBE exchange-correlation functional.

Nanotubes	Diameter (Å)	Bond Length (Å)	Bond Angle (∘)
SWCNT	7.86	1.42	117.4, 120.1
SWGaPNT	11.60 (Ga)	2.37, 2.31	102.1 (Ga-P-Ga), 117.2 (Ga-P-Ga)
	12.56 (P)		114.7 (P-Ga-P), 120.6 (P-Ga-P)

we use relativistic full potential linearized augmented plane wave (FPLAPW) method as implemented in WIEN2k code[198]. It has been observed from our previous studies that *all-electron* based DFT calculations are necessary for the correct prediction of the electronic properties of SWCNTs specifically the ones with small (sub-nm) diameter[294]. We observe from our calculations that SWCNT(10,0) is cylindrical in shape with a diameter of about 7.86 Å. However, the calculated optimized geometry of SWGaPNT shows that the NT is cylindrical with a buckling effect. It is observed that due to the buckling, gallium and phosphorous atoms do not lie at same radial distance from the axis of NT. Thus, the SWGaPNT has an inner (containing gallium atoms) and an outer (containing phosphorous atoms) cylinder with the diameters of 11.60 Å and 12.56 Å respectively. Then the buckling length turns out to be 0.48 Å which is defined as half of the difference between the inner and outer diameters. The buckling effect observed in SWGaPNT clearly indicates that the hybridization in SWGaPNT is not the same as that in SWCNT. It is well known that the SWCNT with large diameter (more than 7.0 Å) has sp^2 hybridization[32, 294]. The presence of sp^2 like hybridization in SWCNT(10,0) is evident from bond lengths and bond angles which are close to 1.42 Å and 120° (geometrical parameters of graphene) respectively. However, for smaller diameter, there exists a mixture of sp^2 and sp^3 hybridizations in SWCNT as is evident from Table 5.1[294]. In case of SWGaPNT, even with larger diameter the hybridization is a mixture of sp^2 and sp^3. It is seen from Table 5.1 that the values of bond angle in SWGaPNT lie in between those of sp^2 and sp^3 hybridizations. This is due to the fact that carbon can form 2D (sp^2 hybridized) and 3D (sp^3 hybridized) structures whereas GaP favors only 3D structures. The nanotube has one-dimensional periodicity along the axis of the tube. The lattice constants of unit cells for SWCNT(10,0) and SWGaPNT(10,0) are found to be 4.26 Å and 7.10 Å, respectively. The unit cell contains 40 atoms in each case.

We observe that there is no significant deformation in the geometry of both the NTs due to doping of single TM or AM atom per unit cell which corresponds to 2.5% of doping. Thus, the TM or AM atom forms a linear chain along the axis of NT due to the one-dimensional periodicity. When concentration of doping increases, SWCNT(10,0) expands with a maximum change in diameter of about 4% in case of doping with Na_4 cluster per unit cell (which corresponds to 10% of doping). For SWGaPNT, we observe that the changes in the optimized structure are negligible even for doping with four atoms. However, when two Mn atoms are intercalated inside the unit cell of SWGaPNT , the Mn atoms do not form dimer as in other cases of two atoms doping and each Mn atom gets closer to the Ga atoms of the inner wall of the SWGaPNT (see Figure 5.1(e)). This is due to the fact that the bond which exists between the Mn atoms in dimer form is weak due to the van der Waals interaction[295, 296]. The consequence of these observations and the effect of different dopings on the electronic structures will be discussed in the next section. In order to check the stability of the NTs, we also calculate the binding energy (BE) of all the NTs considered here. We find that all the doped SWCNT(10,0) and SWGaPNT(10,0) are energetically bound systems. However, the BE/atom of undoped NTs are slightly higher than those of the doped NTs. For example, the BE of single Mn doped SWCNT(10,0) is lower by 0.25 eV as compared to the undoped one.

5.2 Electronic Structures

In the bulk form, both carbon (diamond) and GaP(zinc blende) are semiconductor with indirect band gap of about 5.4 and 2.32 eV, respectively[297]. Our results for the band structures of carbon and gallium phosphide in both bulk and NT(10,0) phases are given in Figure 5.2. It is important to note that, in contrast to their bulk counterparts, both SWCNT(10,0) and SWGaPNT(10,0) are semiconductor with direct band gaps of 0.83 and 1.48 eV, respectively. Hence, these NTs are possible candidates for applications in the light emitting devices. The semiconducting nature of SWCNT(10,0) agrees with the condition of non-metallicity derived on the basis of chirality indices. In order to understand various contributions to the electronic states, we perform detailed analysis of orbital projected band structures. For this nanotube, it is observed that the valence and conduction bands

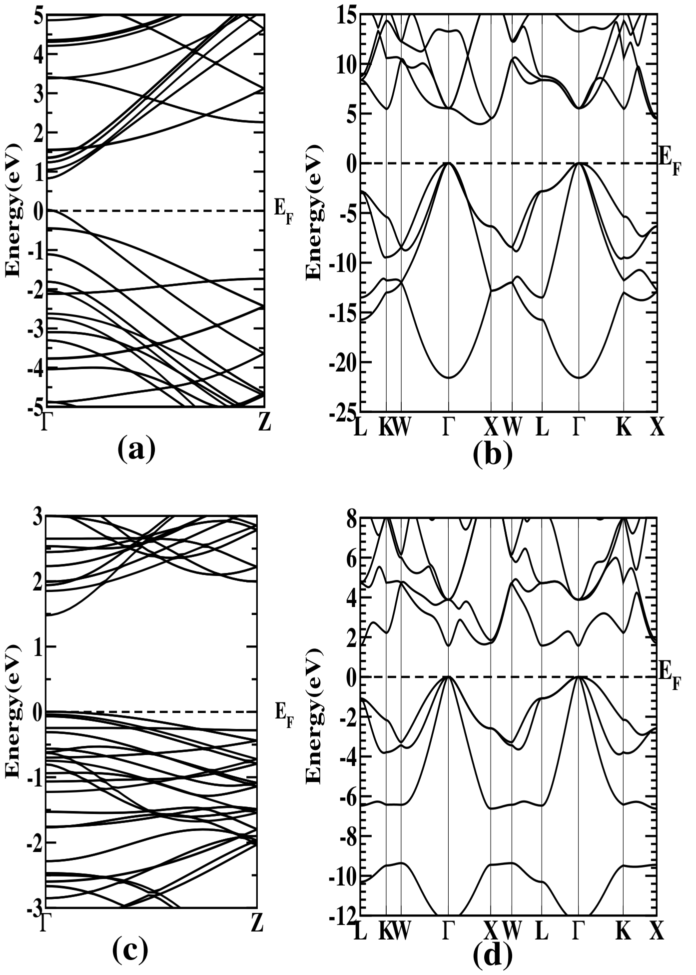

Figure 5.2: The band structures of (a) SWCNT(10,0), (b) carbon bulk (diamond), (c) SWGaPNT(10,0) and (d) GaP bulk (zinc blende) obtained from DFT using GGA (PBE) XC functional. The values of energy are with respect to the Fermi level.

are largely dominated by p-type of carbon. There is little contribution of s-type in the bands -3.0 eV below the Fermi level (E_F). For SWGaPNT, we find that the conduction bands have contributions from s- and p-type of gallium as well as phosphorous, while the valence bands are mainly p-derived bands of phosphorous.

5.2.1 Alkali Metal Doping

Now, we study the effect of intercalation of sodium clusters on the band structure of NTs. The results for the band structure of SWCNT(10,0) intercalated with Na_n clusters are given in Figure 5.3. It is also observed from this figure that SWCNT becomes metallic due to the intercalation of alkali metal atom inside the tube even at a small doping density of 2.5%. We observe the appearance of *nearly-free-electron* (NFE) bands, with parabolic

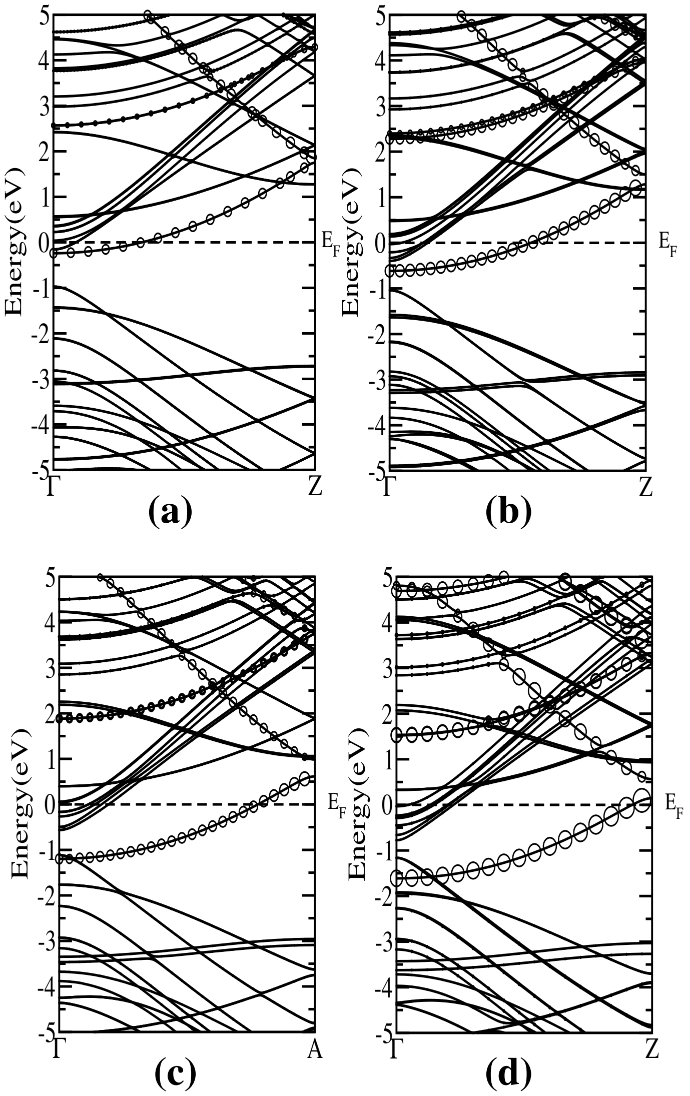

(a) (b) (c) (d)

Figure 5.3: The band structures of SWCNT(10,0) doped with alkali metal clusters containing (a) a Na atom, (b) two Na atoms, (c) three Na atoms and (d) four Na atoms per unit cell. The values of energy are with respect to the Fermi level. The bands with circles and dots are due to the contributions from dopant atoms.

type dispersion, around the Fermi level corresponding to the 3s levels of the intercalated Na atoms. These bands are partially filled and hence they contribute in turning the undoped semiconducting SWCNT to metal as a result of intercalation. Furthermore, the doping of Na atoms increasingly pushes down the carbon-derived conduction bands towards the Fermi level, leading the system to being increasingly more metallic with more doping. The fractional occupancies in the carbon derived conduction bands are due to the transfer of charges from the Na atoms (s bands) to the C atoms (p bands) (see Table 5.2). This has been confirmed by the charge density analysis (see Figure 5.4 (a)). Apart from the apparently rigid shifting of the bands, it has also been observed that the degeneracy

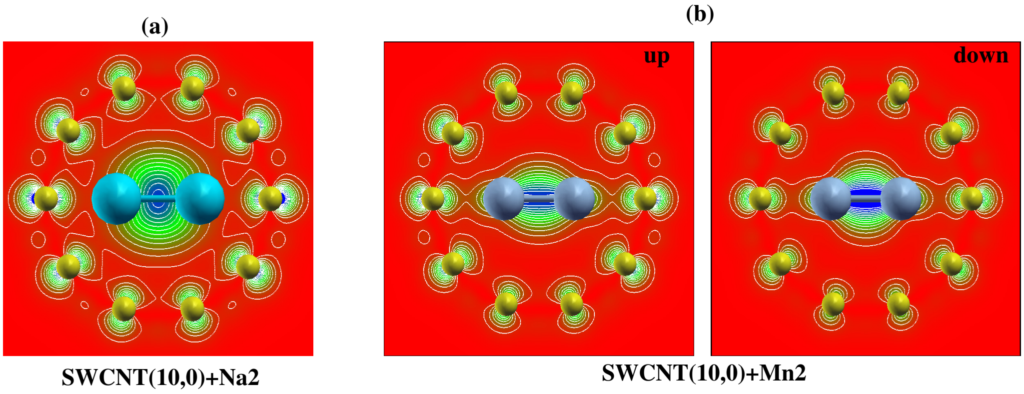

Figure 5.4: The charge densities of SWCNT(10,0) doped with (a) two Na atoms and (b) two Mn atoms (both for up and down spins) in a plane perpendicular to the axis of nanotubes.

of some of the bands is lifted as the concentration of doping increases. It is important to note that the SWCNT intercalated with Na atoms possesses many conducting channels which are due to two types of partially filled bands. They are (a) NFE bands due to linear chain of Na atoms and (b) conduction bands of NT (which are unoccupied in bare NT and now partially occupied in intercalated NT due to the charge transfer). These two types of conducting channels may play an important role in the transport properties of NTs.

In Figure 5.5, we present our results of the band structures of SWGaPNT(10,0) doped with alkali metal clusters containing (a) a Na atom and (b) four Na atoms per unit cell. Similar to SWCNT, there is a semiconductor to metal transition in SWGaPNT due to the intercalation of sodium clusters. Again, it is due to both shifting of Ga and P derived conduction bands down toward the Fermi level and the transfer of charges from the Na (s-type) to Ga and P (p-type). Thus, we can say that the effect of intercalation on the band structures of SWCNT and SWGaPNT is similar. However, we observe that the 3s (Na) bands in SWGaPNT show somewhat less dispersion as compared to those in SWCNT. Moreover, the amount of charge transfer from sodium to NT atoms is also less in this case (see Table 5.2). This is due to the fact that the Na clusters in SWGaPNT are separated by larger distances from NT atoms as compared to those in SWCNT. Thus, we may say that SWGaPNT requires larger concentration of doping as compared to that in SWCNT, in order to produce the similar effect.

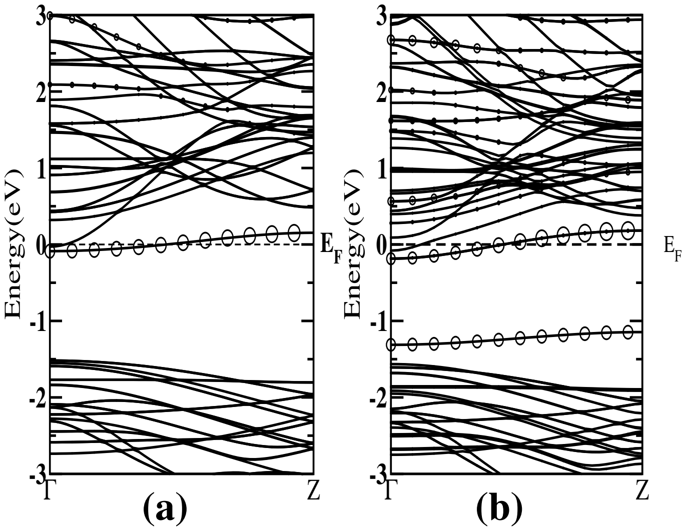

Figure 5.5: The band structures of SWGaPNT(10,0) doped with alkali metal clusters containing (a) a Na atom and (b) four Na atoms per unit cell. The values of energy are with respect to the Fermi level. The bands with circles and dots are due to the contributions from dopant atoms.

5.2.2 Transition Metal Doping

The band structures of SWCNT(10,0) intercalated with single TM atom per unit cell (2.5 % of doping) are shown in Figure 5.6. Our spin polarized calculations show that single TM doped SWCNT(10,0) is half metallic. The system behaves as semiconductor for spin up carriers and metallic for the spin down carriers. It is clearly seen from Figure 5.6 that there is no crossing of bands at the Fermi level for spin up carriers (see (a) and (c)). However, the band structures for the spin down cases possess conducting channels which are mainly due to s-type band of TM atoms ((b) and (d)). These bands near the Fermi level also possess NFE like dispersion and hence they may play an important role in the transport properties of NTs. It is observed that the characteristic bands of undoped SWCNT are not significantly modified because of the doping. *Spin up carriers:* the d-bands of TM corresponding to the carrier with spin up lie around 3-4 eV below the Fermi level. These bands are highly localized and hence they are *nearly-dispersion-free* (NDF) like. We observe that a band (showing dispersion) corresponding to s-electrons of TM atom appears around -2.0 eV at Γ point. *Spin down carriers:* we observe a dispersive band corresponding to the s-electrons of TM atom appears at a lower energy compared to the spin up case (around -1.0 eV at Γ point). At the same time, many flat or

Table 5.2: The amount of charge transfer from the dopant atoms to NTs and total magnetic moments per unit cell.

Nanotubes (10,0)	Charge Transfer Amount	 From	 To	Magnetic moments (μ_B)
SWCNT+Na1	0.33	3s(Na)	2p(C)	-
SWCNT+Na2	0.90	3s(Na)	2p(C)	-
SWCNT+Na3	1.45	3s(Na)	2p(C)	-
SWCNT+Na4	2.16	3s(Na)	2p(C)	-
SWCNT+Mn1	0.05	3d(Mn)	2p(C)	5.07
SWCNT+Fe1	0.00	-	-	4.00
SWCNT+Co1	0.00	-	-	2.70
SWCNT+Mn2	1.00	3d(Mn)	2p(C)	9.08
SWGaPNT+Na1	0.11	3s(Na)	p(GaP)	-
SWGaPNT+Na4	0.23	3s(Na)	pl(GaP)	-
SWGaPNT+Mn1	0.00	-	-	5.00
SWGaPNT+Fe1	0.00	-	-	3.91
SWGaPNT+Co1	0.00	-	-	3.01
SWGaPNT+Mn2	0.00	-	-	9.99

less dispersive bands appear around the Fermi level which correspond to the d-electrons of the TM atom. The results for the charge transfer and total magnetic moment per unit cell are given in Table 5.2. For the single TM atom intercalated cases, the results indicate that there is no significant overlap of charges between the TM atoms and the NTs. Thus, the magnetic moments per TM atom are comparable to the atomic moments.

Similar to TM doped SWCNT, the low percentage (2.5 %) of TM doping shows the signature of half metallicity in SWGaPNT (Figure 5.7). The reason for the presence of half metallic characters of linear chain inserted in SWGaPNT can be similar to the case of SWCNT. As in the case of AM atom doped NTs, the characteristic bands of undoped SWGaPNT are not modified much with intercalation. This again suggests that there is no significant hybridization between the dopant atoms and NTs. *Spin up carriers:* for the Mn atom doping, there is an atomic like level at about 1.0 eV below the Fermi level due to s-type of Mn. Valence bands below the Fermi level are largely dominated by p-type of both Ga and P. We also observe that the bands corresponding to d-electrons of Mn appear at around -3.7 eV (not shown in Figure 5.7 (a)). In case of Fe atom doped NT, there is a atomic like level at about 1.2 eV below the Fermi level due to s-electron of

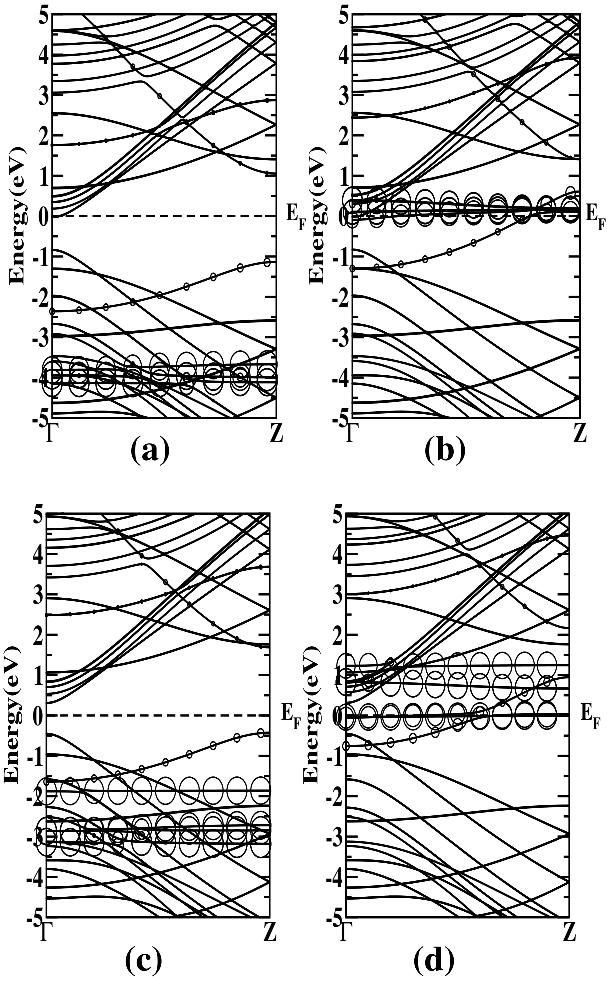

Figure 5.6: The band structures of SWCNT(10,0) doped with single transition metal atom per unit cell. Manganese : (a) up and (b) down spin, and Iron : (c) up and (d) down spin. The values of energy are with respect to the Fermi level. The bands with circles and dots are due to the contributions from dopant atoms.

Fe. Similar to the Mn doped case, the valence bands below the Fermi level are largely dominated by p-electrons of Ga and P atoms. The bands corresponding to d-electrons of Fe occur around -2.3 and -3.0 eV. *Spin down carriers:* the Mn-derived band of s-electron occurs at around the Fermi level and a band due to d-electrons appears at about 0.7 eV above the Fermi level. On the other hand, for Fe doped NT, the Fe-derived band due to s-electron occurs around the Fermi level and a d-type band occurs at about 1.0 eV above the Fermi level. For Co-doping case, the qualitative features in the band structure are quite similar to those of Fe and Mn doped NT. From the charge density analysis of TM-doped NTs, it is observed that there is no significant charge transfer from the transition metal atoms to nanotubes and therefore, the net magnetic moments per unit cell closely match with those of free TM atoms (see Table. 5.2). The lack of a significant overlap of

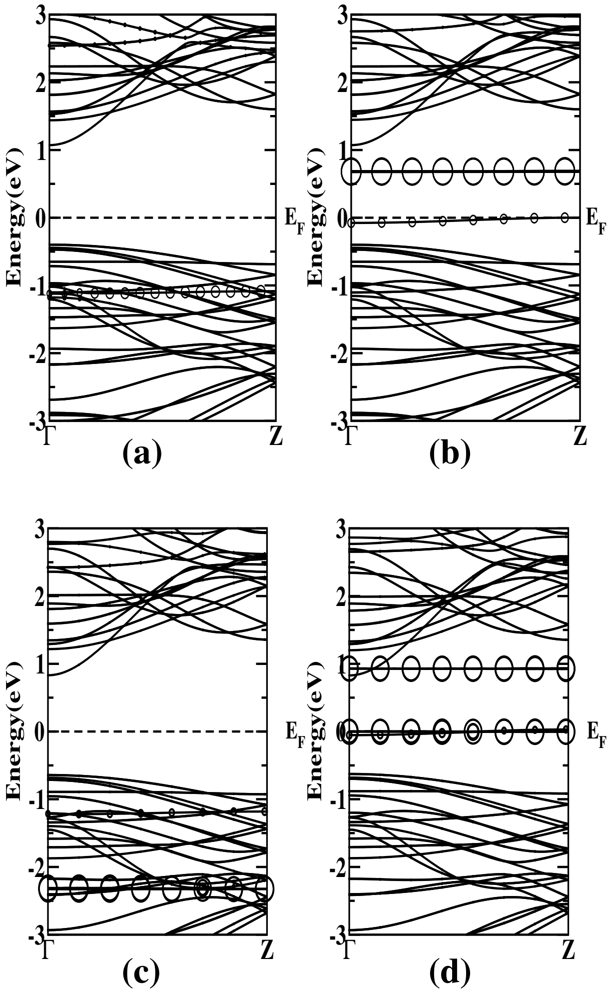

Figure 5.7: The band structures of SWGaPNT(10,0) doped with single transition metal atom per unit cell. Manganese: (a) up and (b) down spin, and Iron: (c) up and (d) down spin. The values of energy are with respect to the Fermi level. The bands with circles and dots are due to the contributions from dopant atoms.

charges between the dopant atoms and the NT is due to a large separation between them which gives rise to a poor charge transfer. However, the situation may change when the number of intercalated TM atoms increased to more than one.

We now discuss the effect of intercalation of TM atoms, beyond 2.5 %, on the electronic structure of NTs. First we discuss the results obtained for SWCNT(10,0). Our band structure calculations indicate that the SWCNT becomes fully metallic when the percentage of intercalation goes beyond 2.5. We can see from Figure 5.8 (a) and (b) that SWCNT intercalated with two Mn atoms (per unit cell) possesses conducting channels for both spin up and down carriers due to partially occupied level at the Fermi level. Hence, the SWCNT doped with two Mn atoms becomes fully metallic. *Spin up carriers :* we ob-

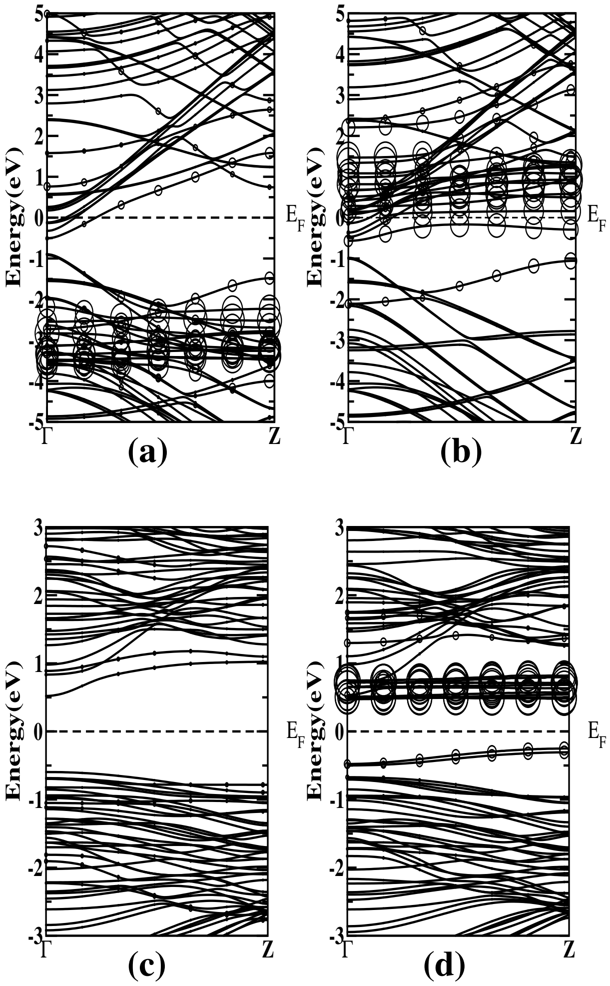

Figure 5.8: The band structures of SWCNT(10,0) doped with two Mn atoms ((a) up and (b) down spins) and SWGaPNT(10,0) doped with two Mn atoms ((c) up and (d) down spins). The values of energy are with respect to the Fermi level. The bands with circles and dots are due to the contributions from dopant atoms.

serve that a band corresponding to s-type of Mn atom appears around -2.8 eV at Γ-point and many atomic-like flat bands appear between -2.4 to -3.5 eV, which correspond to d-type electrons of Mn atoms. These bands also have significant amount of contribution from p-type electrons of carbon atoms. *Spin down carriers :* on the other hand, the band structure for down spin carriers contains a band corresponding to the s-electrons of Mn atom around -2.1 eV at Γ-point. This band also has contributions from d-type electrons of Mn atoms. Our result indicates the presence of significant hybridization between the dopant Mn and C atoms. Here also, we observe many atomic-like flat bands around Fermi level which correspond to d-type electrons of Mn atom. In contrast to the single TM atom intercalation case, there is a large charge transfer from d-type electrons of Mn atoms to p-type electrons of carbon. It is seen from Figure 5.8 (a) and (b) that there are partial occupancies in p-type carbon derived bands due to the charge transfer. The presence of large charge transfer has been confirmed by charge density analysis (see Table. 5.2 and Figure 5.4 (b)).

Similar to the case of SWCNT, the higher concentration of TM intercalation in SWGaPNT is also expected to drive the system to full-metallicity. However, we observe that SWGaPNT doped with two Mn atoms (per unit cell) is a semiconductor. Though there is a reduction in the value of band gap because of doping, it is not enough to make the conduction bands cross the Fermi level. It is important to note that the optimized geometry of SWGaPNT intercalated with two Mn atoms is slightly different from that of SWCNT with two Mn atoms (see Figure 5.1 (e)). We would like to mention here that the free Mn dimer turns out to be an unbound system from our DFT calculations[296]. However, a weak bond between the Mn atoms can result within SWCNT due to the stronger confinement effect. But, in case of SWGaPNT, after geometry optimization, each Mn atom move towards the inner walls of NT and attaches itself with separate Ga atoms. This is due to the fact that there is more room for the unbonded Mn atoms in SWGaPNT as compared to that in SWCNT since the diameter of SWGaPNT(10,0) is about 47 % larger than that of SWCNT(10,0). Furthermore, in contrast to the SWCNT case, no charge transfer takes place from Mn atoms to either Ga or P atoms in SWGaPNT. Therefore, none of the bands corresponding to the SWGaPNT shifted towards the Fermi level and the SWGaPNT retains its semiconducting character. Overall, it is observed from our calculations that the effect of intercalation on the electronic properties of both SWCNT and SWGaPNT are similar. However, our calculations indicate that the SWGaPNT may require higher concentration of intercalation to produce effects similar to that in SWCNT.

5.3 Summary

In this chapter, we have presented our results for the geometric, electronic and magnetic properties of alkali- and transition metal atom clusters doped and undoped SWCNT(10,0) and SWGaPNT(10,0) which have been obtained by using *all-electron* based DFT calculations with GGA (PBE) exchange-correlation functional. Our results of optimized geometric structures show that both the SWCNTs and SWGaPNTs are cylindrical in shape. However, the SWGaPNTs are buckled due to the presence of mixture of sp^2 and sp^3 hybridizations. In contrast to the indirect band gap of the bulk materials: carbon (diamond) and gallium phosphide (zinc blende), we observe that both SWCNT(10,0) and SWGaPNT(10,0) possess direct band gaps of 0.83 and 1.48 eV, respectively. Hence, these NTs are possible candidates for applications in the light emitting devices.

Our calculations of electronic structures of SWCNT intercalated with a single transition metal atom show that it undergoes a transition from semiconducting to a half-metallic state. Our calculations indicate that signature of similar transitions are expected for SWGaPNT(10,0) as well. However, the transition becomes semiconductor to metallic when the concentration of TM atoms increases. The results of SWCNT(10,0) and SWGaPNT(10,0) intercalated with alkali metal atoms give an indication that intercalation leads to metallization in these NTs. Significant overlap between the atoms of alkali metal and the NTs and subsequent charge transfer from the former to the latter holds the key to this semiconductor to metal transition. From the results of our calculations, we conclude that though there are differences in the nature of hybridization and bonding in SWCNT(mostly sp^2) and SWGaPNT (mixture of sp^2 and sp^3), both NTs with the same chirality index are found to be semiconducting in nature and also they exhibit similar effect of intercalations depending upon the concentration of dopant atoms.

Publication based on this chapter

Ab initio Studies Of Effect Of Intercalation On The Properties Of Single Walled Carbon And Gallium Phosphide Nanotubes

C. Kamal, Aparna Chakrabarti, Arup Banerjee, S. K. Deb

Physica E: Low-dimensional Systems and Nanostructures, ***54****, 273 (2013)*

Chapter 6

Optical Response Properties of Carbon Nanostructures

Having studied the ground state properties of carbon and gallium phosphide nanotubes in the previous chapter, we now proceed to present our results for the optical response properties such as static electric dipole polarizability and strength (through C_6 coefficient) of the van der Waals (vdW) interaction of the carbon nanostructures (CNSs) in the current chapter. Main aim of the present chapter is to study the vdW interaction between two CNSs as well as between a CNS and small gas molecules, including the environmentally important ones, from the first-principle calculations. We also investigate the variation of these response properties as a function of different physical parameters such as size and shape of the nanostructures. For this purpose, we choose two different shapes of CNSs namely cages and carbon nanotubes (CNTs) with various sizes (up to 100 carbon atoms).

As mentioned in the introductory chapter, the large surface-to-volume ratio of nanostructures plays a crucial role in many applications. For example, nanostructures are potential candidates for storing or adsorbing significant quantities of different molecules or gases. Recently, the topic of storage or adsorption of hydrogen and other small molecules by nanostructures, especially systems based on carbon, has received overwhelming attention of the researchers[35–49]. It has been shown that a very high hydrogen uptake in CNTs is possible; hence these nanotubes can act as a good hydrogen-storage material for fuel-cell electric vehicles[35]. The fast kinetics and reversibility of the process of hydrogen adsorption in different CNSs indicate that the interaction between the hydrogen molecules and the CNS is due to physisorption[42–45]. The vdW interaction plays an important role in these interactions.

In the literature, there have also been various studies on gas adsorption on CNTs, mainly, aimed towards the application of these structures as gas sensors. The CNTs are good choice of material for producing sensor for gas molecules such as NO_2, NH_3, CO_2, etc since their properties can be significantly altered by adsorption of these gas molecules[50–58]. Moreover, the sensors made from CNTs will be very small in size and has advantages like low power consumption, light weight and low cost. Recently, effort towards sucking up of the hazardous or greenhouse gases from the atmosphere has gained momentum since the accumulation of some of these gases leads to severe global warming[298]. It is expected that the CNTs and carbon cages may adsorb these gases because of their increased surface area which leads to increased absorptive capacity. There have been quite a few studies on adsorption of different gases, including rare and toxic gases, on carbon nanostructures[58, 299–316].

Another interesting aspect of these CNSs is the formation of solid-like superstructure from the nanotube or fullerene units. The prominent force for the formation of these solid-like superstructures is the vdW interaction[317–320]. Similar interaction is also responsible for the formation of bundles or ropes of CNTs[321–323]. Henrard et. al.[324] have shown that the vdW interaction in the bundles of nanotubes has important consequences on the vibrational modes. It has also been shown in the literature, both theoretically[317, 318] and experimentally[325], that beyond a certain diameter, single walled CNTs (SWCNTs) deform due to very large vdW forces. Jiang et. al.[325] have shown that this deformation can be measured from the changes in the electron diffraction intensities. As the distance between two CNTs is of the order of their radius, the vdW interaction between them becomes dominant. Girifalco et. al.[321] have shown that the vdW force between two SWCNTs can be as strong as about 1 eV/nm and values of cohesive energy of CNT bundles can be as high as 4.8 eV/nm. It has been observed by Takanori et. al.[322] that the vdW force is the main adhesion force for deposition of thin straight bundles of CNT lying parallel to the substrate surface during dc anhydrous electrodeposition. Thin films of SWCNT have been grown by Sato et. al.[323] by depositing SWCNT bundles in a layer-by-layer fashion and again, the vdW force is the main driving force for the formation of such a thin film of SWCNT. Popescu et. al. have given simple model for vdW interactions between two radially deformed SWCNTs[326].

It is clearly observed from above discussions that the vdW interaction between two CNSs as well as between a CNS and other molecules or gases plays a crucial role in many processes like formations of solid-like superstructures, thin films and bundles or ropes of nanostructures as well as physisorption of various molecules or gases by nanostructures. Thus, a detailed microscopic study of the vdW interaction and a quantitative estimation of strength of this interaction between different cages or between various nanotubes is extremely helpful to understand the above mentioned processes. Hence, in the present study, we perform the calculation of vdW interaction coefficient between the cages and nanotubes, containing maximum about 100 carbon atoms, by using *all-electron* calculations based on DFT and TDDFT. In addition, we also estimate the vdW coefficients between the CNS and different gas molecules, specifically the environmentally important ones, in order to explore the potential of the adsorption of these gases by the carbon based nanostructures.

6.1 Results and Discussions

We perform the optimization of geometric structures of the CNSs using DFT based geometry optimization procedure as implemented in ADF package[205]. For these calculations, we use Slater type Orbital (STO) basis set with triple-zeta with two added polarization functions (TZ2P basis set as in ADF package) and Perdew-Burke-Ernzerhof XC potential[195]. Our results for the optimized geometric structures of some of the typical CNSs considered in the present study are given in Figure 6.1. We terminate both the ends of the finite-length CNTs with hydrogen atoms in order to avoid the dangling bonds. The results for the optimized geometries of cages obtained in the present work match well with the previous results available in the literature[327–331]. The geometric structures for the carbon cages with 20 and 60 atoms are similar to the corresponding structures available in Ref[327–330]. The cage with 80 atoms corresponds to a structure which is very close to the minimum energy structure found by Sun et. al.[331].

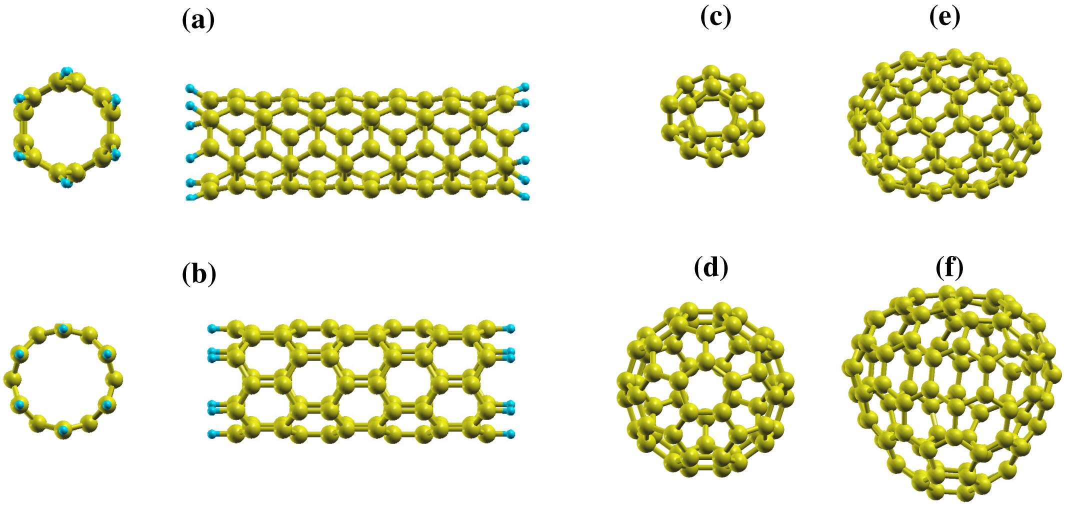

Figure 6.1: Optimized geometric structures of some of the carbon nanostructures. (a) Finite-length CNT(3,3), (b) finite-length CNT(6,0), (c) cage C_{20}, (d) cage C_{60}, (e) cage C_{80}, and (f) cage C_{100}. Finite-length CNTs are terminated with hydrogen atoms at both the ends. Yellow and blue colors depict carbon and hydrogen atoms respectively.

6.1.1 Polarizability of the Carbon Nanostructures

In this sub-section, we discuss the results for the static dipole polarizability of the CNSs. For the calculations of the static and frequency dependent polarizabilities, we use *ab initio* TDDFT based method which is implemented in the RESPONSE module of ADF package[205]. Detailed description of the method adopted in ADF package for obtaining frequency dependent polarizabilities is available in Ref.[218]. We have used TZ2P basis set for the response property calculation of CNSs. In case of small molecules, we have chosen even tempered basis set (ET-QZ3P-2DIFFUSE) with two sets of diffuse functions[205]. As mentioned in Chapter 2, a TDDFT based response property calculation requires approximating the XC functional at two different levels. The first one is the static XC potential needed to calculate the ground-state KS orbitals and their energies. The second approximation is needed to represent the XC kernel $f_{XC}(\mathbf{r}, \mathbf{r}', \omega)$ which determines the XC contribution to the screening of an applied field. For the XC kernel, we use reasonably accurate adiabatic local density approximation (ALDA)[332]. On the other hand, for calculating ground state orbitals and their energies, we use the orbital dependent model potential namely, statistical average of orbital potential (SAOP)[219, 220], which has cor-

Table 6.1: Static polarizability values for carbon cages (in a.u.) obtained using SAOP / ALDA XC potential / kernel. The values are compared to the theoretical data from Ref. [334]. The experimental value is given in the parenthesis.

Fullerene	Present	Ref. [334]	Deviation from Ref.[334]
C_{20}	182.9	-	-
C_{60}	545.6	581.6 (516±54)	≈ 6 %
C_{80}	777.6	811.68	≈ 4 %
C_{90}	956.1	932.47	≈ 3 %
C_{100}	1081.6	1073.2	≈ 1 %

rect behavior both in the asymptotic region and close to the nucleus. This XC potential is chosen since it is well known that the correct behavior of the XC potential, specifically in the asymptotic regime, plays a crucial role in the accurate determination of the response properties[218, 333].

Our results for the polarizability of cages are summarized in Table 6.1. In order to establish the accuracy of our results obtained with the above mentioned choice of the basis set and XC potential, we compare our results for the polarizability with already existing data from the literature[334]. In Ref.[334], the authors report the results obtained by using various basis sets and XC potentials; we compare our data with their results using SAOP XC potential, and the largest basis set used by them, namely, TZP+. We observe that the agreement between the results from the Ref. [334] and the present calculation is quite good. Results from Table 6.1 clearly indicate that the maximum deviation being 6% in the case of C_{60} cage and the deviation keeps decreasing with the increasing size of the cage; the minimum being about 1% for C_{100}. Furthermore, we note that the polarizability value of 545.6 a.u. for C_{60} obtained from our calculation matches well with the experimental value of 515±54 a.u. This establishes the validity of our choice of the XC potential and the basis set.

Next, we discuss our results for the polarizability of CNTs with the chiralities (n,n) and (m,0); where n starts at 2 and ends at 5, and m ranges from 4 to 10. In Figure 6.2 (a), we plot the average static polarizability of CNTs as a function of the length of the nanotubes. We observe from this figure that the CNT(2,2), having the least diameter of 2.81 Å, has the smallest values of polarizability throughout the range of length of

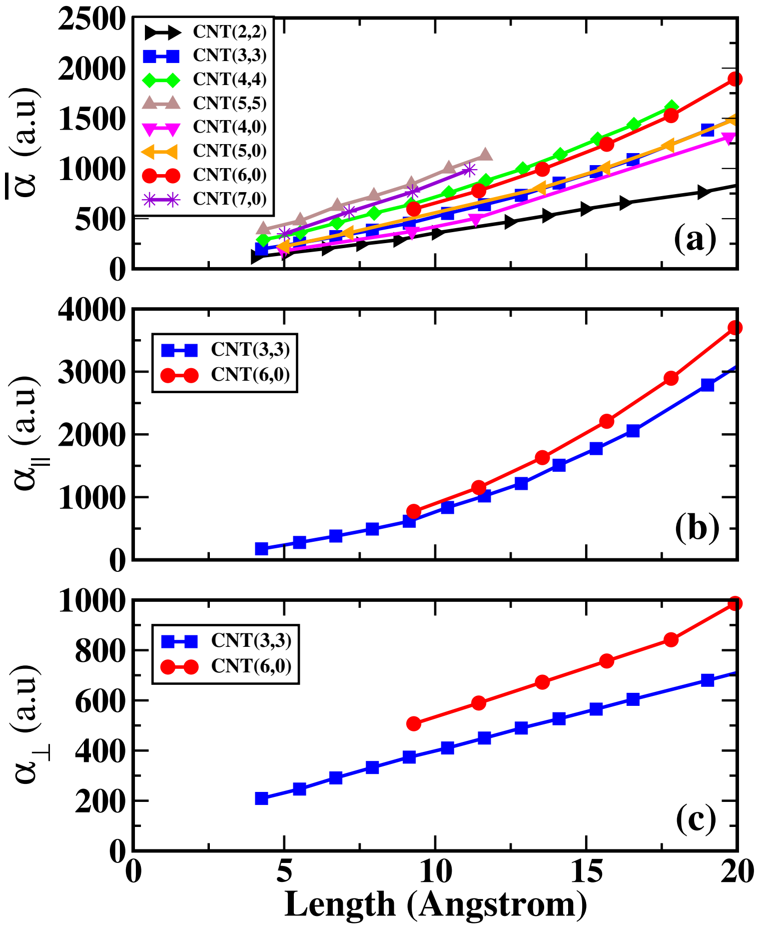

Figure 6.2: (a) Variation of average static polarizability, for the CNTs with different chiralities, as a function of length. (b) The parallel and (c) perpendicular components of the static polarizability are plotted as a function of length for CNT(3,3) and CNT(6,0).

about 4 to 20 Å. CNT(4,0), having diameter of 3.32 Å, has the next largest value of polarizability. We would like to mention here that the armchair CNT(n,n) has smaller diameter as compared to the zigzag CNT($2n$,0). It is observed from Figure 6.2 (a) that the values of polarizability for CNT($2n$,0) are higher than those of CNT(n,n) though both the CNTs have same number of carbon and hydrogen atoms. The reason for this is as follows : the geometries of the zigzag CNT($2n$,0) and armchair CNT(n,n) (see Figure 6.1) are such that the zigzag tubes have more number of bonds along the tube axis as compared to that of the armchair tubes. Thus, a zigzag tube is more polarizable along the tube axis which leads to larger average polarizability. Moreover, a trend of increasing polarizability values with the increase of diameter is very clearly observed from Figure 6.2 (a). For the larger tubes, of (n,0), with n = 8 to 10, we do not display the results in the figure due to limited number of data points. However, the overall trend of the increase

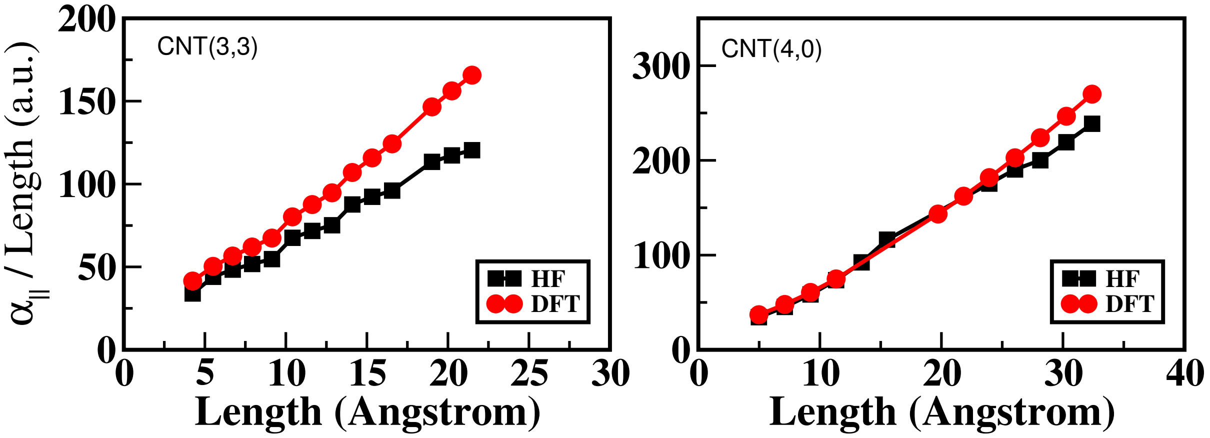

Figure 6.3: The parallel components of the static polarizability per length obtained from HF and DFT methods are plotted as a function of length for CNT(3,3) and CNT(4,0).

in the static polarizability values with the diameter of the CNTs over the entire range of length (4 to 20 Å), is maintained for these tubes as well. From Figure 6.2(a), it is also observed that for all the CNTs, the values of polarizability increase quadratically with increasing length. We show in Figure 6.2(b) and 6.2(c), the parallel or longitudinal and the perpendicular or transverse component of polarizability, respectively, for both CNT(3,3) and CNT(6,0), as a function of the length of the CNTs. It is seen from Figure 6.2(b) that the parallel component of the polarizability increases quadratically with increasing length, while the perpendicular component of polarizability always increases linearly with increasing length (Figure 6.2(c)). This observation agrees very well with results from the literature[335, 336] : Ma et. al. reported a similar trend on the polarizability versus length from their calculations of size-dependent polarizabilities of finite-length SWCNTs of longer lengths (up to 13.5 nm) and the diameters of some of these tubes are comparable with the ones studied here (CNT(4,4) to CNT(6,6) and CNT(8,0) to CNT(10,0))[335].

Before proceeding further, we wish to point out that many authors have observed that conventional XC functionals such as LDA and GGA overestimate the values of (Hyper)polarizabilities for π-conjugated long-chain systems[337–339]. The reason for the overestimation is due to the fact that these XC functionals possess incorrect description of electric field dependence of the response part of the functionals[339]. Since HF method takes the effect of exchange exactly, it does not have the above mentioned shortcoming. Therefore, to assess the role of the non-local field-counteracting potential in the presence of an external electric field, we have carried out calculations of polarizability for two different tubes, namely, the zigzag CNT(4,0) and armchair CNT(3,3), as a function of length, by employing the Hartree-Fock (HF) method (using the package GAMESS[340]). It is to be noted here that the lengths of all finite CNTs considered in the present work are less than or about 20 Å. In this length regime ($\leq$ 20 Å), we find from the HF results, that the trend in variation of parallel component of polarizability with the length of CNT is the same as that obtained by the DFT with SAOP XC functional. The HF and DFT (SAOP) results on CNT(3,3) and CNT(4,0) are displayed in Figure 6.3. It is observed that the parallel component of polarizability (polarizability per length) increases quadratically (linearly) with the length of the tube up to about 20 Å. Thus within this length regime the effect of non-local field-counteracting potential in the presence of external electric field is presumably negligible. However, the values of polarizability obtained by DFT (SAOP) are slightly higher than the corresponding HF data (Figure 6.3). We observe that when we go close to and beyond the length regime of 20 Å, the results for polarizability obtained from both the methods start showing differences.

We know that the values of polarizability depend on the size, symmetry and atomic constituents of a system. Here, we study two different shapes like nearly-spherical (fullerenes/cages) and tubular (nanotubes) structures. We observe that nanotubes are more polarizable than the fullerenes having similar number of atoms. This can be attributed to the geometry of CNT, which can be easily polarized along the tube direction (see the magnitudes in Figure 6.2 (b) and 6.2 (c), parallel component is having higher value). Therefore, these quasi-one-dimensional structures have large anisotropy in polarizability. This large anisotropy can play an important role in electric field aligned growth of carbon nanotubes. The oriented growth of nanotubes are important for nanoelectronics. It has been shown by Ural et. al.[341] that aligned SWCNTs can be grown onto the surfaces of SiO_2/Si substrates in strong electric fields. This is supported by our results on polarizability which shows different length scaling for polarizability along parallel and perpendicular directions to the tube axis. Hence, anisotropy in polarizability will increase as length of the nanotube increases, which in turn gives more torque on off-aligned nanotubes as they grow in electric field.

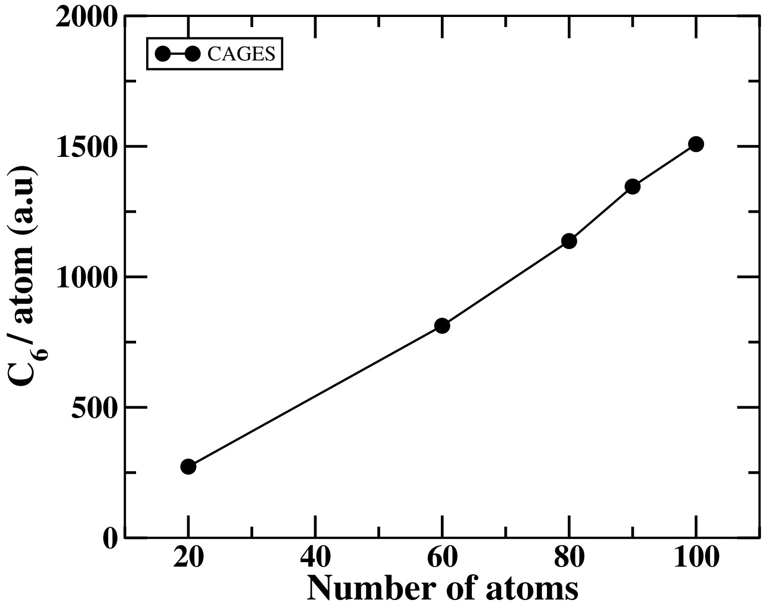

Figure 6.4: Variation of the vdW interaction coefficient (C_6) per atom as a function of the number of atoms in the cages. In this plot, we include the results for the carbon based fullerenes, C_{20}, C_{60}, C_{80}, C_{90} and C_{100}.

6.1.2 van der Waals Coefficient of the Carbon Nanostructures

Having studied the polarizabilities of the carbon cages and the CNTs as a function of length and diameter, we now present our results for the C_6 coefficients between these CNSs (which is obtained by using equation (2.62)). The variation of the vdW coefficient (C_6) per atom as a function of number of atoms in the carbon cage is plotted in Figure 6.4. For the cages, we choose the independent variable as the number of atoms instead of diameter since, unlike cage C_{60}, some of the cages are not spherical in shape. Similar to the results for polarizability, we observe that the values of C_6 also strongly depend on the size and shape of the nanostructures. It is to be noted that the strength of vdW interaction is determined by the polarizability of the systems involved. The polarizability of a system is determined by the number of easily polarizable or loosely bound electrons, the volume over which they are spread and the extent of perturbation of the electron cloud possible. In case of carbon systems, the loosely bound π-electrons play an important role in the polarizability. Bigger the carbon cage the larger is the number of π-electrons and the volume over which these electrons are spread. In case of CNTs, we plot the variation of the vdW coefficient (C_6) per atom as a function of length of the CNTs in Figure 6.5 (a). We observe that the C_6 values per atom, like polarizability, increase with the length

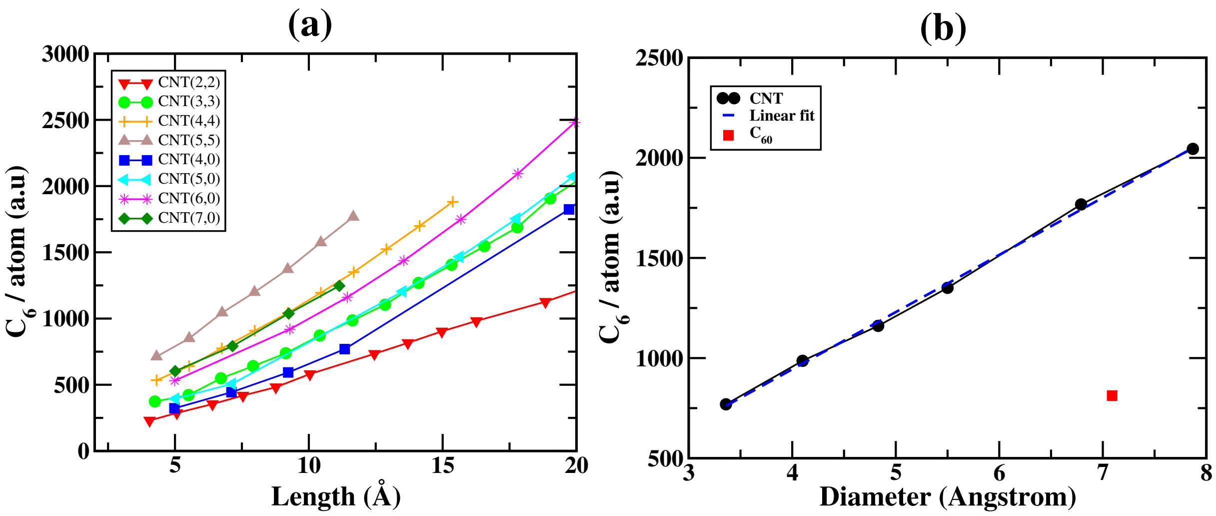

Figure 6.5: Variation of the vdW interaction coefficient (C_6) per atom as a function of (a) length and (b) diameter of CNTs. In case of (b), the length of the CNTs is fixed (about 11.5 Å).

of the tubes in a non-linear fashion. Moreover, when we look at the diameter dependence of the vdW coefficient, a clear trend is noted. CNT(2,2) having the least diameter has the smallest coefficient throughout the length range of about 4 to 20 Å, as observed in Figure 6.5 (a). The CNT(4,0) has the second largest C_6 coefficient. Like the polarizability values, the trend of increasing C_6 values with the increase of diameter is very clearly observed from Figure 6.5 (a). The CNT(10,0) and also CNT(5,5), the two among the largest diameter tubes considered in this work, have large coefficients. This observation of the large increase of the vdW coefficient with the diameter corroborates with the established trend[317, 318, 325]. Furthermore, to assess the dependence of C_6 on the diameter of the CNTs, in Figure 6.5 (b), we plot the values of C_6 per atom as a function of the diameter of the CNTs for a fixed length. In this case, the length of the CNTs has been fixed at about 11.5 Å. The values of C_6 per atom of the CNTs with increasing diameter, in the order of CNT(4,0), CNT(3,3), CNT(6,0), CNT(4,4), CNT(5,5) and CNT(10,0), have been plotted in this figure. We observe that the vdW coefficients increase linearly with the diameter, with a correlation coefficient of 0.999. The number of atoms per CNT with increasing diameter increases leading to larger polarizability and in turn giving rise to larger values of vdW coefficient. For the sake of comparison, we plot the C_6 per atom of C_{60} (with a diameter of 7.09 Å) in the same figure. We note that a large difference in the value of C_6 for C_{60} is observed in comparison with the CNTs.

In order to make a quantitative estimation of difference in values of C_6 and polarizability for CNTs and cages, we have calculated the standard deviation and the mean values of these quantities. For this purpose, we analyze the results of C_6 and polarizability for different CNTs and cages having 60 as well as 80 carbon atoms. We find that the ratio between the values of standard deviation and the mean for C_6 and polarizability values of CNTs with 60 carbon atoms are about 0.038 and 0.043, respectively. On the other hand, for CNTs with 80 carbon atoms, the same ratios are about 4 times more. For this case, these ratios are 0.163 and 0.204, respectively, for C_6 and polarizability. Therefore, CNTs with different chirality and higher total number of atoms have C_6 values which deviate more from each other, compared to the ones containing less number of atoms. As we can see that the cage structures are less polarizable and hence their interaction strengths are consistently lower than those of CNT. We observe that the cages with 60 and 80 atoms are having C_6 and polarizability values which are about 40 - 50 % lower as compared to the corresponding mean values for CNTs with similar number of atoms.

6.1.3 Polarizability and C_6 Coefficient of Gases

In Table 6.2, we give the values of dipole moment, the static polarizability, anisotropy of the static polarizability and the vdW coefficient for the gas molecules considered in this work. We also compare our calculated polarizability values of these molecules, with available experimental data as well as values calculated from Ref.[342, 343] to establish the accuracy of our results. We observe a very good agreement between our results and those available in the literature with the deviations of the order of 0.1 to 3 %. It is observed from Table 6.2 that all the C_6 results available in the literature are overestimated compared to our calculations. We estimate the differences between these results and the corresponding data obtained from our calculations : the maximum deviation being 17 % for the low molecular weight rare gases, He and Ne. However, for high molecular weight rare gases, Ar and Kr, the deviation is small (up to 2.7 %). While for H_2 and H_2O, the deviation is about 10 %, for all the molecules with higher molecular weight the maximum deviation is only about 5 %.

Table 6.2: Dipole moment, static polarizability ($\bar{\alpha}$), anisotropy of the $\bar{\alpha}$ and the C_6 coefficient values for several molecules, obtained using SAOP/ALDA XC potential. [The values for polarizabilities given in parentheses refer to the experimental and theoretical results[342, 343]; the values for C_6 given in parentheses are from theoretical results[343]]

Molecule	Molecular Weight (a.u.)	Dipole Moment (Debye)	polarizability (a.u.)	anisotropy (a.u.)	C_6 (a.u.)
H_2	2.0156	0.0	5.6929 (5.43)	2.0285	12.9249 (14.3)
He	4.0026	0.0	1.4189	0.0	1.503 (1.82)
CH_4	16.0312	0.0	17.61 (17.27)	0.0	132.493
H_2O	18.0105	1.803	9.6167 (9.64)	0.9941	45.2996 (50.1)
Ne	19.9924	0.0	2.5717	0.0	5.9935 (7.26)
CO	27.9949	0.1668	13.088 (13.08)	3.45	79.747 (83.8)
N_2	28.0062	0.0	11.872 (11.74)	4.844	74.0914 (77.2)
F_2	37.9968	0.0	8.124 (8.38)	5.8314	43.135
Ar	39.9624	0.0	11.555	0.0	68.0317 (69.9)
CO_2	43.9898	0.0	17.05 (17.51)	13.009	152.9964 (161.0)
N_2O	44.0011	0.1084	19.26 (19.77)	18.536	180.1426 (186.0)
O_3	47.9847	0.573	18.179	17.337	157.381
SO_2	63.9619	1.652	25.637 (25.61)	13.068	294.6244
Cl_2	69.9378	0.0	31.84 (30.35)	17.273	413.6942
Kr	83.9115	0.0	17.277	0.0	133.2492 (135.0)
CF_4	87.9936	0.0	19.020	0.0	251.4489
CCl_4	151.8756	0.0	73.717	0.0	2154.6822

6.1.4 C_6 Coefficient between Carbon Nanostructures and Gases

In this sub-section, we discuss the results of the vdW interaction coefficient between CNS and various gas molecules such as hydrogen (H_2), Nitrogen (N_2), carbon dioxide (CO_2), carbon monoxide (CO), sulfur dioxide (SO_2), nitrous oxide (N_2O), methane (CH_4), ozone (O_3), water vapor (H_2O), fluorine (F_2), chlorine (Cl_2), carbon tetra fluoride (CF_4), and carbon tetra chloride (CCl_4). We also study the interaction of four rare gas atoms, namely He, Ne, Ar and Kr with the CNS. In Figures 6.6 (a) and (b), we present our results of the vdW interaction coefficient of the above mentioned systems with the CNSs containing about 60 and 100 carbon atoms, respectively. Since for all the nanotubes the trend is the same, we only show the results for some of the typical nanotubes. In Figure 6.6 (a) we show the data for tubes with chiralities (2,2), (3,3), (6,0), (4,4) and (5,5) as well as C_{60}. The results for tubes with chiralities (3,3), (4,4) and (10,0) as well as C_{100} are shown in Figure 6.6 (b).

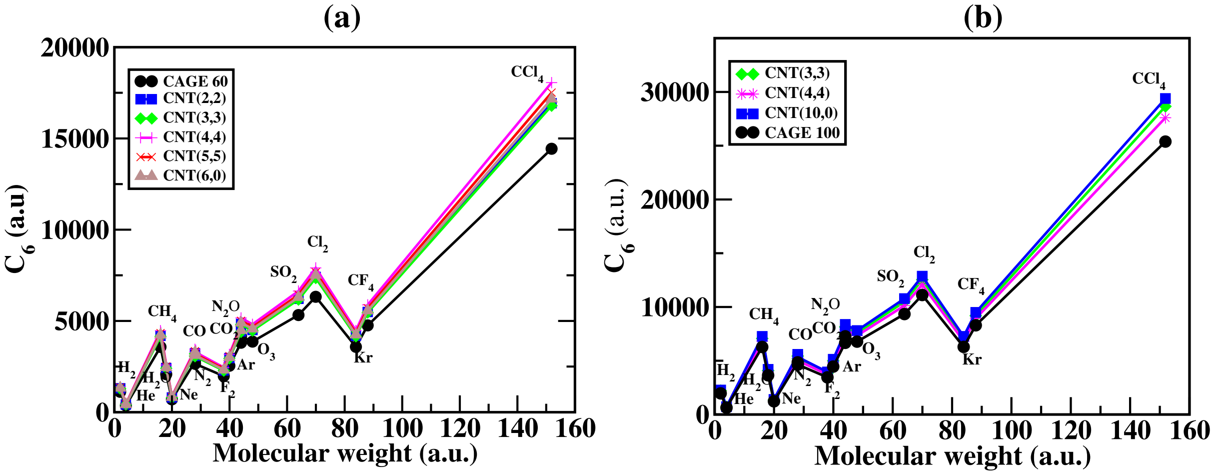

Figure 6.6: The vdW interaction coefficient of the small molecules with the carbon nanostructures containing about (a) 60 and (b) 100 carbon atoms.

We start with a discussion on the results for the vdW interaction of rare gases with the CNS. It is observed from Figure 6.6 that the values of interaction coefficient for the rare gases with the CNS are small. It is well known that due to the shell filling the rare gases are non-polar, chemically very inert and have low polarizability. Thus, they interact weakly with the CNS. However, the C_6 coefficients between inert gas atoms and CNS increase with the size of the atom of these gases. This is due to the fact that as we go from He to Kr, the rare gas atoms become more polarizable since the distance of valence electrons from the nucleus increases. So the magnitude of the dispersion forces increases with increasing system size since the dispersion coefficient is dependent on the polarizability of the system.

Next we proceed to compare the C_6 coefficients between the nanostructures and all other small molecules including H_2 and primarily the environmentally important gases, as listed above. First of all, it is observed that the C_6 coefficients of the carbon cages with all the molecules are consistently smaller than those of the nanotubes. This is due to fact that the nanotubes are more polarizable compared to the cages. It is interesting to see from Figures 6.6 (a) and (b), that for H_2, the C_6 values are much larger compared to those of He even though He and H_2 have the same number of electrons. These reasonably high values of C_6 between the H_2 and the CNS, including cages, expectedly, lead to the easy adsorption of H_2 on these types of nanostructures with high surface-to-volume ratio. This observation is in conformity with the numerous studies on CNT and fullerene derived systems as possible hydrogen storage materials.

Furthermore, Figures 6.6 (a) and (b) show that the hazardous gases such as methane, nitrous oxide, carbon dioxide, carbon tetrachloride, carbon tetrafluoride, and sulfur dioxide interact strongly with the CNS compared to rare gases or other molecules. Carbon tetrachloride (which is an ozone-depleting and a greenhouse gas) and chlorine molecule show very high C_6 values with themselves as well as with the CNS. These two molecules are also having higher values of static dipole polarizability and interact strongly with themselves. This is due to the presence of seven electrons in the valence state for the chlorine atom. Here we would like to mention in support of our result of reasonably high value of C_6 for various gases that Cinke et. al.[300] obtained and they observed that SWCNTs adsorb nearly twice the volume of CO_2 compared to activated carbon; Kowalczyk et. al.[344] showed that the carbon nanotubes are better adsorbents of CF_4 than currently used activated carbons and zeolites.

Next we proceed to compare the data of some pair of molecules. Due to the difference in the electron distribution, the pair N_2O and CO_2 have slightly different C_6 values (N_2O has a 17.7 % higher C_6 value compared to CO_2), as seen from Table 6.2, though these two molecules have very similar molecular weights and same total number of electrons. This difference in the values of C_6 for CO_2-CO_2 and N_2O-N_2O interaction is also reflected in the results for C_6 between these molecules and the CNS. These data are elucidated in Figures 6.6 (a) and (b). It is worth mentioning here that the ozone molecule with comparable molecular weight and the number of electrons with CO_2 and N_2O (see Table 6.2), has C_6 values with the nanostructures which are in between those of CO_2 and N_2O. Next we consider CH_4 and H_2O which have similar molecular weights and same number of electrons (10 each). Though water has a larger permanent electric dipole moment compared to methane, which has none (see Table 6.2), the average electron cloud is more rigid in water than in methane as is reflected by the smaller value of polarizability of water molecule versus methane; this in turn leads to a comparatively larger C_6 value for CH_4 when compared to H_2O. Since the C_6 value between two methane molecules is much higher compared to water (Table 6.2), we observe that the C_6 values between methane and the CNS are also significantly higher compared to those between H_2O molecule and the nanostructures. Finally we consider another pair of molecules, namely, the chlorine molecule and sulfur dioxide, which have comparable number of electrons, 34 and 32, respectively. It can be seen from Figures 6.6 (a) and (b), that the values of C_6 coefficient with CNS of the former is much larger. This may be attributed to the difference in the molecular geometry : While Cl_2 is a linear molecule and more polarizable, SO_2 has a structure of isosceles triangle with an O-S-O angle of about 119°.

6.2 Summary

In this chapter, we employ all-electron *ab initio* TDDFT based method to calculate the static dipole polarizability and the vdW interaction coefficient, C_6, between different finite carbon cages and finite-length carbon nanotubes with different size and chirality, containing maximum about 100 atoms. We also calculate the vdW coefficient between these carbon nanostructures and small gas molecules, including the environmentally important ones. From our calculations, we find that the average static polarizability increases with the length of CNT in a non-linear fashion. These quasi-one-dimensional structures also have large anisotropy in polarizability due to the different scaling of components of polarizability with the length. The large anisotropy in polarizability of the CNTs plays an important role in electric field aligned growth of CNTs. Our results also show that the C_6 values increase linearly and quadratically with the diameter and length of the CNTs, respectively. We also observe that the CNTs are more polarizable than the carbon cages due to the easy polarization along the axis of the former; hence the CNTs, with similar number of atoms, interact strongly with themselves as compared to the cages. For nanostructures with 60 and 80 carbon atoms, it is found that the C_6 and polarizability are about 40 - 50 % lower in the cages compared to the tubes. The nonlinear increase of the C_6 values of the CNSs with length implies a much stronger vdW interaction between the longer CNSs compared to the shorter ones. This result can be useful in understanding the formation of superstructures made up of CNSs.

From our calculations of the vdW coefficients between the small molecules and the carbon nanostructures, it is observed that the C_6 values of H_2 are much larger compared to those of He. These reasonably high values of C_6 between the H_2 and the CNS corroborate with the observations of adsorption of significant quantities of H_2 on these nanostructures. We also found that the interaction coefficients of environmentally hazardous gases with CNSs are quite high as compared to those of rare gases. Our estimation of the vdW coefficients between the CNS and these gases can be useful in providing the microscopic understanding in the studies of adsorption, specifically physisorption, of these gases on CNSs.

Publication based on this chapter

The van der Waals Coefficients Between Carbon Nanostructures And Small Molecules: A Time-Dependent Density Functional Theory Study
C. Kamal, Tapan K. Ghanty, Arup Banerjee, and Aparna Chakrabarti
*Journal of Chemical Physics, **131**, 164708 (2009)*

Chapter 7

Physical Properties of Gallium Phosphide Clusters

In the last two chapters, we have presented our results for quasi-one-dimensional carbon and gallium phosphide nanotubes. Now, in this chapter, we study the static dipole polarizability of stoichiometric gallium phosphide clusters (Ga_nP_n with $n = 2 - 5$) by employing various *ab initio* wave function based methods as well as DFT / TDDFT. We use the following *ab initio* wave function based methods, namely, Hartree-Fock (HF), second order Møller-Plesset perturbation theory (MP2) and coupled cluster theory with single and double with perturbative triple excitations (CCSD(T)) for the calculations of polarizability.

The study of semiconductor clusters has been an active area of research over last two decades because of their novel properties and due to the technological importance of semiconductor materials in electronic industries employed in fabrication of small and fast microelectronic devices. Several theoretical and experimental studies on both homogeneous (Si_n, Ge_n, etc.) and heterogeneous (Ga_mAs_n, Ga_mP_n, Ga_mN_n and Al_mP_n, etc.) semiconductor clusters exist in the literature [80–100]. GaP is one of the important III-V semiconductor materials with an indirect band gap of 2.26 eV[345] and it has been widely used in the manufacture of low-cost light-emitting diodes with low to medium brightness. There exist many studies on nanoclusters of this material. But, most of these works are devoted to the study of geometrical structures, their stabilities and electronic properties by employing various methods of calculating electronic structures. The study on polarizability of stoichiometric GaP clusters are scarce in the literature. However, it is well known that the optical response properties, specifically, the polarizability of materials govern many physical and chemical phenomena. To the best of our knowledge, there exists only one study devoted to the calculation of polarizability of GaP clusters consisting of $GaX_4H_{12}^{3+}$, $XGa_4H_{12}^{3-}$, $H_{3-}GaXH_3$, $Ga_4X_4H_{18}$ and $Ga_3X_3H_{12}$ clusters (with X = N, P and As) [100]. In Ref [100] the calculation of polarizability has been performed by employing time-dependent Hartree-Fock method and structure of all the above mentioned clusters possessing tetrahedral geometries and the outer atoms were terminated by hydrogen atoms which are relevant to crystalline state and thin films.

On the other hand, several studies involving ground state properties like geometric structures, harmonic vibration frequencies and various other properties of GaP clusters have been carried out and reported in the literature[101–113]. For example, Costales et al. have investigated the structural and vibrational properties of stoichiometric Ga_nP_n clusters with n = 1 - 3 in the framework of DFT[101]. A similar study has been performed by Guo et al. on Ga_xP_y clusters with $(x + y = 8)$ using B3LYP XC functional and 6-31 +G(d) basis set. Subsequently, they also calculated photoelectron spectra of neutral and anionic Ga_nP_n clusters with $n = 7 - 9$ within DFT using B3LYP and B3PW91 XC functionals[102, 103]. Li et al. investigated the geometric structure, electronic state and vibrational frequencies of Ga_nP and Ga_nP_2 clusters with $n = 1 - 7$ by using B3LYP XC functional and 6-31 +G(d) basis set[104]. The study on structure, stability and melting point of Ga_nP_n clusters with $n = 2 - 5$ was carried out by Andreoni et al. using *ab initio* molecular dynamics (Car-Parrinello) method[105]. Balasubramanian et al. employed complete active space multi configuration self consistent field and multi-reference single plus double configuration interaction to theoretically study the electronic states of low lying levels of many GaP clusters[106–109]. The spontaneous formation of GaP fullerenes was proposed by Tozzini et al. by using *ab initio* molecular dynamics method[110]. In addition, Archibong et al. studied vertical detachment energy (VDE), adiabatic electron detachment energy (AEDE) and vibrational frequencies of GaP clusters using CCSD(T) and DFT / B3LYP methods[111, 112]. The geometric structures and band gaps of GaP clusters included in Sodalite cages have also been calculated by employing *ab initio* molecular dynamics (Car-Parrinello) method in Ref[113].

In the context of experimental studies on GaP clusters, we note that Neumark and coworkers studied the photodetachment spectra of neutral IV and III-V clusters [115–120].

These studies are important in characterizing the low lying states of these clusters. They also studied photoelectron spectra of $Ga_xP_y^-$ clusters at a photodetachment wavelength (266nm/4.657 eV) and electron affinity and VDE of some neutral clusters. Micic et al. studied optical absorption spectra of passivated nanocrystal in 20-30 $\mathring{A}$ size regime of GaP[346]. Infra-red (IR) absorption spectra of GaP, Ga_2P and GaP_2 clusters trapped in 4K argon matrix have been measured by Weltner et al.[121]. Huang et al. measured the mass spectra of GaP anion clusters produced by laser ablation[347].

In general, it is well known that the results obtained by *ab initio* wave function based methods such as Møller-Plesset perturbation theory and coupled cluster theory are quite accurate. But, these methods are computationally significantly intensive and feasible only for smaller systems. Thus, for bigger systems, the better methods of choice would be the ones based on DFT / TDDFT as these methods are known to yield accurate results for the polarizability of many-electron systems. However, the success of DFT / TDDFT based methods in determining polarizability crucially depends on the nature of approximations used for the exchange-correlation (XC) functionals. Thus, in the present study, we investigate the performance of different XC functionals used in DFT / TDDFT method in determining static dipole polarizability of Ga_nP_n clusters. For this purpose, we carry out the calculations of polarizability, within DFT / TDDFT, by employing various XC functionals, ranging from simple local density approximation (LDA) to asymptotically correct model potential - statistical average of orbital potential (SAOP). Besides assessing the effect of XC functionals on the polarizability we also study of evolution of the polarizability with the size of the clusters.

7.1 Geometric Structure

We perform the optimization of all Ga_nP_n clusters using DFT based geometry optimization procedure as given in ADF package [205]. We employ TZ2P basis set along with Becke-Perdew (BP86) XC potential [191, 192]. The initial structures of Ga_nP_n clusters are similar to those of Ga_nAs_n clusters which have been reported by Karamanis et al. [348]. The optimized structures of Ga_nP_n clusters with different symmetries are shown in Figure 7.1. In Table 7.1, we summarize the interatomic distances between Ga-Ga, P-P

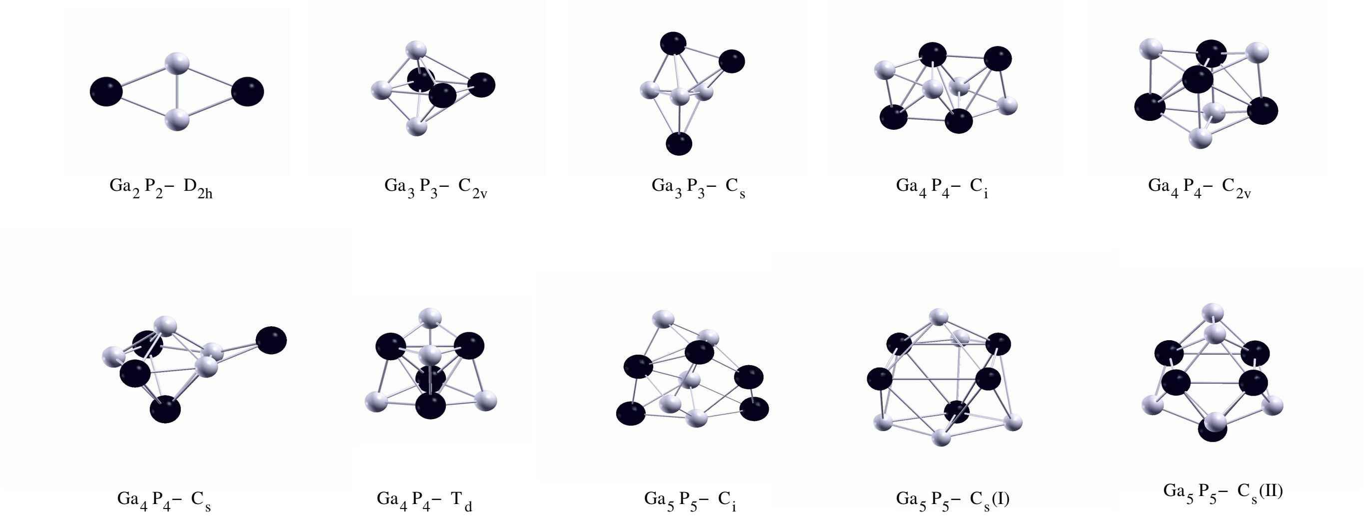

$Ga_2P_2- D_{2h}$ $Ga_3P_3- C_{2v}$ $Ga_3P_3- C_s$ $Ga_4P_4- C_i$ $Ga_4P_4- C_{2v}$

$Ga_4P_4- C_s$ $Ga_4P_4- T_d$ $Ga_5P_5- C_i$ $Ga_5P_5- C_s$(I) $Ga_5P_5- C_s$(II)

Figure 7.1: Optimized geometries of stoichiometric gallium phosphide (Ga_nP_n) clusters with $n = 2 - 5$. The black (grey) circles are the Ga (P) atoms.

and Ga-P atoms in Ga_nP_n clusters. For tetramer (Ga_2P_2), the equilibrium structure is planar rhombus with D_{2h} symmetry, which matches well with the results already available in the literature [104, 106, 111, 349]. This rhombus structure of Ga_2P_2 has been isolated experimentally as part of a large complex by Cowley and coworker in 1989 [350]. It is interesting to note that most of the tetramers, for example C_4, Si_4, Ga_2As_2, Na_4 and K_4, show planar rhombus as equilibrium structure. We observe that the optimized structure of GaP clusters retain similar geometry as that of GaAs clusters obtained by Karamanis et al [348].

We can see from the Table 7.1 that the GaP clusters contain different values of interatomic distances for each Ga-P, Ga-Ga and P-P. It is observed that average interatomic distances of Ga-P and Ga-Ga atoms in Ga_nP_n clusters are higher than their corresponding bond lengths of 2.360 Å, and 2.691 Å, in bulk (zinc blende) GaP and bulk (α - Ga) gallium, respectively. The interatomic distances of P-P atoms are closer to their corresponding bond length of 2.220 Å, in bulk (black) phosphorus except for the octamer Ga_4P_4 with C_{2v} symmetry. The higher values of interatomic distances in Ga_nP_n clusters as compared to those from their bulk structures show that the interaction between atoms in the clusters is weaker than that in the bulk structures. The atoms in bulk make as many covalent bonds (consistent with the valence electron) as possible in order to minimize the total energy of the system. But in case of very small clusters as considered here, most of the atoms are on the surface so they cannot form as many bonds as in a bulk. We know that as the number

Table 7.1: The binding energy (E_B in eV), HOMO-LUMO gap (in eV) and interatomic distances (in Å) of Ga$_n$P$_n$ clusters

n -	E_B	HOMO-LUMO	Interatomic distance (Å)		
Symmetry	(eV)	gap (eV)	Ga-Ga	P-P	Ga-P
2 - D_{2h}	-9.62	1.42	-	2.08	2.56
3 - C_s	-16.06	2.25	2.77	2.22	2.45, 2.63, 2.76
3 - C_{2v}	-15.43	1.71	2.63	2.19	2.49, 2.65, 3.11
4 - C_i	-21.21	1.46	2.61, 3.09	2.20	2.32, 2.41, 2.53, 3.03
4 - C_s	-20.82	1.57	2.61, 3.09	2.21, 2.32	2.57, 2.69, 2.77, 2.85
4 - C_{2v}	-20.37	0.98	2.64, 2.98	2.60	2.39, 2.48
4 - T_d	-20.23	0.37	2.79	-	2.42
5 - $C_s(I)$	-27.55	1.69	2.77, 2.84, 2.91, 3.11	2.24	2.36, 2.44, 2.61, 2.71, 2.82
5 - $C_s(II)$	-27.25	1.53	2.78, 2.87, 2.93, 3.20	2.30	2.28, 2.46, 2.56, 2.99
5 - C_i	-26.82	1.27	2.62, 2.78, 2.99	2.17, 2.31	2.36, 2.56, 2.72, 2.82, 2.95

of bonds increases, the binding between the atoms becomes stronger and then they come closer to each other. Thus, the interatomic distances in small clusters are larger than the corresponding bond lengths in bulk. As the size of the clusters increases, the atoms inside the clusters try to make more bonds than those at the surface. Eventually, the larger size of the clusters allows them to form bulk like geometries, with only small deviations at the surface. The lower binding energy of Ga$_n$P$_n$ clusters with respect to its bulk value confirms the weak interaction between the atoms in the clusters.

In order to check the stability of the clusters, we calculate the binding energies and harmonic vibrational frequencies of these clusters. The binding energies of Ga$_n$P$_n$ clusters are calculated by using the expression

$$E_B = E_{Ga_nP_n} - n(E_{Ga} + E_P) \tag{7.1}$$

where $E_{Ga_nP_n}$, E_{Ga} and E_P are the energies of Ga$_n$P$_n$ cluster, Ga and P atom, respectively. The values of binding energy calculated by the above formula are given in Table 7.1. The negative sign signifies that all the clusters studied here are bound systems and the magnitude of binding energy indicates the relative stability between the isomers. To see how the binding energy changes with the size of Ga$_n$P$_n$ clusters, we plot the variation of binding energy per atom with the size (n) in Figure 7.2. It is clear from this plot that as the size increases, the clusters become more bound. Note that the magnitude of cohesive energy per atom of bulk GaP is 7.02 eV/atom[351], which is much higher than the binding

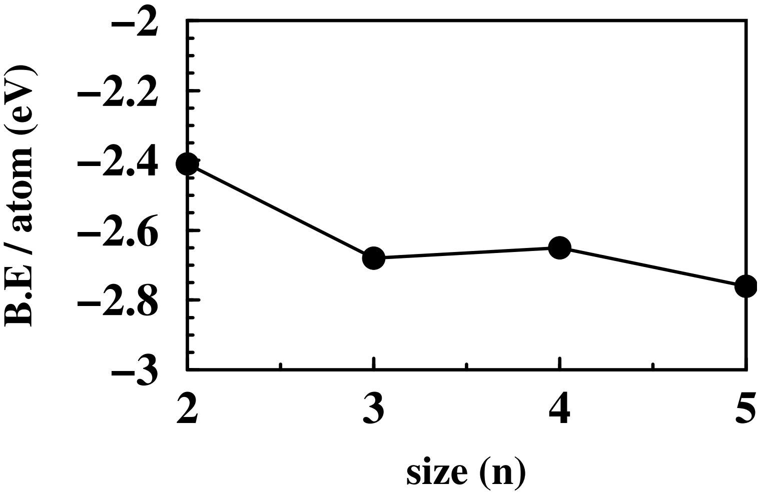

Figure 7.2: Plot of binding energy per atom as a function of size for the most stable isomers.

energy of all these clusters. This also supports the argument presented above about the interatomic distances in cluster. We observe that the most stable structures for hexamer, octamer and decamer are isomers with C_s, C_i and $C_s(I)$ symmetries, respectively. Similar trend was obtained for $\mathrm{Ga}_n\mathrm{As}_n$ clusters by Karamanis et. al.[348]. This indicates that similar type of bonding exists in both GaP and GaAs clusters. In order to study the effect of basis set superposition error (BSSE) on binding energy, we have calculated BSSE for the most stable isomers of $\mathrm{Ga}_n\mathrm{P}_n$ clusters. We find that the values of BSSE are less than 0.2 % of their corresponding binding energies. Therefore the effect of BSSE is small. This is obvious since we have used one of the largest basis sets in our calculations.

To verify whether the clusters considered in this study are stable or not, we calculate the harmonic vibrational frequencies for all the optimized structures. The absence of imaginary frequencies is used to confirm the stability of a structure. The calculated harmonic vibrational frequencies of $\mathrm{Ga}_n\mathrm{P}_n$ clusters are given in Table 7.2. We observe no imaginary frequencies for any of the optimized structure considered here. Therefore, these optimized structures are stable and possible local-minimum-energy-structures on the potential energy surface. Our results of harmonic vibrational frequencies for $\mathrm{Ga}_n\mathrm{P}_n$ clusters match well with the available results in the literature[101, 104]. For example, we can see from Table 7.2 that our results of harmonic vibrational frequencies for tetramer $\mathrm{Ga}_2\mathrm{P}_2$ with D_{2h} and hexamer $\mathrm{Ga}_3\mathrm{P}_3$ with C_s symmetries match very well with those values obtained by Costales et al. [101] . Furthermore, we also note here that for tetramer

Table 7.2: The harmonic vibrational frequencies (in cm^{-1}) of Ga_nP_n clusters. The values in the parenthesis are obtained by Costales et al. [101]

n	Symmetry	Harmonic vibrational frequency (cm^{-1})
2	D_{2h}	68(67), 123(122), 169(166), 262(253), 276(272), 567(564)
3	C_s	52(51), 70(64), 113(109), 115(111), 157(154), 171(167), 238(230), 247(242), 275(272), 387(385), 400(391), 505(498)
3	C_{2v}	44, 120, 154, 168, 191, 223, 247, 316, 442, 450
4	C_i	64, 84, 113, 141, 187, 209, 267, 283, 336, 340, 442
4	C_s	62, 96, 118, 132, 142, 144, 156, 198, 229, 258, 308, 406, 428
4	C_{2v}	103, 132, 146, 153, 193, 214, 233, 244, 256, 304, 319, 352, 369
4	T_d	145, 233, 333
5	$C_s(I)$	84, 101, 145, 156, 161, 185, 194, 206, 228, 244, 272, 300, 361, 373, 396
5	$C_s(II)$	29, 68, 79, 97, 101, 114, 120, 136, 159, 186, 218, 255, 270, 324, 362, 377, 403
5	C_i	72, 81, 114, 159, 180, 204, 222, 235, 246, 293, 322, 430

Ga_2P_2 the lowest and the most intense frequencies obtained by us (68 and 276 cm^{-1} respectively) are also in close agreement with the ones reported by Li et al. (65.1 and 255.1 cm^{-1} respectively)[104].

It is well known that the chemical stability of molecules/clusters may be characterized by their electronic configurations and energy gap between highest occupied molecular orbital (HOMO) and the lowest unoccupied molecular orbital (LUMO). A system having closed shell electron configuration with a large energy gap is chemically inert and hence more stable. All the Ga_nP_n clusters studied in the present work have closed shell configuration. In Table 7.1, we present the values of HOMO-LUMO gap for all the clusters. We can see from the table that the most stable isomers have large HOMO-LUMO gaps (1.42, 2.25, 1.46 and 1.69 eV for tetramer, hexamer, octamer and decamer respectively) which are comparable with or larger than the value 1.57 eV of stable C_{60} fullerene molecule [67]. These large values of HOMO-LUMO gap suggest that Ga_nP_n clusters are inert and stable. We also observe that the HOMO-LUMO gaps for most stable isomers are higher as compared to other isomers. The stability trend observed by HOMO-LUMO gap is also consistent with those of binding energy results.

Table 7.3: Average static polarizability ($\bar{\alpha}$) of various isomers of $\mathrm{Ga}_n\mathrm{P}_n$ clusters by *ab initio* wavefunction based methods and DFT / TDDFT method with several XC functionals. The values of mean and standard deviation (Std.dev) of polarizability are given in the last two columns. The last row contains root mean square error (E_{rms}) with respect to the MP2 method for all the functionals.

n -	Average static polarizability ($\overline{\alpha}$)											
Symmetry	HF	MP2	B3LYP	BLYP	HLYP	HOP	PBELYP	SAOP	VWN	PBEPBE	Mean	Std.dev
2 - D_{2h}	144.76	147.98	142.80	144.54	139.19	139.22	146.09	139.72	143.64	144.96	142.52	2.78
3 - C_s	199.06	206.22	196.57	198.61	192.20	192.30	199.57	193.38	194.22	198.99	195.73	3.08
3 - C_{2v}	200.02	194.24	189.33	189.67	192.94	193.48	191.32	185.99	186.36	188.11	189.65	2.80
4 - C_i	253.92	255.22	247.76	249.37	246.01	245.93	251.30	246.93	245.38	246.44	247.39	2.02
4 - C_s	274.12	285.58	273.75	277.94	264.88	264.86	280.68	270.58	276.22	278.35	273.41	6.09
4 - C_{2v}	264.88	208.13	240.81	240.97	254.88	256.59	242.85	238.45	236.64	238.45	243.70	7.68
4 - T_d	215.44	231.03	225.94	231.47	209.28	208.38	232.97	231.53	226.00	225.52	223.89	9.74
5 - $C_s(I)$	294.99	318.23	294.40	296.42	286.51	286.35	298.57	293.48	292.23	294.01	292.75	4.35
5 - $C_s(II)$	321.92	290.42	303.60	304.72	310.70	311.83	306.88	302.31	299.91	301.63	305.20	4.29
5 - C_i	325.96	328.72	318.17	320.74	315.87	316.38	323.43	315.44	318.43	320.63	318.64	2.79
E_{rms}	24.11	0.00	15.94	14.93	23.64	24.21	14.87	16.48	15.35	14.74	-	-

7.2 Static Polarizability and Anisotropy

We begin this section with the discussion of results obtained for the average static dipole polarizability ($\overline{\alpha}$) and the anisotropy in polarizability ($\Delta\alpha$) of $\mathrm{Ga}_n\mathrm{P}_n$ clusters which are displayed in Figure 7.1. The results for the average static polarizability calculated by various *ab initio* wave function based methods and DFT / TDDFT method with several XC functionals are summarized in Table 7.3 . It is observed from Table 7.3 that the values of average static polarizability strongly depend on size and symmetry of the clusters.

First we discuss the results obtained by various *ab initio* wave function based methods and then compare them with those calculated by TDDFT based method with several XC functionals. We perform the calculation of polarizability by employing *ab initio* wave function based method such as HF and MP2 for all the optimized structures. We carry out the CCSD(T) calculation of polarizability only for the tetramer. The value of $\overline{\alpha}$ obtained for tetramer $\mathrm{Ga}_2\mathrm{P}_2$ with D_{2h} symmetry by CCSD(T) method is 147.02 a.u whereas $\overline{\alpha}$ calculated by MP2 method is 147.98 a.u. which is about 0.6 % higher than the value obtained from CCSD(T) method. The HF method gives a value of $\overline{\alpha} = 144.76$ a.u which is about 1.6 % less than that calculated by CCSD(T) method. The estimation of polarizability value by MP2 method matches very well with that obtained by CCSD(T) method. Since the results obtained by *ab initio* wave function based methods (such as MP2 and CCSD(T)) are quite accurate and the CCSD(T) result available only for tetramer, we compare all our polarizability results with those obtained by MP2 method. It is observed from Table 7.3 that for the most stable isomers of $\mathrm{Ga}_n\mathrm{P}_n$ clusters studied here, the values of $\overline{\alpha}$ obtained by MP2 method are always higher than those calculated with HF method. But, for some other isomers such as, $\mathrm{Ga}_3\mathrm{P}_3$ with C_{2v}, $\mathrm{Ga}_4\mathrm{P}_4$ with C_{2v} and $\mathrm{Ga}_5\mathrm{P}_5$ with $C_s(II)$ symmetries the HF method overestimates the value of $\overline{\alpha}$ as compared to that obtained by MP2 method. Similar results were obtained by Karamanis et al.[348] for $\mathrm{Ga}_n\mathrm{As}_n$ clusters as well.

Now we analyze the results of polarizability obtained by TDDFT method with several XC functionals which are compiled in Table 7.3. We compare these results with the ones calculated by MP2 method which we use for bench marking our DFT / TDDFT results. Here, we use many XC functionals such as simple LDA (VWN), GGA (PBEPBE, PBELYP, BLYP), hybrid (B3LYP, HLYP, HOP) and SAOP[189, 191, 193–196, 219, 220] in order to study the effect of XC functional on the polarizability of $\mathrm{Ga}_n\mathrm{P}_n$ clusters.

For tetramer $\mathrm{Ga}_2\mathrm{P}_2$ with D_{2h} symmetry, the value of $\overline{\alpha}$ calculated with the PBELYP functional gives better result as compared to that obtained with other XC functionals. We calculate polarizability by using HF exchange with two different correlation functionals such as LYP and OP. The values of $\overline{\alpha}$ obtained by HLYP and HOP are $\overline{\alpha} = 139.19$ and $\overline{\alpha} = 139.22$ a.u respectively for LYP and OP correlation functionals. The calculation with SAOP gives $\overline{\alpha} = 139.72$ a.u which is close to HLYP and HOP values of polarizability. All these values are lower than the LDA and GGA results.

We consider two isomers with C_s and C_{2v} symmetries for hexamer $\mathrm{Ga}_3\mathrm{P}_3$ for our calculation. The isomer with C_s symmetry has more binding energy (by 0.6 eV) than the other isomer. For this isomer, the value of polarizability obtained by PBELYP is ($\overline{\alpha} = 199.57$ a.u) the highest and close to the MP2 result. But for the isomer with C_{2v} symmetry the HLYP and HOP functionals produce data closer to MP2 result. For both the isomers, the SAOP results are much lower than the corresponding MP2 results. The isomer with C_s symmetry is found to be more polarizable than the isomer with C_{2v} symmetry. We note that the order in which the value of $\overline{\alpha}$ varies with different XC functionals is different for the two isomers.

As mentioned in the previous section, the isomer with C_i symmetry gives the higher binding energy for octamer Ga_4P_4 compared to other isomers. The variation of $\overline{\alpha}$ with different XC functionals is similar for the isomers with C_i, C_s and T_d symmetries, in which the lowest and highest value of $\overline{\alpha}$ are produced by the HOP and PBELYP functionals, respectively. For these isomers, the values of polarizability obtained by PBELYP are close to those calculated by MP2 method. For the structure with C_{2v} symmetry, we observe that the HLYP and HOP give higher values of $\overline{\alpha}$ compared to other XC functionals. Out of four isomers considered here the isomer with C_s symmetry is more polarizable than the other isomers. We note here that the value of $\overline{\alpha}$ obtained by MP2 method for the isomer with C_{2v} symmetry is the lowest among all the results.

Out of the three isomers considered for decamer Ga_5P_5, the isomer with $C_s(I)$ symmetry has highest binding energy. For this isomer, the DFT / TDDFT method underestimates the values of polarizability compared to MP2 method. The value of $\overline{\alpha} = 298.57$ a.u. obtained by PBELYP functional is the closest to the MP2 result. However, for the isomer with $C_s(II)$ symmetry, the DFT / TDDFT method overestimates the values of polarizability compared to MP2 method. The isomer with C_i symmetry is more polarizable than the other two isomers.

In Table 7.3 , we have included mean and standard deviation of polarizability values obtained by different XC functionals for each isomer. The standard deviation gives the spread of values of polarizabilities around the mean values. It can be seen from the last column of Table 7.3 that the dispersion is highest for Ga_4P_4 with T_d symmetry and lowest for Ga_4P_4 with C_i symmetry. In order to study the overall performance of the different functionals we also calculate the root mean square error E_{rms} with respect to the MP2 method for all the functionals. This value gives closeness of the polarizability values calculated from different XC functionals with respect to those obtained from MP2 method. The results for E_{rms} are presented in the last row of Table 7.3. We find that the E_{rms} for PBELYP, PBEPBE and BLYP functionals are the smallest.

Furthermore, we note from Table 7.3 that LDA and GGA results for polarizability are closer to the corresponding MP2 values than those obtained by employing model potential - SAOP. It is well known from the sum-over-states (SOS) expression of polarizability that it is related to the oscillator strengths associated with all the excited states and their energies. The linear and non-linear optical properties of III-V semiconductor clusters (GaAs, GaSb, InP, InAs and InSb) have been calculated by employing time-dependent Hartree-Fock formalism along with SOS expression [352]. These calculations have been performed with large number of excited states (of the order of 100) to obtain convergence. In this connection we mention that the correct asymptotic behavior of SAOP is capable of yielding quite accurate results for the low lying excited states [353] , however, for high lying excited states it is not that accurate. This may be one reason for the discrepancy between results for polarizability obtained via TDDFT / SAOP and MP2 methods. On the other hand, the closeness of LDA and GGA results to MP2 data may be attributed to the fact that LDA and GGA XC potentials underestimate the contributions to the polarizability arising from transition to bound Rydberg type states and overestimate those from continuum. The cancellation of errors in these two contributions to the polarizability sometimes yields good results accidentally. Therefore, the closeness of LDA and GGA results with MP2 values in some systems may be fortuitous. However, no such cancellations of errors occur when excited states are obtained with SAOP. We believe that it may be this lack of cancellation together with inaccuracy in predicting high lying excited states by SAOP that leads to results for the polarizability which deviate more from MP2 data than the corresponding LDA and GGA values. It is important to note here that unlike III-V semiconductor clusters, for alkali metal clusters of Na and K, the values of polarizability obtained by employing SAOP are very close to data from both accurate wave function based methods (MP2 and CCSD(T)) and experiments [354, 355]. Moreover, for these systems the SAOP results are also significantly higher than both LDA and GGA values. For these systems, only few low lying excited states contribute to the polarizability as these few states are sufficient to saturate the oscillator strength of excitations. It is exactly these low lying states which are well reproduced by SAOP [356], thus giving very accurate values of polarizability of alkali metals clusters.

Having studied the effect of XC functionals on polarizability, we now focus our attention on evolution of polarizability with the size of the clusters. In Figure 7.3, we plot the variation of static mean polarizability per atom with the size of the clusters which

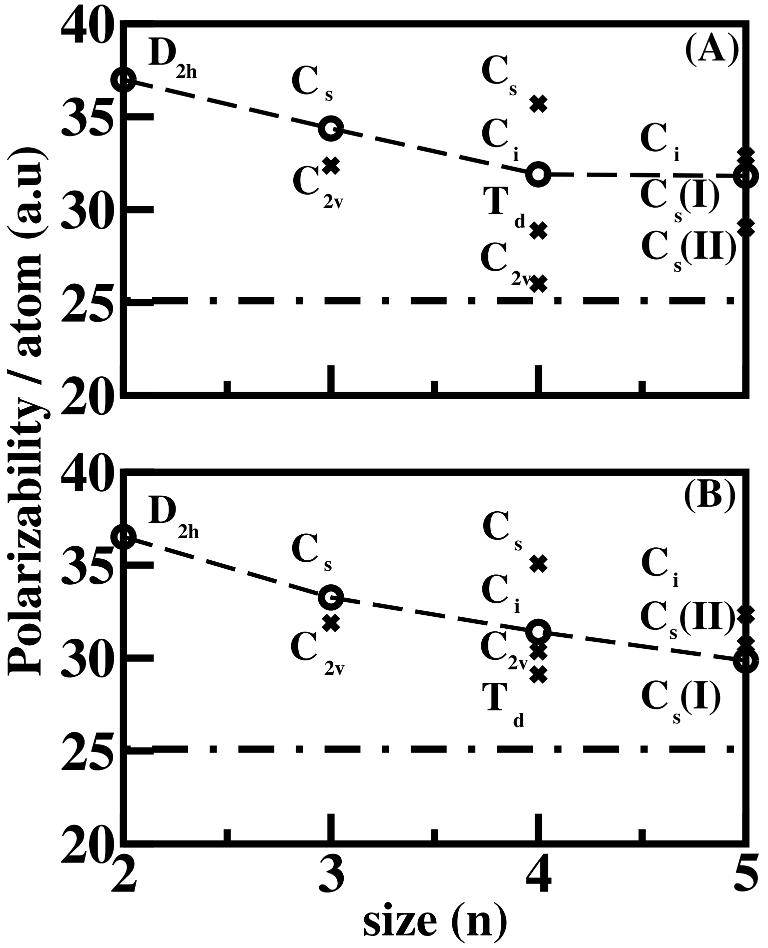

Figure 7.3: Plot of average static polarizability ($\bar{\alpha}$) per atom of stoichiometric gallium phosphide ($\mathrm{Ga}_n\mathrm{P}_n$) clusters obtained by (A) second-order Møller-Plesset perturbation theory (MP2) and (B) DFT with PBEPBE functional. The circle and cross represent the values for the most stable and other isomers, respectively.

has been calculated by MP2 method (top panel) and TDDFT with PBEPBE functional (bottom panel). We observe similar variation of polarizability with the size of the clusters in both calculations. The circle and the cross in the Figure 7.3 represent the values of polarizability for the most stable and other isomers, respectively. The horizontal line represents the value of GaP bulk polarizability per atom calculated by Classius-Mossotti relation. The value of bulk polarizability per atom is 25.1 a.u.. As seen from Figure 7.3, the values of polarizability per atom decrease as the size of the clusters increases and reach the bulk limit from above. This is expected because as the size of the clusters increases, system goes from molecular state to solid and hence all the properties of clusters should reach the bulk limit. In Figure 7.4 we plot the variation of anisotropy in polarizability

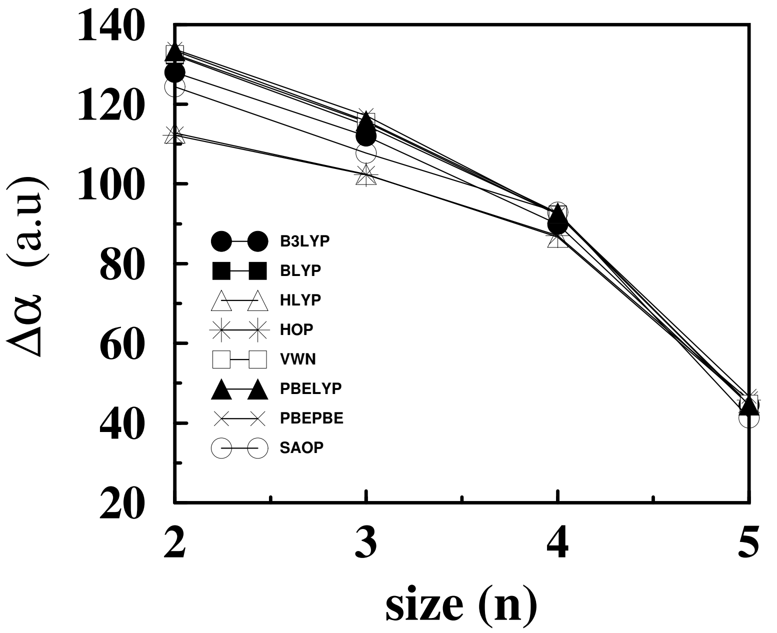

Figure 7.4: Plot of anisotropy in polarizability ($\Delta\alpha$) for the most stable isomers of stoichiometric gallium phosphide ($\mathrm{Ga}_n\mathrm{P}_n$) clusters obtained by various methods.

with size of the clusters. It is observed that the values of $\Delta\alpha$ decrease with the size of clusters. This is expected since the clusters become more symmetric as the size of the clusters increases.

7.3 Summary

In this chapter, we have presented our results for the geometry and harmonic vibrational frequency analysis of small stoichiometric gallium phosphide clusters ($\mathrm{Ga}_n\mathrm{P}_n$ with $n = 2-5$) obtained by DFT based calculations. To establish the stability of the various isomers of $\mathrm{Ga}_n\mathrm{P}_n$ clusters considered here, we do a systematic analysis of vibrational frequencies as well as evaluation of binding energy of all the structures. These investigations show that all the structures considered here are stable. We also observe from the results of geometric analysis and binding energy of optimized structures that the interactions between the atoms in these clusters are weaker than those in the bulk.

Main emphasis of the present investigation is to calculate the static dipole polarizability of these clusters by employing various *ab initio* wave function based methods and DFT / TDDFT method. A systematic investigation is carried out to analyze the performance of different XC functionals used in DFT / TDDFT method in determining static dipole polarizability of these clusters. The results for most stable isomers show that, the DFT / TDDFT method with different XC functionals underestimate the values of polarizability in comparison to the results of MP2 method. We find that among the several XC functionals, the values of polarizability obtained by PBELYP and PBEPBE functionals are the closest to the corresponding MP2 data for Ga_nP_n clusters. However, the values of polarizability obtained by the DFT / TDDFT calculations with model potential - SAOP are found to be lower than those obtained with the LDA and GGA XC functionals. Moreover, the LDA and GGA results for polarizability are closer to the corresponding MP2 values than those obtained by SAOP. This may be due to the accidental cancellation of errors arising from calculations of low lying and high lying excited states by LDA and GGA functionals which contribute to the polarizability. But, there is no such cancellation of errors when excited states are obtained with SAOP. Our study on the evolution of static dipole polarizability per atom shows that the value reaches the bulk limit from above as the size of the clusters increases.

Publication based on this chapter

Ab initio Study Of Stoichiometric Gallium Phosphide Clusters
C. Kamal, Tapan K. Ghanty, Arup Banerjee, and Aparna Chakrabarti
Journal of Chemical Physics, ***130****, 024308 (2009).*

Chapter 8

Periodic Trends in Properties of Homonuclear Diatomic Molecules

Up to now, we have discussed various physical properties of nanostructures, namely, two-dimensional - graphene-like structures: silicene mono-layer and multi-layers, hybrid system made up of silicene and boron nitride, quasi-one-dimensional - carbon and gallium phosphite nanotubes, as well as quasi-zero-dimensional - carbon cages and gallium phosphite clusters, in the preceding chapters. Now, in this chapter, we present and discuss our results for several physical and chemical properties of one of the simplest molecules which exist in nature i.e. homonuclear diatomic molecules.

It is well known that the arrangement of elements in the periodic table elucidates the periodic trend in several physical and chemical properties, for example atomic and ionic radii, ionization energy, electron affinity, electronegativity, metallic and non-metallic character, and chemical reactivity. The periodicity is basically related to the electronic configuration of elements. The electronic configuration of elements exhibits shell structure, and the periodic trend mentioned above is essentially a manifestation of this effect. The manifestation of shell structures is also observed as magic numbers in atomic nuclei and also in metal clusters[357, 358, 66, 359, 360]. However, it is not well established whether the molecules also exhibit similar periodic variation of properties or not. Although several physical and chemical properties of diatomic molecules are extensively studied by both experiment and theory, there is no systematic study on how these properties vary along the rows and columns of the periodic table. This has motivated us to carry out a systematic investigation on variation of different ground state and optical response properties of homonuclear diatomic molecules as function of atomic number of constituent atoms.

For this purpose, we perform the DFT and TDDFT based electronic structure calculations for the homonuclear diatomic molecules of first four rows of the periodic table starting from hydrogen to rubidium including transition metals. The present study includes the variation of following ground state and response properties : binding energy (BE), highest occupied and lowest unoccupied molecular orbital (HOMO and LUMO, respectively), HOMO-LUMO gap, harmonic vibrational frequency (ν), vertical ionization potential (IP), vertical electron affinity (EA), static dipole polarizability ($\bar{\alpha}$) as well as C_6 coefficient which gives the strength of van der Waals (vdW) interaction.

8.1 Ground State properties

In this section, we start our discussions on the results for the ground state properties of homonuclear diatomic molecules which are obtained by performing the electronic structure calculations based on DFT with PBE XC functional[195] and TZ2P basis set (using ADF package[205]). In order to assess the accuracy of our results which are summarized in Table 8.1, we carry out a systematic comparison of these results with the existing theoretical and experimental data[295, 361–379]. Here we wish to point out that Mn_2 molecule turns out to be an unbound system from DFT calculations as is also reported by Susumu et. al.[295] and hence it is excluded from further consideration. It is observed from Table 8.1 that our results for the ground state properties, namely, internuclear distance, binding energy and harmonic vibrational frequency match well with the corresponding data available in the literature[295, 361–379]. The variations in values of ground state properties with the available theoretical and experimental data are small.

Having established the accuracy of our results, we now proceed with the main goal of the chapter i.e. a systematic study of the trends in various properties as one moves across the rows and columns of the periodic table. For this purpose, in Figure 8.1, we plot the ground state properties such as (a) the internuclear distance (R), (b) binding energy (BE), (c) bond order (BO) and (d) harmonic vibrational frequency (ν) as a function of atomic number (Z) of the constituent atom (for example, Z=1 corresponds to H_2 molecule). It can be clearly seen from Figure 8.1, that all the above-mentioned properties show a periodic variation as a function of Z. The periodic variation in these properties can be explained by the nature and number of bonds which exist in the diatomic molecules. First we discuss

Table 8.1: Molecular electronic state, internuclear distance (in Å), binding energy (in eV) and harmonic vibrational frequency (in cm^{-1}) of homonuclear diatomic molecules (X_2) obtained by DFT based calculations with PBE XC functional. 'Present' signifies our results while 'others' signifies experimental and theoretical results available in the literature. References are given in the parentheses.

X_2	State	BE	R (Å)		ν (cm^{-1})	
		(eV)	Present	others	Present	others
H_2	$^1\Sigma_g^+$	-4.56	0.75	0.74[361], 0.74[363]	4323.59	4403.00[361], 4416[363]
He_2	$^1\Sigma_g^+$	-0.01	2.66	3.00[361], 2.77[367]	81.90	12.27[367]
Li_2	$^1\Sigma_g^+$	-0.88	2.71	2.67[361],2.69[363],2.67[364],2.74[365]	334.50	351.40[361],345[363],330.30[365]
Be_2	$^1\Sigma_g^+$	-0.41	2.43	2.45[361], 2.48[363], 2.43[372]	358.33	286[363], 327[372]
B_2	$^3\Sigma_g^-$	-2.84	1.63	1.59[361], 1.61[363]	980.79	1051.30[361], 1005[363]
C_2	$^1\Sigma_g^+$	-6.51	1.28	1.31[361], 1.25[363]	1930.14	1855.00[361], 1876[363]
N_2	$^1\Sigma_g^+$	-10.6	1.10	1.09[361],1.10[363],1.10[364],1.10[365]	2353.28	2358.00[361],2447[363],2347.00[365]
O_2	$^3\Sigma_g^-$	-5.85	1.22	1.21[361],1.20[363],1.21[364],1.23[365]	1529.48	1580.00[361],1636[363],1521.30[365]
F_2	$^1\Sigma_g^+$	-2.85	1.42	1.44[361],1.40[363],1.41[364],1.43[365]	992.59	892.00[361], 1048[363], 968.10[365]
Ne_2	$^1\Sigma_g^+$	-0.01	2.90	3.10[361], 3.09[367]	55.70	14.00[361], 15.39[367]
Na_2	$^1\Sigma_g^+$	-0.78	3.12	3.08[361], 3.04[363], 3.08[364], 3.11[365]	152.33	159.23[361], 163[363], 148.30[365]
Mg_2	$^1\Sigma_g^+$	-0.13	3.50	3.95[363], 3.50[372]	102.34	47[363], 49.57[372]
Al_2	$^1\Sigma_g^+$	-1.04	2.68	2.50[363]	236.74	324[363]
Si_2	$^3\Sigma_g^-$	-2.89	2.22	2.16[363],2.25[364],2.31[365]	412.72	511.00[361],546[363],465.90[365]
P_2	$^1\Sigma_g^+$	-5.26	1.90	1.89[361],1.89[363],1.89[364],1.92[365]	780.09	780.43[361],807[363],767.20[365]
S_2	$^3\Sigma_g^-$	-4.66	1.92	1.89[361],1.90[363],1.89[364], 1.94[365]	692.98	725.68[361],715[363],660.60[365]
Cl_2	$^1\Sigma_g^+$	-3.04	2.01	1.99[361],2.02[363],1.99[364],2.05[365]	539.26	564.90[361],540[363],500.30[365]
Ar_2	$^1\Sigma_g^+$	-0.01	3.93	4.03[367]	25.62	10.83[367]
K_2	$^1\Sigma_g^+$	-0.58	3.95	3.92[361]	91.21	92.64[361]
Ca_2	$^1\Sigma_g^+$	-0.27	4.13	4.11[372]	87.32	49.05[372]
Sc_2	$^5\Sigma_u^-$	-2.18	2.63	2.63[368], 2.62[295], 2.60[369], 2.46[370]	246.02	243[368], 270[369], 240[370]
Ti_2	$^3\Delta_g$	-3.81	1.90	1.90[368], 1.90[295], 1.90[369], 1.94[370]	446.47	462[368], 488[369], 408[370]
V_2	$^3\Sigma_g^-$	-3.54	1.74	1.74[368], 1.74[295], 1.76[369], 1.77[370]	646.46	651[368], 679[369], 537[370]
Cr_2	$^1\Sigma_g^+$	-1.56	1.59	1.72[368], 1.63[295], 1.63[369]	818.09	347[368], 799[369]
Fe_2	$^7\Delta_u$	-4.04	1.99	2.01[368], 2.01[295], 1.96[369], 2.02[370]	411.30	397[368], 460[369], 300[370]
Co_2	$^5\Delta_g$	-3.49	1.92	1.98[368], 1.98[295], 1.95[369], 2.16[370]	399.37	381[368], 424[369], 297[370]
Ni_2	$^3\Sigma_g^-$	-3.09	2.93	2.11[368], 2.10[295], 2.05[369], 2.15[370]	334.08	325[368], 367[369], 259[370]
Cu_2	$^1\Sigma_g^+$	-2.12	2.25	2.25[368], 2.26[295]	258.52	257[368], 298[369], 266[370]
Zn_2	$^1\Sigma_g^+$	-0.08	3.18	3.21[368]	53.19	54[368]
Ga_2	$^3\Sigma_g^-$	-1.11	2.69	2.45[373], 2.50[374]	204.64	210[373], 198[374]
Ge_2	$^1\Sigma_g^+$	-1.94	2.38	2.45[376]	201.26	206[376]
As_2	$^1\Sigma_g^+$	-4.31	2.12	2.10[361], 2.13[375]	431.76	429.44[361], 417[375]
Se_2	$^3\Sigma_g^-$	-3.83	2.2	2.15[361]	372.56	391.77[361]
Br_2	$^1\Sigma_g^+$	-2.62	2.32	2.37[377]	309.63	303[377]
Kr_2	$^1\Sigma_g^+$	-0.01	4.26	4.36[367]	17.00	10.97[367]
Rb_2	$^1\Sigma_g^+$	-0.54	4.33	4.18[371]	54.46	57.28[361]

Ref[361, 364, 370, 371]: experimental values. Ref[363]: DFT with B3LYP. Ref[365]: DFT with RESC-BOP. Ref[367, 368, 295, 372]: DFT with PBE. Ref[369] : DFT with LSDA. Ref[373]: MRSDCI. Ref[374, 375]: CASSCF. Ref[376]: MRCI. Ref[377]: FOCI.

the results of the diatomic molecules which are made up of elements from s- and p-blocks of the periodic table. From Figure 8.1 (a), we find that the internuclear distance R is the

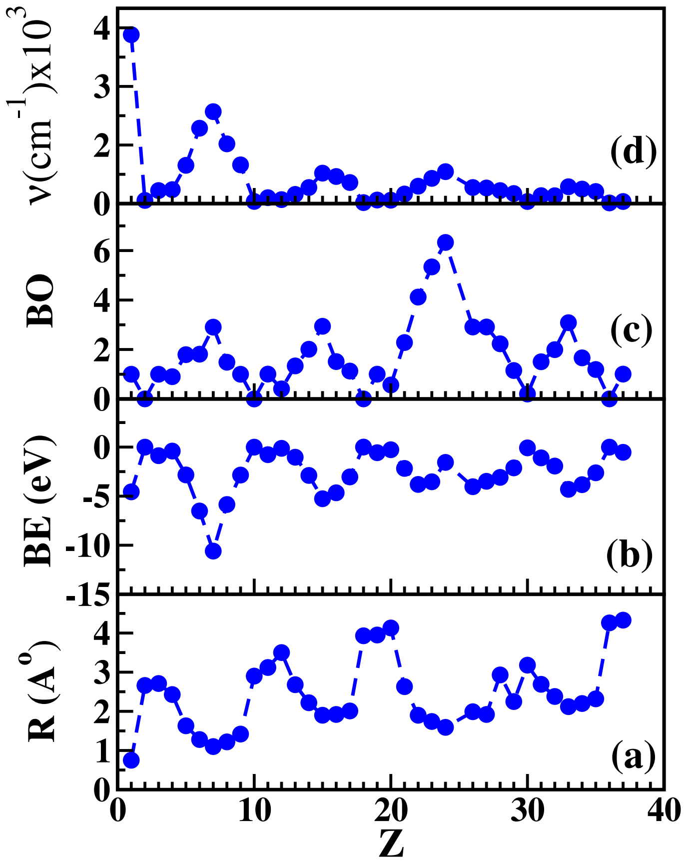

Figure 8.1: The periodic variation in the values of (a) internuclear distance (R in Å), (b) binding energy (BE in eV), (c) bonding order (BO) and (d) harmonic vibrational frequency (ν in cm^{-1}) with atomic number (Z) of the constituent atoms in the diatomic molecules.

lowest for group V diatomic molecules such as N_2, P_2 and As_2. This is due to the strong (triple) covalent like bonds that exist between the atoms in these molecules. The presence of triple bond can be confirmed from the value of bond order i.e BO = 3 (see Figure 8.1 (c)). On the other hand, the noble gas diatomic molecules possess the highest values of internuclear distance. The reason for this is that the noble gas atoms have completely filled valence shell and thus are not likely to form any chemical bond. However, there exists a weak bond between the noble gas atoms because of a long range vdW interaction. Similar to noble gas diatomic molecules, the group II diatomic molecules also have larger values of internuclear distance. In this case, the constituent atoms have filled valence sub-shells such as 2s, 3s and 4s in Be, Mg and Ca atoms, respectively and consequently, these molecules also do not have strong bonds. The value of BO is zero for the diatomic molecule made up of both these two groups (see Figure 8.1 (c)).

In case of alkali-metal diatomic molecules, we observe that the values of R is slightly lower than those of nearby group II diatomic molecules. This happens because the alkali metal atoms have single electron in valence state (2s, 3s and 4s in Li, Na and K, respectively) and two electrons from each of the alkali metal atoms can form a bond (value of BO is 1) and hence there is a decrease in the value of R. However, they cannot form a strong bond due to the free electron-like nature for which an alkali metal atom tends to give away an electron to the other. It is observed that the value of R for other diatomic molecules lies in between those of noble gas and group V diatomic molecules. We observe from Figure 8.1 that the transition metal diatomic molecules follow similar trend in the variation in the values of the BO and R as that of s- and p- block diatomic molecules. However, the value of BO for diatomic molecules of first row transition metal atoms are relatively higher than the others with a maximum value of 6.3 for Cr_2 molecule. These values are consistent with the available DFT based theoretical data in the literature[380, 381]. It is also interesting to see how the values of R change while we go from the first row to second and then to third row of the periodic table. We observe from Figure 8.1 (a) that the internuclear distance of diatomic molecules of each group increases as we go from first row to second row and then to third row due to increase in the value of atomic radius of constituent atoms. Hence the overall trend in variation of R in each row and column of the periodic table is similar.

Next we focus our attention on the binding energy of the diatomic molecules. We calculate the binding energies of these diatomic molecules, say X_2, by using the expression

$$\mathrm{BE} = E_{X_2} - 2E_X \tag{8.1}$$

where E_{X_2} and E_X are the energies of diatomic molecule and the constituent atoms respectively. The results of BE calculations for these diatomic molecules are given in Figure 8.1(b). We observe a periodic variation in the values of BE along the rows of the periodic table. There is a strong correlation between the values of R and the magnitude of BE of diatomic molecules - stronger the binding between the atoms in the molecules, lower the internuclear distance between them. The periodic variation in BE can be explained by the nature and number of bonds which exist in the diatomic molecules. The lowest and highest values in the magnitude of BE are observed for the noble gas and group V diatomic molecules respectively. This is due to the weak vdW bond present in the former as opposed to the strong triple bond which exists in the latter. The value of BE for all other diatomic molecules lies in between these two limits. However, the BE of Cr_2 molecule shows a discrepancy with respect to the general trend as shown by the other diatomic molecules. The lower value of R and the highest value of BO in case of Cr_2 molecule is incommensurate with the relatively low value of BE. This issue has already been addressed in the literature and it still remains unresolved[381, 382].

Now, we discuss the results for the harmonic vibrational frequencies of diatomic molecules. The calculations of harmonic vibrational frequency are also used to check the stability of the molecules. For linear diatomic molecules there is only one degree of freedom for vibrational motion and the results obtained for vibrational frequency are given in Figure 8.1 (d). Within the assumption that vibrational motions of diatomic molecules are harmonic, the frequencies of diatomic molecules are directly proportional to the square root of force constant and inversely proportional to the square root of reduced mass of the diatomic molecules. From Figure 8.1 (d), it is clearly seen that the values of frequency decrease as we go from smaller to bigger molecules because of increase in mass of constituent atoms. Furthermore, we observe that the variations in the frequency have strong correlation with the binding energy of molecules - stronger the binding, higher the values of vibrational frequency. This shows that, as a first approximation, the force constant is directly related to the BE of a molecule. Overall, the variation of harmonic vibrational frequency along the rows and columns of the periodic table is similar to that of BE with opposite sign, except for the Cr_2 molecule. This is due to the discrepancy in case of BE of this diatomic molecule as described above.

Having studied the trends in the results obtained for the binding energy, internuclear distance and harmonic vibration frequency, we now focus our attention on the variation of some important spectroscopic properties such as IP, EA, HOMO and HOMO-LUMO gap of diatomic molecules which are given in Figure 8.2. Before going to the discussion on the variation of these properties, we compare our results with the existing data in the literature. Our results for IP match well with the available experimental and theoretical results[363–365, 368, 383–389]. For example, we obtained the values of IP for H_2, N_2 and

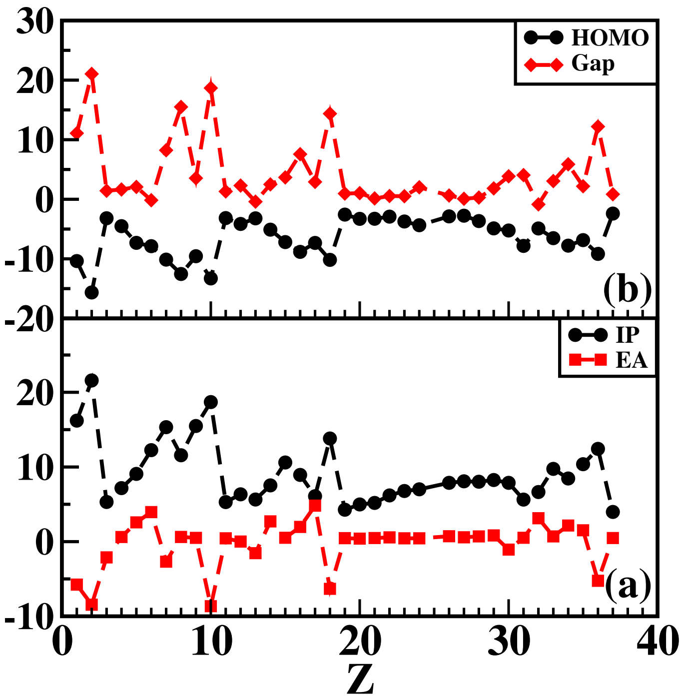

Figure 8.2: The variation in the values of (a) HOMO and HOMO-LUMO gap (in eV) and (b) ionization potential (IP in eV) and electron affinity (EA in eV) with atomic number (Z) of the constituent atoms of the diatomic molecules.

O_2 as 16.210, 15.334 and 11.566 eV, respectively, which agree well with the corresponding experimental values of 15.427, 15.581 and 12.071 eV by Lianga et al [385, 386] and theoretical values of 15.5 and 12.05 eV for N_2 and O_2 respectively. For F_2, we obtained the value of IP as 15. 493 eV which is very close to 15.70 eV calculated by Vladimir et. al.[387]. From Figure 8.2 (b), we observe that the values of IP are maximum for noble gas diatomic molecules and minimum for alkali metal diatomic molecules in a row of the periodic table. This is due to the fact that the electrons in noble gas atoms are completely filled and hence it is very difficult to remove an electron from these elements. On the other hand, free electron-like nature of the alkali metal elements is responsible for their minimum values of IP. All the other molecules are having values lying between these two extremes. The value of IP slowly increases when we go from alkali metal to noble gas molecules. However, the values of IP decrease while we go down in any group because of the increased number of sub-shells which screen the valence electrons more effectively. The variation in IP of diatomic molecules along the row of the periodic table resembles that of the atoms. It is also observed from Figure 8.2 (a) that there is a periodic variation in the values of EA. In Figure 8.2 (b) we plot the variation in HOMO and HOMO-LUMO gap for all the diatomic molecules from hydrogen to rubidium including the transition metals. We observe an oscillation in the values of HOMO similar to that of IP. This is expected since there is a correlation between the values of IP and HOMO. From the Figure 8.2 (b), we also observe that the values of HOMO-LUMO gap are relatively higher for the stable molecules such as H_2, N_2, O_2 and also for noble gas diatomic molecules.

8.2 Optical Response Properties

In the previous section we have presented our results for several ground state properties of the diatomic molecules. In the following, we discuss the results for the optical response properties such as static dipole polarizability and van der Waals interaction coefficient, C_6, of these diatomic molecules. The calculations of response properties are carried out by employing DFT/TDDFT using two different XC functionals (PBE[195] and SAOP[219, 220]) with even tempered basis set with two sets of diffuse functions (ET-QZ3P-2DIFFUSE). We use adiabatic local density approximation (ALDA) for the XC kernel. The results on average static dipole polarizability, anisotropy in polarizability and van der Waals interaction coefficient between diatomic molecules are summarized in Table 8.2 and Table 8.3. In these tables, we also include the results available in the literature for comparison. Here, we carry out the C_6 calculations only for the closed shell molecules. The calculation of static dipole polarizability for open-shell molecules have been performed by using finite field approach since the response property calculation in ADF packages[205] is implemented only for closed-shell systems.

8.2.1 Static Dipole Polarizability

It is clearly seen from Table 8.3 that our results on static polarizability match well with the data available in the literature[342, 343, 371, 385, 386, 390–412]. For example, with SAOP XC functional, we obtain the values of static polarizability and anisotropy for N_2 as 11.87 and 4.84 a.u., respectively which match very well with the experimental values (11.74 and 4.70 a.u.)[385] and other theoretical results (CCSD(T), 11.70 and 4.79 a.u.)[390]. We observe that the values of polarizability obtained by SAOP functional are much higher for alkali and group II diatomic molecule as compared to those obtained by employing PBE

Table 8.2: Average static polarizability ($\overline{\alpha}$) (in a.u.) and anisotropy in polarizability ($\Delta\alpha$) (in a.u.) of diatomic molecules (X_2) obtained by DFT/TDDFT with SAOP and PBE XC functionals. 'Others' signify experimental and theoretical results available in the literature. References are given in the parentheses.

X_2	$\overline{\alpha}$			$\Delta\alpha$		
	SAOP	PBE	Others	SAOP	PBE	Others
H_2	5.69	5.75	5.4068[398], 6.10[343], 5.1892[394], 6.10[386]	2.03	1.95	2.0539[398]
He_2	2.83	3.16		0.07	0.10	
Li_2	226.69	200.45	212.99[394], 203.5[391], 201.7, 215.7[371], 229.45[392]	99.49	105.33	
Be_2	102.38	96.48	87.81[400]	93.97	93.04	75.16[400]
B_2^*		65.96				
C_2	33.28	39.29	27.07[399]	0.00	8.31	
N_2	11.87	12.38	11.7709[401],11.70[390],11.74[393],12.3[343]	4.84	4.76	4.6074[401],4.79 [390]
O_2^*		10.41	10.67[393]			
F_2	8.12	9.02	8.219 (8.38)[342],8.4812[404]	5.83	5.67	4.915[342],5.9446 [404]
Ne_2	5.15	6.19		0.19	0.27	
Na_2	269.72	243.81	272.64[394], 203.5[391], 269.91[392], 259.5[371]	163.05	148.25	171.64 [403]
			263.28[403]			171.64 [403]
Mg_2	174.71	163.61		126.87	126.99	
Al_2	90.65	55.89	128.21± 13.49 [411]	145.91	198.55	
Si_2^*		57.77	47.08 [409]			
P_2	51.82	50.89	49.20 [402]	30.71	29.56	28.02 [402]
S_2^*		40.38	40.53 [410]			30.39 [410]
Cl_2	31.84	32.05	30.556 (30.35) [342], 30.98 [406]	17.27	16.87	16.558 (17.53)[342]
Ar_2	23.13	23.96		1.78	2.02	3.37±1.35 [412]
K_2	472.93	463.73	497.5, 507.5[371], 519.58[392]	340.05	296.72	
Ca_2	375.77	351.67		280.85	281.79	
Sc_2^*		244.76				
Ti_2^*		155.76				
V_2^*		142.94				
Cr_2	100.91	122.94		50.32	53.67	
Fe_2^*		95.53				
Co_2^*		83.64				
Ni_2^*		83.89				
Cu_2	64.54	78.63	77.62 (93.82)[397]	47.56	44.6	44.73 (67.09)[397]
Zn_2	73.36	89.55	76.92 [405]	43.37	61.36	
Ga_2^*		118.72				
Ge_2	66.40	60.64		77.05	81.07	
As_2	62.87	64.30	61.87 [408]	42.22	41.40	39.86 [408]
Se_2^*		57.83				
Br_2	45.85	46.76	44.72[407]	26.37	25.53	25.26[407]
Kr_2	34.64	36.35		3.21	3.61	4.72±1.35 [412]
Rb_2	493.22	497.38	544.90[394], 533.08[392], 565.6, 582.4[371]	504.55	466.72	

$*$ The values of static polarizability have been obtained by finite field calculations (see text).
Ref[371]: DFT with B3PW91 and CCSD. Ref[386, 392, 411, 412]]: experimental values. Ref[390, 398, 401–404, 407, 409, 410]: CCSD(T). Ref[391]: Time Dependent Gauge Invariant (TDGI) method. Ref[393]]: Time-Dependent CCSD. Ref[342]]: MP2 (experimental values are given in bracket). Ref[394]]: QDFG (Greens function formalism in quantum defect theory). Ref[343]]: TDDFT within ALDA. Ref[397]]: DFT with B3LYP and CCSD(T). Ref[[399]]: MRSCF. Ref[[400]]: TDGI method. Ref[[405]]: MP2. Ref[[406]]: SDQ-MP4. Ref[[408]]: MP4.

functional (except for Rb_2). The large differences in values of polarizability are observed for Na_2 and Li_2 where SAOP values of polarizability are 14.04 % (for Na_2) and 13.09 %

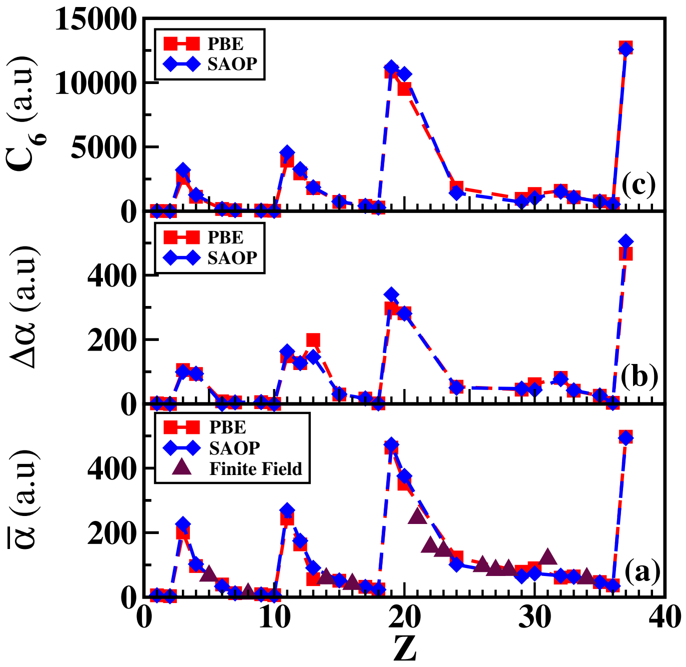

Figure 8.3: The variation in the values of (a) average static polarizability ($\bar{\alpha}$ in a.u.), (b) anisotropy in polarizability ($\Delta\alpha$ in a.u.) and (c) the vdW interaction coefficient (C_6 in a.u.) with atomic number (Z) of the constituent atoms in the diatomic molecules.

(for Li_2) higher than the values obtained by using PBE functional. But, for most of the other diatomic molecules the values of polarizability obtained by using SAOP are lower as compared to those obtained by PBE functional. However the trend in variation of polarizability along the rows are similar for the two XC functionals used here.

In order to see how the polarizability varies along rows of the periodic table, we plot values of average static polarizability ($\overline{\alpha}$) and anisotropy in polarizability ($\Delta\alpha$) as a function of Z in Figure 8.3 (a) and (b), respectively. Here also, we observe that there is a periodic variation in values of polarizability along the rows of the periodic table. We find that the alkali metal and noble gas diatomic molecules have highest and lowest values of $\overline{\alpha}$ respectively, in each row of the periodic table. The alkali metal molecules have higher values of polarizability because of their free electron-like nature, whereas the lower values of polarizability of noble gas molecules are due to their closed-shell configurations in which electrons are tightly bound and hence they are less polarizable. The values of $\overline{\alpha}$ decrease monotonically as we go from alkali metal to noble gas diatomic molecules. The trend in variation is similar for all three rows but the second and third rows have higher values of polarizability because the size of constituent atoms increases as we go down a group. This variation in polarizability may be correlated with the variation of metallic character

Table 8.3: The van der Waals interaction coefficient C_6 (in a.u.) of diatomic molecules obtained by DFT/TDDFT with SAOP and PBE XC functionals. 'Others' signifies experimental and theoretical results available in the literature. References are given in the parentheses.

Molecules	C_6 (a.u.)		
	SAOP	PBE	Others
H_2	12.92	12.92	12.058[413], 11.99[395], 11.324[396], 14.3[343], 12.5[415]
He_2	5.99	6.90	
Li_2	3205.88	2583.74	2877[391], 2626, 2862[371]
Be_2	1266.19	1120.06	1072.8 [400]
C_2	173.74	170.07	
N_2	74.13	77.36	77.2[343], 77.6[415], 72.9[393]
F_2	43.07	49.30	
Ne_2	23.97	29.82	
Na_2	4559.66	3931.83	4313[391], 4174, 4659[371]
Mg_2	3267.03	2938.92	
Al_2	1854.41	1789.56	
P_2	749.12	720.25	
Cl_2	412.47	409.91	336.8[415]
Ar_2	272.28	279.80	
K_2	11188.45	10856.71	12000, 13150[371]
Ca_2	10667.06	9505.86	
Cr_2	1410.56	1821.00	
Cu_2	708.16	955.23	
Zn_2	1003.36	1334.52	
Ge_2	1514.50	1581.60	
As_2	1052.92	1078.68	
Br_2	751.47	764.35	
Kr_2	534.46	560.19	
Rb_2	12577.45	12735.60	15320, 167000[371]

of these elements in the periodic table where the metallic character increases while going down in any group and decreases across a period from left to right.

8.2.2 van der Waals Interaction Coefficient (C_6)

Our results for the vdW coefficient, C_6, between the diatomic molecules are summarized in Table 8.3. We can see from this table that our results on the vdW coefficient between alkali metal and other molecules (hydrogen and nitrogen) match well with the data available in the literature [343, 354, 371, 385, 390, 391, 395, 396, 413–415]. In order to see how the C_6 coefficient varies along rows of the periodic table we also plot the strength of vdW interaction between diatomic molecules against atomic number of constituent atoms in Figure 8.3 (c). We observe that the variation in strength of vdW interaction is very similar to that of static polarizability. We find that the alkali metal diatomic molecules are expected to interact strongly with each other since they are highly polarizable as compared to the other diatomic molecules. A weak interaction is observed between two noble gas diatomic molecules. This is expected since they are less polarizable and have low static polarizability values. The values of C_6 coefficient for other diatomic molecules lie in between the coefficients of these two types of molecules.

8.3 Summary

In the present chapter we have discussed the trends in variation of several ground state and response properties of homonuclear diatomic molecules along the rows and columns of the periodic table by using DFT and TDDFT based calculations. It is observed from our calculations that several properties of homonuclear diatomic molecules show periodic variations as a function of atomic number of the constituent atoms. The periodic variations in the ground state properties such as the binding energy, interatomic distance, harmonic vibration frequency, etc. can be explained by the nature and type of the bond that exists between the constituent atoms. We also observe that the trends in periodic variations of the response properties such as static dipole polarizability and strength of the van der Waals interaction between diatomic molecules have strong correlation with the variations in metallic character of the elements along the periodic table.

Publication based on this chapter

Interesting Periodic Variations in Physical and Chemical Properties of Homonuclear Diatomic Molecules

C. Kamal, Arup Banerjee, Tapan K. Ghanty, and Aparna Chakrabarti

*International Journal of Quantum Chemistry, **112**, 1097 (2012)*

Chapter 9

Conclusion

The study of nanostructures such as graphene-like structures, nanotubes, and nanoclusters is an active area of research because of their novel properties and also due to their potential applications in nanotechnology. In this thesis, we have carried out a detailed computational study on several ground state and optical response properties of nanostructures by employing *ab initio* density functional theory and time dependent density functional theory (DFT/TDDFT) based calculations. For our investigations, we have considered the following materials : Two-dimensional graphene-like structures - silicene as well as hybrid system made up of honeycomb silicene and boron nitride (BN) layers, one-dimensional systems - carbon and gallium phosphide nanotubes, as well as zero-dimensional systems - carbon cages, gallium phosphide clusters, and homonuclear diatomic molecules.

In the first two chapters of the thesis, we have given a brief introduction to the nanostructures and the computational methods employed in DFT / TDDFT based calculations to study the properties of nanostructures. The results of our investigations for the above mentioned nanostructures have been discussed in the remaining chapters of the thesis.

In chapters 3 and 4, we have presented our results for various physical properties of silicene as well as hybrid structure made up of honeycomb silicene and boron nitride layers. We wish to point out here that silicene, the silicon based nanostructure, can be more compatible with the existing semiconductor technology than graphene. In chapter 3, we have discussed the geometric, electronic and optical properties of mono-layer of silicene and then compared these properties with those of mono-layer of graphene. It is observed from our results that, in the absence of any external influences, the electronic structures of both silicene and graphene mono-layers around the Fermi level are similar. Our calculations predict that a band gap in mono-layer of silicene can be induced and also tuned over a wide range by applying an external static electric field. Contrary to these results, for mono-layer graphene it is not possible to open up a band gap by applying an electric field. Importantly, we have observed that the value of induced band gap in mono-layer of silicene can be more than the thermal energy at room temperature for the applied electric field strength of few volts/nm. Hence, silicene is one of the promising materials for application in nanodevice, even at room temperature. We have also carried out studies on optical response property of mono-layers of silicene. The results of these calculations show that the dielectric function strongly depends on the direction of polarization of incident light. The anisotropic response in dielectric function is a consequence of two-dimensional characteristic of silicene.

In order to study the influence of the number of layers (n) and the stacking sequences on the properties of multi-layers of silicene, we have carried out detailed investigations on the geometric and electronic properties of multi-layers of silicene with four different stacking configurations (AAAA, AABB, ABAB and ABC) and the results are discussed in chapter 4. Our calculations show that the geometric and electronic properties of multi-layers of silicene are distinctly different from those of multi-layers of graphene. Main reason for the differences is the presence of strong inter-layer covalent bonding between the layers in multi-layers of silicene as opposed to weak van der Waals (vdW) bonding which exists between the graphene layers. We have observed that the inter-layer bonding strongly affects the properties of silicene multi-layers. Like bi-layers of graphene, silicene with two different stacking configurations AA and AB exhibits linear and parabolic dispersions around the Fermi level, respectively. However, for bi-layers of silicene, these dispersion curves are shifted in both energy and momentum directions of the band diagram as compared to those in graphene bi-layer; this is due to the strong inter-layer bonding present in the former. For multi-layers with $n \geq 3$, the results of cohesive energy calculation predict that the ABC stacking sequence is the minimum energy configuration. Furthermore, our calculations predict that the Bernal (ABAB) stacking, energetically the most stable stacking sequence in multi-layer of graphene and graphite, is the least stable stacking sequence in multi-layers of silicene. This is due to the different hybridizations in Si (sp^3) and C (sp^2).

It is understood from the above discussions that the multi-layers of silicene can not behave like multi-layers of graphene and graphite, due to the presence of strong interlayer covalent bonding. However, it is desirable to obtain graphene-like silicon based layered systems possessing exciting and novel properties similar to those of multi-layer of graphene. In chapter 4, we have also proposed an energetically stable hybrid graphite-like layered system made up of alternate layers of honeycomb silicene and honeycomb BN. Our calculations predict that this hybrid system possesses some physical properties similar to those of bulk graphite. The coupling between the layers of this hybrid system is due to weak vdW interaction which is same as that in graphite and multi-layers of graphene. Thus, our calculations show that the hybrid bulk system based on silicon and BN can be a possible candidate for two-dimensional layered soft material akin to graphite.

Chapters 5 and 6 of the present thesis are devoted to the discussions on the properties of quasi-one-dimensional nanotubes. In chapter 5, we have studied the effect of intercalation of alkali and transition metal atom clusters on the geometric, electronic and magnetic properties of single walled carbon (SWCNT) as well as gallium phosphide nanotubes (SWGaPNT), both with the chirality index (10,0). We have observed from the results of geometric structures that both the pristine SWCNTs and SWGaPNTs are cylindrical in shape. However, the atoms in SWGaPNTs are buckled due to the presence of mixture of sp^2 and sp^3 hybridizations. In contrast to the indirect band gap of their bulk counterparts, our calculations predict that both SWCNT(10,0) and SWGaPNT(10,0) possess direct band gaps of 0.83 and 1.48 eV, respectively. Hence, these NTs are possible candidates for applications in the light emitting devices.

We have observed interesting changes in the electronic structures of these nanotubes when they are intercalated with alkali and transition metal atom clusters. Our calculations of electronic structures for the SWCNT(10,0) show that the system undergoes a transition from semiconducting to a half-metallic state due to the intercalation of linear chain of transition metal atom. We have also observed signature of similar transition in SWGaPNT(10,0). The situation becomes different for higher concentration of intercalation. In this case, the system undergoes a transition from semiconductor to a fully metallic state. Intercalation of alkali metal atoms in SWCNT(10,0) and SWGaPNT(10,0) leads to semiconductor to metal transition in these NTs. The reason for the metallization in these NTs is due to a significant charge transfer from the alkali metal atoms to the NTs. Overall, we have observed from the results of our calculations that the effect of the above mentioned intercalations on both the NTs is quite similar though there are differences in the nature of hybridization in SWCNT (primarily sp^2) and SWGaPNT (mixture of sp^2 and sp^3).

It is well known that the optical response properties such as the polarizability and van der Waals interaction, play an important role in many physical, chemical and biological phenomena. In chapter 6, we have carried out a detailed investigation on the static dipole polarizability and the strength of vdW interaction (through coefficient, C_6) between carbon nanostructures (CNS) with different sizes and shapes. Our results indicate that the CNTs possess large anisotropy in polarizability due to the different scaling of components of polarizability with the length. A large anisotropy is known to play an important role in electric field aligned growth of CNTs. We have observed that the C_6 scales linearly and quadratically with the diameter and length of the CNTs, respectively. CNTs are easily polarizable along the axis of the tube, and hence they interact strongly with themselves as compared to carbon cages containing similar number of atoms. Our estimation of the C_6 values between the CNS and their variation with the size and shape can be useful in understanding the formation of superstructures made up of carbon nanostructures. We have also studied the vdW interaction between these CNS and small gas molecules, including the environmentally important ones. Our results indicate that the C_6 coefficients of H_2 as well as environmentally hazardous gases with CNS are quite high. Thus, the CNS can be a promising candidate for adsorption and storage of these gases.

In chapter 7, we have calculated the static polarizability of small stoichiometric gallium phosphide clusters (Ga_nP_n) by employing various *ab initio* wave function based methods and DFT / TDDFT method. A systematic investigation has been carried out to study the performance of various XC functionals used in DFT / TDDFT method in determining static dipole polarizability of these clusters. We have observed that the DFT / TDDFT method with different XC functionals underestimate the values of polarizability in comparison to those obtained from MP2 method. Among the several XC functionals, the performance of PBELYP and PBEPBE XC functionals is best since the values of polarizability obtained from these two functionals are the closest to the corresponding MP2 data. Surprisingly, our detailed analysis indicates that the values of polarizability obtained with model potential - SAOP, which is expected to give good results due to its correct asymptotic behavior, are lower than those obtained with the standard LDA and GGA XC functionals. Finally, our study on the evolution of static dipole polarizability per atom shows that the value reaches the bulk limit from above as size of the clusters increases.

In chapter 8, we have studied the trends of several ground state and optical response properties of homonuclear diatomic molecules along the rows and columns of the periodic table. Our calculations reveal that many properties of diatomic molecules exhibit periodic variations as a function of atomic number of the constituent atoms. We have explained the periodic variations in the ground state properties in terms of the nature and type of the bond that exists between the constituent atoms. Similarly, we have also observed that the periodic variation in the response properties such as static dipole polarizability and strength of the vdW interaction (C_6 coefficient) has strong correlation with the variations in metallic / non-metallic character of the elements along the periodic table.

One of the primary goals of researchers working in the field of material science is to search for novel materials with desirable physical and chemical properties. In the present thesis, we have studied various ground state and optical response properties of few such materials - nanostructures made up of carbon, silicon, BN and GaP. However, there exists a great possibility of producing variety of novel nanomaterials made up of several other elements in the periodic table. Computational studies, like the one carried out in the present thesis, play an important role in explaining and understanding novel properties of new materials. We wish to mention here that the present thesis has mainly concentrated on the ground state as well as optical response properties of nanostructures, but, there exist many other interesting properties namely, the electron-phonon interactions, vibrational and transport properties, charged and neutral excitations (quasi-particle energies, excitons). Some of these properties require calculations beyond DFT such as the calculations using Hedin's GW approximation and the Bethe-Salpeter equation. We would pursue the studies on these properties of nanostructures in our forthcoming research works.

References

[1] R. P. Feynman, There's plenty of room at the bottom - An invitation to enter a new field of physics, Engineering and Science Magazine of Cal. Inst. of Tech., **23**, 22 (1960)

[2] M. Kohler and W. Fritzsche, Nanotechnology - An Introduction to Nanostructuring Techniques, Wiley VCH

[3] E. L. Wolf, Nanophysics and Nanotechnology - An Introduction to Modern Concepts in Nanoscience, Wiley VCH

[4] L. Tilstra, S. A.Broughton, R. S. Tanke, D. Jelski, et. al., The Science of Nanotechnology - An introductory Text, Nova Science Publishers, Inc. New York.

[5] M. Pagliaro, Nano-Age: How Nanotechnology Changes our Future, Wiley VCH, Weinheim (2010)

[6] H. G. Rubahn, Basics of Nanotechnology, Wiley VCH (2008)

[7] V. E. Borisenko, S. Ossicini, What is What in the Nanoworld: A Handbook on Nanoscience and Nanotechnology, WileyVCH, Weinheim (2004)

[8] E. Rietman, Molecular Engineering of Nanosystems, Springer, New York (2000)

[9] K. D. Sattler, Handbook of Nanophysics- Functional nanomaterials, CRC Press, Taylor & Francis Group (2011)

[10] D. K. Ferry, S. M. Goodnick, Transport in Nanostructures, Cambridge University Press, Cambridge (1997)

[11] L. Yarris, P. Preuss, Coming of the nano-age : shaping the world atom by atom, Berkeley, California

[12] M. Grundmann, Nano-optoelectronics: concepts, physics, and devices, Springer Berlin (2002)

[13] C. P. Poole, F. J. Owens, Introduction to Nanotechnology, Wiley VCH, Weinheim (2003)

[14] C. M. Niemeyer, C. A. Mirkin, Nanobiotechnology : Concepts, Applications and Perspectives, WileyVCH, Weinheim (2004)

[15] R. Waser, Nanoelectronics and Information Technology, Wiley VCH, Weinheim (2003)

[16] H. S. Nalwa, Nanostructured Materials and Nanotechnology, Academic Press, London (2002)

[17] M. Haruta, Catal. Today, **36**, 153 (1997)

[18] M. Valden, X. Lai, D. W. Goodman, Science, **281**, 1647 (1998)

[19] B. Seplvedaa, P. C. Angelomb, L. M. Lechugaa, et al., Nano Today, **4**, 244 (2009)

[20] C. A. Mirkin, Small, **1**, 14 (2005)

[21] A. J. Haes, D. A. Stuart, S. Nie, R. P. V. Duyne, J. Fluoresc., **14**, 355 (2004)

[22] H. W. Kroto, J. R. Heath, S. C. O'Brien, R. F. Curl, et al., Nature, **318**, 162 (1985)

[23] S. Iijima, Nature (London), **354**, 56 (1991)

[24] A. K. Geim and K. S. Novoselov, Nature Mater., **6**, 183 (2007)

[25] K. S. Novoselov, A. K. Geim, S. V. Morozov, et al., Nature, **438**, 197 (2005)

[26] K. S. Novoselov, E. McCann, S. V. Morozov, et al., Nature Phys., **2**, 177 (2006)

[27] M. S. Dresselhaus, G. Dresselhaus and P.C. Eklund, Science of fullerenes and carbon nanotubes, Academic Press, San Diego (1996)

[28] M. S. Dresselhaus, G. Dresselhaus, and P. Avouris, Carbon Nanotubes: Synthesis, Structure, Properties, and Applications, Springer Topics in Applied Physics, Berlin/Heidelberg (2001)

[29] R. Saito, G. Dresselhaus and M.S. Dresselhaus, Physical properties of carbon nanotubes, Imperial College Press , London (1998)

[30] S. Reich, C. Thomsen, J. Maultzsch, Carbon nanotubes: basic concepts and physical properties, Wiley-VCH, Weinheim (2004)

[31] K. Tanaka, T. Yamabe, K. Fukui, The Science and technology of carbon nanotubes, Elsevier Science, Amsterdam (1999)

[32] S. Ciraci, T. Yildirim, S. Dag, et al., J. Phys.: Cond. Matt., **16**, R901 (2004)

[33] R. H. Baughman, A. A. Zakhidov and W. A. de Heer, Science, **297**, 787 (2002)

[34] S. Hong, S. Myung, S, Nature Nanotechnology, **2**, 207 (2007)

[35] A. C. Dillon, K. M. Jones, T. A. Bekkedahl, et al., Nature, **386**, 377 (1997)

[36] L. Schlapbach and A. Zuttel, Nature, **414**, 353 (2001)

[37] P. Chen, X. Wu, J. Lin and K. L. Tan, Science, **285**, 91 (1999)

[38] C. Liu, Y. Y. Fan, M. Liu, H. T. Cong, et al., Science, **286**, 1127 (1999)

[39] Y. Ye, C. C. Ahn, C. Witham, B. Fultz, et al., Appl. Phys. Lett., **74**, 2307 (1999)

[40] G. Gundiah, A. Govindaraj, N. Rajalakshmi, et al., J. Mater. Chem., **13**, 209 (2003)

[41] A. G. Lipson, B. F. Lyakhov, E. I. Saunin, et al., Phys. Rev. B, **77**, 081405 (2008)

[42] L. Zubizarreta, E. I. Gomez, A. Arenillas, et al., Adsorption, **14**, 557 (2008)

[43] D. Henwood and J. David Carey, Phys. Rev. B, **75**, 245413 (2007)

[44] K. Tada, S. Furuya and K. Watanabe, Phys. Rev. B, **63**, 155405 (2001)

[45] B. Panella, M. Hirscher and S. Roth, Carbon, **43**, 2209 (2005)

[46] X. Yang, R. Q. Zhang and J. Ni, Phys. Rev. B, **79**, 075431 (2009)

[47] H. J. Liu and C. T. Chan, Phys. Rev. B, **73**, 113405 (2006)

[48] D. Sung, S. Hong, Y. -H. Kim, N. Park, et al., Appl. Phys. Lett., **89**, 243110 (2006)

[49] K. Ichimura, K. Imaeda, C. Jin and H. Inokuchi, Physica B, **323**, 137 (2002)

[50] W. Wongwiriyappan, S. Inoue, S. Honda, et al., Jpn. J. Appl. Phys., **47**, 8145 (2008)

[51] F. Picaud, C. Girardet and A. M. Rao, J. Appl. Phys., **105**, 014315 (2009)

[52] S. Kim, H. R. Lee, Y. J. Yun, S. Ji, et al., Appl. Phys. Lett., **91**, 093126 (2007)

[53] H. Y. Jung, S. M. Jung, J. Kim and J. S. Suh, Appl. Phys. Lett., **90**,153114 (2007)

[54] E. H. Espinosa, R. Ionescu, C. Bittencourt, et al., Thin Solid Films, **515**, 8322 (2007)

[55] T. Hashishin and J. Tamaki, J. Nanomaterials, **2008**, 352854 (2008)

[56] M. Y. Faizah, A. Fakhrul-Razi, et al., Int. J. Eng. and Tech., **4**, 106 (2007)

[57] S. Kim, Sensors, **6**, 503 (2006)

[58] A. Ricca and C. W. Bauschlicher Jr., Chem. Phys., **323**, 511 (2006)

[59] V. N. Soloviev, A. Eichhfer, D. Fenske, et al., J. Am. Chem. Soc. **122**, 2673 (2000)

[60] C. Weisbuch, B. Vinter, Quantum semiconductor structures - fundamentals and applications, Academic press, Londan (1991)

[61] M. Dutta, M. A. Stroscio, Advances in semiconductor lasers and applications to optoelectronics, world Scientific, Singapore (2000)

[62] P. S. Zory, Quantum well laser, Academic Press, Boston (1993)

[63] H. C. Liu, F. Capasso, R. K. Willardson, Intersubband transitions in quantum wells: physics and device applications I, Academic Press, San Diego (2000)

[64] P. R. Wallace, Phys. Rev., **71**, 622 (1947)

[65] J. A. Alonso, Structure and Properties of Atomic Nanoclusters, Imperial College Press (2005)

[66] W. D. Knight, K. Clemenger K, et al., Phys. Rev. Lett., **52**, 2141 (1984)

[67] X. B. Wang, C. F. Ding, L. S. Wang, J. Chem. Phys., **110**, 8217 (1999)

[68] A. F. Hebard et al., Nature, **350**, 600 (1991); M. J. Rosseinsky et al., Phys. Rev. Lett., **66**, 1154 (1991)

[69] L. E. Brus, J. Phys. Chem., **90**, 2555 (1986)

[70] M. G. Bawendi, M. L. Steigerwald, L. E. Brus, Annu. Rev. Phys. Chem., **41**, 477 (1990)

[71] Y. Wang, A. Suna, W. Mahler, R. Kasowsky, J. Chem. Phys., **87**, 7315 (1987)

[72] Y. Wang, N. Herron, J. Phys. Chem., **95**, 525 (1991)

[73] J. L. Elkind, J. M. Alford, F. D. Weiss, et al., J. Chem. Phys., **87**, 2397 (1987)

[74] L. R. Anderson, S. Maruyama, R. E. Smalley, Chem. Phys. Lett. **176**, 348 (1991)

[75] J.A. Cogardan, L.E. Sansores, et al., J. Non-Cryst. Solids, **181**, 135 (1995)

[76] M. R. Pederson, D. V. Porezag, et al., Phys. Rev. B, **54**, 2863 (1996)

[77] J. Song, S. E. Ulloa, D. A. Drabold Phys. Rev. B, **53**, 8042 (1996)

[78] P.V. Santos, B. Koopmans, et al., Phys. Rev. Lett., **77**, 759 (1996)

[79] R. J. Baierle, M. J. Caldas, et al., Solid State Commun., **102**, 545 (1997)

[80] K. Jackson, M. R. Pederson, D. Porezag, et al., Phys. Rev. B, **55**, 2549 (1997)

[81] B. K. Panda, S. Mukherjee, and S. N. Behera, Phys. Rev. B, **63**, 045404 (2001)

[82] B. Li, Phys. Rev. B, **71**, 235311 (2005)

[83] A. Rubio, J. A. Alonso, X. Blase, et al., Phys. Rev. Lett., **77**, 247 (1996)

[84] J. Wang, G. Wang, F. Ding, H. Lee, et al., Chem. Phys. Lett., **341**, 529 (2001)

[85] M. Tang, Wencai Lu, C. Z. Wang, and K. M. Ho, Chem. Phys. Lett., **377**, 413 (2003)

[86] S. Ma and G. Wang, J. Mol. Struct. (Theochem), **767**, 75 (2006)

[87] I. Vasiliev, S. Ogut, and J. R. Chelikowsky, Phys. Rev. Lett., **78**, 4805 (1997)

[88] S. Bulusu, S. Yoo, and X. C. Zenga, J. Chem. Phys., **122**, 164305 (2005)

[89] J. Zhao, L. Wang, J. Jia, X. Chen, et al., Chem. Phys. Lett., **443**, 29 (2007)

[90] Z. Y. Liu, C. R. Wang, et al., Int. J. Mass Spectrom. Ion Proces., **141**, 201 (1995)

[91] A. Costales and R. Pandey, J. Phys. Chem. A, **107**, 191 (2003)

[92] P. Karamanis and J. Leszczynski, J. Chem. Phys., **128**, 154323 (2008)

[93] H. Gomez, T. R. Taylor, and D. M. Neumark, J. Phys. Chem. A, **105**, 6886 (2001)

[94] W. Zhao, P. Cao, W. Duan, Phys. Lett. A, **349**, 224 (2006)

[95] Y. P. Feng, T. B. Boo, H. H. Kwong, et al., Phys. Rev. B, **76**, 045336 (2007)

[96] J. Zhao, R. H. Xie, X. Zhou, X. Chen, and W. Lu, Phys. Rev. B, **74**, 035319 (2006)

[97] R. Schäfer, S. Schlecht, J. Woenckhaus, et al., Phys. Rev. Lett., **76**, 471 (1996)

[98] W. Zhao, P. Cao, B. Li, B. Song, et al., Phys. Rev. B, **62**, 17138 (2000)

[99] I. Vasiliev, S. Ogut, and J. R. Chelikowsky, Phys. Rev. B, **60**, R8477 (1999)

[100] P. P. Korambath and S. P. Karna, J. Phys. Chem. A, **104**, 4801 (2000)

[101] A. Costales, A. K. Kandalam, et al., J. Phys. Chem. B, **106**, 1940 (2002)

[102] C. H. Guo, J. F. Jia, et al., Acta. Phys. Chim. Sin., **22**, 1253 (2006)

[103] C. H. Guo, J. F. Jia, et al., J. Mol. Struct. (Theochem), **851**, 167 (2008)

[104] E. Li, X. Luo, W. Shi, X. Wang, J. Mol. Struct. (Theochem), **723**, 79 (2005)

[105] W. Andreoni, Phys. Rev. B, **45**, 4203 (1992)

[106] P. Y. Feng, K. Balasubramanian, Chem. Phys. Lett., **258**, 387 (1996)

[107] P. Y. Feng, K. Balasubramanian, Chem. Phys. Lett., **265**, 41 (1997)

[108] P. Y. Feng, K. Balasubramanian, Chem. Phys. Lett., **265**, 547 (1997)

[109] P. Y. Feng, K. Balasubramanian, Chem. Phys. Lett., **288**, 1 (1998)

[110] V. Tozzini, F. Buda, A. Fasolino, Phys. Rev. Lett., **85**, 4554 (2000)

[111] E. F. Archibong, A. St Amant, Chem. Phys. Lett., **330**, 199 (2000)

[112] E. F. Archibong, A. St-Amant, Chem. Phys. Lett., **316**, 151 (2000)

[113] F. Buda and A. Fasolino, Phys. Rev. B, **60**, 6131 (1999)

[114] S.C. OBrien, Y. Liu, Q. L. Zhang, F.K. Tittel, R.E. Smalley, J. Chem. Phys., **84**, 4074 (1986)

[115] T. R. Taylor, K. R. Asmis, C. Xu, et al., Chem. Phys. Lett., **297**, 133 (1998)

[116] T. R. Taylor, K. R. Asmis, C. Xu, et al., Eur. Phys. J. D, **9**, 317 (1999)

[117] T. R. Taylor, K. R. Asmis, C. Xu, et al., J. Chem. Phys., **115**, 4620 (2001)

[118] C. C. Arnold, D.M. Neumark, Can. J. Phys., **72**, 1322 (1994)

[119] C. Xu, G. R. Burton, T. R. Taylor, et al., J. Chem. Phys., **107**, 3428 (1997)

[120] G. R. Burton, C. C. Arnold, C. Xu, et al., J. Chem. Phys., **104**, 2757 (1996)

[121] S. Li, R. J. van Zee, W. Weltner, J. Phys. Chem., **97**, 11393 (1993)

[122] P. Hohenberg and W. Kohn, Phys. Rev., **136**, B864 (1964)

[123] W. Kohn and L. J. Sham, Phys. Rev., **140**, A1133 (1965)

[124] R. M. Martin, Electronic Structure Basic Theory and Practical Methods, Cambridge University Press (2004)

[125] W. Koch, M. C. Holthausen, A Chemists Guide to Density Functional Theory, Wiley-VCH Verlag GmbH (2001)

[126] A. L. Ivanovskii, Russian Chemical Reviews, **81**, 571 (2012)

[127] L. Pan , H.J. Liu, Y.W. Wen, X.J. Tan, et al., Phys. Lett. A, **375**, 614 (2011)

[128] K. Takeda and K. Shiraishi, Phys. Rev. B, **50**, 14916 (1994)

[129] S. Cahangirov, M. Topsakal, E. Akturk, et al., Phys. Rev. Lett., **102**, 236804 (2009)

[130] H. Sahin, S. Cahangirov, M. Topsakal, et al., Phys. Rev. B, **80**, 155453 (2009)

[131] G. G. Guzman-Verri and L. C. Lew Yan Voon, Phys. Rev. B, **76**, 075131 (2007).

[132] C. Kamal, A. Chakrabarti, et al., J. Phys.: Cond. Matt., **25**, 085508 (2013)

[133] Z. Ni, Q. Liu, K. Tang, J. Zheng, J. Zhou, et al., Nano Lett., **12**, 113 (2012)

[134] N. D. Drummond, V. Zolyomi, and V. I. Falko, Phys. Rev. B, **85**, 075423 (2012)

[135] M. Ezawa, New Journal of Physics, **14**, 033003 (2012)

[136] C. Kamal, http://arxiv.org/abs/1202.2636

[137] M. Ezawa, Phys. Rev. Lett., **109**, 055502 (2012)

[138] M. Ezawa, Phys. Rev. B, **86**, 161407 (R) (2012)

[139] C. C. Liu, W. Feng, and Y. Yao, Phys. Rev. Lett., **107**, 076802 (2011)

[140] M. Houssa, G. Pourtois, V. V. Afanasev, et al., Appl. Phys. Lett., **97**, 112106 (2011)

[141] S. Lebegue and O. Eriksson, Phys. Rev. B, **79**, 115409 (2009)

[142] D. Jose and A. Datta, Phys. Chem. Chem. Phys., **13**, 7304 (2011)

[143] M. J. S. Spencer, T. Morishita, et al., Phys. Chem. Chem. Phys., **13**, 15418 (2011)

[144] T. H. Osborn, A. A. Farajian, et al., Phys. Lett., **511**, 101 (2011)

[145] D. Jose, A. Datta, Accounts of Chemical Research, Unpublished

[146] P. Vogt, P. De Padova, C. Quaresima, et al., Phys. Rev. Lett., **108**, 155501 (2012)

[147] Y. Zhang, T. Tang, C. Girit, Z. Hao, et al., Nature, **459**, 820 (2009)

[148] J. B. Oostinga, H. B. Heersche, X. Liu, et al., Nature Mater., **7**, 151 (2008)

[149] E. V. Castro, K. S. Novoselov, et al., Phys. Rev. Lett., **99**, 216802 (2007)

[150] S. B. Trickey, F. Muller-Plathe, et al., Phys. Rev. B, **45**, 4460 (1992)

[151] T. Ohta, A. Bostwick, T. Seyller, et al., Science, **313**, 951 (2006)

[152] E. McCann, Phys. Rev. B, **74**, 161403(R) (2006)

[153] C. J. Tabert, and E. J. Nicol, Phys. Rev. B, **86**, 075439 (2012)

[154] J. L. Manes, F. Guinea, et al., Phys. Rev. B, **75**, 155424 (2007)

[155] T. Ohta, A. Bostwick, J. L. McChesney, et al., Phys. Rev. Lett., **98**, 206802 (2007)

[156] S. Latil, V. Meunier, and L. Henrard, Phys. Rev. B, **76**, 201402R (2007)

[157] K. F. Maka, M. Y. Sfeirb, et al., Proc. Nat. Am. Sci., **107**, 14999 (2010)

[158] J. W. Jiang, H. Tang, B. S. Wang, Z. B. Su, Phys. Rev. B, **77**, 235421 (2008)

[159] J. A. Yan, W. Y. Ruan, M. Y. Chou, Phys. Rev. B, **77**, 125401 (2008)

[160] S. K. Saha, U. V. Waghmare, et al., Phys. Rev. B, **78**, 165421 (2008)

[161] K. H. Michel, B. Verberck, Phys. Rev. B, **78**, 085424 (2008)

[162] J. A. Yan, W. Y. Ruan, M. Y. Chou, Phys. Rev. B, **79**, 115443 (2009)

[163] Q. Wu, Z. Hu, C. Liu, X. Wang, et al., J. Phys. Chem. (B), **109**, 19719 (2005)

[164] W. S. Shi, Y. F. Zheng, N. Wang, et al., J. Vac. Sci. Technol. (B), **19**, 1115 (2001)

[165] C. J. Novotny, E. T. Yu and P. K. L. Yu, Nano Lett., **8**, 775 (2008)

[166] S. Roy and M. Springborg, J. Phys. Chem. (C), **113**, 81 (2009)

[167] W. HallStrom, T. Martensson, C. Prinz, et al., Nano Lett., **7**, 2960 (2007)

[168] M. Mirzaei, M. Mirzaei, Physica E, **43**, 1343 (2011)

[169] M. Mirzaei, M. Youse, M. Meskinfam, Solid State Sci., **14**, 801 (2012)

[170] C. B. E. Santos and T. M. Schmidt, J. App. Phys., **108**, 103715-1 (2010)

[171] B. Liu, L. Wei, Q. Ding, J. Yao, Nanotechnology, **15**, 1745 (2004)

[172] S. C. Lyu, Y. Zhang, H. Ruh, et al., Chem. Phys. Lett., **367**, 717 (2003)

[173] H. W. Seo, S. Y. Bae, J. Park, et al., Chem. Phys. Lett., **378**, 420 (2003)

[174] Y. Huang, X. Duan, Q. Wei, C. M. Lieber, Science, **291**, 630 (2001)

[175] E. Runge, E. K. U. Gross, Phys. Rev. Lett., **52**, 997 (1984)

[176] M. Born and R. Oppenheimer. Ann. Phys. (Leipzig), **84**, 457 (1927)

[177] D. R. Hartree, Proc. R. Soc. London, **A113**, 621 (1928)

[178] V. Fock, Z. Phys., **61**, 126 (1930)

[179] J. C. Slater, Phys. Rev., **81**, 385 (1951)

[180] R. G. Parr and W. Yang, Density Functional Theory of Atoms and Molecules, Oxford University Press, NewYork (1989)

[181] A. Szabo, N. S. Ostlund, Modern Quantum Chemistry: Introduction to Advanced Electronic Structure Theory, NewYork (1996)

[182] S. F. Sousa, P.A. Fernandes, M. J. Ramos, J. Phys. Chem. A, **111**, 10439 (2007)

[183] L. H. Thomas. Proc. Camb. Phil. Soc., **23**, 542 (1927)

[184] E. Fermi. Rend. Accad. Naz. Lincei, **6**, 602 (1927)

[185] E. Fermi. Z. Phys., **48**, 73 (1928)

[186] P. A. M. Dirac, Proc. R. Soc. London, **A112**, 661 (1926)

[187] C. F. v. Weizscker, Zeitschrift fr Physik, **96**, 431 (1935)

[188] M. K. Harbola, A. Banerjee, J. Theo. Comp. Chem., **2**, 301 (2003)

[189] S. H. Vosko, L. Wilk, M. Nusair, Can. J. Phys., **58**, 1200 (1980)

[190] J. P. Perdew and Y. Wang, Phys. Rev. B, **46**, 12947 (1992)

[191] A. D. Becke, Phys. Rev. A, **38**, 3098 (1988)

[192] J. P. Perdew, Phys. Rev. B, **33**, 8822 (1986)

[193] A. D. Becke, J. Chem. Phys., **98**, 5648 (1993)

[194] C. Lee, W. Yang, and R. G. Parr, Phys. Rev. B, **37**, 785 (1988)

[195] J. P. Perdew, K. Burke, and M. Ernzerhof, Phys. Rev. Lett., **77**, 3865 (1996)

[196] T. Tsuneda and K. Hirao, Chem. Phys. Lett., **268**, 510 (1997); T. Tsuneda, T. Suzumura, and K. Hirao, J. Chem. Phys., **110**, 10664 (1999); M. Kamiya, T. Tsuneda, and K. Hirao, ibid., **117**, 6010 (2002)

[197] D. M. Ceperley and B. J. Alder, Phys. Rev. Lett., **45** 566 (1980)

[198] P. Blaha, K. Schwartz, G. K. H. Madsen, D. Kvasnicka and J. Luitz, WIEN2K, An Augmented Plane Wave plus Local Orbitals Program for Calculating Crystal Properties, (Karlheinz Schwarz, Tech. Universität, Wien, Austria), 2002, ISBN 3-9501031-1-2.

[199] G. Kresse, J. Furthmuller, Phys. Rev. B, **54**, 11169 (1996); G. Kresse, D. Joubert, Phys. Rev. B, **59**, 1758 (1999); VASP 5.2 programme package within the MedeA platform (Materials Design, Inc.).

[200] P. Ordejon, E. Artacho, and J. M. Soler, Phys. Rev. B, **53**, R10441 (1996)

[201] D. Sanchez-Portal, P. Ordejon, et al., Int. J. Quantum Chem., **65**, 453 (1997)

[202] J. M. Soler, E. Artacho, J. D. Gale, A. Garca, et al., J. Phys. Condens. Matter., **14**, 2745 (2002); see also http://www.uam.es/siesta

[203] O. F. Sankey and D. J. Niklewski, Phys. Rev. B, **40**, 3979 (1989)

[204] N. Troullier and J. L. Martins, Phys. Rev. B, **43**, 1993 (1991)

[205] E. J. Baerends, J. Autscbach, A. Berces, et al. *Amsterdam Density Functional*, Theoretical Chemistry, Vrije Universiteit, Amsterdam, URL http://www.scm.com

[206] I. Mayer, Chem. Phys. Lett., **97**, 270 (1983)

[207] S. K. Ghosh and B. M. Deb, Chem. Phys., **71**, 295 (1982)

[208] B. M. Deb and S. K. Ghosh, J. Chem. Phys., **77**, 342 (1982)

[209] L. J. Bartolotti, Phys. Rev. A, **24**, 1661 (1981)

[210] L. J. Bartolotti, Phys. Rev. A, **26**, 2243 (1982)

[211] S. Chakravarty, M. B. Fogel and W. Kohn, Phys. Rev. Lett., **43**, 775 (1979)

[212] E. K. U. Gross and W. Kohn, Phys. Rev. Lett., **55**, 2850 (1985)

[213] D. Mearns and W. Kohn, Phys. Rev. A, **35**, 4796 (1987)

[214] E. K. U. Gross and W. Kohn, Adv. Quant. Chem., **21**, 255 (1990)

[215] M. Marques, A. Castro, and A. Rubio, J. Chem. Phys., **115**, 3006 (2001)

[216] K. Yabana and G. F. Bertsch, Int. J. Quantum Chem., **75**, 55 (1999)

[217] H. B. G. Casimir and D. Polder, Phys. Rev., **73**, 360 (1948)

[218] S. J. A. van Gisbergen, J. G. Snijders, et al., J. Chem. Phys., **109**, 10657 (1998)

[219] O. V. Gritsenko, P. R. T. Schipper, et al., Chem. Phys. Lett., **302**, 199 (1999)

[220] R. P. T. Schipper, O. V. Gritsenko, et al., J. Chem. Phys., **112**, 1344 (2000)

[221] B. Lalmi, H. Oughaddou, H. Enriquez, et al., Appl. Phys. Lett., **97**, 223109 (2010).

[222] B. Aufray, A. Kara, S. Vizzini, et al, Appl. Phys. Lett., **96**, 183102 (2010)

[223] A. Kara, S. Vizzini, C. Leandri, et. al., J. Phys.: Cond. Matt., **22**, 045004 (2010)

[224] P. D. Padova, C. Quaresima, et al., Appl. Phys. Lett., **96**, 261905 (2010)

[225] B. Feng, Z. Ding, S. Meng, Y. Yao, X. He, et al., Nano Lett., **12**, 3507 (2012).

[226] L. Chen, C. C. Liu, B. Feng, X. He, et al., Phys. Rev. Lett., **109**, 056804 (2012).

[227] H. Enriquez, S. Vizzini, et al., J. Phys.: Condens. Matter, **24**, 314211 (2012)

[228] G. L. Lay, P. D. Padova, A. Resta, et al., J. Phys. D: Appl. Phys., **45**, 392001 (2012)

[229] H. Jamgotchian, Y. Colignon, et al., J. Phys.: Cond. Matt., **24**, 172001 (2012)

[230] L. Meng et al., Nano Lett., **13**, 685 (2013)

[231] C. L. Lin, R. Arafune, K. Kawahara, et al., Appl. Phys. Express, **5**, 045802 (2012)

[232] A. Fleurence, R. Friedlein, et al., Phys. Rev. Lett., **108**, 245501 (2012)

[233] D. Chiappe, C. Grazianetti, G. Tallarida, et al., Adv. Mater., **24**, 5988 (2012)

[234] R. Arafune, C. L. Lin, K. Kawahara, et al., Surf. Sci., **608**, 297 (2012)

[235] C. L. Lin, R. Arafune, K. Kawahara, et al., Phys. Rev. Lett., **110**, 076801 (2013)

[236] P. D. Padova, O. Kubo, et al., Nano Lett., Articles ASAP, DOI: 10.1021/nl302598x

[237] L. Chen, B. Feng, and K. Wua, App. Phys. Lett., **102**, 081602 (2013)

[238] C. Li, S. Yang, S. S. Li, J. B. Xia, J. Li, J. Phys. Chem. C, **117**, 483 (2013)

[239] X. Lin, J. Ni, Phys. Rev. B, **86**, 075440 (2012)

[240] H. H. Gurel, S. Ciraci, J. Phys.: Cond. Matt., **25**, 275302 (2013)

[241] J. Zhang, B. Zhao, and Z. Yang, Phys. Rev. B, **88**, 165422 (2013)

[242] X. L. Zhang, L. F. Liu, W. M. Liu, Sci. Rep., **3**, 2908 (2013)

[243] N. Y. Dzade, K. O. Obodo, et al., J. Phys.: Cond. Matt., **22**, 375502 (2010)

[244] B. Huang, H. J. Xiang, and S. H. Wei, Phys. Rev. Lett., **111**, 145502 (2013)

[245] Y. Dai, S. N, Z. Li and J. Yang, J. Phys.: Cond. Matt., **25**, 405301 (2013)

[246] C. Kamal, http://arxiv.org/abs/1205.5099

[247] Y. Yao, F. Ye, X. L. Qi, S. C. Zhang, and Z. Fang, Phys. Rev. B, **75**, 041401 (2007)

[248] M. Houssa, E. Scalise, K. Sankaran, et al., Appl. Phys. Lett., **98**, 223107 (2011)

[249] L. C. L. Y. Voon, E. Sandberg, et al., Appl. Phys. Lett., **97**, 163114 (2011)

[250] A. Kara , H. Enriquez, A. P. Seitsonen, et al., Surf. Sci. Rep., **67**, 1 (2012)

[251] M. H. F. Sluiter, Y. Kawazoe, Phys. Rev. B, **68**, 085410 (2003)

[252] L. Li, X. Wang, X. Zhao, M. Zhao, Phys. Lett. A., **377**, 2628 (2013)

[253] H. Liu , J. Gao , J. Zhao, J. Phys. Chem. C, **117**, 10353 (2013)

[254] T. P. Kaloni, M. Tahir, U. Schwingenschlogl, Sci. Rep., **3**, 3192 (2013)

[255] Z. Guo, S. Furuya, J. Iwata, A. Oshiyama, Phys. Rev. B, **87**, 235435 (2013)

[256] M. Hanand, H. Beister, K. Syassen, Phys Rev. B, **39**, 12598 (1989).

[257] http://www.ioffe.rssi.ru/SVA/NSM/Semicond/BN/basic.html

[258] http://www.ioffe.rssi.ru/SVA/NSM/Semicond/Si/mechanic.html

[259] M. P. Persson, A. Di Carlo, J. Appl. Phys., **104**, 073718-1 (2008)

[260] S. M. Lee, Y. H. Lee, Y. G. Hwang, J. Elsner, et al., Phys. Rev. B, **60**, 7788 (1999)

[261] F. Wang, G. -Q. Jin and X. -Y. Guo, Materials Lett., **60**, 330 (2006)

[262] D. J. Carter, J. D. Gale, B. Delley, et al., Phys. Rev. B, **77**, 115349-1 (2008)

[263] M. Zhao, Y. Xia, D. Zhang and L. Mei, Phys. Rev. B, **68**, 235415-1 (2003)

[264] N. G. Chopra, R. J. Luyken, K. Cherrey, et al., Science, **269**, 966 (1995)

[265] H. Yilmaz, S. P. Singh, C. Marin, et al., J. Nanosci. Nanotechnol., **11**, 7753 (2011)

[266] G. X. Chen, Y. Zhang, D. D. Wang, et al., Solid State Commun., **151**, 139 (2011)

[267] E. Li, L. Hou, Z. Cui, D. Zhao, M. Liu and X. Wang, Nano, **7**, 1250014-1 (2012)

[268] G. X. Chen, Y. Zhang, D. D. Wang, J. M. Zhang, Physica E, **43**, 22 (2010)

[269] G. X. Chen, Y. Zhang, D. D. Wang, et al., Comput. Theor. Chem., **963**, 18 (2011)

[270] Y. Guo, X. Yan, Y. Yang, Phys. Lett. A, **373**, 367 (2009)

[271] L. C. Ma, Y. Zhang, J. M. Zhang, K. W. Xu, Physica B, **406**, 3502 (2011)

[272] G. Zhou and L. Li, J. Appl. Phys., **112**, 014317-1 (2012)

[273] M. M. Rahman, M. Kisaku, T. Kishi, et al., J. Phys. Soc. Japan, **74**, 742 (2005)

[274] P. P. Baruselli, A. Smogunov, et al., Phys. Rev. Lett., **108**, 206807-1 (2012)

[275] T. Zoberbier, T. W. Chamberlain, et al., J. Am. Chem. Soc., **134**, 3073 (2012)

[276] C. H. Lee and C. K. Yang, RSC Adv., **2**, 9958 (2012)

[277] Z. Liu, Y. Bando, M. Mitome and J. Zhan, Phys. Rev. Lett., **93**, 095504-1 (2004)

[278] W. Li, M. Zhao, Y. Xia, T. He, C. Song, et al., Phys. Rev. B, **74**, 195421-1 (2006)

[279] Y. Miyamoto, A. Rubio, X. Blase, et al., Phys. Rev. Lett., **74**, 2993 (1995)

[280] X. Yang, J. Ni, Phys. Rev. B, **71**, 165438-1 (2005)

[281] C. M. Chang, A. F. Jalbout, Thin Solid Films, **518**, 2070 (2010)

[282] W. Liu, S. Xu, C. Li, G. Yuan, Diam. Relat. Mater., **29**, 59 (2012)

[283] S. F. Xu, G. Yuan, C. Li, H. Mimura, J. Vac. Sci. Technol. B, **29**, 04E101-1 (2011)

[284] S. F. Xu, G. Yuan, C. Li, et al., Appl. Phys. Lett., **96**, 233111-1 (2010)

[285] M. Bouhrara, Y. Saih, T. Wagberg, et al., J. Appl. Phys., **110**, 054306-1 (2011)

[286] N. Minami, S. Kazaoui, R. Jacquemin, et al., Synthetic Met., **116**, 405 (2001)

[287] H. Muramatsu, T. Hayashi, Y. A. Kim, et al., Nano Lett., **8**, 237 (2008)

[288] V. Meunier, H. Muramatsu, T. Hayashi, et al., Nano Lett., **9**, 1487 (2009)

[289] S. -F. Wang, L. -Y. Chen, J. -M. Zhang, et al., Physica E, **49**, 97 (2013)

[290] Y. Xie, J. -M. Zhang, Physica E, **44**, 405 (2011)

[291] J. -M. Zhang, H. -H. Li, Y. Zhang, K. -W. Xu, Physica E, **43**, 1249 (2011)

[292] S. Ghosh, S. Nigam, G. P. Das, C. Majumdar, J. Chem. Phys., **132**, 164704-1(2010)

[293] S. Yuan, Y. Kong, F. Wen, F. Li, J. Phys.: Cond. Matt., **19**, 466203 (2007)

[294] C. Kamal and A. Chakrabarti, Phys. Rev. B, **76**, 075113-1 (2007)

[295] S. Yanagiswa, T. Tsuneda, K. Hirao, J. Chem. Phys., **112**, 545 (2000)

[296] C. Kamal, A. Banerjee, et al., Int. J. Quantum Chem., **112**, 1097 (2012)

[297] C. Kittel, Introduction to Solid State Physics, Wiley India, Reprint 2007, p. 201

[298] N. Jones, Nature, **458**, 1094 (2009)

[299] J. Zhao, A. Buldum, J. Han and J. P. Li, NanoTechnology, **13**, 195 (2002)

[300] M. Cinke, J. Li, C. W. Bauschlicher Jr., et al., Chem. Phys. Lett., **376**, 761 (2003)

[301] A. Ricca, C. W. Bauschlicher Jr. and A. Maiti, Phys. Rev. B, **68**, 035433 (2003)

[302] M. Bienfait, P. Zeppenfeld, et al., Phys. Rev. B, **70**, 035410 (2004)

[303] C. W. Bauschlicher Jr. and A. Ricca, Phys. Rev. B, **70**, 115409 (2004)

[304] P. A. Denis, Chem. Phys., **353**, 79 (2008)

[305] F. Su, C. Lu, W. Cnen, H. Bai et al., Sci. Envir., **407**, 3017 (2009)

[306] A. J. Zambano, S. Talapatra and A. D. Migone, Phys. Rev. B, **64**, 075415 (2001)

[307] S. Talapatra, A. Z. Zambano, S. E. Weber, et al., Phys. Rev. Lett., **85**, 138 (2000)

[308] S. Talapatra and A. D. Migone, Phys. Rev. Lett., **87**, 206106 (2001)

[309] S. Talapatra, V. Krungleviciute, et al., Phys. Rev. Lett., **89**, 246106 (2002)

[310] G. Stan and M. W. Cole, Surf. Sci., **395**, 280 (1998)

[311] D. -H. Yoo, G. -H. Rue, J. -Y. Seo, et al., J. Phys. Chem. B, **106**, 9000 (2002)

[312] X. Y. Zhu, S. M. Lee, Y. H. Lee, et al., Phys. Rev. Lett., **85**, 2757 (2000)

[313] S. Chiashi, S. Watanabe, T. Hanashima and Y. Homma, Nano Lett., **8**, 3097 (2008)

[314] M. R. Pederson and J. Q. Broughton, Phys. Rev. Lett., **69**, 2689 (1992)

[315] D. S. Rawat and A. D. Migone, Phys. Rev. B, **75**, 195440 (2007)

[316] E. Dujardin, T. W. Ebbesen, H. Hiura and K. Tanigaki, Science, **265**, 1850 (1994)

[317] R. S. Ruoff, J. Tersoff, D. C. Lorents, et al., Nature, **364**, 514 (1993)

[318] J. Tersoff and R. S. Ruoff, Phys. Rev. Lett., **73**, 676 (1994)

[319] T. Hertel, R. E. Walkup and P. Avouris, Phys. Rev. B, **58**, 13870 (1998)

[320] J. M. Npoles-Duarte, M. Reyes-Reyes, et al., Phys. Rev. B, **78**, 035425 (2008)

[321] L. A. Girifalco, M. Hodak and R. S. Lee, Phys. Rev. B, **62**, 13104 (2000)

[322] T. Matsumoto and M. Sano, Chem. Phys. Lett., **453**, 229 (2008)

[323] M. Sato and M. Sano, Langmuir, **21**, 11490 (2005)

[324] L. Henrard, E. Hernandez, P. Bernier and A. Rubio, Phys. Rev. B, **60**, 8521 (1999)

[325] Y. Y. Jiang, W. Zhou, T. Kim, et al., Phys. Rev. B, **77**, 153405 (2008)

[326] A. Popescu, L. M. Woods and I. V. Bondarev, Phys. Rev. B, **77**, 115443 (2008)

[327] J. H. Weaver, J. L. Martins, T. Komeda, et al., Phys. Rev. Lett., **66**, 1741 (1991)

[328] X. -Q. Wang, C. Z. Wang, B. L. Zhang, et al., Phys. Rev. Lett., **69**, 69 (1992)

[329] S. V. Kozyrev, V. V. Rotkin, Semiconductors, **27**, 777 (1993)

[330] http://altair.physics.ncsu.edu/projects/c20/c20.html

[331] G. Sun and M. Kertesz, Chem. Phys. Lett., **328**, 387 (2000)

[332] E. K. U. Gross, J. F. Dobson and M. Petersilka, Top. Curr. Chem., **181**, 81 (1996)

[333] A. Banerjee and M. K. Harbola, Phys. Rev. A, **60**, 3599 (1999)

[334] M. van Faassen, L. Jensen, et al., Chem. Phys. Lett., **395**, 274 (2004)

[335] S. Ma and W. Guo, Phys. Lett. A, **372**, 4835 (2008)

[336] E. N. Brothers, K. N. Kudin, et al., Phys. Rev. B, **72**, 033402 (2005)

[337] B. Champagne, E. A. Perpete, et al., J. Phys. Chem. A, **104**, 4755 (2000)

[338] A. Karolewski, R. Armiento, S. Kummel, J. Chem. Theory Comput., **5**, 712 (2009)

[339] S. J. A. van Gisbergen, P. R. T. Schipper, et al., Phys. Rev. Lett.,**83**, 694 (1999)

[340] M. W. Schmidt, K. K. Baldridge, et al., Comput. Chem., **14**, 1347 (1993)

[341] A. Ural, Y. Li and H. Dai, Appl. Phys. Lett., **81**, 3464 (2002)

[342] S. A. C. McDowell, R. D. Amos, N. C. Handy, Chem. Phys. Lett., **235**, 1 (1995)

[343] S. J. A. van Gisbergen, J. G. Snijders et al., J. Chem. Phys., **103**, 9347 (1995)

[344] P. Kowalczyk and R. Holyst, Environ. Sci. Technol., **42**, 2931 (2008)

[345] http://www.ioffe.ru/SVA/NSM/Semicond/GaP/bandstr.html

[346] O. I. Micic, J. R. Sprague, C. J. Curtis, et al., J. Phys. Chem., **99**, 7754 (1995)

[347] R. B. Huang, P. Zhang, W. Y. Li, et al., Univ. (Nat. Hist.), **31**, 160 (1992)

[348] P. Karamanis, C. Pouchan, and G. Maroulis, Phys. Rev. A, **77**, 013201 (2008)

[349] S. Burrill and F. Grein, J. Mol. Struct.(Theochem), **757**, 137 (2005)

[350] A. H. Cowley, R. A. Jones, Angew. Chem., **102**, 1235 (1989)

[351] P. P. Rushton, S. J. Clark, and D. J. Tozer, Phys. Rev. B, **63**, 115206 (2001)

[352] Y. -Z. Lan, W. -D. Cheng, D. -S. Wu, et al., Chem. Phys. Lett., **372**, 645 (2003)

[353] M. Gruning, O. V. Gritsenko, et al., J. Chem. Phys., **116**, 9591 (2002)

[354] A. Banerjee, A. Chakrabarti, T. K. Ghanty, J. Chem. Phys., **127**, 134103 (2007)

[355] A. Banerjee, T. K. Ghanty, A. Chakrabarti, J. Phys. Chem. A, **112**, 12303 (2008)

[356] S. J. A. van Gisbergen, J. M. Pacheco, et al., Phys. Rev. A, **63**, 063201 (2001)

[357] R. G. Parr, Z. Zhou, Acc. Chem. Res., **26**, 256 (1993)

[358] M. G. Mayer, J. H. D. Jensen, Elementary Theory of Nuclear Shell Structures, John Wiley & Sons: New York (1955)

[359] W. A. De Heer, et al., Sol. State Phys: Adv. in Res. and Appl., **40**, 93 (1987)

[360] M. K. Harbola, Proc. Natl. Acad. Sci. U.S.A., **89**, 1036 (1992)

[361] G. Herzberg, Molecular Spectra and Molecular Structure I. Spectra of Diatomic Molecules, New York: Van Nostrand: Reinhold (1950)

[362] K. P. Huber, G. Herzberg, Molecular Spectra and Molecular Structure IV. Constants of Diatomic Molecules, New York: Van Nostrand: Reinhold (1979)

[363] R. Janoschek, Pure Appl. Chem., **73**, 1521 (2001)

[364] L. A. Curtiss, K. Raghavachari, et al., J. Chem. Phys., **94**, 7221 (1991)

[365] S. Yanagisawa, T. Nakajima, et al., J. Mol. Struct. (Theochem), **537**, 63 (2001)

[366] D. C. Patton, M. R. Pederson, Int. J. Quantum Chem., **69**, 619 (1998)

[367] D. C. Patton, M. R. Pederso, Phys. Rev. A, **56**, R2495 (1997)

[368] G. L. Gutsev, C. W. Bauschlicher Jr, J. Phys. Chem. A, **107**, 4755 (2003)

[369] D. Fritsch, K. Koepernik, M. Richter, H. Eschrig, J. Comp. Chem., **29**, 2210 (2008)

[370] J. R. Lombardi, B. Davis, Chem. Rev., **102**, 2431 (2002)

[371] A. Jiemchooroj, B. E. Sernelius, P. Norman, J. Comp. Meth. Sci. Eng., **7**, 475 (2007)

[372] I. C. Gerber, J. G. Angyan, Chem. Phys. Lett., **416**, 370 (2005)

[373] T. K. Ghosh, K. Tanaka, Y. Mochizuki, J. Mol. Struct. (Theochem), **451**, 61 (1998)

[374] K. Balasubramanian, J. Phys. Chem., **94**, 7764 (1990)

[375] Y. Mochizuki, K. Tanaka, Chem. Phys. Lett., **274**, 264 (1997)

[376] I. Shim, M. Sai Baba, K. A. Gingerich, Chem. Phys., **277**, 9 (2002)

[377] K. Balasubramanian, Chem. Phys., **119**, 41 (1988)

[378] S. Lee, D. M. Bylander, L. Kleinman, Phys. Rev. B, **37**, 10035 (1988)

[379] E. S. Chen, E. C. M. Chen, J. Phys. Chem. A, **107**, 169 (2003)

[380] B. O. Roos, A. C. Borin, L. Gagliardi, Angew. Chem. Int. Edn., **46**, 1469 (2007)

[381] M. Brynda, L. Gagliardi, B. O. Roos, Chem. Phys. Lett., **471**, 1 (2009)

[382] H. Dachsel, R. J. Harrison, D. A. Dixon, J. Phys. Chem. A, **103**, 152 (1999)

[383] M. A. Ali, Y. K. Kim, J. Phys. B: At. Mol. Opt. Phys., **41**, 145202 (2008)

[384] A. F. Jalbout, et al., J. Mol. Struct. (Theochem), **585**, 205 (2002)

[385] Y. Liang, A. Talebpour, et al., J. Phys. B: At. Mol. Opt. Phys., **30**, 1369 (1997)

[386] Y. Liang, S. Augst, et al., J. Phys. B: At. Mol. Opt. Phys., **27**, 5119 (1994)

[387] V . I. Usachenko, P. E. Pyak, V. V. Kim, Phys. Rev. A, **79**, 023415 (2009)

[388] T. K. Kjeldsen, L. B. Madsen, Phys. Rev. A, **71**, 023411 (2005)

[389] A. R. Miedema, K. A. Gingerich, J. Phys. B, **12**, 2081 (1979)

[390] D. Paschoal, M. F. Costa, et al., J. Mol. Struct. (Theochem), **913**, 200 (2009)

[391] M. Merawa, A. Dargelos, J. Chim. Phys., **95**, 1711 (1998)

[392] V. Tarnovsky, M. Bunimovicz, et al., J. Chem. Phys., **98**, 3894 (1993)

[393] R. J. Wheatley, J. Comput. Chem., **29**, 445 (2007)

[394] E. V. Akindinova, V. E. Chernov, et al., Phys. Rev. A, **79**, 032506 (2009)

[395] W. B. De Almeida, J. Braz. Chem. Soc., **16**, 345 (2005)

[396] V. Magnasco, M. Ottonelli, Chem. Phys. Lett., **248**, 82 (1996)

[397] G. Maroulis, J. Phys. Chem. A, **107**, 6495 (2003)

[398] G. Maroulis, J. Phys. Chem., **104**, 4772 (2000)

[399] A. Abdurahman, A. Shukla, G. Seifert, Phys. Rev. B, **66**, 155423 (2002)

[400] D. Begue, M. Merawa, M. Rerat, C. Pouchan, Chem. Phys. Lett., **301**, 43 (1999)

[401] G. Maroulis, J. Phys. Chem., **118**, 2673 (2003)

[402] G. Maroulis, D. Xenides, J. Phys. Chem. A, **107**, 712 (2003)

[403] G. Maroulis, J. Phys. Chem., **121**, 10519 (2004)

[404] G. Maroulis, Chem. Phys. Lett., **442**, 265 (2007)

[405] M. G. Papadopoulos, H. Reis, A. Avramopoulos, et al., Mol. Phys., **104**, 2027 (2006)

[406] G. Maroulis, Mol. Phys., **77**, 1085 (1992)

[407] G. Maroulis, C. Markis, Mol. Phys., **91**, 333 (1997)

[408] G. Maroulis, P. Karamanis, Chem. Phys., **269**, 137 (2001)

[409] V. E. Bazterra, M. C. Caputo, et al., J. Phys. Chem., **117**, 11158 (2002)

[410] S. Millefiori, A. Alparone, J. Phys. Chem. A, **105**, 9489 (2001)

[411] P. Milani, I. Moullet, W. A. de Heer, Phys. Rev. A, **42**, 5150 (1990)

[412] S. Minemoto, H. Tanji, H. Sakai, J. Chem. Phys., **119**, 7737 (2003)

[413] D. M. Bishop, J. Pipin, J. Chem. Phys., **98**, 522 (1993)

[414] A. Banerjee, J. Autschbach, A. Chakrabarti, Phys. Rev. A, **78**, 032704 (2008)

[415] O. A. Vydrov, T. V. Voorhis, Phys. Rev. Lett., **103**, 063004 (2009)